

#### Underwater sound propagation and mitigation in offshore pile driving

Peng, Y.

10.4233/uuid:61f71fd9-1b7f-4bd0-b47b-e6c43abdf279

**Publication date** 

**Document Version** Final published version

Citation (APA)

Peng, Y. (2025). *Underwater sound propagation and mitigation in offshore pile driving*. [Dissertation (TU Delft), Delft University of Technology]. https://doi.org/10.4233/uuid:61f71fd9-1b7f-4bd0-b47b-e6c43abdf279

Important note

To cite this publication, please use the final published version (if applicable). Please check the document version above.

Copyright

Other than for strictly personal use, it is not permitted to download, forward or distribute the text or part of it, without the consent of the author(s) and/or copyright holder(s), unless the work is under an open content license such as Creative Commons.

Please contact us and provide details if you believe this document breaches copyrights. We will remove access to the work immediately and investigate your claim.

This work is downloaded from Delft University of Technology. For technical reasons the number of authors shown on this cover page is limited to a maximum of 10.

# Underwater sound propagation and mitigation in offshore pile driving

# Underwater sound propagation and mitigation in offshore pile driving

#### **Proefschrift**

ter verkrijging van de graad van doctor aan de Technische Universiteit Delft, op gezag van de Rector Magnificus prof. dr. ir. T.H.J.J. van der Hagen, voorzitter van het College voor Promoties, in het openbaar te verdedigen op Vrijdag 21 Maart 2025 om 10:00 uur

door

#### Yaxi PENG

Master of Science in Offshore and Dredging Engineering, Technische Universiteit Delft, Nederland

Dit proefschrift is goedgekeurd door de promotoren.

#### Samenstelling promotiecommissie:

Rector Magnificus, voorzitter

Dr. ir. A. Tsouvalas, Technische Universiteit Delft, promotor Prof. dr. A. V. Metrikine, Technische Universiteit Delft, promotor

Onafhankelijke leden:

Prof. dr. W.S.J. Uijttewaal,
Dr. ir. D.J. Verschuur,
Prof. dr. S. Sorokin,
Prof. dr. M. Taroudakis,
Prof. dr. M. Taroudakis,
Technische Universiteit Delft, Nederland
Alborg Universiteit, Denemarken
Universiteit van Kreta, Griekenland

Dr. N. Favretto-Cristini, Laboratoire de Mécanique et d'Acoustique, Frankrijk Prof. dr. ir. A.C. Viré, Technische Universiteit Delft, Nederland, reserve member

This work is partly financed by Delft university of Technology and China Scholarship Council.





Keywords: Underwater acoustics, Green's function, Offshore Pile Driving, Noise

mitigation, Offshore Wind Farm, Boundary Element Integral, Analytical

solution

Printed by: Gildeprint B.V. - Enschede

Cover design by: Friday GoldFish Studio

Copyright © 2025 by Y.Peng

ISBN: 978-94-6496-364-9

An electronic version of this dissertation is available at

http://repository.tudelft.nl/.

念念不忘,必有回响。

Wong Kar-wai

# **CONTENTS**

Su	mma	ry		хi
Sa	menv	atting		xiii
Pr	eface			xv
1	Intro	oductio	on	1
1.1 Research Background and Motivation				
		1.1.1	Offshore wind farm and installation of monopiles	2
		1.1.2	Noise assessment	4
		1.1.3	Noise mitigation	5
	1.2	State-o	of-the-art in noise prognosis	7
		1.2.1	Physics and modelling of pile driving noise emissions	7
		1.2.2	Physics and modelling of noise mitigation systems	8
	1.3	Scope	of study	10
	1.4	Thesis	outline	13
2	Acou	ısto-el:	astodynamic Green's Functions	15
	2.1	Theore	etical background	16
	2.2	Cylind	rically symmetric Green's Functions	19
		2.2.1	Propagation of P-SV waves	19
		2.2.2	Root finding in complex plane for acousto-elastic wave propagation	30
		2.2.3	Comparison of various analytical approaches	32
		2.2.4	Validation	41
	2.3	Three	dimensional Green's Functions	43
		2.3.1	Equations of motion	43
		2.3.2	Hankel transform	45
		2.3.3	Transformed displacement and stress fields	45
		2.3.4	Transformed loading conditions	47
		2.3.5	Solutions of Green's function	48
		2.3.6	Validation	48
	2.4	Bound	ary integral equations in an acousto-elastic half-space	51
		2.4.1	Reciprocity theorem in elastodynamics	51
		2.4.2	Boundary integral formulation	51
		2.4.3	Boundary Integral Equation method in three-dimensional field. $$ . $$	53
		2.4.4	Validation	54
2.5 Conclusions			58	

viii Contents

3	Nea	r- and far-field noise and vibration prediction due to offshore pile
	driv	ving 59
	3.1	Model description and governing equations 60
		3.1.1 Description of the model
		3.1.2 Governing equations
		3.1.3 An overview of the computational method 66
	3.2	Sound generation module
	3.3	Sound propagation module
	3.4	Numerical considerations
		3.4.1 Root-finding algorithm and poles
		3.4.2 The branch cuts and branch line integrals 69
	3.5	Numerical results and model validation
		3.5.1 Theoretical benchmark case COMPILE I
		3.5.2 Offshore wind farm in German North Sea
	3.6	Particle motion in seawater and seabed vibration
		3.6.1 Prediction of seabed vibration
		3.6.2 Prediction of particle motion
	3.7	Conclusions
4	Unc	certainty quantification in soil dynamic characterization and its effect
		sound levels 83
	4.1	Model description
	4.2	Geoacoustic modelling of the seabed
		4.2.1 Shear wave speed
		4.2.2 Density
		4.2.3 Compressional wave speed
		4.2.4 Attenuation
		4.2.5 Conclusions
	4.3	Statistical soil modelling
		4.3.1 Statistical analysis of the soil stratifications
		4.3.2 Statistical analysis of the soil properties
		4.3.3 Generation of input data samples
	4.4	Numerical results
	4.5	Conclusions
5	Stud	dy of Sound Escape with the Use of an Air Bubble Curtain 105
	5.1	Model description and mathematical statement
		5.1.1 Description of the model
		5.1.2 Governing equations
	5.2	Noise predictions of non-mitigated field
	5.3	Modelling the air bubble curtain
		5.3.1 Local effective wavenumber in a bubble curtain
		5.3.2 Local transmission coefficients of a bubble curtain

Contents ix

	5.4 5.5		study of the effective wavenumber model study of the complete model including the air-bubble curtain		
		5.5.1 Ma	aximum noise reduction level		
			rtain		
	5.6	Conclusion	ns	126	
6	A T		nsional multi-physics model of an air-bubble curtain	127	
	6.1		ible flow model		
			escription of the model		
			overning equations		
			eld tests campaign		
	6.2		amic and acoustic model for air-bubble curtain		
	6.3		mensional noise prediction model		
	6.4		analysis		
			r volume injection rate		
			ze of the bubble curtain		
			ozzle configuration		
			onfiguration of the DBBC		
			mmary of the analysis		
	6.5				
			xisymmetric model		
			aree-dimensional model		
	6.6	Conclusio	ns	147	
7	Sou	nd maps fo	or impact pile driving	149	
	7.1	Model des	cription	151	
	7.2		rce modelling		
	7.3	Sound pro	pagation in range-dependent environments	152	
	7.4		implementation		
	7.5	Conclusio	ns	159	
8	Con	clusions a	nd recommendations	161	
	8.1	Conclusion	ns	161	
	8.2	Recommen	ndations	164	
A	App	endix		165	
Bi	bliog	raphy		167	
	ossar			181	
	Acknowledgements				
	Curriculum Vitæ				
	List of Publications 18				

## **SUMMARY**

Wind energy plays a significant role as a sustainable source in facilitating the transition to a carbon-free energy supply. As offshore wind farms continue to develop, more wind turbines are being installed at deeper water depths, necessitating larger monopiles as primary foundations. However, this presents technical challenges and environmental concerns. To address these, high blow energy hydraulic hammers are being developed to drive piles into the sediment. Yet, during this installation process, a substantial amount of energy is radiated into the ocean environment through seawater and marine sediment, posing potential risks to aquatic animals. To mitigate the impact of impulsive sound generated by pile driving, regulatory bodies in many countries enforce noise thresholds and mandate assessments of the environmental impact on animal habitats in relevant areas.

In recent decades, extensive research has focused on modeling the underwater noise generated by offshore pile driving, utilizing various computational methods. Typically, a two-step modeling approach is employed, beginning with a sound generation model based on finite elements (FE) or finite differences, followed by a sound propagation model using methods such as the normal-mode method or the parabolic equation method. The seabed is often represented as an equivalent fluid with additional attenuation, despite pile-driving sources emitting both compressional and shear waves. Detailed soil descriptions are crucial for accurately capturing pile vibrations. Semi-analytical models offer valid predictions in the near-field but lack accuracy at larger horizontal distances from the pile. Empirical models struggle to accurately predict sound levels, particularly when considering different soil conditions and noise mitigation systems. This work seeks to address this gap by providing accurate noise prediction over large distances, incorporating detailed sediment descriptions as the first challenge tackled.

Existing models primarily focus on specific aspects of pile driving noise with bubble curtain systems, highlighting the need for a comprehensive and unified framework. Previous studies emphasize the importance of accurately describing the acoustic characteristics of the bubbly layer and the vibro-acoustic interaction between the pile and the surrounding water-soil for effective noise reduction. However, predicting noise reduction achieved by mitigation systems relies heavily on past project experiences, as the formation of bubble flow in offshore environments lacks detailed and accurate measurements. In this study, we aim to capture the acoustic performance of a noise mitigation system and integrate it with the noise prediction model for pile driving, addressing the second identified challenge.

The assessment of particle motions and seabed vibrations is often overlooked in evaluating environmental impact, despite being critical for fish, invertebrates, and crustaceans living in the benthic zone. As these species reside and feed near the ocean floor, changes in particle motion and seabed vibrations can significantly impact their lives, sometimes more so than changes in pressure. This work considers detailed modeling of the seabed for both sound generation and propagation, focusing on particle motions and seabed vibrations as critical indicators for benthic species.

xii Summary

The first objective of the thesis is to develop a computationally efficient method for predicting the generation and propagation of underwater sound associated with impact pile driving at large distances. This model comprises two modules: a sound generation module accurately describing pile-water-soil interaction and sound emission near the pile, and a sound propagation module ensuring high accuracy in wavefield propagation over extended distances. The model significantly advances prediction accuracy, computational efficiency, and flexibility in both near- and far-fields, capturing the vibroacoustic behavior of the pile-water-soil system and accurately describing input wavefields for propagation analysis.

The second objective is to integrate an air bubble curtain into the noise prediction model for offshore pile driving, presenting a complete and efficient modeling approach. This involves modeling the foundation pile, fluid layer, elastic half-space soil medium, and the inhomogeneous bubbly layer of the air bubble curtain. The model includes a noise prediction module for non-mitigated pile driving noise and a noise reduction module for the air bubble curtain system. Boundary integral equations couple the wave field from sound generation and propagation, considering wave attenuation through at the air bubble curtain. This approach allows independent examination of sub-systems, offering flexibility and computational efficiency in noise reduction prediction for various configurations of the air bubble curtain system and pile system.

Finally, a modeling framework is presented for noise generated by impact pile driving, considering range-dependent environments with and without the use of an air bubble curtain system. The framework transforms the wave field into Source Level (SL) for both fluid and soil sources, utilizing diverse mathematical models at accurate and feasible distances. This approach allows examination of uncertainty in environmental and pile parameters individually for each region, providing essential data for assessing the impact of sound on marine life. Sound maps facilitate estimation of maximum impact distances based on sensitivity thresholds of different marine animals inhabiting both the seawater and benthic zones.

## SAMENVATTING

Windenergie speelt een significante rol als duurzame bron bij het faciliteren van de overgang naar een koolstofvrije energievoorziening. Naarmate offshore windparken zich blijven ontwikkelen, worden er steeds meer windturbines geïnstalleerd op grotere waterdiepten, wat grotere monopiles als primaire funderingen vereist. Dit brengt echter technische uitdagingen en milieukwesties met zich mee. Om deze aan te pakken, worden hydraulische hamers met hoge slagenergie ontwikkeld om palen in het sediment te drijven. Tijdens dit installatieproces wordt echter een aanzienlijke hoeveelheid energie uitgestraald in de oceaanomgeving via zeewater en marien sediment, wat potentiële risico's voor aquatische dieren oplevert. Om de impact van impulsief geluid dat door heien wordt gegenereerd te verminderen, handhaven regelgevende instanties in veel landen geluidsdrempels en verplichten zij beoordelingen van de milieueffecten op dierenhabitats in relevante gebieden.

In de afgelopen decennia is uitgebreid onderzoek gedaan naar het modelleren van het onderwatergeluid dat door offshore heien wordt gegenereerd, waarbij verschillende rekenmethoden worden gebruikt. Meestal wordt een tweestaps modelleringbenadering toegepast, te beginnen met een geluidsgeneratiemodel op basis van eindige elementen (FE) of eindige verschillen, gevolgd door een geluidsvoortplantingsmodel met methoden zoals de normalemode-methode of de paraboolvergelijkingsmethode. De zeebodem wordt vaak weergegeven als een equivalent fluïdum met extra demping, ondanks het feit dat heigeluiden zowel compressie- als schuifgolven uitzenden. Gedetailleerde bodemomschrijvingen zijn cruciaal voor het nauwkeurig vastleggen van paalvibraties. Semi-analytische modellen bieden geldige voorspellingen in het nabije veld, maar missen nauwkeurigheid op grotere horizontale afstanden van de paal. Empirische modellen hebben moeite om geluidsniveaus nauwkeurig te voorspellen, vooral bij het beschouwen van verschillende bodemcondities en geluidsbeperkingssystemen. Dit werk probeert deze kloof te overbruggen door nauwkeurige geluidspredictie over grote afstanden te bieden, waarbij gedetailleerde sedimentomschrijvingen als eerste uitdaging worden aangepakt.

Bestaande modellen richten zich voornamelijk op specifieke aspecten van heigeluid met bellenschermsysteem, wat de noodzaak benadrukt voor een alomvattend en verenigd kader. Eerdere studies benadrukken het belang van een nauwkeurige beschrijving van de akoestische eigenschappen van de bellenlaag en de vibro-akoestische interactie tussen de paal en het omringende water-zand voor effectieve geluidsreductie. Het voorspellen van geluidsreductie bereikt door mitigeringssystemen is echter sterk afhankelijk van eerdere projectervaringen, aangezien de vorming van bellenvloeiing in offshore omgevingen gedetailleerde en nauwkeurige metingen mist. In deze studie streven we ernaar de akoestische prestaties van een geluidsbeperkingssysteem vast te leggen en te integreren met het geluidsvoorspellingsmodel voor heien, waarbij de tweede geïdentificeerde uitdaging wordt aangepakt.

De beoordeling van deeltjesbewegingen en bodemvibraties wordt vaak over het hoofd gezien bij het evalueren van de milieueffecten, ondanks dat deze van cruciaal belang zijn xiv Samenvatting

voor vissen, ongewervelden en kreeftachtigen die in de bentische zone leven. Omdat deze soorten zich nabij de oceaanbodem bevinden en voeden, kunnen veranderingen in deeltjesbeweging en bodemvibraties hun leven aanzienlijk beïnvloeden, soms meer dan veranderingen in druk. Dit werk beschouwt gedetailleerde modellering van de zeebodem voor zowel geluidsgeneratie als -voortplanting, waarbij de focus ligt op deeltjesbewegingen en bodemvibraties als kritische indicatoren voor bentische soorten.

Het eerste doel van het proefschrift is het ontwikkelen van een rekenkundig efficiënte methode voor het voorspellen van de generatie en voortplanting van onderwatergeluid dat gepaard gaat met impactheien op grote afstanden. Dit model bestaat uit twee modules: een geluidsgeneratiemodule die nauwkeurig de interactie tussen paal, water en bodem beschrijft en geluidsemissie nabij de paal, en een geluidsvoortplantingsmodule die een hoge nauwkeurigheid in golfveldvoortplanting over lange afstanden waarborgt. Het model verbetert de voorspellingsnauwkeurigheid, rekenefficiëntie en flexibiliteit aanzienlijk in zowel nabije als verre velden, waarbij het vibroakoestische gedrag van het paal-water-bodem systeem wordt vastgelegd en invoergolfvelden voor voortplantingsanalyse nauwkeurig worden beschreven.

Het tweede doel is om een luchtbellenscherm te integreren in het geluidsvoorspellingsmodel voor offshore heien, waarbij een complete en efficiënte modelleringsaanpak wordt gepresenteerd. Dit omvat de modellering van de funderingspaal, vloeistoflaag, elastische half-ruimtegrondmedium en de inhomogene bellenlaag van het luchtbellenscherm. Het model omvat een geluidsvoorspellingsmodule voor niet-gemeten heigeluid en een geluidsreductiemodule voor het luchtbellenscherm. Grensintegrale vergelijkingen koppelen het golfveld van geluidsgeneratie en -voortplanting, waarbij golfdemping door het luchtbellenscherm wordt beschouwd. Deze aanpak maakt een onafhankelijke beoordeling van subsystemen mogelijk, met flexibiliteit en rekenefficiëntie in geluidsreductievoorspelling voor verschillende configuraties van het luchtbellenschermsysteem en het paalsysteem.

Ten slotte wordt een modelleringskader gepresenteerd voor geluid gegenereerd door impactheien, waarbij omgevingen met variërende afstanden worden beschouwd, met en zonder het gebruik van een luchtbellenscherm. Het kader transformeert het golfveld naar Source Level (SL) voor zowel vloeistof- als bodembronnen, waarbij diverse wiskundige modellen op nauwkeurige en haalbare afstanden worden gebruikt. Deze aanpak maakt de beoordeling van onzekerheid in milieu- en paalparameters mogelijk voor elk gebied afzonderlijk, wat essentiële gegevens levert voor het beoordelen van de impact van geluid op het zeeleven. Geluidskaarten vergemakkelijken de schatting van maximale impactafstanden op basis van gevoeligheidsdrempels van verschillende zeedieren die zowel de zeewater- als bentische zones bewonen.

## **PREFACE**

I decided to pursue an academic career as a PhD student in 2017 while finalizing my master's thesis on "Modeling and Development of a Resonator-Based Noise Mitigation System for Pile Driving." At the time, Apostolos was my supervisor, and I remember asking him and Andrei whether I could continue as a PhD student in the group. Looking back, I had just begun to develop an interest in underwater acoustics and Green's functions, but I had no idea that this curiosity would become a defining pivot in my life. To my surprise (and relief), both of them agreed—and so began an incredible journey into the world of underwater acoustics.

This thesis starts with the foundation of Green's functions, exploring their formulations across different media and various analytical solution approaches. Even today, I am still amazed by their universality and elegance. The thesis then introduces a noise prediction model capable of analysing noise and vibration propagation over large distances from a monopile. While the model is quite accurate under the assumption of stratified marine sediments, significant uncertainties remain, particularly in the soil properties—a reminder of the challenges inherent in environmental modelling.

Another key aspect of this work is the modelling of noise mitigation systems. This effort involved developing a multi-physics model for air-bubble curtain systems, integrating multiple components to estimate the noise field when various mitigation strategies are applied. Finally, to assess the impact of underwater noise on marine life, sound maps are essential tools for evaluating noise exposure over large areas. This thesis presents a methodology for generating such sound maps, combining multiple modules developed throughout the research. I hope this section, in particular, will be of interest not only to acousticians but also to marine biologists, regulators, and anyone concerned with the impact of underwater noise on the environment.

I hope you find something intriguing in these pages—whether it's the mathematical beauty of Green's functions, the practical challenges of noise modelling, or the broader implications for marine life. If so, then this journey has been well worth it.

Yaxi Peng Delft, February 2025

1

# Introduction

Offshore wind farms are being installed around the word to generate wind-power electricity. The offshore wind energy can help reduce  $CO_2$  emissions and move towards renewable energy. However, the installation of foundations of offshore wind turbines can generate high-intensity impulsive noise, which has a significant impact on the marine environment. This chapter introduces the research background and the motivation of this thesis. The state of the art of underwater noise prediction for offshore pile driving is reviewed followed by the scope of this work and the research methodology.

W ind energy is expected to contribute significantly to global renewable energy production in the coming decades. The European Union (EU) currently possesses the highest wind energy capacity worldwide [1–3], and its energy target for 2035 includes achieving 350 GW, which equates to supplying 24% of its electricity demand [1]. Offshore wind presents a significant opportunity for achieving carbon neutrality in the foreseeable future. Geospatial analysis, as shown in Fig. 1.1, highlights wind resources across various regions, with high capacity factors indicating abundant wind resources in many areas globally. Numerous countries, particularly within the EU, have substantial offshore wind resources. As illustrated in Fig. 1.2, the capacity of offshore wind energy has been steadily increasing over the years. Wind energy plays a crucial role in progressing toward net zero emissions.

Despite the positive outlook, several challenges must be addressed to accelerate the installation of offshore wind power generators. These include limitations related to wind resource quality and available turbine technologies, as well as significant concerns that are associated with environmental factors, such as the suitability of seabed conditions and regulations concerning competing uses and environmental protection [1–3]. The potential impact of installing and operating wind farms on the environment needs thorough assessment, and knowledge about the potential impact must be improved.

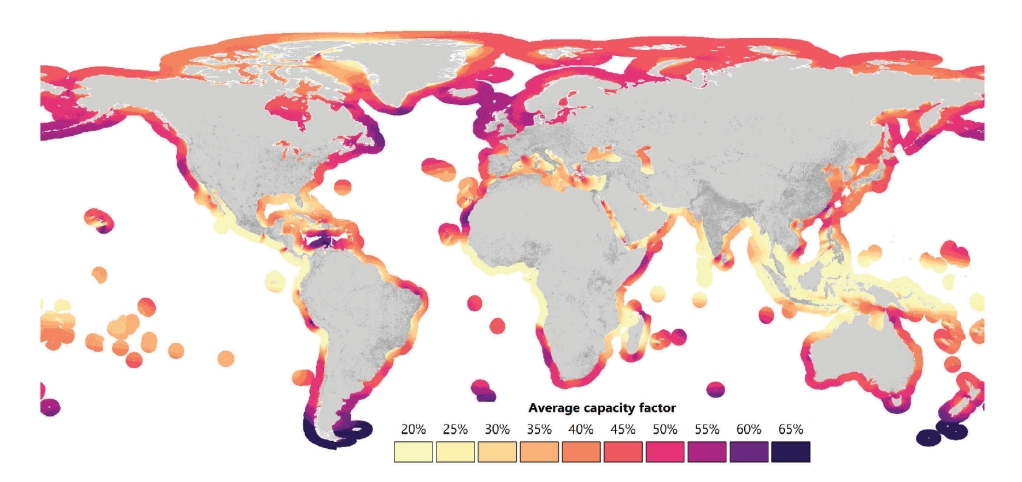


Figure 1.1: Average capacity factors reflect the quality of the wind resources available offshore around the world [1].

#### 1.1 Research Background and Motivation

#### 1.1.1 Offshore wind farm and installation of monopiles

The majority of wind turbines are supported by bottom-founded structures, particularly in shallower water depths, as illustrated in Fig. 1.3. In contrast, floating foundations become a more economical solution in deeper waters. However, several complex challenges still remain when it comes to floating platforms, such as the lifespan of the dynamic power cables and the allowable motions of the systems, especially under harsh offshore environment.

This study is mainly focused on the assessment of the potential impact of the installation of the monopile foundations for offshore wind farms (OWF), which constitute the most widely used foundation systems [4].

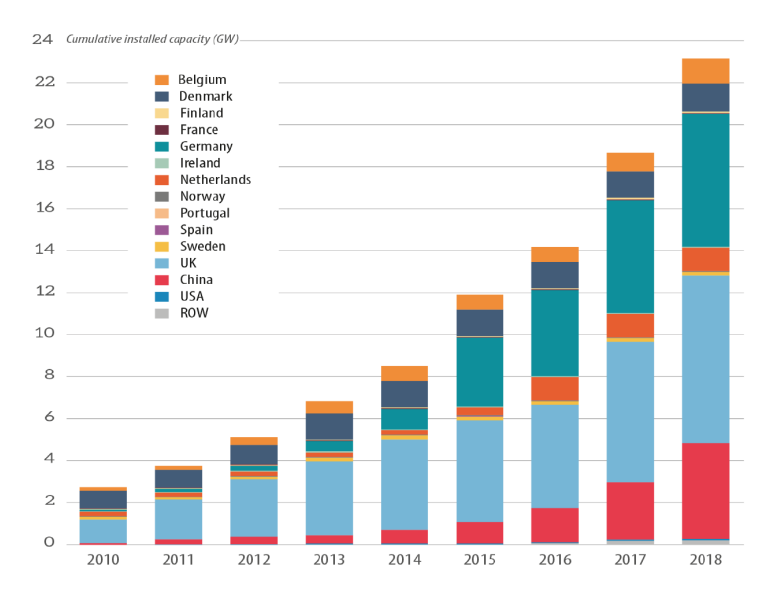
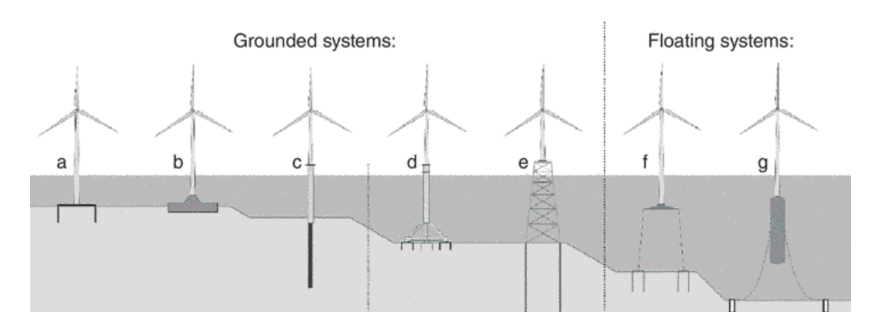


Figure 1.2: Cumulative installed capacity of offshore wind energy worldwide [5].

With the rapid expansion of offshore wind, impact pile driving activities are increasing around the globe. Impulsive pile driving becomes a major noise source of concern [6]. Research regarding the underwater noise pollution has shown that anthropogenic ocean noise related to impact piling can impair sound-sensitive animals' ability to detect vital sound cues, and can have detrimental physiological, behavioural, and ecological impacts on marine animals [6, 7], fishes [8, 9] and aquatic invertebrates [10]. As the pile size grows with the increasing water depth, the occurrence rate and spatial distribution of pile driving noise are increasing accordingly. The noise pollution resulting from piling activities will aggravate the adverse impacts on marine species. The spectrum of the anthropogenic noise emission and hearing range of the fish and marine mammals are depicted in Fig. 1.4, which indicates the wide-band noise exposures on the animals in terms of the frequency content [11]. The issue of underwater noise pollution has drawn attention of the general public, NGOs, and authorities. Thus, the prediction of the underwater noise prior to pile driving activities becomes an indispensable part of environmental impact assessments (EIA's) including noise mitigation plans.

To better predict the offshore piling noise, many studies focused on the mechanisms of noise generation and propagation over the last decade [13–29]. For impact piling, after a single hammer strike, a compressional wave in the pile is generated which propagates along the pile. Due to the Poisson's effect in steel, the vertical compression induces radial expansion of the pile, which causes sound to propagate into the water column and seabed through a coupled fluid-soil–structure interaction. The downward-propagating radial displacement wave within the pile, has a supersonic velocity ( $\sim$ 5015 m/s), surpasses the



1 Introduction

Figure 1.3: Foundations for offshore wind turbines: (a) Bucket/suction caisson: (b) gravity-based; (c) monopile; (d) tripod on bucket/suction caisson; (e) jacket/lattice structure; (f) tension leg platform; and (g) spar buoy floating concept [12].

speed of sound in water, as well as the velocities of compressional and shear waves in the sediment. This results in the formation of an acoustic pattern as an axisymmetric cone, often referred to as a *Mach* cone, within the surrounding medium. The emission of sound during offshore pile driving exhibits significant reliance on factors such as pile configuration, bathymetry, geoacoustic characteristics of the seabed, hammer type and blow energy [30, 31].

#### 1.1.2 Noise assessment

To unify the noise evaluation criteria for impact pile driving, dual exposure metrics are applied widely, including the cumulative sound exposure level SEL and the peak sound pressure level  $L_{p,pk}$  [32–34]. Exposures exceeding either one of the thresholds would possibly lead to auditory injury and increase the risk of causing impaired hearing in the form of temporary threshold shift (TTS) and permanent threshold shift (PTS) [35–37].

However, estimating the effects of anthropogenic noise on fish, invertebrates, crustaceans and marine mammals [37–40] can be challenging. Not only the exposure levels and peak pressure levels demonstrate the severity of the potential effects, frequency of the exposure, duration, spatial and temporal pattern of sound pressure can be critical in the impact assessment. Resent study has demonstrated that particle motion in water and substrate vibration play critical roles in evaluating the adverse effects of noise on the hearing and aquatic life of animals [41–43].

To address the importance of sound frequency, recent efforts in predicting and mitigating underwater noise effects have employed auditory weighting functions [35, 37]. To emphasize noise at frequencies animals are more susceptible to, these weighting functions essentially act as bandpass filters applied to noise exposure before calculating a single, weighted sound pressure level (SPL) or sound exposure level (SEL). However, the accuracy and validity of these marine mammal weighting functions are limited due to the lack of comprehensive data showing the effects of noise frequency among the species. Furthermore, the current regulatory noise threshold for pile driving remains confined to SEL and  $L_{p,pk}$ , suggesting the need for improvement in future assessments.

There is also growing interest in examining the influence of particle motions on the fish and other species that are known to be detectors of such motion [41, 42, 44]. Given

that a substantial amount of energy is transmitted into the seabed during pile driving, it is likely to be detectable by fish and aquatic invertebrates residing in or near the seabed [45]. Considering the significance of water particle motion and substrate vibrations for noise effect on fish and invertebrates, regulators must pay proper attention to assessing their impacts on numerous species. Additionally, addressing data gaps is essential to enhance our understanding of the interactions between water particle motion, substrate vibrations, and perception by aquatic animals [44, 45].

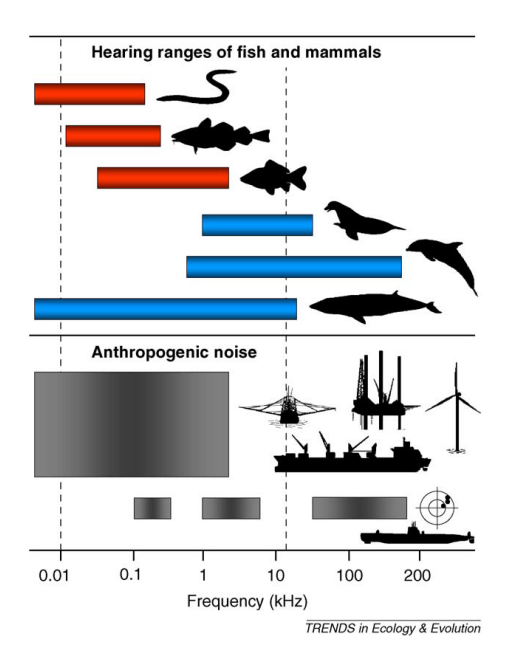


Figure 1.4: Hearing ranges of the fish and mammal species, and the spectrum of the anthropogenic noise [11].

#### 1.1.3 Noise mitigation

To protect the marine ecosystem, regulators in many countries have imposed strict guidelines and rules for the noise emission thresholds in offshore construction activities. Government and international organizations have been taking actions in forming the international policies and strategic plans to understand anthropogenic underwater noise and improve the mitigation and measures to reduce the noise more effectively [46–50]. Many noise mitigation systems (NMS), (i.e. bubble curtains, hydro-sound damper, noise mitigation screen, etc.) have been developed over the last decade to prevent exceeding the threshold limits during pile installation [36, 51–54]. Noise mitigation strategy is required in the phase of planning and assessment of the offshore wind farm project. Effective mitigation measures can largely prevent and reduce the impact of pile driving noise. This requires both, scientific knowledge of environmental impacts, generation and propagation of the noise and the consideration of noise mitigation techniques. The fundamental principles of noise mitigation for offshore pile driving can be divided into two main approaches. The 6 1 Introduction

1

first approach focuses on mitigation methods to minimize the noise generated directly at the source, whereas in the framework of the second approach, measures are taken to attenuate the sound as it travels through the water column [55, 56].

To reduce noise emissions originating from the source, ongoing developments have been focusing on minimizing the noise generated by impact hammers as presented in Table 1.1. One promising approach involves extending the duration of the ram impulse by temporarily storing energy within the hammer components. This energy storage can effectively alter the frequency spectrum of the energy, thereby decreasing noise emissions [57]. New technologies employ various methods to extend the impulse duration. For example, BLUE piling utilizes a water column, PULSE employs an adjustable fluid column positioned between the hammer components, and the MENCK Noise Reduction Unit (MNRU) incorporates an additional elastic hammer component situated between the impact weight and the anvil [56, 57]. Besides the impact hammer, vibratory techniques are being employed during the installation of the monopile, either as a replacement or in combination with impact hammers. The emitted wave field is significantly altered with the change in the installation method [30, 31, 56, 58]. Furthermore, the non-linear conditions at the pile-soil interface can have a substantial impact on the dynamic response of the pile and the wave field in the surrounding medium [59–62].

To mitigate the sound by the blockage of the noise transmission paths in the water column, various technologies have been developed over the last decades, e.g., the air-bubble curtain system, the hydro-sound damper system, the noise mitigation screen and resonatorbased noise mitigation systems as shown in Table 1.1 [51-53]. The primary mechanisms employed by noise mitigation systems blocking the water-borne path can be categorized into two main approaches. Firstly, they create an impedance mismatch in the transmission path within the water column, which reduces noise through reflection, scattering, and refraction of sound waves. Secondly, they dissipate and dampen energy through resonance or local absorption. One example of such a system is the Air Bubble Curtain (ABC), which achieves noise reduction through a substantial impedance mismatch between seawater and the bubble-fluid mixture, as well as the resonance of bubbles [63]. Prior to monopile installation, perforated hoses are strategically positioned on the seabed in a circular or elliptical layout. Air is then injected from air-compressor vessels through risers connected to the hoses, releasing freely rising air bubbles from nozzles and creating a layer of bubbly mixture [64-68]. The noise mitigation screen (NMS) employs a shielding effect by using an air-filled interspace to acoustically decoupled the double shell [56]. Similarly, the cofferdam system consists of a single wall steel tube, which allows the pile be installed into the system with radiating sound into the air instead of the seawater [69]. Hydro-Sound-Damper system (HSD) consists of encapsulated balloons and PE foam elements connected to a ballasted net, which can be lowered to the sea floor near the pile using winches [56, 70, 71]. Its main mechanism involves the absorption and scattering of acoustic waves by the resonators and material damping. Another system, an alternative to the HSD, is the open-ended resonators' system. This system differs from fully encapsulated resonators and employs two fluids, air and water, to tune and broaden the range of resonant frequencies [52]. The near-field systems discussed above, such as the NMS, HSD, and Helmholtz resonator-based systems, can be used in combination with air bubble curtain systems deployed at relatively far-field, including single big bubble curtains (SBC), double big bubble curtains (DBBC),

1

and even triple big bubble curtains (TBBC), to enhance noise mitigation performance.

#### 1.2 STATE-OF-THE-ART IN NOISE PROGNOSIS

#### 1.2.1 Physics and modelling of pile driving noise emissions

Over the past decades, extensive research has focused on modelling the underwater noise generated by offshore pile driving using various computational methods [58]. Most models employ a two-step approach: first, a sound generation model based on either finite elements (FE) [13, 14] or finite differences [21] is used; second, a sound propagation model transmits the sound over larger distances, utilizing methods such as the normal-mode method [22, 23], the wavenumber integration method [24], or the parabolic equation method [25]. Reinhall and Dahl [13] were the first to systematically examine the noise generated by impact pile driving. Their FE simulations demonstrated that sound waves in seawater originate from the radial expansion of the pile surface, caused by compressional waves traveling down the pile at supersonic speeds, radiating waves in the form of Mach cones. Fricke and Rolfes [26] proposed a comprehensive physics-based noise prediction model, including soil modelling as an elastic medium in the near-field and the impact hammer. Their results agreed well with noise measurements, confirming the model's validity and showing that the primary damping mechanism for pile vibration is the radiation of shear waves into the soil, rather than frictional sliding between the pile and soil. Several simplified models have replicated the sound field from pile driving using the wavenumber integration technique [72] or the parabolic equation method [13, 27]. These results generally showed good qualitative agreement with more detailed FE simulations. Lippert and Estorff [24] presented a coupled FE and wavenumber integration model, investigating the influence of sediment parameter uncertainties through Monte-Carlo simulations. Different models' numerical predictions were broadly consistent with each other [24]. With few exceptions [26], the seabed is usually approximated by an equivalent acoustic fluid with additional attenuation. However, pile-driving sources located in the seafloor emit both compressional and shear waves [73-75]. Accurate noise source characterization requires a detailed soil description to capture pile vibrations correctly. Recent models [23, 28] have examined the influence of pile inclination and three-dimensional effects, applicable to both raked and vertically positioned piles in various environments.

In addition to the aforementioned models, several semi-analytical models have been developed to predict underwater noise from pile driving [15–20]. Tsouvalas and Metrikine [15] developed a model that adequately describes critical system components, such as the hydraulic hammer, the pile, and the water, with the seabed represented by linear springs and dashpots to account for soil elasticity and energy absorption. This model primarily focuses on pile dynamics and near-field noise prediction, not very close to the seabed surface. Subsequently, Tsouvalas and Metrikine [16, 76] developed a more comprehensive pile-water-soil interaction model, including a three-dimensional description of the water-saturated seabed as a layered elastic medium. Their work also investigated the significance of seabed-water interface waves (Scholte waves), later confirmed by measurement data [55]. Although Scholte waves travel at relatively low speeds and attenuate quickly, they must be accounted for to accurately describe pile vibrations and energy distribution [77–79]. The primary noise transmission path is in the water column as Mach cones, with the secondary

path primarily through Scholte waves propagating along the seabed-water interface [74, 75]. Examining these transmission paths is crucial for effectively blocking noise propagation and optimizing noise mitigation systems. Deng et al. [19], similar to the semi-analytical model by Tsouvalas [15], focused on the influence of non-axisymmetric impact loading and the interaction between the anvil and the pile. In addition to these semi-analytical models, Lippert et al. [80] developed a damped cylindrical spreading (DCS) model to estimate the sound exposure level due to impact piling using an analytical approach. A linear mixed model was then introduced [81] that accounts for sound propagation variability, later extended with regression analysis for acoustic impact criteria [32].

#### 1.2.2 Physics and modelling of noise mitigation systems

#### OVERVIEW OF NOISE MITIGATION MEASURES

As discussed briefly in section 1.1, various noise mitigation techniques have been developed for offshore pile driving. An overview of the existing noise mitigation measures is summarized in Table 1.1, where the applicability and performance<sup>1</sup> of these systems are evaluated.

Mitigating noise at the source is considered the most effective and primary approach, achieved either through modifying the impact hammer or substituting it with a vibratory shaker. Modified hammer components, such as Blue Piling and Pulse units, do not completely change the waveform but prolong the pulse duration, shifting a portion of the energy to lower frequencies. Vibratory installation techniques, such as Gentle Driving of Piles (GDP), involve low-frequency axial and high-frequency torsional vibrations, reducing noise emissions by shifting more soil vibration from axial to torsional motion [60]. The models developed to predict noise emission from impact pile driving can still be suitable for the modified impact hammer units by adjusting the forcing functions at the pile head. However, for vibratory pile driving, more advanced models are required as pile-soil interaction becomes essential for noise generation [59, 60, 62].

Both the Noise Mitigation Screen (NMS) system and the cofferdam employ a shielding effect to decouple pile vibration from pressure waves radiated into the seawater. However, as monopile sizes and water depths increase, deploying such systems offshore becomes challenging. Ground vibrations can excite the entire system, potentially radiating more energy at lower frequencies, and sound may escape through the seabed, channelling back into the water column. Resonator-based systems like HSD and the Helmholtz resonator system offer flexibility in adjusting the range of resonance frequencies to suit specific needs and can be customized for various water depths and pile dimensions [82]. Both systems can be attached to the ballast net or gripper of the monopile, enabling fast and easy deployment and making them less sensitive to the wave and current conditions. However, for all near-field noise mitigation systems, especially in the presence of thicker soft clay layers, it can be challenging to mitigate the sound as a significant amount of energy is radiated through the sediment and at lower frequencies.

<sup>&</sup>lt;sup>1</sup>The noise reduction levels presented in this table are approximate and have been compiled from numerical simulations and measurement data obtained across various pile configurations, blow energy levels, and offshore environmental conditions (including variations in the bathymetry, currents and soil conditions). This variability reflects the considerable uncertainties associated with the expected noise reduction levels.

1

The air bubble system utilizes the impedance mismatch to reflect the incident wave field and resonance of bubbles to absorb acoustic energy [83]. This system can be deployed at a greater distance, up to 200 meters from the pile. Performance is adjustable through hosenozzle configurations, air volume injection rates, and hose geometry. It can also be used in combination with other systems, such as modified impact hammers, HSD, and Helmholtz resonator-based systems, to achieve better noise reduction. Although the bubble curtain system is commonly used and it is effective, its performance is not entirely predictable. This is due to the limited availability of publicly accessible measurement data and available noise prediction models specifically designed for the bubble curtain system. The industry is making efforts to understand the working mechanism of bubble curtains and improve noise reduction performance. Additionally, there is increasing interest in investigating the main mechanisms of noise attenuation with the use of bubble curtains and predicting their acoustic performance when applied to offshore pile driving [63, 66–68].

#### MODELLING OF AIR-BUBBLE CURTAIN SYSTEMS

The DBBC system is usually modelled as a fully absorbing impedance boundary condition around the pile in the finite element models [84]. In the semi-analytical model by Tsouvalas and Metrikine [63], the air-bubble curtain is considered as a more realistic homogeneous medium with a constant thickness over the entire water depth and with frequency- and depth -dependent wave speed. Based on the dynamic sub-structuring approach, the modelling domain is divided into the pile, water, soil and bubbly mixture sub-domains [63]. The technique allows the coupling of the complete system through the interface between the structure, surrounding medium and the bubble curtains. Sertlek and Tsouvalas developed a coupled mode theory model for the wave propagation through an air bubble curtain, which is based on the orthogonality of the acousto-elastic modes [85]. To understand the bubble dynamics within the bubble curtains, a Computational Fluid Dynamic (CFD) model was proposed by Gottsche [65]. The bubble distribution and gas volume fraction are determined with a CFD model. The noise radiation during pile driving is simulated by Finite Element Analysis and an Effective Medium Approach in the near field, while a Parabolic Equation model is employed in the far field. However, the bubble distribution is assumed constant over the entire domain, which is not valid for accurate predictions. An integral approach for deriving the local distribution of the air fraction was developed later by Bohne in 2019 [66]. The model presents a local distribution of the effective wavenumber, which can be used in the acoustic model for determining the transmission characteristics of the bubble curtain. The bubble formation process directly at the nozzle is later incorporated into the model in [67], which is coupled to the fluid mechanism and allows the bubble generation to a greater distance from the nozzle. Measurements have been conducted to examine the hydraulic properties of the bubble curtain including the local void fractions and bubble size distributions [86]. The hydrodynamic models [66, 67] emphasize the importance of providing an accurate description of the acoustic characteristics of the bubbly layer when modelling noise mitigation using the air-bubble curtain system. It is crucial to note that the performance of air-bubble curtains can exhibit significant variations in the azimuthal direction due to inherent differences in airflow circulation through the perforated pipes situated on the seabed surface. Additionally, the rate of airflow through the nozzles significantly influences bubble generation and development. Accurately determining the airflow velocity is crucial, as the initial conditions at the nozzle are highly sensitive factors in 10 1 Introduction

1

the generation and development of the air-bubble curtain in water. Furthermore, the soil conditions play a critical role in the effectiveness of the air-bubble curtain, considering that a substantial amount of energy is transmitted through marine sediments. It is worth noting that the existing models primarily focus on specific aspects of the modelling process related to pile driving noise when using the bubble curtain system, which highlight the need for a more comprehensive and unified modelling framework that accounts for all these critical factors.

#### 1.3 Scope of study

From the discussion above, it is clear that the prediction of the radiated sound field with and without the noise mitigation systems is a critical step in assessing the environmental impact of the underwater noise induced by offshore pile driving. Over the last decades, many models have been developed for predicting unmitigated noise from impact pile driving, which can be further classified into three categories: detailed FE models coupled to the far-range sound propagation models, semi-analytical models and simplified empirical models. Models of the first category require considerable computational efforts due to the very fine meshes used for waves propagating at higher frequencies. The semi-analytical models of the second category are valid in the near-field but not at a larger horizontal distance from the pile. For the third group of empirical models, the sound levels cannot be accurately predicted, especially when different soil conditions and noise mitigation systems need to be considered.

To date, there is limited research in the underwater noise prediction modelling when the noise mitigation systems are deployed. Previous works show the significance of the accurate description of the acoustic characteristics of the bubbly layer and the vibro-acoustic interaction between the pile and the surrounding water-soil in the noise reduction with the use of an air bubble curtain. However, the prediction of noise reduction achieved by mitigation systems is mainly estimated by accumulated experiences from past projects. The formation of the bubble flow in offshore environment still lacks sufficient and accurate offshore measurements. Several models have been developed for the air bubble curtain system. The semi-analytical model developed by Tsouvalas and Metrikine [63] considers the complete pile-water-soil system with an air-bubble curtain layer. However, the bubbly layer is described as a homogeneous medium with invariant thickness along the water depth by assuming the air bubbles rise solely vertically and are not drifting. The formation and the break-up of the bubbles were modelled by Bohne et al in 2019 [66]. This study considers the local distribution of the gas fraction within the bubble curtain and the formation of the bubbly flow are influenced by the water depth, nozzle configuration and air volume injection. The complex turbulent flow in bubble curtain is described with a bimodal bubble size distribution in a follow-up work by Bohne [67]. However, all modelling efforts here focus on specific aspects of the modelling process, and there is still a lack of a unified modelling framework.

The aim of this thesis is to present a computationally efficient method for the prediction of the generation and propagation of the sound field associated with impact piling at large (from the pile) distances overcoming the limitations of earlier models. The complete model consists of two modules: i) a sound generation module aiming at the accurate description of the pile-water-soil interaction together with the sound emission in the

Table 1.1: Overview of existing noise mitigation systems for offshore pile driving [53, 56, 69] including concepts of various approaches shown for each system.

#### Noise Mitigation Measures

#### **Noise Mitigation Measures**

#### Modified impact hammer unit: EQ-piling, PULSE

Mitigation Principle: prolongation of the pulse duration Description:

- the frequency spectrum of radiated waves is modified
- the capacity and reliability to be improved
- compatible with certain types of hammers
- $\Delta$  SEL: 19-24 dB (EQ),  $\sim$  9dB (PULSE) [56] © IOIP



#### Vibro-hammer

 $\label{eq:mitigation} \textit{Mitigation Principle}: \ \text{modification of the frequency and form of the radiated waves}$ 

Description:

- the frequency spectrum of radiated waves are modified
- the drivability and reliability to be improved
- Δ SEL: 10-20 dB [56]
- © GDP © CAPE Holland

#### ABC system

Mitigation Principle: impedance mismatch by air-bubble layer and resonance of bubbles (depends on the frequency spectrum of radiated noise)

Description:- reflection, scattering and refraction of the radiated waves, resonance of the bubbles

- influenced by the environmental conditions; sound escape through the soil-borne path at a larger distance above the radius of the bubble curtain; adjustable by hose-nozzle configuration and air compression volume rate
- Δ SEL: up to 18 dB by DBBC, 40m water depth [56]
   © Hydrotechnik Lübeck





### Integrated monopile installer (Noise Mitigation Screen System)

Mitigation Principle: impedance mismatch, using air to decouple the pile from the seawater

Description:

- reflection and scattering of the waves
- significant amount of energy radiated through the soil-borne path
- complex and slow deployment and heavy structure
- $\Delta$  SEL: 13-16 dB, less than 40m water depth [56]
- © Ørsted © IOIP

#### Cofferdam system

Mitigation Principle: impedance mismatch, using air to decouple the pile from the seawater

Description:

- significant amount of energy radiated through the soil-borne path
- complex and slow deployment and heavy structure
- $\Delta$  SEL: up to 23 dB,  $\sim$  15m water depth [56]
- © K.E. Thomsen

#### Helmholtz resonator-based system

 ${\it Mitigation Principle}: {\it modification of the frequency and form of the radiated waves}$ 

Description:

- the resonance of the Helmholtz system
- the tonable frequency spectrum of noise reduction
- significant amount of energy
- radiated through the soil-borne path
- fast deployment and customizable system
- Δ SEL: 8 dB, up to ~ 40m water depth [87]
- © AdBM Technology

#### HSD system

 ${\it Mitigation Principle}: resonance of the encapsulated balloon and material absorption$ 

Description:

- absorption of the energy by the resonance, scattering, reflection and damping of the sound waves
- significant amount of energy radiated through the soil-borne path
- fast deployment and customizable system
- Δ SEL: 10-13 dB, less than 45m water depth [56]
- © K.-H. Elmer, OffNoise Solutions











12 1 Introduction

1

vicinity of the pile, and ii) a sound propagation module aiming at the propagation of the wavefield at larger distances with high accuracy. The main contribution of this study is that it advances the accuracy, computational efficiency and flexibility of the noise prediction in both near- and far-fields. The vibroacoustic behaviour of the coupled pile-water-soil system is described in the model in the near-field. It provides an accurate description of the input wavefield in terms of both stresses and displacements at the pile proximity. This field is subsequently fed into the sound propagation module. The contour integration technique in the wavenumber domain, as adopted in the latter approach, enhances the mathematical treatment of the Green's function for an acousto-elastic layered half-space. The choice of the branch cuts ensures both stability and convergence of the obtained solution. The attenuation in multilayered soil is included by identifying the exact poles and branch cuts in the complex wavenumber plane, which is especially important for noise predictions up to a few kilometres provided that the bathymetry is constant. The accuracy of the model predictions is demonstrated by means of comparison against measurement data up to 1500m from the pile. Apart from the pressure waves in the water column and compressional and shear waves in the seabed, the Scholte and Stoneley waves at the water-soil and soil-soil interfaces are captured in both modules. Compared to the classical FE models coupled to the propagation models, the model presented herein is computationally more efficient and can be used in probabilistic analysis of noise prediction involving a large number of simulations with less computational effort. Compared to the equivalent fluid-based, far-range sound propagation model, the sound propagation module provides a more detailed description of the elastic seabed. Finally, in the proposed modelling framework, the eigenproblems of the shell and the surrounding acousto-elastic medium are solved independently, which provides great flexibility in examining various configurations of the system. The response of the pile and the acousto-elastic medium can then be derived for the coupled problem using the given modal sets and the mode-matching method, which reduce the computation time significantly. The present model allows to conduct an in-depth analysis of water- and soil-borne noise transmission paths independently and can be used for the prediction of noise reduction level by combining it with various noise mitigation systems, i.e., air bubble curtain system, hydro-sound damper system and underwater Helmholtz resonators. This unified modelling framework is the first novel contribution of this work.

This thesis also aims to present a complete and computationally efficient modelling approach, which incorporates the air bubble curtain into the noise prediction model in offshore pile driving. To the best of the author's knowledge, no model to date includes the complete system involving the foundation pile modelled as a linear elastic thin shell, a fluid layer overlying an elastic half-space soil medium and the inhomogeneous bubbly layer with the fluid dynamic and turbulent-flow characteristics of an air bubble curtain. In this work, a two-step approach is used to predict the noise reduction by an air bubble curtain. The complete model consists of two parts; the noise prediction model for the non-mitigated field from pile driving which includes two modules, the sound generation module in the vicinity of the pile, the sound propagation module to propagate the radiated wave field at larger distances, and the noise reduction model capturing the transmission characteristics of an air bubble curtain. The sound generation module is based on the earlier work by Tsouvalas and Metrikine [16], and captures the pile-water-soil interaction and propagate the radiated waves in the pile proximity. The sound propagation module

1

describes the seabed as a layered elastic half-space and allows one to propagate the wave field at larger distances [29, 68, 88]. The noise reduction module considers the sound mitigation by the air bubble curtain and is based on the integral model developed by Bohne et al. [67]. The local transmission functions of the bubble curtain including both depth- and frequency-dependence are coupled to the sound propagation module. Boundary integral equations are then employed to couple the wave field from the sound generation and propagate it to larger distances from the pile with the use of the sound propagation module considering the local attenuation at the air bubble curtain. The modelling approach ensures an accurate description of the individual systems with the individual module being verified by measurement data and results from the benchmark cases in literature.

The adopted modelling approach allows one to examine the sub-systems independently and is the first one which is generated for a 3D configuration of the BBC system. Compared to the FEM-models, this gives great flexibility and computational efficiency in the noise reduction prediction for examining various configurations of the air bubble curtain system and pile system. The model can be used for sensitivity studies and probabilistic analysis, which usually involves a great number of simulations with less computational effort. The influence of local air fraction, nozzle size and location of the air bubble curtain and the configuration of the pile-water-soil system on the reduced noise can be examined. The maximum noise reduction potentials at specific site can also be predicted by eliminating the water-borne transmission path and allowing the transmission of energy through the soil alone. The integration of the air-bubble curtain into the earlier mentioned modelling framework is the second novel contribution of this thesis.

#### 1.4 THESIS OUTLINE

The structure of this thesis is as follows.

Chapter 2 presents the derivation of the Green's functions for the acousto-elastodynamic problem, which provides the theoretical background of the study. The formulation of the Green's functions advance the mathematical and computational treatments of the boundary value problem involving an three-dimensional acousto-elastic multilayered half-space. By virtue of a method of displacement potentials, it is shown that there is an elegant mathematical structure underlying this class of three-dimensional elastodynamic problems which warrant further attention. To encompass arbitrarily distributed loads, ring-load Green's functions for stresses and displacements are generalized into complex-plane line-integral representations.

In Chapter 3, a computationally efficient modelling approach is presented for predicting underwater noise radiation from offshore pile driving. The complete noise prediction model comprises two modules. First, a sound generation module is adopted to capture the interaction between the pile, the fluid, and the seabed, aiming at modelling the sound generation and propagation in the vicinity of the pile. Second, a sound propagation module is developed to propagate the sound field at larger distances from the pile. To couple the input wavefield obtained from the sound generation module, the boundary integral equations (BIEs) are formulated based on the acousto-elastodynamic reciprocity theorem. To advance the mathematical formulation of the BIEs, the Green's tensor for an axisymmetric ring load is derived using the contour integration technique. The model advances the computational efficiency and flexibility of the noise prediction in both near-

14 1 Introduction

and far-fields from the pile. Finally, model predictions are benchmarked against a theoretical scenario and validated using measurement data from a recent offshore pile-installation campaign.

In Chapter 4, a probabilistic quantification framework is established to evaluate the significance of the uncertainties and quantify its influence over the range. Considering the uncertainties through statistical approaches, the sound levels with the probabilities of occurrence are evaluated. An investigation is performed to highlight correlation between the soil properties and the sound levels obtained. To examine the parameter uncertainties in noise prediction through probabilistic modelling approach such as Monte-Carlo simulation. The approach is significant to quantify the risk of the exceeding the upper bound of sound levels.

In Chapter 5, the effectiveness of an air bubble curtain system is examined. The focus is placed on the evaluation of noise transmission paths, which are essential for the effective blockage of sound propagation. A coupled two-step approach for the prediction of underwater noise is adopted, which allows one to treat the waterborne and soil-borne noise transmission paths separately. The complete model consists of two modules: a noise prediction module for offshore pile driving aiming at the generation and propagation of the wave field and a noise reduction module for predicting the transmission loss in passing through an air bubble curtain.

In Chapter 6, a multi-physics model for modelling noise mitigation using an air-bubble curtain is developed. The complete modelling chain is introduced. The proposed approach allows capturing the air transportation in the hose, bubble generation and development through each nozzle, noise mitigation at the ABC and propagation in the field. The formulation of the three-dimensional acousto-elastic boundary integral equation is also presented. The method provides a foundation for evaluating the three-dimensional behaviour of the air bubble curtain system. The model incorporates the azimuthal dependent behaviour of the air-bubble curtain, which allows to examine the variation in the airflow circulation through the hoses.

In Chapter 7, a framework is presented for modelling underwater noise from impact pile driving, considering both scenarios with and without an air-bubble curtain system, across large distances. The model incorporates range-dependent water depth and elastic multilayered sediment. Additionally, sound mapping is implemented to estimate the potential impact area of the radiated noise on various species, including analysis of the broadband frequency spectrum.

In Chapter 8, the main findings of this thesis are summarized with an eye on future developments in the field.

1

2

# ACOUSTO-ELASTODYNAMIC GREEN'S FUNCTIONS

To advance the mathematical and computational treatments of the boundary value problem involving a three-dimensional acousto-elastic multilayered half-space, the derivation of the Green's functions for the acousto-elastodynamic problem is presented. By virtue of the method of displacement potentials, it is shown that there is an elegant mathematical structure underlying this class of three-dimensional dynamic problems which warrant further attention. To encompass arbitrarily distributed loads, ring-load Green's functions for stresses and displacements are transformed into complex-plane line-integral representations. This chapter delves into numerical considerations, highlights assumptions of the various computational methods, and lays the groundwork for subsequent chapters where the models undergo further verification and application. As such, this chapter refrains from presenting novel findings. However, the theoretical framework discussed and the numerical methods adopted are tailored to the vibroacoustic problems at hand resulting at computational approaches which are considerably faster than others typically applied in standard Finite Element or Boundary Element packages.

The oceanic environment is a highly complex domain characterized by variations in salinity, temperature, water depth, sediment composition, soil characteristics, geological strata, and more. These variances in medium properties, bathymetry, and geological features, lead to the changes in the density and speed of sound waves as they propagate through the media. Nevertheless, the inherent heterogeneity of the medium can be reduced to a horizontally stratified waveguide problem, which can be effectively addressed using both numerical and analytical methods as discussed in this chapter. This horizontal stratification of the sediment layers is caused by natural geological processes and can be considered realistic at least for close-range sound predictions. In Fig. 2.1, a simplified representation of the oceanic environment is illustrated, under the assumptions of parallel interfaces and homogeneous material properties within each layer.

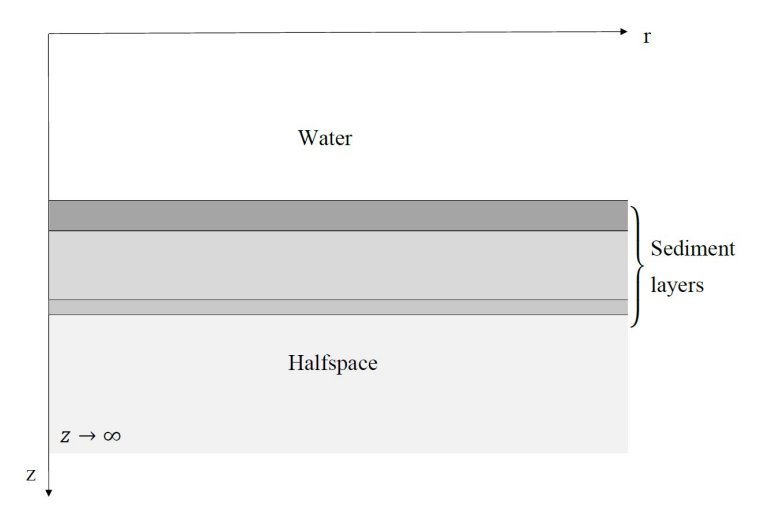


Figure 2.1: Schematic depiction of the horizontally stratified marine environment.

#### 2.1 Theoretical background

Sound propagation models based on normal mode method (NM) have been used in many fields of underwater acoustics research during the last half century. The solutions can be applied in the field of seismic wave propagation, acoustic monitoring in ocean environments, shipping noise, acoustics of renewable energy development, especially increasing anthropogenic activities such as pile driving [89]. The primary feature of the normal mode method is that it allows one to examine the individual contributions of different wave forms in the total acoustic field.

The normal mode solutions to the sound propagation problem in a fluid layer overlying a liquid half-space, called the *Pekeris ocean environment* after its originator, was developed by Pekeris [90] as indicated in Fig. 2.2. Due to the difficulty in direct numerical evaluation of the inverse Hankel transform over the wavenumber  $k_r$  in 1960's, the complex contour integration was applied. To ensure the function to be integrated was single-valued in the domain of integration, a branch cut was introduced [91–94]. The two most common cuts

are called the Pekeris cuts [95] and the Ewing-Jardetzky-Press (EJP) cuts [94], the former one is vertical and the latter one is hyperbolic as depicted in Fig. 2.5. The comparison of the result of the complex contour integration using the two different cuts introduced has been discussed by Barberger and Stickler [96, 97], but the discussion is restricted to the fluid half-space with the source positioned in the water column and observation point placed in the fluid layer away from the seabed, which can be used as a starting point of the analysis in this chapter. Since our analysis aims to accurately predict the wave field in both fluid and sediment close to the source, it is important to discuss in detail the differences between the solutions when different branch cuts are introduced. By examining these differences, we can better understand how the choice of branch cuts affects the accuracy and convergence of the modelled wave fields near the source.

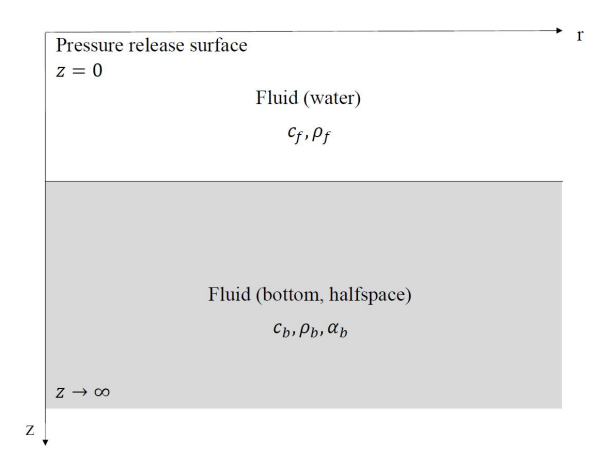


Figure 2.2: Schematic depiction of the Pekeric waveguide.

The pressure field of the *Pekeris ocean environment* shown in Fig. 2.2 can be computed as a finite sum of modes and a complex wavenumber integral with the use of Ewing-Jardetzky-Press (EJP) cut [93] when the complex contour integration method is adopted. Stickler [97] stated that EJP can give significant contributions to the predicted transmission loss to the range of at least one or multiple water depths. He also found that "improper" modes originating when the Pekeris cuts are introduced can adequately approximate the contribution of the continuous spectrum as the EJP branch cuts. These "improper" modes are characterized by violation of the radiation condition in the bottom half-space, meaning their amplitudes grow exponentially with depth, which is mathematically considered "improper" since each of these modes diverges with depth. These improper modes are also referred to, somewhat inconsistently, as leaky modes in other publications [98, 99]. Bartberger stated that when the contributions of all terms are properly evaluated, the solutions based on different branch cuts should theoretically yield the same results [96]. However, the above discussion was constrained by the restriction of the source position primarily in the fluid and the observation point being distant from the source at the frequencies of interest. In this thesis, where the focus lies on solutions near the source and when the source is partially embedded in the sediment, the choice of branch cuts can

significantly influence the accuracy of the evaluated solutions. This can potentially lead to variations in the numerical results, highlighting the importance of carefully selecting branch cuts for accurate wave field predictions in these specific scenarios.

A solution of the wave equation in acousto-elastic ocean environments was first developed by Press and Ewing [100]. They extended the Pekeris theory from two liquid layers into the case of a fluid layer overlying a solid bottom as illustrated in Fig. 2.3. The normal mode solution with solely the contribution of the superposition of modes presented by Press and Ewing is approximate and holds for observation points at large radial positions solely, which renders the contribution of the branch line integrals to the total solution insignificant. The complete solution, including branch cuts for sources in an elastic half-space, is discussed extensively in [101, 102]. Ewing considered a compressional wave source in the solid substratum of the acousto-elastic half-space [101]. However, the study focused solely on the contributions from residues, as it was concerned with large values of r. Since the contribution from EJP branch line integrals decays as  $r^{-2}$ , these integrals were neglected in the solution. The physical interpretation of these branch cuts and their contributions at various frequencies and for sources located in the sediment are not extensively discussed. Early work by Schmidt and Jensen [103] addresses multilayered viscoelastic media using a wavenumber integration approach similar to that used by Ewing et al. [91], whose method serves as a benchmark case for our model. The solution for Green's function by Nealy et al. [73] generalizes previous approaches by considering a point source in the elastic seabed or on the acousto-elastic interface. Bakr [104] applies Boundary Integral Equation (BIE) methods to analyze axisymmetric acoustic and elastic problems, further expanding on the theoretical framework for understanding wave propagation in complex elastic media.

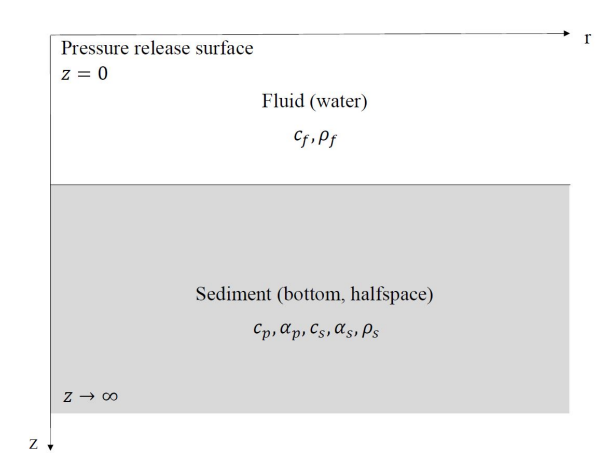


Figure 2.3: Schematic depiction of the acousto-elastic layerd half-space.

One alternative solution for replacing the branch line integrals is evaluation of the "virtual modes" [105, 106]. The modes are called "virtual" because they correspond to the wavenumbers at which the integrand has local maximal contributions to the integral when the "real" modes are close to the integration path of the branch cut. Hence, the virtual modes arise from the "resonant" behaviour along the integration path. Another approach

given by Westwood et al. [107] is to insert a thick layer as "false bottom" which has the same material properties as the original half-space while increasing the attenuation in the half-space. This causes the branch points to extend further away from the real axis in the complex wavenumber plane at large imaginary wavenumbers and the branch line contributions to the total acoustic field become secondary. In this chapter, we focus on comparing the complex wavenumber integration approaches with the two different choices of branch cuts introduced; the alternative approximations of the branch line integrals are out of consideration here.

The primary purpose of the present work is to compare multiple approaches to the seismo-acoustic problem resulting from axisymmetric sources locating in the fluid layer and/or seafloor. The structure of this chapter is outlined as follows. In Section 2.2, we present the normal mode formulation with two different methods for the complete field, including the build up of the Green's tensors for axisymmetric sources with the observation points located in fluid, seafloor and fluid-soil interface. In Section 2.3, we present the numerical evaluation of the solutions based on the two approaches addressing the numerical stability and investigate the physical interpretation of contributions from discrete modes and branch cuts. A benchmark case using direct wavenumber integration method is compared to the results from the normal mode method. Section 2.4 is dedicated to a numerical analysis of axisymmetric cylindrical sources emitting compressional waves in the fluid and combined shear sources in the sediment layer, which is a typical pressure field radiated from offshore pile driving. A thin marine sediment layer is introduced at the upper few meters of the seafloor to mimic the behaviour typically encountered in offshore conditions. The conclusions are given in Section 2.5.

#### 2.2 Cylindrically symmetric Green's Functions

#### 2.2.1 Propagation of P-SV waves

In this section, the solution of Green's functions for ring load in acousto-elastic half-space, as illustrated in Fig. 2.4, is derived and the boundary integral formulation is extended for the acousto-elastic half-space.

#### GOVERNING EQUATIONS

Cylindrical coordinates are employed, where r represents the radial distance, and z denotes the depth from the sea surface. The sea surface is defined at  $z=z_0$ , the interface between the fluid and sediment is located at a depth of  $z_1$ , and the interfaces between the sediment layers are situated at  $z=z_j$ , where j ranges from 2 to N. It is assumed that the seabed extends to infinity in both radial and vertical direction. A ring source is situated at a depth designated as  $z_s$ , which can be either in the fluid or in the sediment. The fluid is modeled as a three-dimensional inviscid compressible medium with constants  $c_f$  and  $\rho_f$  being the wave speed and the density of the fluid. The soil is modeled as a three-dimensional elastic continuum with the constants  $\lambda_{s_j}$ ,  $\mu_{s_j}$ ,  $\rho_{s_j}$  correspond to the Lamé coefficients and the density of the solid, with the index  $j=1,2,\ldots,N$  specifying the soil layers including the bottom soil half-space. The material dissipation (damping) in the soil is introduced in the form of complex Lamé constants as  $\tilde{\lambda}_{s_j}=\lambda_{s_j}(1+i\alpha_{1_j}\mathrm{sgn}(\omega))$  and  $\tilde{\mu}_{s_j}=\mu_{s_j}(1+i\alpha_{2_j}\mathrm{sgn}(\omega))$ . The attenuation coefficients  $\alpha_{1_j}$  and  $\alpha_{2_j}$  are defined as  $(20\pi\log_{10}e)\alpha_{p_j}$  and  $(20\pi\log_{10}e)\alpha_{s_j}$ , with  $\alpha_{p_j}$  and  $\alpha_{s_j}$  being the compressional and shear damping coefficients in the unit of dB

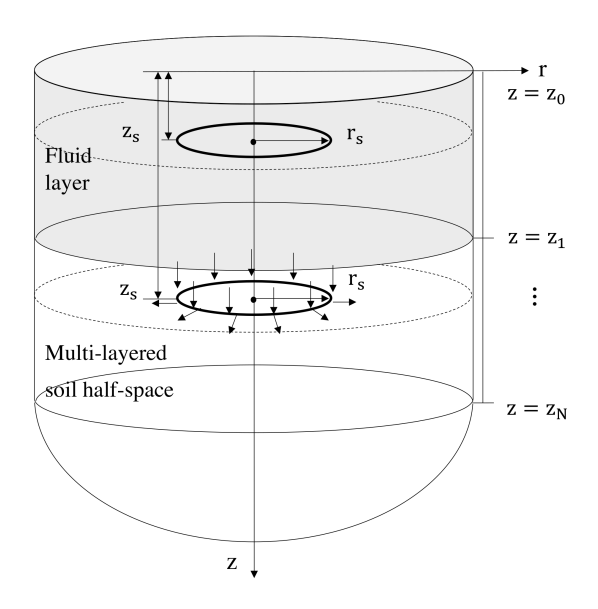


Figure 2.4: Geometry of the model of a ring load for the axisymmetric Green's function.

per wavelength. The following partial differential equations govern the dynamic response of the acousto-elastic media in time domain:

$$\nabla^2 p_f(r, z, t) - \frac{1}{c_f^2} \ddot{p}_f(r, z, t) = 0 , \qquad (2.1)$$

$$(\lambda_{s_j} + 2\mu_{s_j})\nabla(\nabla \cdot \mathbf{u}_{s_j}) - \mu_{s_j}\nabla \times (\nabla \times \mathbf{u}_{s_j}) = \rho_{s_j}\ddot{\mathbf{u}}_{s_j}. \tag{2.2}$$

In Eq. (2.1),  $p_f(r, z, t)$  is the pressure field of the fluid. In Eq. (2.2),  $\mathbf{u}_{s_j} = [u_{s_j}(r, z, t) \ w_{s_j}(r, z, t)]^T$  is the radial and vertical displacements of each soil layer.

The Helmholtz decomposition is applied to the fluid-soil domain by introducing the displacement potentials  $\phi_f$ ,  $\phi_{s_i}$  and  $\psi_{s_i}$  as:

$$\mathbf{u}_f = \nabla \phi_f \,, \tag{2.3}$$

$$\mathbf{u}_{s_i} = \nabla \phi_{s_i} + \nabla \times \nabla \times (0, \psi_{s_i}, 0) \,. \tag{2.4}$$

Substitution of Eqs. (2.3) and (2.4) into Eqs. (2.1) and (2.2) yields [101]:

$$\nabla^2 \phi_f(r, z, t) = \frac{1}{c_f} \frac{\partial^2 \phi_f}{\partial t^2} , \qquad (2.5)$$

$$\nabla^2 \phi_{s_j}(r, z, t) = \frac{1}{c_{p_j}} \frac{\partial^2 \phi_{s_j}}{\partial t^2} , \qquad (2.6)$$

$$\nabla^2 \psi_{s_j}(r, z, t) = \frac{1}{c_{s_j}} \frac{\partial^2 \psi_{s_j}}{\partial t^2} . \tag{2.7}$$

In the equations above,  $c_{p_j}$  and  $c_{s_j}$  denote the speeds of the compressional and shear waves in soil layer j, respectively.

The pressure release boundary condition is imposed at the sea surface. This assumption is sufficiently accurate in the frequency range considered in this problem. At the fluid-soil interface  $z=z_1$ , the vertical stress equilibrium and the vertical displacement continuity are imposed, while the shear stress vanishes since no tangential stresses present in an ideal fluid that is chosen to describe the acoustic behaviour of sea water. Given the full-contact at the soil-soil interface, both stress equilibrium and displacement continuity are applied. This set of boundary and interface conditions reads:

$$p_f(r, z_0, t) = 0,$$
 (2.8)

$$\sigma_{zz_1}(r, z_1, t) + p_f(r, z_1, t) = 0, \quad u_{z,f}(r, z_1, t) = w_{s_1}(r, z_1, t), \quad \sigma_{zr_1}(r, z_1, t) = 0,$$
 (2.9)

$$w_{s_i}(r, z_j, t) = w_{s_{i-1}}(r, z_j, t), \quad u_{s_i}(r, z_j, t) = u_{s_{i-1}}(r, z_j, t), \quad 2 \le j \le N,$$
 (2.10)

$$\sigma_{zz_{i}}(r, z_{j}, t) = \sigma_{zz_{j-1}}(r, z_{j}, t), \quad \sigma_{zr_{i}}(r, z_{j}, t) = \sigma_{zr_{j-1}}(r, z_{j}, t), \quad 2 \le j \le N.$$
 (2.11)

In Eq. (2.11),  $\sigma_{zz_j}$  and  $\sigma_{zr_j}$  designate the normal and tangential stresses in the soil layer j. After applying the forward Fourier transform over time, the governing equations in frequency domain are obtained. The Fourier transform pair used in this thesis is expressed as:

$$g(t) = 1/2\pi \int_{-\infty}^{+\infty} \widetilde{G}(\omega) e^{i\omega t} d\omega$$
 and  $\widetilde{G}(\omega) = \int_{-\infty}^{+\infty} g(t) e^{-i\omega t} dt$  (2.12)

in which g(t) and  $\widetilde{G}(\omega)$  denote the physical quantities in the time and frequency domains, respectively.

To propagate the axisymmetric wavefield generated by a ring load, Green's tensors for a fluid layer overlying a multilayered soil half-space are first derived for an arbitrary source excitation. The Hankel transform and complex contour integration approach are used to obtain a closed-form solution in the frequency domain. The Hankel transform pair reads [108]:

$$\hat{f}_{\nu}(k_r) = \int_0^\infty f(r) J_{\nu}(k_r r) r dr$$
 and  $f(r) = \int_0^\infty \hat{f}_{\nu}(k_r) J_{\nu}(k_r r) k_r dk_r$  (2.13)

in which f(r) and  $\hat{f}_{\nu}(k_r)$  denote the functions in the frequency and Hankel domains, respectively.  $J_{\nu}(k_r r)$  is the Bessel function of the first kind of order  $\nu$  and  $k_r$  is the horizontal wavenumber of the medium. Transformation of Eqs. (2.8)–(2.11) using the zero order Hankel transform, i.e.  $\nu = 0$ , yields:

$$\hat{p}_f(k_r, z_0, \omega) = 0, \tag{2.14}$$

$$\hat{\sigma}_{zz_1}(k_r, z_1, \omega) + \hat{p}_f(k_r, z_1, \omega) = 0, \quad \hat{u}_{z,f}(k_r, z_1, \omega) = \hat{w}_{s_1}(k_r, z_1, \omega), \quad \hat{\sigma}_{zr_1}(k_r, z_1, \omega) = 0, (2.15)$$

$$\hat{w}_{s_j}(k_r, z_j, \omega) = \hat{w}_{s_{j-1}}(k_r, z_j, \omega), \quad \hat{u}_{s_j}(k_r, z_j, \omega) = \hat{u}_{s_{j-1}}(k_r, z_j, \omega), \quad 2 \le j \le N,$$
 (2.16)

$$\hat{\sigma}_{zz_j}(k_r, z_j, \omega) = \sigma_{zz_{j-1}}(k_r, z_j, \omega), \quad \hat{\sigma}_{zr_j}(k_r, z_j, \omega) = \hat{\sigma}_{zr_{j-1}}(k_r, z_j, \omega), \quad 2 \le j \le N. \quad (2.17)$$

The displacement fields in the Hankel domain expressed in the form of Eqs. (2.3) and (2.4) are subsequently substituted into the boundary and interface conditions, Eqs. (2.14)–(2.17)

to give:

$$-\rho_f \omega^2 \hat{\phi}_f(k_r, z_0, \omega) = 0, \qquad (2.18)$$

$$-\lambda_{s_1} k_{p_1}^2 \hat{\phi}_{s_1} + 2\mu_{s_1} \left( \frac{\partial^2 \hat{\phi}_{s_1}(k_r, z_1, \omega)}{\partial z^2} + \frac{\partial^3 \hat{\psi}_{s_1}(k_r, z_1, \omega)}{\partial z^3} + k_{s_1}^2 \frac{\partial \hat{\psi}_{s_1}(k_r, z_1, \omega)}{\partial z} \right) -\rho_f \omega^2 \hat{\phi}_f(k_r, z_1, \omega) = 0,$$
(2.19)

$$\frac{\partial \hat{\phi}_f(k_r, z_1, \omega)}{\partial z} - \frac{\partial \hat{\phi}_{s_1}(k_r, z_1, \omega)}{\partial z} - \frac{\partial^2 \hat{\psi}_{s_1}(k_r, z_1, \omega)}{\partial z^2} = k_{s_1}^2 \hat{\psi}_{s_1}(k_r, z_1, \omega), \tag{2.20}$$

$$\mu_{s_1}(\frac{\partial \hat{\phi}_{s_1}(k_r, z_1, \omega)}{\partial z} + \frac{\partial^2 \hat{\psi}_{s_1}(k_r, z_1, \omega)}{\partial z^2} + k_{s_1}^2 \partial \hat{\psi}_{s_1}(k_r, z_1, \omega)) = 0, \tag{2.21}$$

$$\frac{\partial \hat{\phi}_{s_j}(k_r, z_j, \omega)}{\partial z} + \frac{\partial^2 \hat{\psi}_{s_j}(k_r, z_j, \omega)}{\partial z^2} + k_{s_j}^2 \hat{\psi}_{s_j}(k_r, z_j, \omega) = \frac{\partial \hat{\phi}_{s_{j-1}}(k_r, z_1, \omega)}{\partial z}$$
(2.22)

$$+ \frac{\partial^2 \hat{\psi}_{s_{j-1}}(k_r, z_j, \omega)}{\partial z^2} + k_{s_{j-1}}^2 \hat{\psi}_{s_{j-1}}(k_r, z_j, \omega), \quad 2 \le j \le N$$

$$\hat{\phi}_{s_{j}}(k_{r}, z_{j}, \omega) + \frac{\partial \hat{\psi}_{s_{j}}(k_{r}, z_{j}, \omega)}{\partial z} = \hat{\phi}_{s_{j-1}}(k_{r}, z_{j}, \omega) + \frac{\partial \hat{\psi}_{s_{j-1}}(k_{r}, z_{j}, \omega)}{\partial z}, 2 \leq j \leq N,$$
(2.23)

$$-\lambda_{s_{j}}k_{p_{j}}^{2}\hat{\phi}_{s_{j}} + 2\mu_{s_{j}}\left(\frac{\partial^{2}\hat{\phi}_{s_{j}}(k_{r},z_{j},\omega)}{\partial z^{2}} + \frac{\partial^{3}\hat{\psi}_{s_{j}}(k_{r},z_{j},\omega)}{\partial z^{3}} + k_{s_{j}}^{2}\frac{\partial\hat{\psi}_{s_{j}}(k_{r},z_{j},\omega)}{\partial z}\right) = (2.24)$$

$$-\lambda_{s_{j-1}}k_{p_{j-1}}^{2}\hat{\phi}_{s_{j-1}} + 2\mu_{s_{j-1}}\left(\frac{\partial^{2}\hat{\phi}_{s_{j-1}}(k_{r},z_{j},\omega)}{\partial z^{2}} + \frac{\partial^{3}\hat{\psi}_{s_{j-1}}(k_{r},z_{j},\omega)}{\partial z^{3}} + k_{s_{j-1}}^{2}\frac{\partial\hat{\psi}_{s_{j-1}}(k_{r},z_{j},\omega)}{\partial z}\right), \quad 2 \leq j \leq N$$

$$\mu_{s_{j}}\left(\frac{\partial \hat{\phi}_{s_{j}}(k_{r}, z_{j}, \omega)}{\partial z} + \frac{\partial^{2} \hat{\psi}_{s_{j}}(k_{r}, z_{j}, \omega)}{\partial z^{2}} + k_{s_{j}}^{2} \partial \hat{\psi}_{s_{j}}(k_{r}, z_{j}, \omega)\right)$$

$$= \mu_{s_{j-1}}\left(\frac{\partial \hat{\phi}_{s_{j-1}}(k_{r}, z_{j}, \omega)}{\partial z} + \frac{\partial^{2} \hat{\psi}_{s_{j-1}}(k_{r}, z_{j}, \omega)}{\partial z^{2}} + k_{s_{j-1}}^{2} \partial \hat{\psi}_{s_{j-1}}(k_{r}, z_{j}, \omega)\right), \quad 2 \leq j \leq N.$$
(2.25)

#### FLUID SOURCE

To derive the Green's functions for an acoustic source, a pressure-type unit amplitude ring source is placed at  $[r_s, z_s]$  in the fluid domain as shown in Fig. 2.4. The equation of motion for the displacement potential  $\tilde{\phi}_{f,f}^g$  reads:

$$[\nabla^2 + k_f^2] \tilde{\phi}_{f,f}^g(r, z; r_s, z_s, \omega) = \frac{1}{-\rho \omega^2} \frac{\delta(r - r_s, z - z_s)}{2\pi r}, \quad r_s \ge R, \quad z_0 \le z_s \le z_1$$
 (2.26)

in which the first subscript of the Green's potential function denotes the location of the receiver, and the second subscript denotes the location of the source with "f" being the fluid domain. The homogeneous equations of motion for the displacement potentials  $\phi_{s,f}$  and  $\psi_{s,f}$  in the soil are given by Eqs. (2.6) and (2.7). Applying the forward Hankel transform

to Eqs. (2.6), (2.7) and (2.26), the wave equations are reduced to depth-separated wave equations in the Hankel domain [104].

$$\left[\frac{d^2}{dz^2} + k_{z,f}^2\right] \hat{\phi}_{f,f}^g(k_r, z; r_s, z_s, \omega) = \frac{1}{-\rho\omega^2} \delta(z - z_s) \frac{J_0(k_r r_s)}{2\pi} , \qquad (2.27)$$

$$\left[\frac{d^2}{dz^2} + k_{z,p_j}^2\right] \hat{\phi}_{j,f}^g(k_r, z; r_s, z_s, \omega) = 0, \qquad (2.28)$$

$$\left[\frac{d^2}{dz^2} + k_{z,s_j}^2\right] \hat{\psi}_{j,f}^g(k_r, z; r_s, z_s, \omega) = 0.$$
 (2.29)

in which  $k_{z,\xi} = \sqrt{k_{\xi}^2 - k_r^2}$  is the vertical wavenumber in the domain  $\xi$  (=f,  $p_j$  or  $s_j$ ). The boundary conditions of the acousto-elastic medium along the z-coordinate have been specified in Eqs. (2.18)–(2.25) in the Hankel domain.

The solutions for the displacement potentials are the sum of a particular solution and the general solution to the homogeneous equation:

$$\hat{\phi}_{f,f}^{g}(k_{r},z;r_{s},z_{s},\omega) = \frac{1}{-\rho\omega^{2}} \frac{e^{-ik_{z,f}|z-z_{s}|}}{4\pi i k_{z,f}} + A_{1}^{g} e^{ik_{z,f}z} + A_{2}^{g} e^{-ik_{z,f}z}, \tag{2.30}$$

$$\hat{\phi}_{i,f}^{g}(k_r, z; r_s, z_s, \omega) = A_{4j-1}^{g} e^{ik_{z,p_j}z} + A_{4j}^{g} e^{-ik_{z,p_j}z}, \tag{2.31}$$

$$\hat{\psi}_{j,f}^{g}(k_r, z; r_s, z_s, \omega) = A_{4j+1}^{g} e^{ik_{z,s_j}z} + A_{4j+2}^{g} e^{-ik_{z,s_j}z}.$$
(2.32)

in which the coefficients  $A_i^g$  (i=1,2,...,4N+2) are undetermined complex amplitudes. Two unknown amplitude coefficients in the potential function  $\hat{\phi}_{f,f}^g$  indicating upward- and downward-waves in the fluid, four unknown amplitude coefficients in the functions  $\hat{\phi}_{j,f}$  and  $\hat{\psi}_{j,f}$  indicating upward- and downward-propagating waves in each soil layer. When j=N, the amplitudes in front of the first term in both Eqs. (2.31) and (2.32) vanish to ensure that the radiation condition at  $z\to\infty$  is satisfied. By substituting the expressions into the boundary and interface conditions shown in Eqs. (2.18) and (2.25), the final set of linear algebraic equations with unknowns  $A_i^g$  for i=1,2,...,4N+2 is obtained and given in Appendix A. Once the amplitude coefficients are solved for every  $k_r$ , the Green's tensor for a pressure-type ring source placed in the fluid domain is obtained.

Applying the inverse Hankel transform with the use of the following relationships of the Bessel functions [108],

$$J_{\nu}(\xi) = \frac{1}{2} (H_{\nu}^{(2)}(\xi) + H_{\nu}^{(1)}(\xi)), \tag{2.33}$$

$$H_{\nu}^{(1)}(-\xi) = -e^{-\nu\pi i}H_{\nu}^{(2)}(\xi), \quad H_{\nu}^{(2)}(-\xi) = -e^{\nu\pi i}H_{\nu}^{(1)}(\xi), \tag{2.34}$$

the Green's tensor of the acousto-elastic medium in the frequency domain is obtained as:

$$\tilde{\Phi}_{\Xi,f}^{g}(r,z;r_{s},z_{s},\omega) = -\frac{1}{2} \int_{-\infty}^{+\infty} \hat{\Phi}_{\Xi,f}^{g}(k_{r},z;r_{s},z_{s},\omega) H_{0}^{(2)}(k_{r}r) k_{r} dk_{r}$$
 (2.35)

in which  $\hat{\Phi}_{\Xi,f}^g = [\hat{\phi}_{f,f}^g, \hat{\phi}_{j,f}^g, \hat{\psi}_{j,f}^g]^T$  denotes the solutions of displacement potential functions in Hankel domain,  $\tilde{\Phi}_{\Xi,f}^g$  are the corresponding potential functions in frequency domain.

The pressure, displacements and stresses of the acousto-elastic medium are expressed by the Green's functions of displacement potentials, which are omitted here for the sake of brevity [101, 109].

#### SOIL SOURCE

For a radial or vertical ring load applied in the soil as shown in Fig. 2.4, the corresponding jump condition is applied for the stresses at the plane of the source level  $z=z_s$ . The soil layer containing the source is divided in two layers, above and below the soil source, to obtain homogeneous equations of motion and the excitation included in the interface conditions. This introduces extra four unknown amplitudes of  $\hat{\phi}_{j,s_n}^g$  and  $\hat{\psi}_{j,s_n}^g$ . Therefore, the total number of unknown amplitude coefficients are 4N+2 for the fluid sources and 4N+6 for the soil sources. Because all soil layers are free of body-force sources in that case, the solutions for the potential functions can be defined as:

$$\hat{\phi}_{f,s_n}^g(k_r, z; r_s, z_s, \omega) = A_1^g e^{ik_{z,f}z} + A_2^g e^{-ik_{z,f}z}, \tag{2.36}$$

$$\hat{\phi}_{j,s_n}^g(k_r, z; r_s, z_s, \omega) = A_{4j-1}^g e^{ik_{z,p_j}z} + A_{4j}^g e^{-ik_{z,p_j}z}, \tag{2.37}$$

$$\hat{\psi}_{j,s_n}^g(k_r, z; r_s, z_s, \omega) = A_{4j+1}^g e^{ik_{z,s_j}z} + A_{4j+2}^g e^{-ik_{z,s_j}z}. \tag{2.38}$$

in which the coefficients  $A_i^g$  (i=1,2,...,4N+6) are undetermined complex amplitudes, the subscript n denotes the layer of the soil source. When j=n, the soil layer j is separated into two sublayers at  $z=z_s$ , which denoted as  $\hat{\phi}_{s_n^+,s_n}$  and  $\hat{\phi}_{s_n^-,s_n}$  with "+" and "-" indicating the layer above and below the source level. Same notation is used for the shear potentials as  $\hat{\psi}_{s_n^+,s_n}$  and  $\hat{\psi}_{s_n^-,s_n}$ . Similar to the case of the fluid source, when j=N, the amplitudes  $A_{4j-1}^g$  and  $A_{4j+1}^g$  are set to zero in order to satisfy the radiation condition at  $z\to\infty$ .

For the radial load case, the following set of interface conditions hold at  $z=z_s$  in the Hankel domain:

$$\hat{\sigma}_{zr_{s_{n}^{+},s_{n}}}^{g}(k_{r},z_{s},\omega) - \hat{\sigma}_{zr_{s_{n}^{-},s_{n}}}^{g}(k_{r},z_{s},\omega) = \frac{J_{0}(k_{r}r_{s})}{2\pi},$$
(2.39)

$$\hat{\sigma}_{zz_{s^{+}s_{-}}}^{g}(k_{r}, z_{s}, \omega) = \hat{\sigma}_{zz_{s_{n}, s_{n}}}^{g}(k_{r}, z_{s}, \omega), \tag{2.40}$$

$$\hat{u}_{\alpha_{s_{n},s_{n}}}^{g}(k_{r},z_{s},\omega) = \tilde{u}_{\alpha_{s_{n},s_{n}}}^{g}(k_{r},z_{s},\omega), \quad \alpha = r,z.$$
(2.41)

Similarly, for the vertical load case, one obtains:

$$\hat{\sigma}_{zz_{s_{n}^{+},s_{n}}}^{g}(k_{r},z_{s},\omega) - \hat{\sigma}_{zz_{s_{n}^{-},s_{n}}}^{g}(k_{r},z_{s},\omega) = \frac{J_{0}(k_{r}r_{s})}{2\pi},$$
(2.42)

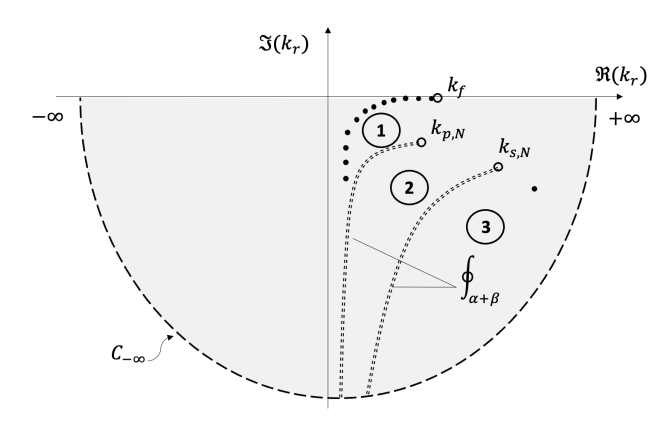
$$\hat{\sigma}_{zr_{s_{n},s_{n}}}^{g}(k_{r},z_{s},\omega) = \hat{\sigma}_{zr_{s_{n},s_{n}}}^{g}(k_{r},z_{s},\omega), \tag{2.43}$$

$$\hat{u}_{\alpha_{s_{+},s_{n}}}^{g}(k_{r},z_{s},\omega) = \tilde{u}_{\alpha_{s_{n},s_{n}}}^{g}(k_{r},z_{s},\omega), \quad \alpha = r,z.$$
 (2.44)

Combining Eqs. (2.39)–(2.44) with Eqs. (2.18)–(2.25), and after substitution of the solutions Eqs. (2.36)-(2.38) into the obtained set of equations, a linear algebraic system is formed with unknowns  $A_i^g$  for i = 1, 2, ..., 4N + 6. Once the displacement potentials are determined in the Hankel domain, the expressions for the Green's tensors of displacement and stress in the frequency domain can be obtained.

#### CLOSED-FORM RESPONSE IN THE FREQUENCY DOMAIN

The evaluation of the integrals given by Eq. (2.35) can be carried out in two ways: (1) by the direct numerical wavenumber integration along the real axis of  $k_r$ ; (2) by using the complex contour integration technique.



(a) Ewing-Jardetzky-Press (EJP) cuts

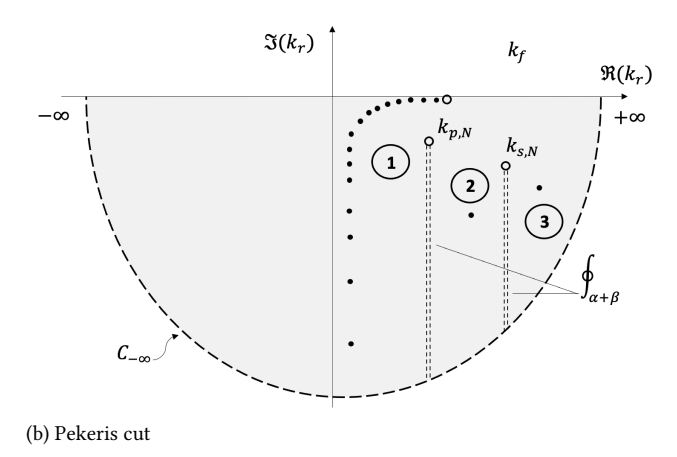


Figure 2.5: Visualization of normal mode solutions based on various choices of branch cuts for an acousto-elastic halfspace. In the case of fluid halfspace, the second branch cut associated with the shear waves vanishes in both approaches.

The first approach utilizes the direct numerical wavenumber integration (WNI) on the real axis of horizontal wavenumbers  $k_r$  from  $-\infty$  to  $+\infty$ . This approach is straightforward but requires extremely fine integration step when the integrand changes rapidly as function of  $k_r$  which often is the case when frequency is relatively high or the receiver at closer range needs to be evaluated. The second approach is essentially an alternative mathematical evaluation of the integrals in Eq. (2.35). Based on Cauchy's theorem, we can write the contour integral as (provided that the contour is closed over the lower half-plane of the

complex  $k_r$  plane)

$$\int_{-\infty}^{+\infty} f(k_r)dk_r + \int_{C_{\infty}} f(k_r)dk_r + \int_{\text{branch cuts}} f(k_r)dk_r = -2\pi i \sum_{m=1}^{M} \text{Res}(f(k_r), k_r^{(m)}) \quad (2.45)$$

in which  $\operatorname{Res}(f(k_r),k_r^{(m)})$  is the residue of a general function  $f(k_r)$  to a simple pole at  $k_r = k_r^{(m)}$ . The integrand,  $f(k_r)$ , is a multi-valued function. By introducing branch cuts, a single-valued representation of  $f(k_r)$  can be defined in the complex  $k_r$  plane, which is a necessary condition for the applicability of the contour integration method. The term  $\int_{C_\infty} f(k_r) dk_r$  represents the integral along an infinite semi-circle in the lower half of the complex plane of  $k_r$ . The term  $\int_{\text{branch cuts}} f(k_r) dk_r$  corresponds to the integration along a selected branch cut in the complex plane of  $k_r$ , as illustrated in Fig. 2.5. A specific choice of branch cut is typically made to ensure the single-valuedness of the function while avoiding other singularities and maintaining mathematical consistency. Therefore, the solution represented by the integral along the real axis of  $k_r$  can be expressed as:

$$\int_{-\infty}^{+\infty} f(k_r) dk_r = -2\pi i \sum_{m=1}^{M} \text{Res}(f(k_r), k_r^{(m)}) - \int_{\text{branch cuts}} f(k_r) dk_r - \int_{C_{\infty}} f(k_r) dk_r \quad (2.46)$$

The EJP solution is depicted in Fig. 2.5 (a). Assuming direct wavenumber integration along the real axis from  $-\infty$  to  $+\infty$ , the integration path along the semicircle  $C_{\infty}$  also extends to infinity. Its contribution diminishes with  $|k_r| \to \infty$ . Therefore, the NM solution with EJP cuts can be expressed as:

$$\int_{-\infty}^{+\infty} f(k_r) dk_r = -2\pi i \sum_{m=1}^{M} \text{Res}(f(k_r), k_r^{(m)}) - \int_{\text{EJP cuts } k_{p,N}} f(k_r) dk_r - \int_{\text{EJP cuts } k_{s,N}} f(k_r) dk_r$$
(2.47)

The total solution now consists of three terms: a) a sum of discrete modes corresponding to the residues, which can be finite in the case of a fluid layer overlying an elastic half-space, or infinite when dealing with a fluid layer overlying a multi-layered elastic half-space. In both cases, each term in this sum is finite for all values of z; b) a hyperbolic branch line integration associated with the branch point of compressional wavenumber  $k_p$ ; c) a hyperbolic branch line integration associated with the branch point of shear wavenumber  $k_s$ . All terms in this method satisfy the radiation condition at infinite depth. Therefore, the solution is evaluated by truncating the branch line integrations and discrete modes, which allows us to accurately represent the complete wave field, regardless of the location of the source and the observation point. A case study is introduced for a fluid layer overlying an elastic half-space. The properties and dimensions of each layer are presented in Table 2.1. Based on this case study, an illustration of the multi-valued characteristic functions for an acousto-elastic half-space is shown in Fig. 2.6, where the branch points, EJP branch cuts, and poles are depicted in the complex  $k_r$ -plane. The same material properties used in this case study are examined further in section 2.2.3.

By applying the complex contour integration technique, the expressions of the displacement potential functions  $\widetilde{\Phi}^g_{\Xi,\mathcal{E}}$  in frequency domain are given as a summation over a finite

Parameter	Depth	$\rho$	$c_L$	$c_T$	$\alpha_p$	$\alpha_s$
	[m]	$[kg/m^3]$	[m/s]	[m/s]	$[dB/\lambda]$	$[dB/\lambda]$
Fluid	40	1000	1500	-	-	-
Bottom soil	$\infty$	1908	1725	370	0.88	2.77

Table 2.1: Basic input parameters for the validation study of the Green's functions.

number of poles supplemented by the Ewing-Jardetsky-Press (EJP) branch line integrations  $\int_{\alpha+\beta} f(k_r) dk_r$ , i.e. :

$$\widetilde{\Phi}_{\Xi,\xi}^{g}(r,z;r_{s},z_{s};\omega) = -\pi i \sum_{m=1}^{M} \left[ \operatorname{Res}(\widehat{\Phi}_{\Xi,\xi}^{g}(k_{r}^{(m)},z;r_{s},z_{s})) H_{0}^{(2)}(k_{r}^{(m)}r) k_{r}^{(m)} \right] \\
+ \frac{1}{2} \int_{\alpha+\beta} \widehat{\Phi}_{\Xi,\xi}^{g}(k_{r},z;r_{s},z_{s}) H_{0}^{(2)}(k_{r}r) k_{r} dk_{r} \tag{2.48}$$

With this method, a complete expression for the normal mode solution to the multilayered acousto-elastic ocean environment is derived using the Green's tensors for ring sources located either in the fluid or in the sediment.

Alternatively, the Pekeris branch cuts (vertical cuts) can be chosen, and they have been widely adopted in solutions of many applications in underwater acoustics. However, it is important to note that when vertical branch cuts are used, the integration along the parts of the Pekeris branch cuts that correspond to high values of  $|\mathfrak{T}(k_r)|$  is divergent. This can lead to numerical instability, particularly in cases where the source is embedded in the sediment or the observation points are close to the source. Because the complex contour is smooth and continuous, and the semi-circle extended to the infinity connects to the branch cuts in the lower half-plane of the complex  $k_r$ , it also causes the integral along the infinite semicircle to diverge at some of its parts. Consequently, the NM solution with Pekeris cuts is expressed as:

$$\int_{-\infty}^{+\infty} f(k_r) dk_r = -2\pi i \sum_{m=1}^{M^*} \text{Res}(f(k_r), k_r^{(m)}) - \int_{\text{Pekeris cuts } k_{p,N}} f(k_r) dk_r$$

$$- \int_{\text{Pekeris cuts } k_{s,N}} f(k_r) dk_r - \int_{\text{Pekeris cuts } C_{\infty}} f(k_r) dk_r$$
(2.49)

where  $M^*$  indicates a different set of modes, which includes the so-called "improper" or leaky modes. These modes arise because the plane of searching for roots is modified due to the choice of vertical branch cuts.

The solution with Pekeris cuts consists of four terms: a) an infinite sum of discrete modes; b) a vertical branch line integration associated with the branch point of compressional wavenumber  $k_p$ ; c) a vertical branch line integration associated with the branch point of shear wavenumber  $k_s$ ; d) a semi-circle that goes to infinity in the lower half plane of the complex  $k_r$ . However, the evaluation of this solution requires truncation and simplification because the "improper" or leaky modes, along with the integrals, are numerically unstable due to their divergent behaviour at large imaginary wavenumber. Therefore, the

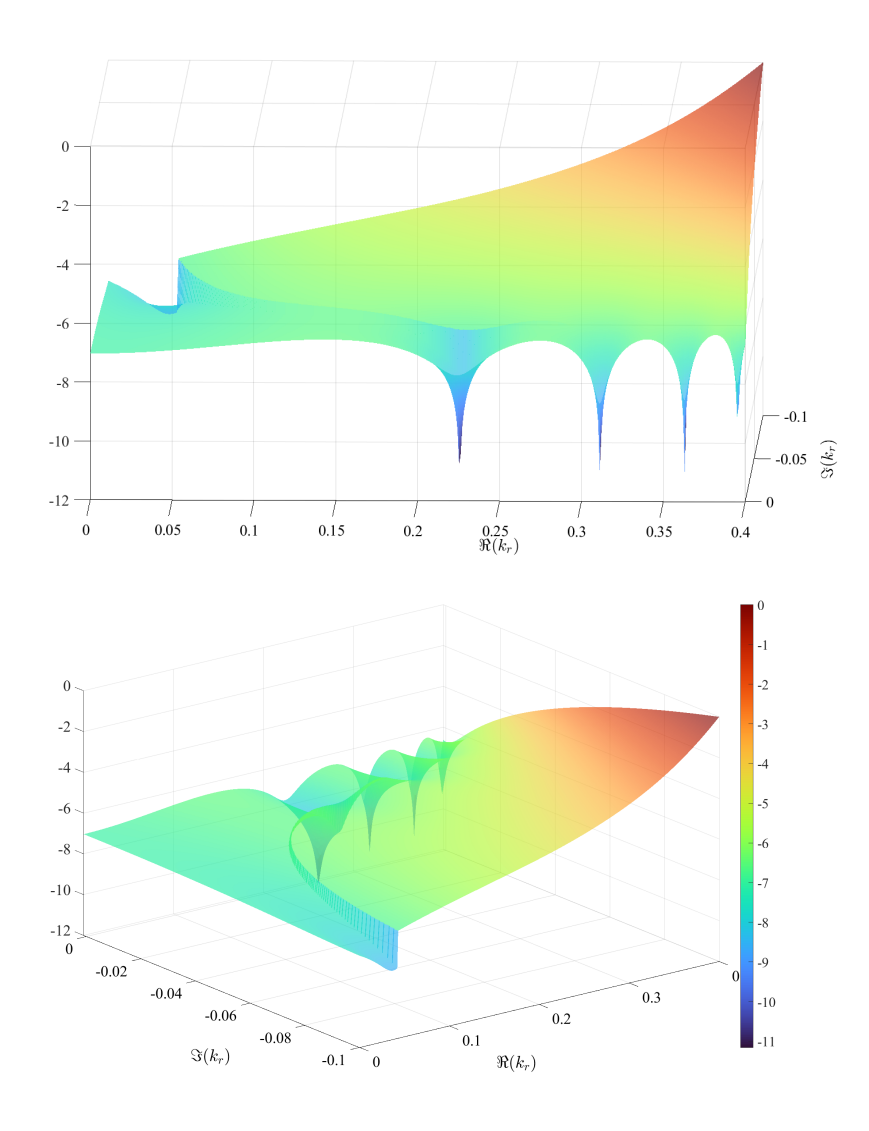


Figure 2.6: Visualization of characteristic function  $\det(k_r)$  as being the determinant of the coefficient matrix for an acousto-elastic halfspace on the Riemann surfaces at f=100Hz: branch points, EJP branch cuts, poles are indicated in the  $k_r$  complex plane. For the visualization purpose, vertical axis is defined as  $\log(|\det|)$ , the branch line is indicated by the hyperbolic curvature of the surface, in which a sharp jump can be observed between the two Riemann surfaces. The four poles can be found at the peaks pointing down to the negative vertical axis, which numerically resemble the zeros of  $\det(k_r)$ .

as:

$$\widetilde{\Phi}_{\Xi,\xi}^{g}(r,z;r_{s},z_{s};\omega) \approx -\pi i \sum_{m=1}^{M^{*}} \left[ \operatorname{Res}(\widehat{\Phi}_{\Xi,\xi}^{g}(k_{r}^{(m)},z;r_{s},z_{s})) H_{0}^{(2)}(k_{r}^{(m)}r) k_{r}^{(m)} \right] \\
+ \frac{1}{2} \int_{\sigma^{*}+\beta^{*}} \widehat{\Phi}_{\Xi,\xi}^{g}(k_{r},z;r_{s},z_{s}) H_{0}^{(2)}(k_{r}r) k_{r} dk_{r} \tag{2.50}$$

where  $\alpha^*$  and  $\beta^*$  indicate the truncated vertical branch line integration and the integral along the  $C_\infty$  is neglected to simplify the final solution. However, this simplification is only valid when the source is located in the fluid, and for observation points in the fluid that are at large distances from the source. The criteria for truncation of the solution with both EJP and Pekeris cuts ensure that the ratio between the contribution of the branch line integration and the cumulative branch line integration is less than 1E-5 for the wave field in the fluid. Since the response in the soil for the solution with Pekeris cuts exhibits inherent divergence, this criterion is applied solely to the fluid response.

This study is focused on those common types of branch cuts as introduced above, Pekeris cuts and Ewing-Jardetzky-Press (EJP) cuts. It is important to note that, in the case of a fluid layer overlying a multi-layered half-space, an infinite number of poles are exposed when using the complex contour integration method with the choice of EJP branch cuts. From a computational perspective, the complex contour integration with either Pekeris or EJP cuts requires truncation of integrals and summations. However, the use of Pekeris cuts requires careful consideration of the upper truncation limits for the modes and branch line integrals and the integral over the infinite half-plane. We have found that the results are highly sensitive to the choices in this regard, particularly when calculating the wave field close to the source or when the source is embedded in the sediment. In contrast, the choice of EJP cuts appears to be less sensitive to the selection of the upper bounds of the branch line integrals and the sum of modes, while also providing faster convergence of the solution for the problems studied in this thesis. For these reasons, the author has decided to adopt the use of EJP cuts for the computations in the subsequent chapters. The physical interpretation and the numerical implications of these various choices are discussed further in section 2.2.3.

2

# 2.2.2 ROOT FINDING IN COMPLEX PLANE FOR ACOUSTO-ELASTIC WAVE PROPAGATION

By definition of EJP cuts proposed by Press and Ewing, the branch cuts are chosen based on the conditions of  $\mathfrak{F}(k_{z,p})=0$  and  $\mathfrak{F}(k_{z,s})=0$ , which yields two hyperbolas associated to the branch points  $k_p$  and  $k_s$  in the complex plane as shown in the Fig. 2.5 (a). Three Riemann surfaces are specified in Table 2.2.

By use of Cauchy's theorem and residue theorem, the full solution for the acoustic field is derived as:

$$\widetilde{\Phi}_{\xi}^{g}(r,z;0,z_{s};\omega) = -\pi i \sum_{m=1}^{M} \left[ \frac{\widehat{\Phi}_{\xi}^{num}(k_{r}^{(m)};z;z_{s})}{\det'(k_{r}^{(m)})} H_{0}^{(2)}(k_{r}^{(m)}r) H_{0}^{(1)}(k_{r}^{(m)}r_{s}) k_{r}^{(m)} \right] 
+ \frac{1}{2} \int_{L_{\alpha}} \widehat{\Phi}_{\xi}(k_{r};z;z_{s}) H_{0}^{(1)}(k_{r}r_{s}) H_{0}^{(2)}(k_{r}r) k_{r} dk_{r} 
+ \frac{1}{2} \int_{L_{\beta}} \widehat{\Phi}_{\xi}(k_{r};z;z_{s}) H_{0}^{(1)}(k_{r}r_{s}) H_{0}^{(2)}(k_{r}r) k_{r} dk_{r}$$
(2.51)

in which  $\hat{\Phi}_{\xi}^{num}$  denotes the numerator of the solutions in wavenumber domain,  $\det'(k_r^{(m)})$  denotes the derivative of the characteristic equation as being the determinant of the coefficient matrix.

Table 2.2: Riemann surface on the complex plane of horizontal wavenumber  $k_r$ .

Surface	$k_p$	$k_s$
1	$+\sqrt{k_p^2-k_r^2}$	$+\sqrt{k_s^2-k_r^2}$
2	$-\sqrt{k_p^2-k_r^2}$	$+\sqrt{k_s^2-k_r^2}$
3	$-\sqrt{k_p^2-k_r^2}$	$-\sqrt{k_s^2-k_r^2}$

The full wave solutions corresponding to the Pekeris cuts are shown in Eq. (2.46), but both normal modes and integration path differ from the EJP solutions. The numerical evaluation of the two methods is discussed in section 2.2.3 in more detail. Based on the contour integration of the wave number integrals, the solution in the acoustic domain is derived. It consists of two components, a finite number of modes and branch line integrals around EJP branch cuts based on our choice. In general, attenuation is introduced in the bottom half-space of the seabed. The presence of a lossy bottom makes the acoustic wavenumbers  $k_p, k_s$  complex. Because residue theorem allows us to derive the line integrals of an analytical function over a closed curve; the contour C is chosen to be along the real line from  $-\infty$  to  $\infty$  and then clockwise along a semicircle centered at 0 from  $-\infty$  to  $\infty$ . Since both  $\hat{\phi}$  and  $\hat{\psi}$  in this case are not single-valued functions, the branch cut integrals are also needed for closing the contour. We have the following vertical wavenumbers to consider:

$$k_{z,p} = \pm \sqrt{k_p^2 - k_r^2} (2.52)$$

$$k_{z,s} = \pm \sqrt{k_s^2 - k_r^2} \tag{2.53}$$

Let us consider first the branch cut associated with the compressional wavenumber as an example. We assume that:

$$k_r = x + iy, \quad k_p = a + ib \quad (with \quad a > 0, b < 0)$$
 (2.54)

and

$$k_{z,p} = \sqrt{k_p^2 - k_r^2} = c + id$$
 (2.55)

By definition, we have  $k_{z,p}^2 = k_p^2 - k_r^2$ :

$$c^{2} - d^{2} + 2icd = (a^{2} - b^{2}) - (x^{2} - y^{2}) + (2iab - 2ixy)$$
(2.56)

Since we require  $\mathfrak{F}(k_{z,p})=0$ , therefore, d=0. The above equation becomes:

$$c^2 = 0 (2.57)$$

That is to say the imaginary part of the right hand side is zero, so we obtain the hyperbola defined as:

$$y = \frac{ab}{x} \tag{2.58}$$

For the real part, we require that:

$$y^2 \ge x^2 - a^2 + b^2 \tag{2.59}$$

Based on this condition, both the upper and lower sides of the hyperbola are by definition at  $\mathfrak{F}(k_{z,p}) = 0$ .

The alternative way to evaluate the branch line integration is to change the integration variable from  $k_r$  to  $k_{z,p}$  and  $k_{z,s}$ . By doing so, the  $k_{z,p}$  or  $k_{z,s}$  on the branch line are real everywhere, are positive on the upper edge, negative on the lower edge and are zero at the branch point. Therefore, we can rewrite one EJP branch line integral for  $k_{z,p}$  into:

$$f_{\text{EJP}}(r, z, \omega) = \int_{\text{EJP}} F(k_r) dk_r$$

$$= \int_{+\infty}^{0} F(k_{z,p}) dk_{z,p} + \int_{0}^{+\infty} F(-k_{z,p}) dk_{z,p}$$

$$= -\int_{0}^{+\infty} F(k_{z,p}) dk_{z,p} + \int_{0}^{+\infty} F(-k_{z,p}) dk_{z,p}$$

$$= \int_{0}^{+\infty} \left( F(-k_{z,p}) - F(k_{z,p}) \right) dk_{z,p}$$
(2.60)

Given the direct integration, we can have

$$f_{\text{EJP}}(r,z,\omega) = \int_{\text{EJP}} F(k_r) dk_r = \int_a^b (u - v \frac{dy}{dx}) dx + i \int_a^b (u \frac{dy}{dx} + v) dx$$
 (2.61)

where  $F(k_r) = u(x, y) + iv(x, y)$  and dz = dx + idy. If  $k_p = \alpha + i\beta(\beta < 0)$ , then the y-x relation can be written as  $y = \frac{\alpha\beta}{x}$ , we have:

$$\frac{d}{dx}(y) = -\frac{\alpha\beta}{x^2} \tag{2.62}$$

which define the branch cut as a hyperbolic line with  $\alpha$  and  $\beta$  being the  $\Re$  and  $\Im$  part of the wavenumber.

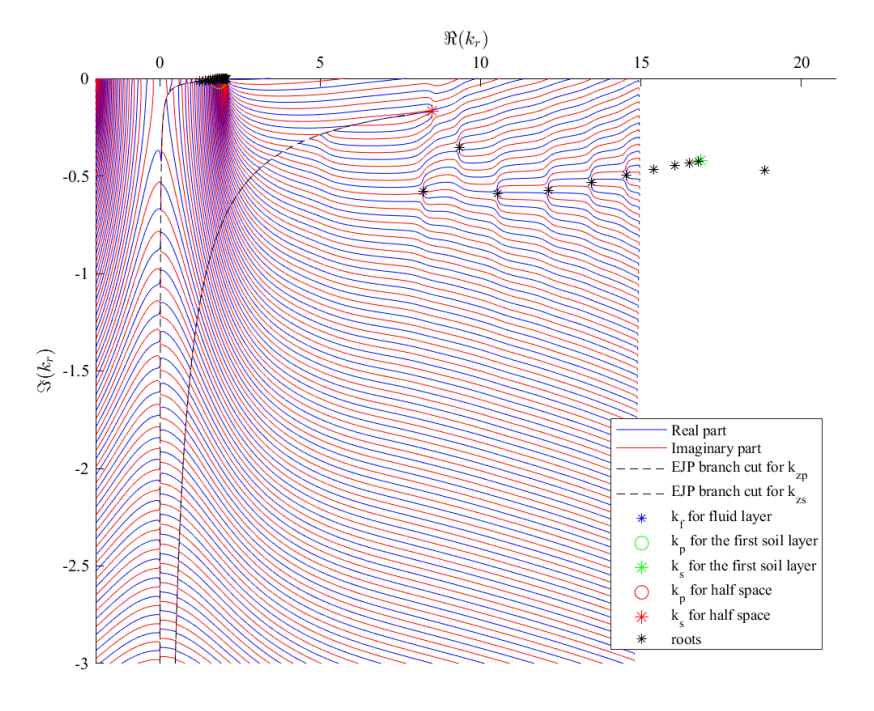


Figure 2.7: Example of typical Complex contour integration for P-SV waves.

#### 2.2.3 Comparison of various analytical approaches

In this section four methods of solution are discussed:

- Normal-mode with PML
- Direct Wavenumber Integration
- Complex Contour Integration with EJP cuts
- Complex Contour Integration with Pekeris cuts

The solution based on various analytical approaches including Normal Mode with Perfectly Matched Layer, Direct Wavenumber Integration and Complex Wavenumber Integration with EJP and Pekeris branch cuts are discussed in this section and the main findings are summarized in Table 2.3.

#### NORMAL MODE WITH PERFECTLY MATCHED LAYER

The perfectly matched layer (PML) was introduced by Berenger in 1994 [110] to truncate the unbounded domain, and was improved for the problem of elastic waves with a complex coordinate for the cylindrical and spherical coordinates [111]. It is an additional layer below the bottom layer of the sediment, by applying a complex coordinate transformation, the amplitudes of the waves decay as depicted in Fig. 2.8.

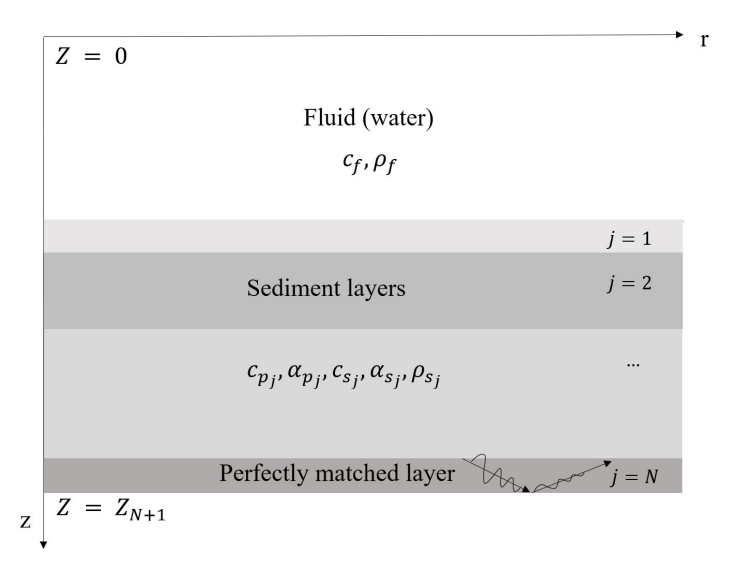


Figure 2.8: Schematic depiction of the horizontally stratified marine environment.

The complex coordinate transformation is introduced as

$$\tilde{z} = \int_{0}^{z} e_{z}(z')dz' = A(z) + i\Omega_{z}(z)/\omega, \quad z_{N} < z \le z_{N+1}$$
 (2.63)

where  $e_z = a_z + \mathrm{i}\omega_z/\omega$  is the complex PML stretching variable in the frequency domain and  $a_z$  and  $\omega_z$  are the real and positive function of vertical coordinate z. Using the complex variable  $\tilde{z}$  to replace the original z variables, the frequency domain equations corresponding to Eqs. (2.31), (2.32, (2.37), and (2.38) can be rewritten as,

$$\hat{\phi}_{N,\xi}^{g}(k_{r},z;r_{s},z_{s},\omega) = A_{4j-1}^{g} e^{ik_{z,p_{j}}\tilde{z}} + A_{4j}^{g} e^{-ik_{z,p_{j}}\tilde{z}}, \tag{2.64}$$

$$\hat{\psi}_{N,\xi}^{g}(k_r, z; r_s, z_s, \omega) = A_{4j+1}^{g} e^{ik_{z,s_j}\tilde{z}} + A_{4j+2}^{g} e^{-ik_{z,s_j}\tilde{z}}.$$
(2.65)

where  $\xi = f$ ,  $s_n$  with n = 1, 2, ..., N - 1. The boundary and interface conditions for the  $z_j$  with j = 1, 2, ..., N remains the same, with the rigid boundary condition imposed at the bottom of the PML layer with the transformed boundary conditions in the Hankel domain as,

$$\hat{w}_{s_N}(k_r, \tilde{z}; r_s, z_s, \omega)|_{z=z_{N+1}} = 0, \tag{2.66}$$

$$\hat{u}_{s_N}(k_r, \tilde{z}; r_s, z_s, \omega)|_{z=z_{N+1}} = 0.$$
(2.67)

The solution of the waveguide problem with PML is quite different from the solution of the acousto-elastic layered halfspace, which consists of the infinite sum of discrete modes including so-called leaky modes and PML modes. Leaky modes refer to modes that represent a decaying wave field, irrespective of whether the waveguide is attenuated. PML modes, on the other hand, approximate the branch line integrals along the EJP branch cuts [99].

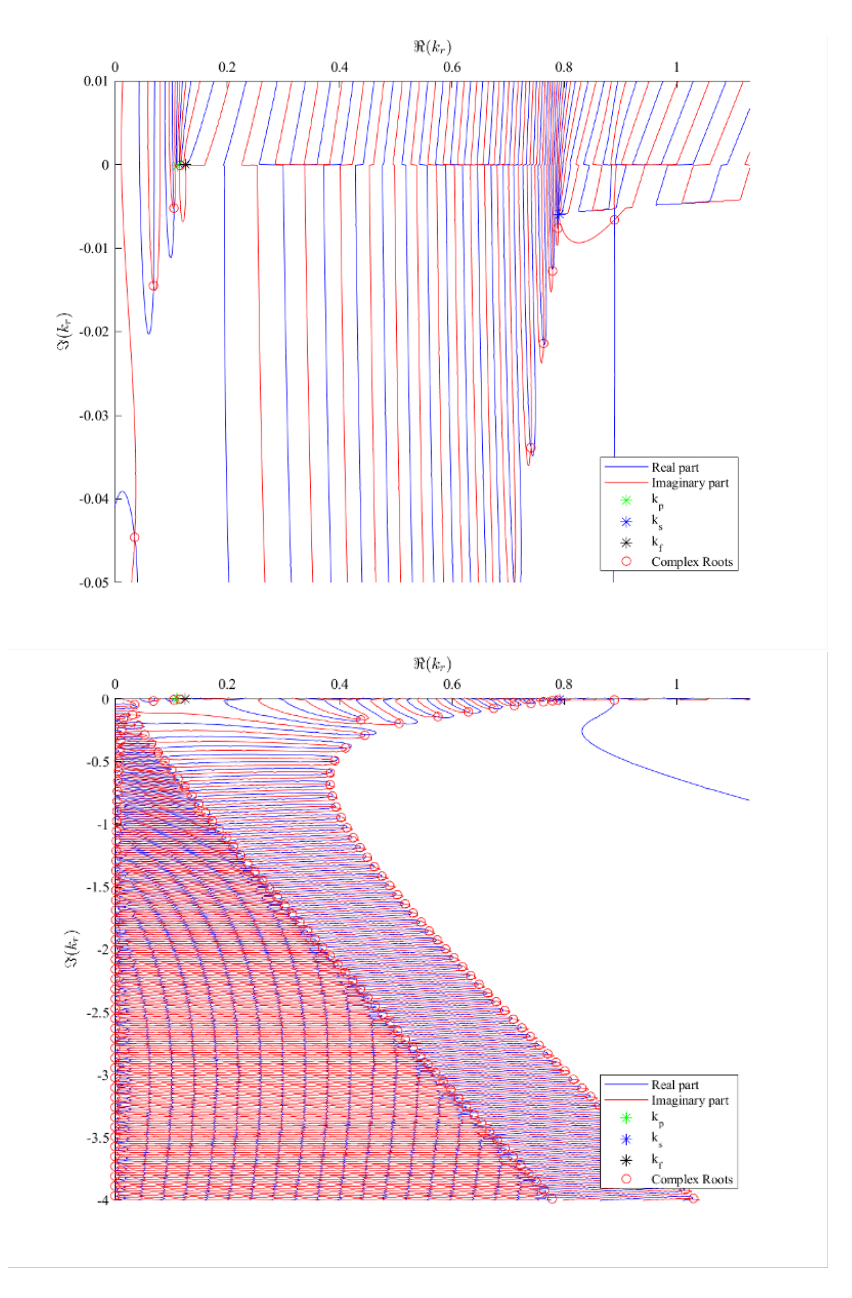


Figure 2.9: Complex roots in NM-PML solution for a point source at the excitation frequency 30 Hz: roots representing the propagating modes with relatively large real part and small imaginary part of the wavenumber (upper); zoomed out complex  $k_r$  plane including all roots truncated at the  $\Im(k_r) = -4$ .

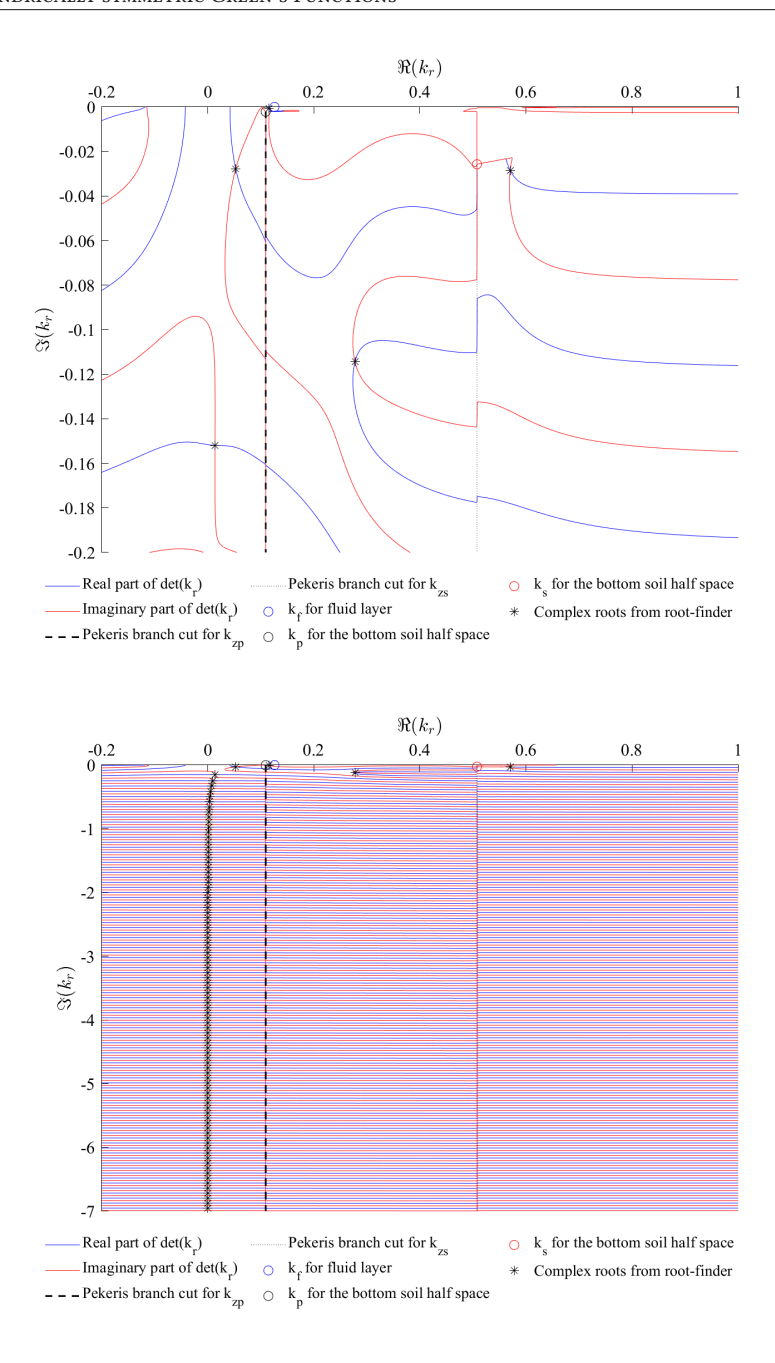


Figure 2.10: Complex roots and vertical branch line integration in Pekeris complex wavenumber solution for a point source at the excitation frequency 30 Hz: complex  $k_r$  plane(top); the enlarged complex  $k_r$  plane (bottom).

As indicated in Fig. 2.9, there are infinite number of roots. Therefore, the proper truncation of the number of roots is required. The NM-solution is sensitive to the properties chosen for the PML layer and numerical instability can occur at large depth in the soil layer. The advantage of this approach is that the solution includes only an infinite sum of normal modes.

#### COMPLEX WAVENUMBER INTEGRATION WITH PEKERIS BRANCH CUTS

The complex wavenumber integration solution with Pekeris cuts consists of number of modes, two vertical branch line integrations and the integral over the infinite semi-circle  $\int_{C_\infty}$  as indicated in Fig. 2.10. Not all modes decay with  $z\to\infty$  as shown in Fig. 2.11, part of the branch lines also do not converge and so the integral over the infinite semi-circle also diverges. In fact, the radiation condition does not necessarily need to be satisfied by these individual components in the complex wavenumber plane as the contour integration method require only the the radiation condition to be satisfied for the solution with the wavenumber on the real axis of  $k_r$ . However, the violation against the radiation condition at  $z\to\infty$  leads to the instability in the numerical solution of the complex wavenumber integration with the Pekeris branch cuts since both branch cut integrals and integrals over the infinite semi-circle diverge. The poles are shown in the complex wavenumber plane in Fig. 2.10. Among the four mode shapes presented in Fig. 2.11, only the mode related to the Scholte wave satisfies the radiation condition at  $z\to\infty$ , which is a type of surface wave that propagates along the interface between acoustic and elastic medium.

#### COMPLEX WAVENUMBER INTEGRATION WITH EJP BRANCH CUTS

The complex wavenumber integration solution with EJP cuts consists of number of modes and two hyperbolic branch line integrations as indicated in Fig. 2.12. In this solution, all modes and branch lines satisfy the boundary and interface conditions, and radiation condition as shown in Fig. 2.13. The numerical example is given for the two eigenshape functions based on the roots shown in Fig. 2.12. Most of the propagating and evanescent modes correspond to the waves that are trapped in the water column and are located on the principal Riemann surface. The pole associated with the Scholte wave is located on the third Riemann surface.

#### SUMMARY

The benchmark case depicted in Fig. 2.14 features a point source situated within a fluid medium, operating at excitation frequencies of 30 Hz, 125 Hz, and 1 kHz. Green's tensors are presented based on normal mode (NM-PML), direct wavenumber integration (WNI), EJP-complex wavenumber integration and Pekeris complex wavenumber approach.

As summarized in the Table 2.3, each of these analytical methodologies exhibits its unique set of advantages and drawbacks. Notably, complex wavenumber integration with EJP cuts emerges as the most robust and computationally faster solution for the problem under consideration. Conversely, the NM method with PML and complex WNI with Pekeris cuts manifest instability in dynamic responses within the sediment domain, even though they are convergent for fluid responses.

Furthermore, the direct WNI method achieves convergence in solutions for waves within both the fluid and sediment domains. However, fine integration steps are required

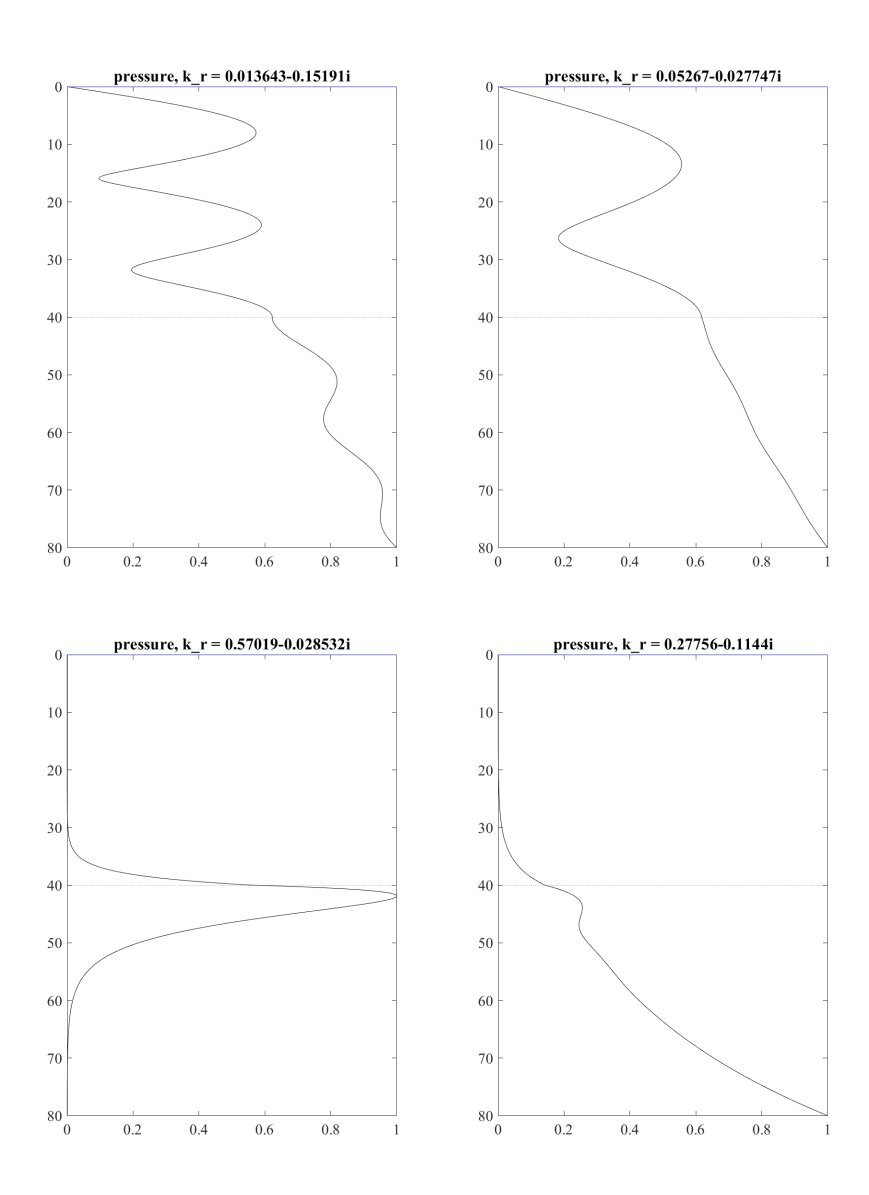


Figure 2.11: Modes shapes based on the Pekeris complex wavenumber approach for a point source at the excitation frequency 30 Hz.

to capture the integrand along the real  $k_r$  axis, which leads to substantial computational costs.

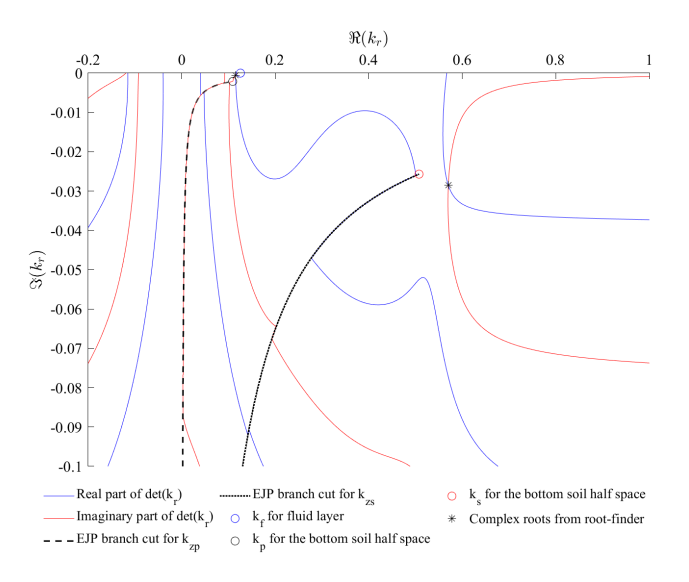


Figure 2.12: Complex roots and hyperbolic branch line integration in EJP complex wavenumber solution for a point source at the excitation frequency 30 Hz.

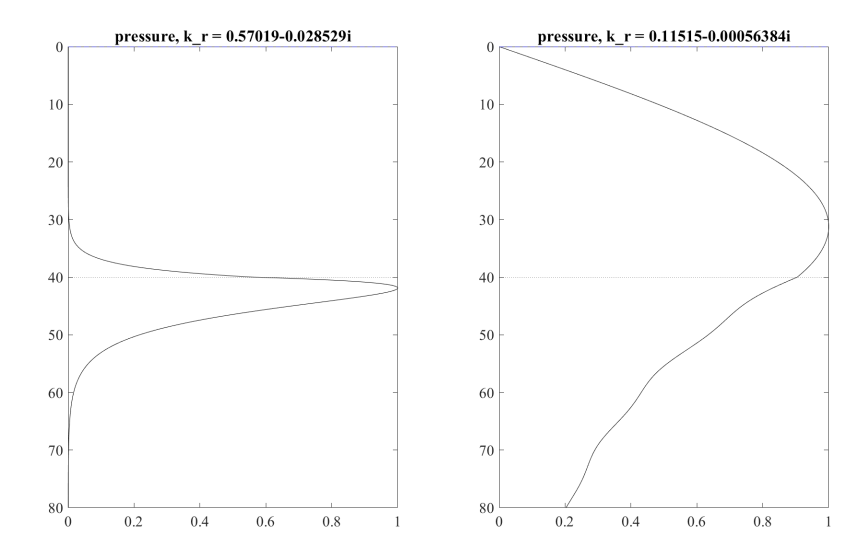


Figure 2.13: Modes shapes based on the EJP complex wavenumber approach for a point source at the excitation frequency 30 Hz.

Table 2.3: Overview of analytical approaches for wave propagation in acousto-elastic halfspace.

Method	Description	Schematic diagram
Normal Mode - PML	1. closed form solution by introducing the PML layer; 2. infinite number of roots, the proper truncation of the number of roots is required; 3. the solution is sensitive to the PML layer, numerical instability can occur.	$3(k_r)$ $k_r$ $k_{p,N}$ $k_{z,N}$
WNI	<ol> <li>the solution consists of integration of k<sub>r</sub> along the real axis;</li> <li>the proper truncation of the integration path is required;</li> <li>numerical instability can occur due to the choice of the integration step and limits.</li> </ol>	$\begin{array}{c c} & & & & & & & & & & & & & & & & & & &$
C-WNI with EJP	1. the solution consists of number of modes and two hyperbolic branch line integrations; 2. because all modes and branch lines satisfy the boundary and interface conditions, and radiation condition at $z \to \infty$ , the solution is numerically stable.	$3(k_r)$ $k_r$ $1 \dots k_p$ $k_{\pi,N}$ $2 \dots k_{\pi,N}$ $4 \dots k_{\pi,N}$
C-WNI with Pekeris	1. the solution consists of number of modes, two vertical branch line integrations and the integral along the infinite semi-circle; 2. because not all modes satisfy the radiation condition (soil half-space), and part of the integrals also do not satisfy the radiation condition at $z \to \infty$ , the solution is numerically unstable.	$S(k_{\tau})$ $(1)$ $k_f$ $g(k_{\tau})$ $k_{\tau}$ $k_{\tau}$ $g(k_{\tau})$ $g(k$

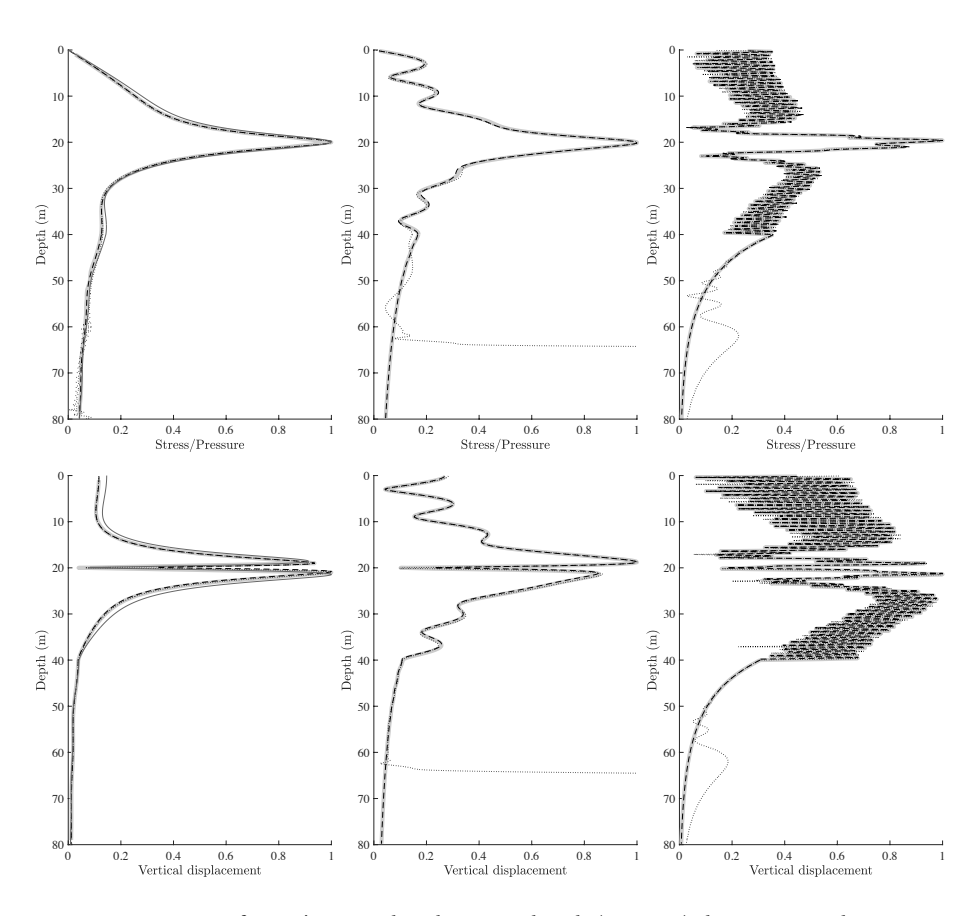


Figure 2.14: Comparison of Green's tensors based on normal mode (NM-PML), direct wavenumber integration (WNI), EJP-complex wavenumber integration and Pekeris complex wavenumber approach for a point source at three excitation frequencies 30 Hz, 125 Hz and 1kHz as indicated in Fig. 2.15: the pressure and normal stress for a fluid circular source; at f=30 Hz (left), f=125 Hz (middle), and f=1000 Hz (right). Grey thick line indicates the results from the EJP-complex wavenumber approach, black dotted line indicates the Pekeris-complex wavenumber approach, black dashed line indicates the WNI approach, and the black solid line represents the results from the normal mode approach.

#### 2.2.4 VALIDATION

In order to validate the Green's tensors for a source located either in the fluid or in the soil, a case study is performed and results are compared with the finite element model build in the COMSOL Multiphysics  $^{\circ}$  software [112].

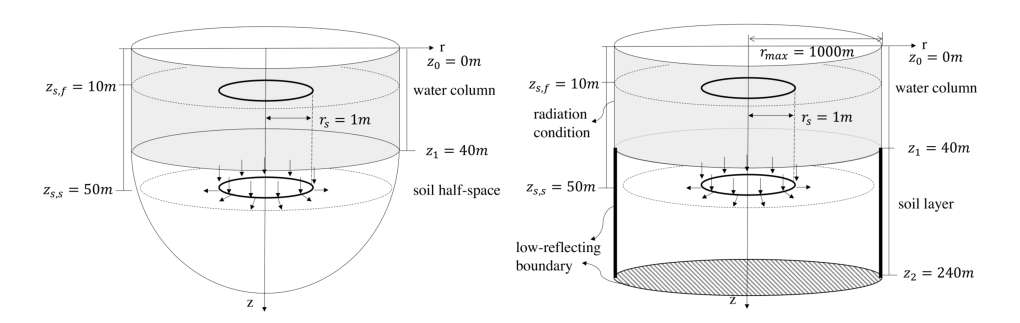


Figure 2.15: Geometry of the model for ring load for the validation of the Green's tensors: semi-analytical model (sound propagation module) (left); finite-element model in COMSOL (right).

The material properties in both models and the configuration of the acousto-elastic half-space for the sound propagation model are given in Table 2.1 in accordance with Fig. 2.15. In the sound propagation module, the domain is modeled as an acoustic layer overlying an elastic half-space with pressure release boundary at the sea surface and the interface conditions at the seabed. The radiation conditions are satisfied at both  $r \to \infty$  and  $z \to \infty$ . In the COMSOL model, the acousto-elastic waveguide is truncated at 200m below the seabed by a low-reflecting boundary as indicated in Fig. 2.15, which is used to reduce the computational domain to a practical size while ensuring the satisfaction of the radiation condition within an accurate range. In practice, the low-reflecting boundary works ideally for waves propagating in the normal direction to the boundary as it creates a perfect impedance match for compressional and shear waves. The dissipation in the soil is expressed by the frequency-dependent complex compressional and shear wave speeds in both models. In Fig. 2.15,  $z_{s,f}$  and  $z_{s,s}$  define the depth of the loading level,  $r_s$  is the radius of the ring source,  $z_1$  is the depth of the water column, and  $z_2$  in the COMSOL model gives the depth of the bottom low-reflecting boundary.

The predictions of the two models are compared for three load cases at three excitation frequency of 30Hz, 125 Hz and 1 kHz, namely a circular source in the fluid, a ring load in r- and z-directions in the soil, named after  $\mathbf{R}$ -ring and  $\mathbf{Z}$ -ring load in the Fig. 2.16. The response on the cylindrical surface at r=2m is shown in Fig. 2.16. The numerical results from both models are in good agreement for various loading cases, which validates the sound propagation module.

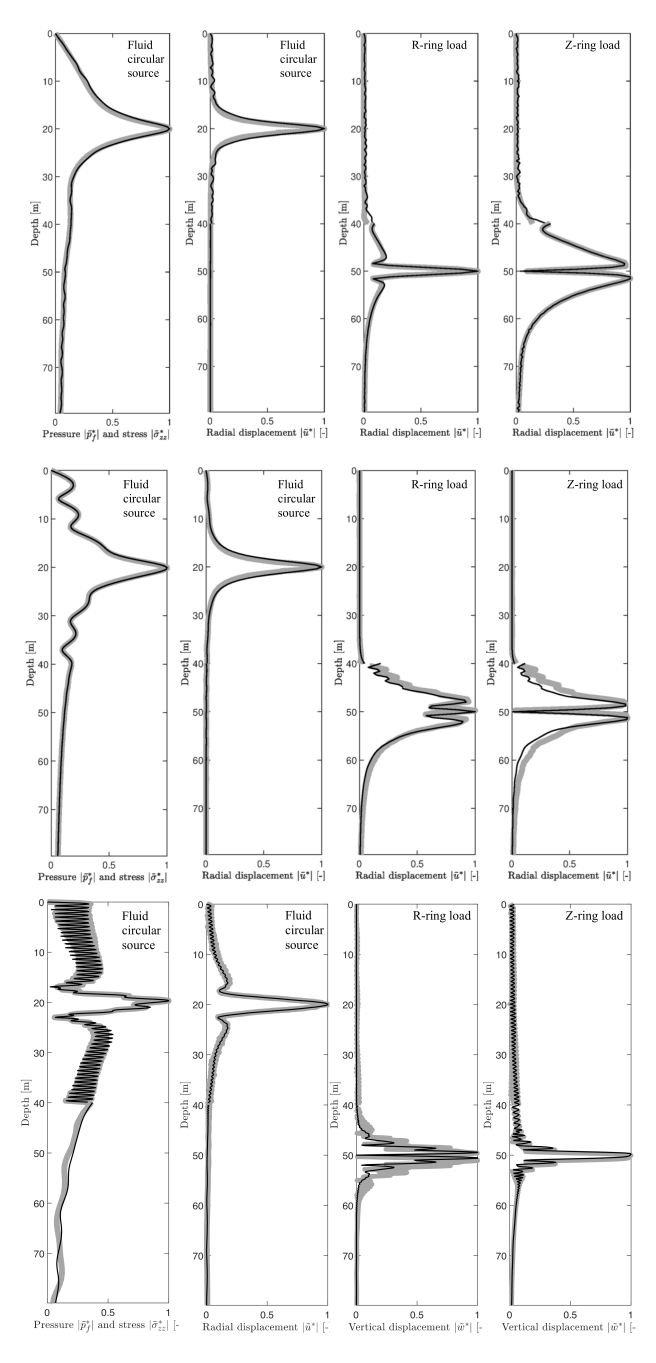


Figure 2.16: Comparison of Green's tensors from sound propagation model and FEM for a point source at three excitation frequencies 30 Hz, 125 Hz and 1kHz as indicated in Fig. 2.15: the pressure and normal stress for a fluid circular source; the radial displacement for a fluid circular source; the radial displacement for a **Z**-ring load in the soil; the radial displacement for a **Z**-ring load in the soil at f=30 Hz (top), at f=125 Hz (middle), and f=1000 Hz (bottom). Black thin line indicates the results from the sound propagation model, and the grey thick line represents the numerical results from COMSOL model.

## 2.3 Three dimensional Green's Functions

To solve the three dimensional problems of wave propagation and to build dynamic Green's functions of transversely isotropic layered media, an efficient and robust approach for the derivation of the three-dimensional dynamic Green's functions is presented. By virtue of the method of displacement potentials [113, 114], a three dimensional ring load in either fluid domain or in the soil domain is introduced. The full solution is given in the complex wavenumber integration with the EJP cuts as discussed in section 2.2.

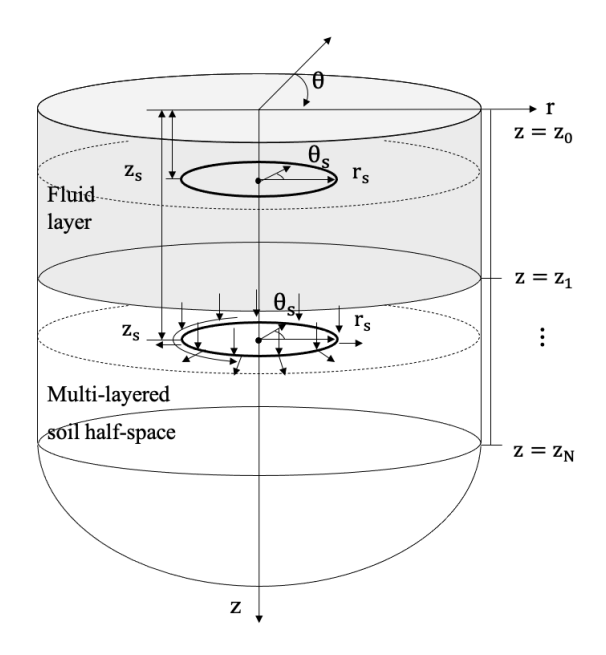


Figure 2.17: Geometry of the model for ring load for the three dimensional Green's function.

## 2.3.1 Equations of motion

We introduce a cylindrical coordinate system denoted as  $(r, \theta, z)$ , wherein r is the radial distance, z represents the depth from the sea surface, and  $\theta$  denotes the angular coordinate.

Similar to the cylindrically symmetric Green's function discussed in section 2.2, the sea surface, the boundary between the fluid and the sediment, and the interfaces between the sediment layers are defined as  $z=z_j$ , where j spans from 0 to N Both the fluid and the soil are modelled as three-dimensional media with the same properties as defined in the cylindrically symmetric case. Material dissipation within the soil is also introduced in the same manner. It is assumed that the sediment extends infinitely in both radial and vertical direction as shown in the Fig. 2.17. A three-dimensional ring source is positioned at a depth  $z=z_s$ , which can reside within either the fluid or the sediment. The governing partial differential equations that describe the three-dimensional dynamic response of the acousto-elastic medium in the time domain are as follows:

$$\nabla^2 p_f(r, \theta, z, t) - \frac{1}{c_f^2} \ddot{p}_f(r, \theta, z, t) = 0, \qquad (2.68)$$

$$(\lambda_{s_j} + 2\mu_{s_j})\nabla(\nabla \cdot \mathbf{u}_{s_j}) - \mu_{s_j}\nabla \times (\nabla \times \mathbf{u}_{s_j}) = \rho_{s_j}\ddot{\mathbf{u}}_{s_j}. \tag{2.69}$$

In Eq. (2.68),  $p_f(r, \theta, z, t)$  is the pressure field of the fluid. In Eq. (2.69),  $\mathbf{u}_{s_j} = [u_{s_j}(r, \theta, z, t) v_{s_i}(r, \theta, z, t) w_{s_i}(r, \theta, z, t)]^T$  is the radial, and vertical displacements of each soil layer.

The regular Helmholtz decomposition is applied to the displacement field as noted in [113, 114],

$$\mathbf{u}_f = \nabla \phi_f \,, \tag{2.70}$$

$$\boldsymbol{u}_{s_i} = \nabla \phi_{s_i} + \nabla \times \left[ \chi_{s_i} \boldsymbol{e}_z + \nabla \times \left[ \eta_{s_i} \boldsymbol{e}_z \right] \right], \tag{2.71}$$

The acousto-elastic wave equations can be solved by finding the solutions to a set of scalar potential wave equations in frequency domain by applying the fourier transform [113, 114],

$$[\nabla^2 + k_f^2(z)]\tilde{\phi}_f(r,\theta,z) = 0$$
 (2.72)

$$[\nabla^2 + k_{p_i}^2(z)]\tilde{\phi}_{s_i}(r,\theta,z) = 0$$
 (2.73)

$$[\nabla^2 + k_{s_i}^2(z)]\tilde{\chi}_{s_i}(r,\theta,z) = 0$$
 (2.74)

$$[\nabla^2 + k_{s_j}^2(z)]\tilde{\eta}_{s_j}(r,\theta,z) = 0$$
 (2.75)

For the solutions of Eq. (2.72-2.75), it is convenient to employ an angular Fourier decomposition in the form of:

$$\tilde{\phi}_f(r,\theta,z) = \sum_{m=-\infty}^{\infty} \phi_{fm}(r,z)e^{\mathrm{i}m\theta}$$
 (2.76)

$$\tilde{\phi}_{s_j}(r,\theta,z) = \sum_{m=-\infty}^{\infty} \phi_{s_j,m}(r,z)e^{\mathrm{i}m\theta}$$
(2.77)

$$\tilde{\chi}_{s_j}(r,\theta,z) = \sum_{m=-\infty}^{\infty} \chi_{s_j,m}(r,z) e^{\mathrm{i}m\theta}$$
(2.78)

$$\tilde{\eta}_{s_j}(r,\theta,z) = \sum_{m=-\infty}^{\infty} \eta_{s_j,m}(r,z) e^{\mathrm{i}m\theta}$$
(2.79)

in which the  $m^{th}$  series coefficients  $\Phi_m = [\phi_{fm}, \phi_{s_j,m}, \chi_{s_j,m}, \eta_{s_j,m}]$  given by:

$$\Phi_m(r,z) = \int_{-\pi}^{+\pi} \tilde{\Phi}(r,\theta,z) e^{-im\theta} d\theta$$
 (2.80)

with  $\theta = [-\pi, +\pi]$ .

#### 2.3.2 HANKEL TRANSFORM

Applying the Hankel transform pairs to the  $m^{th}$  angular order function  $f_m(r,z)$  and its potential functions in Hankel domain with  $m^{*,th}$  order Bessel function as  $\hat{f}_m^{m^*}$ ,

$$f_m(r,z) = \int_0^\infty \hat{f}_m^{m^*}(k_r, z) k_r J_m(k_r r) dk_r$$
 (2.81)

$$\hat{f}_{m}^{m^{*}}(k_{r},z) = \int_{0}^{\infty} f_{m}(r,z)rJ_{m}(k_{r}r)dr$$
 (2.82)

in which the subscript indicates the order of the Angular Fourier Transform (AFT), and the superscript represents the order of the Hankel transform. For the potential functions in the Hankel domain ,  $\hat{\Phi}_m^{m^*}$  is abbreviated as  $\hat{\Phi}_m$  for simplification.

The governing equations are transformed to the depth-dependent wave equations as:

$$\frac{d^2}{dz^2}\hat{\phi}_{fm}(k_r,z) + (k_f^2 - k_r^2)\hat{\phi}_{fm}(k_r,z) = 0$$
 (2.83)

$$\frac{d^2}{dz^2}\hat{\phi}_{jm}(k_r,z) + (k_{p_j}^2 - k_r^2)\hat{\phi}_{jm}(k_r,z) = 0$$
 (2.84)

$$\frac{d^2}{dz^2}\hat{\chi}_{jm}(k_r,z) + (k_{s_j}^2 - k_r^2)\hat{\chi}_{jm}(k_r,z) = 0$$
 (2.85)

$$\frac{d^2}{dz^2}\hat{\eta}_{jm}(k_r,z) + (k_{s_j}^2 - k_r^2)\hat{\eta}_{jm}(k_r,z) = 0$$
 (2.86)

The general solutions to Eqs. (2.83)–(2.86) read:

$$\hat{\phi}_{fm}(k_r, z) = A_1(k_r)e^{ik_{z,f}z} + A_2(k_r)e^{-ik_{z,f}z}$$
(2.87)

$$\hat{\phi}_{jm}(k_r, z) = A_{4j-1}(k_r)e^{ik_{z,p_j}z} + A_{4j}(k_r)e^{-ik_{z,p_j}z}$$
(2.88)

$$\hat{\chi}_{jm}(k_r, z) = B_{2j-1}(k_r)e^{ik_{z,s_j}z} + B_{2j}(k_r)e^{-ik_{z,s_j}z}$$
(2.89)

$$\hat{\eta}_{im}(k_r, z) = A_{4i+1}(k_r)e^{ik_{z,s_j}z} + A_{4i+2}(k_r)e^{-ik_{z,s_j}z}$$
(2.90)

For the numerical stability, the reference z coordinate can be shifted to the either upper or lower boundaries of each layer, the solutions now read:

$$\hat{\phi}_{fm}(k_r, z) = A_1(k_r)e^{ik_{z,f}(z-D_1)} + A_2(k_r)e^{-ik_{z,f}z}$$
(2.91)

$$\hat{\phi}_{im}(k_r, z) = A_{4i-1}(k_r)e^{ik_{z,p_j}(z-D_{j+1})} + A_{4i}(k_r)e^{-ik_{z,p_j}(z-D_j)}$$
(2.92)

$$\hat{\chi}_{jm}(k_r, z) = B_{2j-1}(k_r)e^{ik_{z,s_j}(z-D_{j+1})} + B_{2j}(k_r)e^{-ik_{z,s_j}(z-D_j)}$$
(2.93)

$$\hat{\eta}_{jm}(k_r, z) = A_{4j+1}(k_r)e^{ik_{z,s_j}(z-D_{j+1})} + A_{4j+2}(k_r)e^{-ik_{z,s_j}(z-D_j)}$$
(2.94)

in which j indicates the index of soil layer and  $D_j$  and  $D_{j+1}$  indicate the depth of the upper and lower boundary of the soil layer j.

#### 2.3.3 Transformed displacement and stress fields

The transformed displacement  $[\hat{u}_{r_{\xi m}}, \hat{u}_{\theta_{\xi m}}, \hat{u}_{z_{\xi m}}]$ , pressure field  $\hat{p}_f$  and stress-field  $[\hat{\tau}_{zz_{jm}}, \hat{\tau}_{zr_{jm}}, \hat{\tau}_{zr_{jm}}, \hat{\tau}_{rr_{jm}}, \hat{\tau}_{\theta\theta_{jm}}, \hat{\tau}_{r\theta_{jm}}, ]$  (with  $\xi = f, j$  and j = 1, 2, ..., N) are obtained, the solutions are

very convenient form to ensure the expression is in the same circumferential order,

$$\hat{u}_{r_{fm}}(k_r, z) = \hat{u}_{fm}^{m+1}(k_r, z) + i\hat{v}_{fm}^{m+1}(k_r, z)$$
(2.95)

$$\hat{u}_{z_{fm}}(k_r, z) = \hat{w}_{fm}^m(k_r, z) \tag{2.96}$$

$$\hat{u}_{\theta_{f_m}}(k_r, z) = \hat{u}_{f_m}^{m-1}(k_r, z) - i\hat{v}_{f_m}^{m-1}(k_r, z)$$
(2.97)

$$\hat{p}_{fm}(k_r, z) = \hat{p}_{fm}^m(k_r, z) \tag{2.98}$$

$$\hat{u}_{z_{im}}(k_r, z) = \hat{w}_{im}^m(k_r, z) \tag{2.99}$$

$$\hat{u}_{r_{im}}(k_r, z) = \hat{u}_{im}^{m+1}(k_r, z) + i\hat{v}_{im}^{m+1}(k_r, z)$$
(2.100)

$$\hat{u}_{\theta_{im}}(k_r, z) = \hat{u}_{im}^{m-1}(k_r, z) - i\hat{v}_{im}^{m-1}(k_r, z)$$
(2.101)

$$\hat{\tau}_{zz_{jm}}(k_r, z) = \hat{\sigma}_{zz_{jm}}^m(k_r, z)$$
 (2.102)

$$\hat{\tau}_{zr_{jm}}(k_r, z) = \hat{\sigma}_{zr_{jm}}^{m+1}(k_r, z) + i\hat{\sigma}_{z\theta_{jm}}^{m+1}(k_r, z)$$
(2.103)

$$\hat{\tau}_{z\theta_{jm}}(k_r, z) = \hat{\sigma}_{zr_{jm}}^{m-1}(k_r, z) - i\hat{\sigma}_{z\theta_{jm}}^{m-1}(k_r, z)$$
(2.104)

$$\hat{\tau}_{rr_{jm}}(k_r, z) = \hat{\sigma}_{rr_{jm}}^{m+1}(k_r, z) + 2\mu(\frac{\hat{u}_{jm}^m(k_r, z)}{r} + im\frac{\hat{v}_{jm}^m(k_r, z)}{r})$$
(2.105)

$$\hat{\tau}_{\theta\theta_{jm}}(k_r, z) = \hat{\sigma}_{\theta\theta_{jm}}^{m+1}(k_r, z) - 2\mu(\frac{\hat{u}_{jm}^m(k_r, z)}{r} + im\frac{\hat{v}_{jm}^m(k_r, z)}{r})$$
(2.106)

$$\hat{\tau}_{r\theta_{jm}}(k_r, z) = \hat{\sigma}_{r\theta_{jm}}^{m+1}(k_r, z) + 2\mu(\frac{\hat{u}_{jm}^m(k_r, z)}{r} - im\frac{\hat{v}_{jm}^m(k_r, z)}{r})$$
(2.107)

in which the superscripts indicate the order of the Hankel transform as indicated in Eqs. (2.81) and (2.82). Once Eqs. (2.70) and (2.71) are introduced the resulting expression read:

$$\hat{u}_{r,c}(k_r, z) = -k_r \hat{\phi}_{fm}(z) \tag{2.108}$$

$$\hat{u}_{z_{fm}}(k_r, z) = \hat{\phi}'_{fm}(z) \tag{2.109}$$

$$\hat{u}_{\theta_{fm}}(k_r, z) = k_r \hat{\phi}_{fm}(z) \tag{2.110}$$

$$\hat{p}_{fm}(k_r, z) = -\rho_f \omega^2 \hat{\phi}_{fm}(z) \tag{2.111}$$

$$\hat{u}_{z_{jm}}(k_r, z) = \hat{\phi}_{jm}(z) + k_r^2 \hat{\eta}_{jm}(z)$$
(2.112)

$$\hat{u}_{r_{jm}}(k_r, z) = -k_r(\hat{\phi}_{jm}(z) + \hat{\eta}'_{jm}(z) - i\hat{\chi}_{jm}(z))$$
(2.113)

$$\hat{u}_{\theta_{jm}}(k_r, z) = k_r(\hat{\phi}_{jm}(z) + \hat{\eta}'_{jm}(z) + i\hat{\chi}_{jm}(z))$$
(2.114)

$$\hat{\tau}_{zz_{jm}}(k_r, z) = -\lambda k_r^2 \hat{\phi}_{jm}(z) + (\lambda + 2\mu) \hat{\phi}''_{jm}(z) + 2\mu k_r^2 \hat{\eta}'_{jm}(z)$$
 (2.115)

$$\hat{\tau}_{zr_{jm}}(k_r, z) = -\mu k_r (2\hat{\phi}'_{jm}(z) + \hat{\eta}''_{jm}(z) + k_r^2 \hat{\eta}_{jm}(z) - i\hat{\chi}'_{jm}(z))$$
(2.116)

$$\hat{\tau}_{z\theta_{jm}}(k_r, z) = \mu k_r (2\hat{\phi}'_{jm}(z) + \hat{\eta}''_{jm}(z) + k_r^2 \hat{\eta}_{jm}(z) + i\hat{\chi}'_{jm}(z))$$
(2.117)

$$\hat{\tau}_{rr_{im}}(k_r, z) = \lambda \hat{\phi}''_{im}(z) - (\lambda + 2\mu)k_r^2 \hat{\phi}'_{im}(z) - 2\mu k_r^2 \hat{\eta}'_{im}(z)$$
 (2.118)

$$\hat{\tau}_{\theta\theta_{jm}}(k_r, z) = \lambda \hat{\phi}_{jm}^{\prime\prime}(z) - \lambda k_r^2 \hat{\phi}_{jm}(z)$$
(2.119)

$$\hat{\tau}_{r\theta_{jm}}(k_r, z) = \mu k_r^2 \hat{\chi}_{jm}(z) \tag{2.120}$$

In the equations above, a prime denotes an ordinary derivative with respect to coordinate z.

It is convenient to define an alternative set of displacement and stress variables for the soil as:

$$\hat{u}_{1_{im}}(k_r, z) = \hat{u}_{r_{im}}(k_r, z) - \hat{u}_{\theta_{im}}(k_r, z) \tag{2.121}$$

$$\hat{u}_{2_{im}}(k_r, z) = \hat{u}_{z_{im}}(k_r, z) = \hat{w}_{im}^m(k_r, z)$$
(2.122)

$$\hat{u}_{3im}(k_r, z) = \hat{u}_{rim}(k_r, z) + \hat{u}_{\theta im}(k_r, z) \tag{2.123}$$

$$\hat{\tau}_{22_{jm}}(k_r, z) = \hat{\tau}_{zz_{jm}}(k_r, z) = \hat{\sigma}_{zz_{jm}}^m(k_r, z)$$
(2.124)

$$\hat{\tau}_{21_{jm}}(k_r, z) = \hat{\tau}_{zr_{jm}}(k_r, z) - \hat{\tau}_{z\theta_{jm}}(k_r, z)$$
(2.125)

$$\hat{\tau}_{23_{im}}(k_r, z) = \hat{\tau}_{zr_{im}}(k_r, z) + \hat{\tau}_{z\theta_{im}}(k_r, z)$$
(2.126)

$$\hat{\tau}_{11_{jm}}(k_r, z) = \hat{\tau}_{rr_{jm}}(k_r, z) = \hat{\sigma}_{rr_{jm}}^{m+1}(k_r, z) + 2\mu(\frac{\hat{u}_{jm}^m(k_r, z)}{r} + im\frac{\hat{v}_{jm}^m(k_r, z)}{r})$$
(2.127)

$$\hat{\tau}_{33_{jm}}(k_r, z) = \hat{\tau}_{\theta\theta_{jm}}(k_r, z) = \hat{\sigma}_{\theta\theta_{jm}}^{m+1}(k_r, z) - 2\mu(\frac{\hat{u}_{jm}^m(k_r, z)}{r} + im\frac{\hat{v}_{jm}^m(k_r, z)}{r})$$
(2.128)

$$\hat{\tau}_{13_{jm}}(k_r, z) = \hat{\tau}_{r\theta_{jm}}(k_r, z) = \hat{\sigma}_{r\theta_{jm}}^{m+1}(k_r, z) + 2\mu(\frac{\hat{u}_{jm}^m(k_r, z)}{r} - im\frac{\hat{v}_{jm}^m(k_r, z)}{r})$$
(2.129)

#### 2.3.4 Transformed loading conditions

The arbitrarily (non-uniformly or uniformly) distributed ring load on the plane  $z_s$  can be represented as a set of jump conditions across the interface [113, 114]:

$$\sigma_{zz}(r_s, \theta, z_s^+) - \sigma_{zz}(r, \theta, z_s^-) = \sum_{m=-\infty}^{\infty} \hat{Z}_m e^{im\theta} \frac{J_m(k_r r_s)}{2\pi} = F_v(r_s, \theta, z_s)$$
(2.130)

$$\sigma_{zr}(r_s, \theta, z_s^+) - \sigma_{zr}(r, \theta, z_s^-) = \sum_{m = -\infty}^{\infty} \hat{R}_m e^{im\theta} \frac{J_m(k_r r_s)}{2\pi} = F_h(r_s, \theta, z_s)$$
(2.131)

$$\sigma_{z\theta}(r_{s}, \theta, z_{s}^{+}) - \sigma_{z\theta}(r, \theta, z_{s}^{-}) = \sum_{m=-\infty}^{\infty} \hat{T}_{m} e^{im\theta} \frac{J_{m}(k_{r}r_{s})}{2\pi} = F_{\theta}(r_{s}, \theta, z_{s})$$
(2.132)

(2.133)

In the Fourier-Hankel domain, the transformed loading conditions read:

$$\hat{\tau}_{22_m}(k_r, z_s +) - \hat{\tau}_{22_m}(k_r, z_s -) = \hat{Z}_m \frac{J_m(k_r r_s)}{2\pi}$$
(2.134)

$$\hat{\tau}_{21_m}(k_r, z_s +) - \hat{\tau}_{21_m}(k_r, z_s -) = \frac{\hat{Y}_m - \hat{X}_m}{2} \frac{J_m(k_r r_s)}{2\pi}$$
(2.135)

$$\hat{\tau}_{23_m}(k_r, z_s +) - \hat{\tau}_{23_m}(k_r, z_s -) = \frac{\hat{Y}_m + \hat{X}_m}{2} \frac{J_m(k_r r_s)}{2\pi}$$
(2.136)

with  $X_m$  and  $Y_m$  defined as:

$$\hat{X}_m = \hat{R}_m - i\hat{T}_m \tag{2.137}$$

$$\hat{Y}_m = \hat{R}_m + i\hat{T}_m \tag{2.138}$$

#### 2.3.5 Solutions of Green's function

With the aid of the rearrangement Eqs. (2.122)–(2.129), the foregoing equations become decoupled to two of algebraic equations; one related to the coupled P-SV waves,

$$\hat{u}_{1m}(k_r, z) = 2k_r(\hat{\phi}_m(z) + \hat{\eta}'_m(z)) \tag{2.139}$$

$$\hat{u}_{2m}(k_r, z) = (\hat{\phi}'_m(z) + k_r^2 \hat{\eta}_m(z)$$
(2.140)

$$\hat{\tau}_{21_m}(k_r, z) = -2\mu k_r (2\hat{\phi}_m'(z) + 2\hat{\eta}_m''(z) + k_s^2 \hat{\eta}_m(z) + \hat{\eta}_m'(z))$$
(2.141)

$$\hat{\tau}_{22_m}(k_r, z) = -\lambda k_p^2 \hat{\phi}_m(z) + 2\mu (k_s^2 \hat{\eta}_m'(z) + \hat{\phi}_m''(z) + \hat{\eta}_m''(z))$$
(2.142)

$$\hat{\tau}_{33_m}(k_r, z) = -\lambda k_p^2 \hat{\phi}_m(z)$$
 (2.143)

$$\hat{\tau}_{11_m}(k_r, z) = -\lambda k_p^2 \hat{\phi}_m(z) - 2\mu k_r^2 (\hat{\eta}_m'(z) + \hat{\phi}_m(z))$$
 (2.144)

(2.145)

in which only the potential functions  $\hat{\phi}_m(z)$  and  $(\hat{\eta}_m(z))$  are involved, and another set of equations for the uncoupled SH wave propagation,

$$\hat{u}_{3_m}(k_r, z) = 2ik_r \hat{\chi}_m(z) \tag{2.146}$$

$$\hat{\tau}_{23_m}(k_r, z) = 2ik_r \mu \hat{\chi}'_m(z) \tag{2.147}$$

$$\hat{\tau}_{13_m}(k_r, z) = \mu k_r^2 \hat{\chi}_m(z) \tag{2.148}$$

in which the potential functions  $\hat{\chi}_m(z)$  remains. By applying the loading, boundary and interface conditions into both two subsystems the amplitude coefficients in Eqs. (2.91)–(2.94) can be obtained.

#### 2.3.6 VALIDATION

To validate the Green's tensors for a source located either in the fluid or in the soil, a case study is performed, and the results are compared with the finite element model built in COMSOL Multiphysics  $^{\circ}$  software [112]. As illustrated in Fig. 2.18, the problem of wave propagation in an acousto-elastic halfspace is examined. The domain consists of a fluid layer with a water depth of 10m overlying an elastic halfspace with properties including density, compressional and shear wave speeds, and attenuation coefficients, as listed in Table 2.4. The ring load is positioned at 2m below the seabed and has the form shown in Fig. 2.18. In this case, the source term can be expressed by m = 1 and m = -1 as summarized in Table 2.5 to facilitate the loading conditions as indicated in the Fig. 2.18, which results in the following expression for  $F_h$ ,  $F_v$  and  $F_\theta$ .

Table 2.4: Basic input parameters for the validation study of the Green's functions.

Parameter	Depth	ρ	$c_L$	$c_T$	$\alpha_p$	$\alpha_s$
-	[m]	$[kg/m^3]$	[m/s]	[m/s]	$[dB/\lambda]$	$[dB/\lambda]$
Fluid	10	1000	1500	-	-	-
Bottom soil	$\infty$	1908	1725	370	0.88	2.77

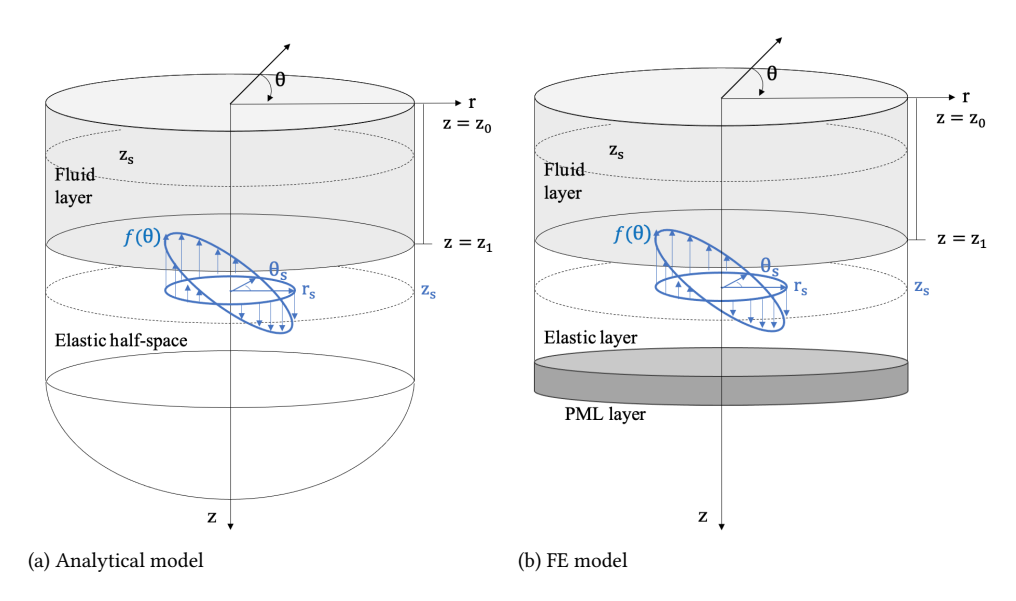


Figure 2.18: The loading condition of the model for the validation of the three dimensional Green's function.

Table 2.5: Loading conditions for an inclined vertical ring load in Hankel-domain .

	m	$\hat{R}_m$	$\hat{T}_m$	$\hat{Z}_m$	$e^{\mathrm{i}m heta}$
Ī	+1	0	0	$\frac{r_s}{2} \frac{2\pi}{J_{+1}(k_r r_s)}$	$e^{\mathrm{i} heta_0}$
	-1	0	0	$\frac{r_s}{2} \frac{\frac{1}{2\pi}}{I_{-1}(k_r r_s)}$	$e^{-\mathrm{i} heta_0}$

$$F_h(r_s, \theta, z_s) = \sum_{m=-\infty}^{\infty} \hat{R}_m e^{im\theta} \frac{J_m(k_r r_s)}{2\pi} = 0$$
 (2.149)

$$F_v(r_s, \theta, z_s) = \sum_{m=-\infty}^{\infty} \hat{Z}_m e^{\mathrm{i}m\theta} \frac{J_m(k_r r_s)}{2\pi} = f(\theta)$$
 (2.150)

$$F_{\theta}(r_s, \theta, z_s) = \sum_{m=-\infty}^{\infty} \hat{T}_m e^{\mathrm{i}m\theta} \frac{J_m(k_r r_s)}{2\pi} = 0$$
 (2.151)

The expression for the inclined load for  $F_v$  is expressed as,

$$f(\theta) = r_s \cdot \cos(\theta) = \frac{r_s}{2} (e^{i\theta} + e^{-i\theta})$$
 (2.152)

Therefore, the transformed load components  $\hat{X}_m$ ,  $\hat{Y}_m$  and  $\hat{Z}_m$  are obtained in Table 2.6.

For validation purposes, a COMSOL model is constructed with the same configuration, incorporating a perfectly matched layer (PML) below the truncated elastic domain with a layer of 40m depth for comparison with the elastic halfspace. The dynamic responses of

Table 2.6: Transformed conditions for an inclined vertical ring load.

m	$\hat{X}_m$	$\hat{Y}_m$	$\hat{Z}_m$
+1	0	0	$\frac{2\pi}{J_{+1}(k_r r_s)}$
0	0	0	0
-1	0	0	$\frac{2\pi}{I_{-1}(k_r r_s)}$

both the fluid and the soil are evaluated and compared with the finite element solutions. Figure 2.19 displays the pressure in the fluid 2m above the seabed and the displacement in the soil at the source level, demonstrating a good agreement between the results of the two analyses.

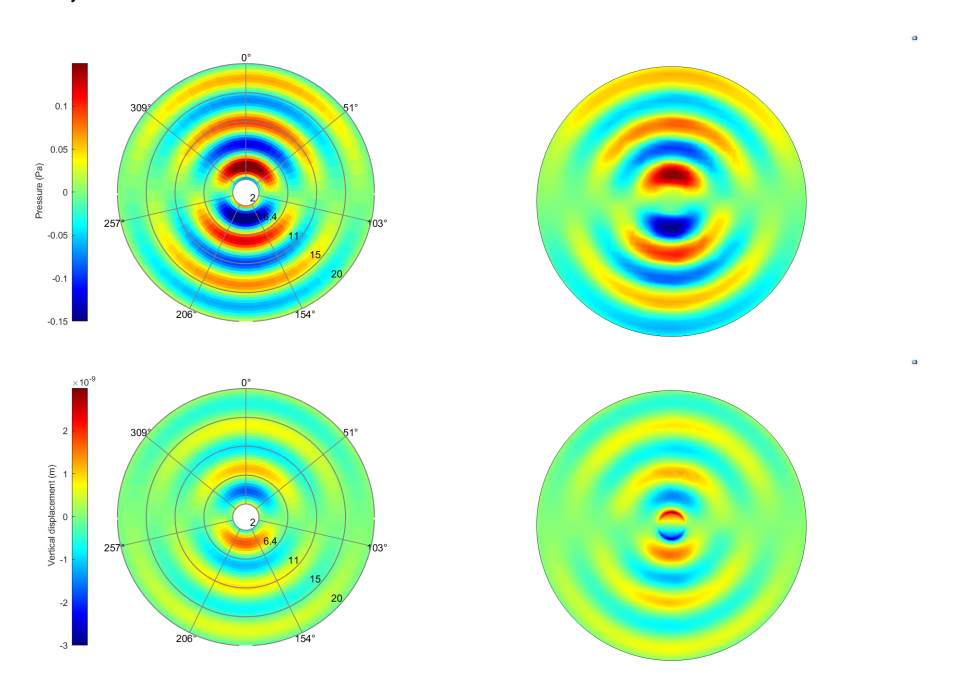


Figure 2.19: Comparison of the pressure field in the fluid and the displacement field between the FEM and the semi-analytical model for the three dimensional Green's function for 50 Hz.

# 2.4 BOUNDARY INTEGRAL EQUATIONS IN AN ACOUSTO-ELASTIC HALF-SPACE

#### 2.4.1 RECIPROCITY THEOREM IN ELASTODYNAMICS

In this section, a boundary element method (BEM) model for acousto-elastic layered half-space is developed and used in the analysis of axisymmetric disturbances radiated from a cylindrical surface. The complete wave field characterized by the Green's function for the sources emitting both compressional waves and shear waves and the resulting amplitude of the displacement potentials on the surface of disturbance at a radial distance of  $r_s$  are connected through the boundary integral equation. Based on the derived Green's tensor, the boundary integral is formulated as:

$$\widetilde{\boldsymbol{\Phi}}(\boldsymbol{r},\omega) = \int_{\Gamma} \left( \frac{\partial \widetilde{\boldsymbol{\Phi}}_{0}(\boldsymbol{r}_{0},\omega)}{\partial n} \widetilde{\boldsymbol{G}}(\boldsymbol{r},\boldsymbol{r}_{0},\omega) - \frac{\partial \widetilde{\boldsymbol{G}}(\boldsymbol{r},\boldsymbol{r}_{0},\omega)}{\partial n} \widetilde{\boldsymbol{\Phi}}_{0}(\boldsymbol{r}_{0},\omega) \right) d\Gamma_{0},$$

$$\widetilde{\boldsymbol{G}}(\boldsymbol{r},\boldsymbol{r}_{0},\omega) = \begin{cases} \widetilde{\phi}_{f,f}^{g} & \widetilde{\phi}_{f,p_{1}}^{g} & \widetilde{\phi}_{f,s_{1}}^{g} & \cdots & \widetilde{\phi}_{f,p_{N}}^{g} & \widetilde{\phi}_{f,s_{N}}^{g} \\ \widetilde{\phi}_{p_{1},f}^{g} & \widetilde{\phi}_{p_{1},p_{1}}^{g} & \widetilde{\phi}_{p_{1},s_{1}}^{g} & \cdots & \widetilde{\phi}_{p_{1},p_{N}}^{g} & \widetilde{\phi}_{p_{1},s_{N}}^{g} \\ \widetilde{\phi}_{s_{1},f}^{g} & \widetilde{\psi}_{s_{1},p_{1}}^{g} & \widetilde{\psi}_{s_{1},s_{1}}^{g} & \cdots & \widetilde{\phi}_{s_{1},p_{N}}^{g} & \widetilde{\phi}_{p_{N},s_{N}}^{g} \\ \vdots & \vdots & \vdots & \ddots & \vdots & \vdots \\ \widetilde{\phi}_{p_{N},f}^{g} & \widetilde{\phi}_{p_{N},p_{1}}^{g} & \widetilde{\phi}_{p_{N},s_{1}}^{g} & \cdots & \widetilde{\phi}_{p_{N},p_{N}}^{g} & \widetilde{\phi}_{p_{N},s_{N}}^{g} \\ \widetilde{\psi}_{s_{N},f}^{g} & \widetilde{\psi}_{s_{N},p_{1}}^{g} & \widetilde{\psi}_{s_{N},s_{1}}^{g} & \cdots & \widetilde{\psi}_{s_{N},p_{N}}^{g} & \widetilde{\psi}_{s_{N},s_{N}}^{g} \end{cases}, \quad \widetilde{\boldsymbol{\Phi}} = \begin{cases} \widetilde{\phi}_{f} \\ \widetilde{\phi}_{p_{1}} \\ \widetilde{\psi}_{s_{1}} \\ \vdots \\ \widetilde{\phi}_{p_{N}} \\ \widetilde{\psi}_{s_{N}}^{g} \end{cases}$$

$$(2.153)$$

in which r = [r, z],  $r_0 = [r_s, z_s]$ ,  $\Gamma$  denotes the surface of axisymmetric sources,  $\tilde{\phi}_{p,q}^g$  with the index g denotes the Green's function.  $\tilde{G}(r, r_0, \omega)$  denotes the Green's tensor for the sources locating in fluid and soil domain emitting compressional or shear waves. The index p represents the location of the receiver and the index q represents the location and type of the source. Especially, for the notation of q, the index f indicates the fluid domain, the index f indicates the compressional source locating in the soil layer f and the index f indicates the shear source locating in the soil layer f.

#### 2.4.2 BOUNDARY INTEGRAL FORMULATION

The direct boundary element method (BEM) is adopted to couple the boundary of an acousto-elastic domain. The solution of the acousto-elastic wavefield employs Somigliana's identity in elastodynamics and Green's third identity in potential theory [115, 116]. The velocity, displacement and pressure/stresses on the cylindrical boundary surface  $r = r_s$  are obtained from the sound generation module. The Green's functions obtained in section 2.2 and 2.3 are the fundamental solutions of the boundary integral equations.

The fundamental solutions of Green's displacement tensors  $\widetilde{U}_{\alpha\beta}^{\Xi\xi}(\mathbf{r},\mathbf{r}_s,\omega)$  are derived from the potential functions [109] given the receiver point at  $\mathbf{r}=(r,z)$  (in medium  $\Xi$ ) in  $\alpha$ -direction due to a unit impulse at source  $\mathbf{r}_s=(r_s,z_s)$  (in medium  $\xi$ ) in  $\beta$ -direction:

$$\widetilde{U}_{\alpha\beta}^{s\xi}(\mathbf{r},\mathbf{r}_{s},\omega) = \nabla \widetilde{\phi}_{j,\xi}^{g}(\mathbf{r},\mathbf{r}_{s},\omega) + \nabla \times W , \qquad (2.154)$$

$$\widetilde{U}_{\alpha\beta}^{f\xi}(\mathbf{r},\mathbf{r}_s,\omega) = \nabla \widetilde{\phi}_{f,\xi}^g(\mathbf{r},\mathbf{r}_s,\omega). \tag{2.155}$$

in which  $W=-\partial \psi^g_{s_j,\xi}({\bf r},{\bf r}_s,\omega)/\partial r$ . The displacement potential functions of acousto-elastic domain have been derived in Eq. (2.48). The Green's stress tensors  $\widetilde{T}^{\Xi\xi}_{\alpha\beta}({\bf r},{\bf r}_s,\omega)$  related

to  $\widetilde{U}_{\alpha\beta}^{\Xi\xi}(\mathbf{r},\mathbf{r}_s,\omega)$  can be obtained through substitution of Eqs. (2.154) and (2.155) into the constitutive equations [109].

#### BOUNDARY INTEGRALS FOR SOURCES LOCATED IN THE ACOUSTIC LAYER

Based on a set of acoustic sources in the form of pressure  $\tilde{p}_f(\mathbf{r_s},\omega)$ , radial displacement  $\tilde{u}_f(\mathbf{r_s},\omega)$ , and radial velocity fields  $\tilde{v}_{r_f}(\mathbf{r_s},\omega)$  obtained from the sound generation modules on the cylindrical surface in the water column, the pressure, velocity, and displacement expressions read:

$$\tilde{p}_{f,f}(\mathbf{r},\omega) = \int_{\mathcal{S}^f} \left( \tilde{p}_{f,f}^{g}(\mathbf{r}, \mathbf{r}_s, \omega) \tilde{u}_f(\mathbf{r}_s, \omega) - \tilde{u}_{f,f}^{g}(\mathbf{r}, \mathbf{r}_s, \omega) \tilde{p}_f(\mathbf{r}_s, \omega) \right) dS(\mathbf{r}_s), \tag{2.156}$$

$$\tilde{v}_{\alpha_{f,f}}(\mathbf{r},\omega) = \int_{Sf} \left( \tilde{v}_{\alpha_{f,f}}^{g}(\mathbf{r},\mathbf{r}_{s},\omega) \frac{\tilde{v}_{r_{f}}(\mathbf{r}_{s},\omega)}{\mathrm{i}\omega} + \frac{1}{\rho\omega^{2}} \frac{\partial \tilde{v}_{\alpha_{f,f}}^{g}(\mathbf{r},\mathbf{r}_{s},\omega)}{\partial r} \tilde{p}_{f}(\mathbf{r}_{s},\omega) \right) dS(\mathbf{r}_{s}),$$

$$\alpha = z, r$$
(2.157)

$$\tilde{u}_{\alpha_{s,f}}(\mathbf{r},\omega) = \int_{Sf} \left( \tilde{u}_{\alpha_{s,f}}^{g}(\mathbf{r},\mathbf{r}_{s},\omega) \frac{\tilde{v}_{r_{f}}(\mathbf{r}_{s},\omega)}{\mathrm{i}\omega} + \frac{1}{\rho\omega^{2}} \frac{\partial \tilde{u}_{\alpha_{s,f}}^{g}(\mathbf{r},\mathbf{r}_{s},\omega)}{\partial r} \tilde{p}_{f}(\mathbf{r}_{s},\omega) \right) dS(\mathbf{r}_{s}),$$

$$\alpha = z, r.$$
(2.158)

in which  $S^f$  and indicates the integration surface in the fluid domain at  $r=r_s$ . The stress components  $\tilde{\sigma}_{zz_{s,f}}(\mathbf{r},\omega)$ ,  $\tilde{\sigma}_{rr_{s,f}}(\mathbf{r},\omega)$ , and  $\tilde{\sigma}_{zr_{s,f}}(\mathbf{r},\omega)$  are obtained through the stress-displacement relationships [104], in terms of the displacement components  $\tilde{u}_{\alpha_{s,f}}$ .

#### BOUNDARY INTEGRALS FOR SOURCES LOCATED IN THE ELASTIC LAYERED HALF-SPACE

Based on a set of soil sources in the form of stresses  $[\tilde{t}_r^n(\mathbf{r}_s,\omega),\tilde{t}_z^n(\mathbf{r}_s,\omega)]$  and displacements  $[\tilde{u}_r(\mathbf{r}_s,\omega),\tilde{u}_z(\mathbf{r}_s,\omega)]$  obtained from the sound generation modules on the cylindrical surface in the soil domain at  $r=r_s$ , the pressure, velocity, and displacement expressions read:

$$\tilde{p}_{f,s}(\mathbf{r},\omega) = \int_{S^s} \left( \widetilde{P}_r^{fs}(\mathbf{r}, \mathbf{r}_s, \omega) \cdot \widetilde{t}_r^{\mathbf{n}}(\mathbf{r}_s, \omega) + \widetilde{P}_z^{fs}(\mathbf{r}, \mathbf{r}_s, \omega) \cdot \widetilde{t}_z^{\mathbf{n}}(\mathbf{r}_s, \omega) \right) \\
+ \widetilde{L}_p^{fs}(\mathbf{r}, \mathbf{r}_s, \omega) \cdot \widetilde{u}_z(\mathbf{r}_s, \omega) + \widetilde{L}_p^{fs}(\mathbf{r}, \mathbf{r}_s, \omega) \cdot \widetilde{u}_r(\mathbf{r}_s, \omega) \right) dS^s(\mathbf{r}_s), \tag{2.159}$$

$$\widetilde{v}_{\alpha_{f,s}}(\mathbf{r},\omega) = i\omega \int_{S^s} \left( \widetilde{U}_{\alpha r}^{fs}(\mathbf{r}, \mathbf{r}_s, \omega) \cdot \widetilde{t}_r^{\mathbf{n}}(\mathbf{r}_s, \omega) + \widetilde{P}_{\alpha}^{fs}(\mathbf{r}, \mathbf{r}_s, \omega) \cdot \widetilde{u}_{\alpha}(\mathbf{r}_s, \omega) \right) \\
+ \widetilde{U}_{\alpha z}^{fs}(\mathbf{r}, \mathbf{r}_s, \omega) \cdot \widetilde{t}_z^{\mathbf{n}}(\mathbf{r}_s, \omega) dS^s(\mathbf{r}_s), \quad \alpha = z, r, \tag{2.160}$$

$$\tilde{u}_{\alpha_{s,s}}(\mathbf{r},\omega) = \sum_{\beta=r,z} \int_{S^s} \left( \widetilde{U}_{\alpha\beta}^{ss}(\mathbf{r},\mathbf{r}_s,\omega) \cdot \widetilde{t}_{\beta}^{\mathbf{n}}(\mathbf{r}_s,\omega) - \widetilde{T}_{\alpha\beta}^{\mathbf{n},ss}(\mathbf{r},\mathbf{r}_s,\omega) \cdot \widetilde{u}_{\beta}(\mathbf{r}_s,\omega) \right) dS^s(\mathbf{r}_s),$$

$$\alpha = z, r.$$
(2.161)

$$\widetilde{L}_{p}^{fs}(\mathbf{r},\mathbf{r}_{s},\omega) = \rho_{f}c_{f}^{2}\left(\frac{\partial \widetilde{P}_{r}^{fs}}{\partial r} + \frac{\widetilde{P}_{r}^{fs}}{r} + \frac{\partial \widetilde{P}_{z}^{fs}}{\partial z}\right)$$
(2.162)

in which  $S^s$  indicates the integration surface in the soil domain at  $r = r_s$ ,  $\widetilde{L}_p$  is defined as the pressure operator using the strain-displacement relationships and Hooke's law,  $\widetilde{P}_{\alpha}^{fs}(\mathbf{r},\mathbf{r}_s,\omega)$  is the pressure Green's function at the receiver location  $\mathbf{r}$  due to a unit load along  $\alpha$ -direction applied in the soil domain at  $\mathbf{r}_s$ ,  $\alpha$  denotes also the direction of the displacement at the receiver point. The derivation of the soil source in  $\alpha$  direction is given in the section 2.2.1. As tangential stress vanishes in the fluid domain, the terms  $\widetilde{T}_{rz}^{\mathbf{n},fs}(\mathbf{r},\mathbf{r}_s,\omega)$  and  $\widetilde{T}_{zr}^{\mathbf{n},fs}(\mathbf{r},\mathbf{r}_s,\omega)$  vanish for the receiver in the fluid. Similarly, the stress tensors are obtained through the constitutive relationships [104] from the displacement functions and their derivatives.

#### COUPLED ACOUSTO-ELASTODYNAMIC BOUNDARY INTEGRAL EQUATION

By utilizing Betti's reciprocal theorem in elastodynamics [115] and Green's theorem for acoustic problem [116] as discussed in section 2.4.2 and 2.4.2, the complete solution for the acousto-elastic domain reads:

$$\widetilde{u}_{\alpha}^{\Xi}(\mathbf{r},\omega) = \widetilde{u}_{\alpha}^{\Xi,f}(\mathbf{r},\omega) + \widetilde{u}_{\alpha}^{\Xi,s}(\mathbf{r},\omega) 
= \sum_{\beta=r,z} \int_{S^{s}} \left( \widetilde{U}_{\alpha\beta}^{\Xi,s}(\mathbf{r},\mathbf{r}_{s},\omega) \cdot \widetilde{t}_{\beta}^{\mathbf{n}}(\mathbf{r}_{s},\omega) - \widetilde{T}_{\alpha\beta}^{\mathbf{n},\Xi,s}(\mathbf{r},\mathbf{r}_{s},\omega) \cdot \widetilde{u}_{\beta}(\mathbf{r}_{s},\omega) \right) dS^{s}(\mathbf{r}_{s}) 
+ \int_{S^{f}} \left( \widetilde{U}_{\alpha r}^{\Xi,f}(\mathbf{r},\mathbf{r}_{s},\omega) \cdot \widetilde{p}(\mathbf{r}_{s},\omega) - \widetilde{T}_{\alpha r}^{\mathbf{n},\Xi,f}(\mathbf{r},\mathbf{r}_{s},\omega) \cdot \widetilde{u}_{r}(\mathbf{r}_{s},\omega) \right) dS^{f}(\mathbf{r}_{s}), \quad \mathbf{r} \in V$$
(2.163)

in which **n** is the outward normal to the cylindrical boundary. The cylindrical surface in both fluid and soil domains needs to be discretized when employing the direct BEM associated with the acousto-elastic layered half-space Green's functions. The rule of thumb for using six elements per wavelength is adopted in the numerical integration of the line integral with the trapezoidal scheme applied for the integration [117]. In the fluid domain, the integration is based on the shortest wavelength of the compressional waves at the frequency of interest. In the soil domain, the size of the element is governed by the shortest shear wavelength in accordance with the maximum frequency of interest.

# 2.4.3 BOUNDARY INTEGRAL EQUATION METHOD IN THREE-DIMENSIONAL FIELD

Based on potential theory and Green's third theorem, the boundary integral equation formulated in the three-dimensional case reads:

$$\boldsymbol{v}_{\alpha}^{f} = \int_{S} \left( \sum_{m=-\infty}^{\infty} (\tilde{V}_{\alpha_{m}}^{f,G}(\boldsymbol{r},\boldsymbol{r}_{0}) \frac{\tilde{V}_{r}^{f}(\boldsymbol{r}_{0})}{i\omega} - \frac{\partial \tilde{V}_{\alpha_{m}}^{f,G}(\boldsymbol{r},\boldsymbol{r}_{0})}{\partial \boldsymbol{r}} \frac{\tilde{p}_{f}(\boldsymbol{r}_{0})}{-\rho\omega^{2}}) e^{\mathrm{i}m\theta} \right) dS 
+ \sum_{\beta=r,\theta,z} \int_{S^{s}} \left( \sum_{m=-\infty}^{\infty} (\tilde{U}_{\alpha\beta_{m}}^{fs}(\boldsymbol{r},\boldsymbol{r}_{0},\omega) \cdot \tilde{t}_{\beta}^{n}(\boldsymbol{r}_{0},\omega) - \tilde{T}_{\alpha\beta_{m}}^{n,fs}(\boldsymbol{r},\boldsymbol{r}_{0},\omega) \cdot \tilde{u}_{\beta}(\boldsymbol{r}_{0},\omega)) e^{\mathrm{i}m\theta} \right) dS_{0}^{s}(\boldsymbol{r}_{0})$$
(2.164)

Similarly to the expressions used in section 2.4.2, now the solution of the physical quantities are expressed by the three potential functions. The angular Fourier decomposition is employed in the boundary integral equation formulation, which enables efficient computation.

#### 2.4.4 VALIDATION

In order to validate the boundary integral formulations, two theoretical case studies are performed. The first case study considers a point source to examine the validity of the axisymmetric boundary integral equation formulation. The second case study focuses on a three dimensional surface load to examine the integral solution in the more general three dimensional configuration.

#### AXISYMMETRIC BIE

Based on the results in section 2.2, the Green's functions have been already verified. As shown in Fig. 2.20, four scenarios are examined: (i) direct method: to generate the wavefield at r=200 m from the Green's function of a source positioned either in the fluid or in the soil; (ii)-(iv) boundary integral equation (BIE) method: to generate the wavefield at r=200 m through BIE with the input on the cylindrical boundary at (ii)  $r_s=5$  m; (iii)  $r_s=20$  m; (iv)  $r_s=40$  m, which were obtained from the Green's function for a point source positioned either in the fluid or in the soil. The material parameters and geometry of the acousto-elastic media are given in Table 2.7. As discussed in section 2.4.2, the sound propagation

Table 2.7: Basic input parameters for the validation study.

Parameter	Depth	ρ	$c_L$	$c_T$	$\alpha_p$	$\alpha_s$
-	[m]	$[kg/m^3]$	[m/s]	[m/s]	$[dB/\lambda]$	$[dB/\lambda]$
Fluid	40	1000	1500	-	-	-
Upper soil	30	1888	1775	198	0.2	0.8
Bottom soil	$\infty$	1950	1976	370	1.0	2.5

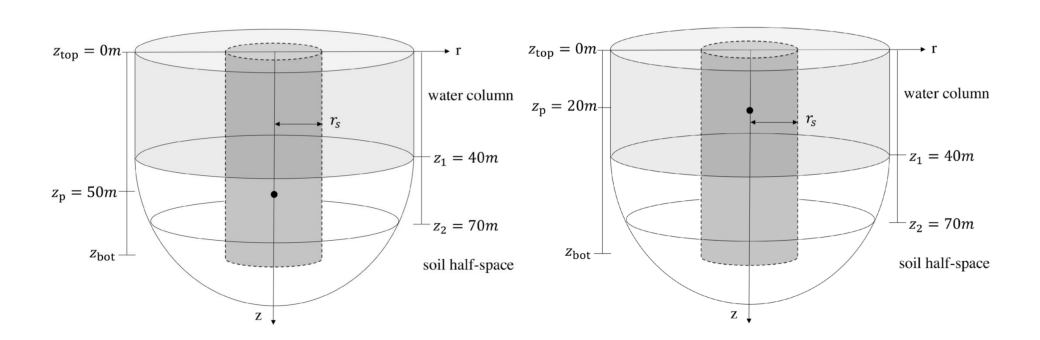


Figure 2.20: Geometry of the model for the validation of the boundary integrals formulations for a point source positioned: in the seabed as a r-load soil source (left); in the fluid domain as a pressure source (right).

module is based on a boundary integral equation, in which the input is obtained from the source generation module. In this case, the sound generation module delivers the Green's function for a point source. The input is obtained on a cylindrical surface as indicated by the dark grey surface shown in Fig. 2.20. The results are presented for three excitation frequencies: 30Hz, 125Hz and 1kHz for both scenarios as shown in Fig. 2.21. In the presence

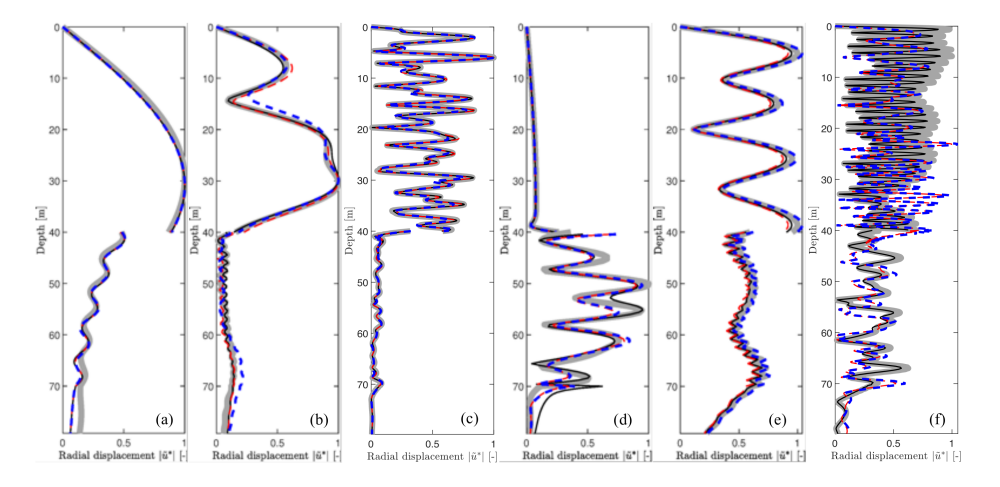


Figure 2.21: Comparison for the results based on direct method (Green's function) and boundary element method for a ring load at three excitation frequencies 30 Hz, 125Hz and 1 kHz as indicated in the Fig. 2.20: the radial displacement for a fluid circular source at (a) f = 30 Hz at (b) f = 125 Hz at (c) f = 1 kHz; the radial displacement for a **R**-ring load in the soil at (d) f = 30Hz at (e) f = 125 Hz at (f) f = 1 kHz. Black thin line indicates results from BIE at  $r_s = 5$  m, red dashed line indicates results from BIE at  $r_s = 20$  m, blue dashed line indicates results from BIE at  $r_s = 40$  m, and the grey thick line represents the results from the Green's function (direct method).

of either fluid or soil source in the domain, the solutions show a good agreement between two approaches, which validates the BIE formulation for the sound propagation model. Figure 2.21 also shows that the BIE solutions agree well at different coupling radius  $r_s$ , which indicates that the influence of the choice of  $r_s$  is insignificant and the solutions are stable. However, a sufficient area of the cylindrical surface at  $r = r_s$  needs to be coupled in order to propagate the full waveforms. In this scenario, a value of  $z_{bot} = 80m$  is selected for both cases to ensure that energy transmission is captured to an adequate depth on the cylindrical surface.

#### THREE-DIMENSIONAL BIE

Similarly to the case study discussed above, the three-dimensional fluid layer overlying an elastic half-space is modelled in COMSOL Multiphysics with a non-symmetric loading condition. We introduce the function  $\widetilde{H}(r,\theta,z)$  as the transmission coefficient at  $r=r_s$ . In practice, this function can be considered an idealized noise-cancelling screen based on any noise mitigation system applied in the water column. A more detailed discussion on the derivation of the transmission coefficients is provided in Chapters 6 and 7. As the 3D case in COMSOL requires more computational effort due to the increased mesh, number of degrees of freedom and resulted modelling integrations in the MUMP solver, the size of the model is reduced compared to the previous case by decreasing the water depth and soil depth examined. The comparison between the FEM model and semi-analytical model based on the boundary integral equation formulation are shown in Figs. 2.24-2.26.

The  $\theta$  dependent transfer function is defined in Fig. 2.23, which can be transformed into the complex Fourier domain as  $\widehat{H}_m(r,z)$ . The input parameters including the geometry

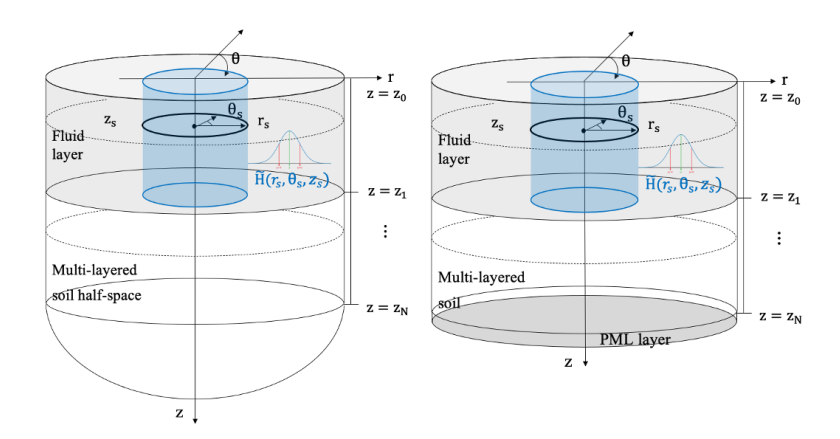


Figure 2.22: Geometry of the model for the validation of the boundary integrals formulations for a surface load positioned in the fluid domain.

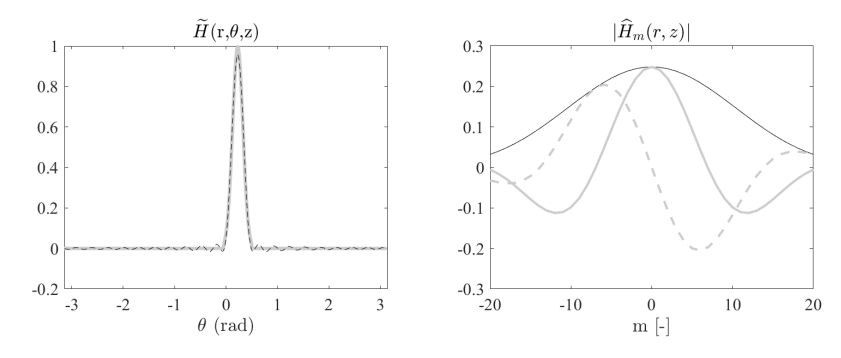


Figure 2.23: Non-fully blocked idealized noise cancelling screen:  $\widetilde{H}(r,\theta,z)$  is the transmission coefficient and  $\widehat{H}_m(r,z)$  is transformed complex Fourier coefficient with m-th order.

Table 2.8: Basic input parameters for the validation study.

Parameter	Depth	ρ	$c_L$	$c_T$	$\alpha_p$	$\alpha_s$
-	[m]	$[kg/m^3]$	[m/s]	[m/s]	$[dB/\lambda]$	$[dB/\lambda]$
Fluid	40	1000	1500	-	-	-
Bottom soil	$\infty$	1888	1775	198	0.2	0.8

of the domain and the material properties are given in Table 2.8. A surface load with unit amplitude in both pressure and velocity as defined in  $\widetilde{H}(r, \theta, z)$  is placed at  $r_s = 10$ m throughout the entire water depth as indicated in the Fig. 2.22.

In the FE model, the soil half-space is substituted by a perfectly-matched layer to account for the radiation condition at  $z \to \infty$ . The comparison between the FEM model and semi-analytical model based on the boundary integral equation formulation are shown in Figs. 2.24 - 2.27. The Green's tensors and Boundary Integral solutions are compared to the

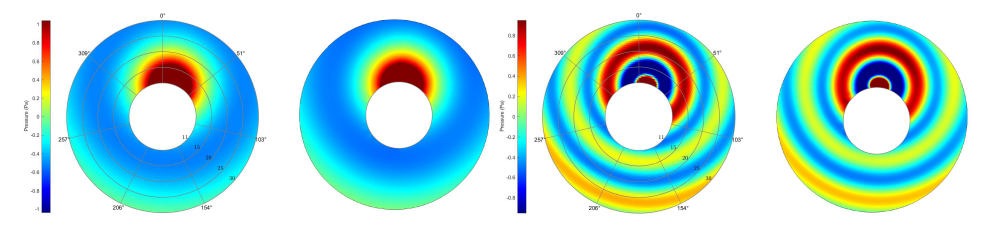


Figure 2.24: Comparison of Green's tensors from the proposed model (left) and FEM (right) at excitation frequencies 30 Hz (left) and 125 Hz (right) as indicated in Fig. 2.22 for the mid of the water depth.

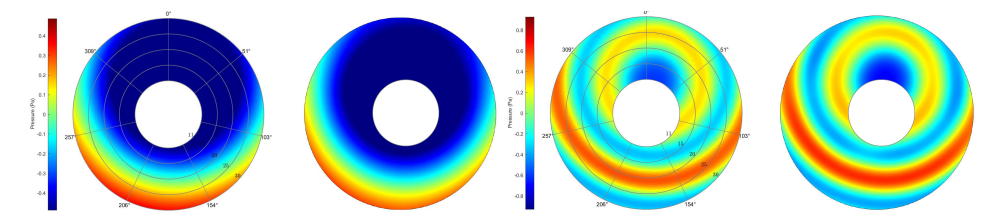


Figure 2.25: Comparison of Green's tensors based on EJP-complex wavenumber integration and FEM (COMSOL) at excitation frequencies 30 Hz (left) and 125 Hz (right) as indicated in Fig. 2.22: the pressure at 2m above the seabed.

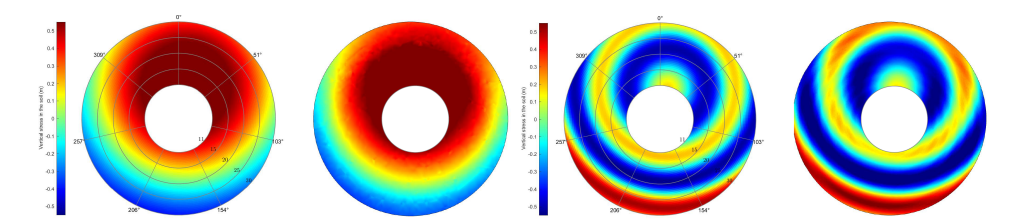


Figure 2.26: Comparison of Green's tensors from the proposed model (left) and FEM (COMSOL, right) at excitation frequencies 30 Hz (left) and 125 Hz (right) as indicated in Fig. 2.22: the normal stress of the soil  $\sigma_{zz}$  at 1m below the seabed.

numerical results from the FEM. As shown, the semi-analytical approach yields results in excellent agreement with the FEM solutions. This demonstrates the accuracy and reliability of the semi-analytical method in modelling complex wave propagation, as it effectively captures the key characteristics of the problem while maintaining computational efficiency.

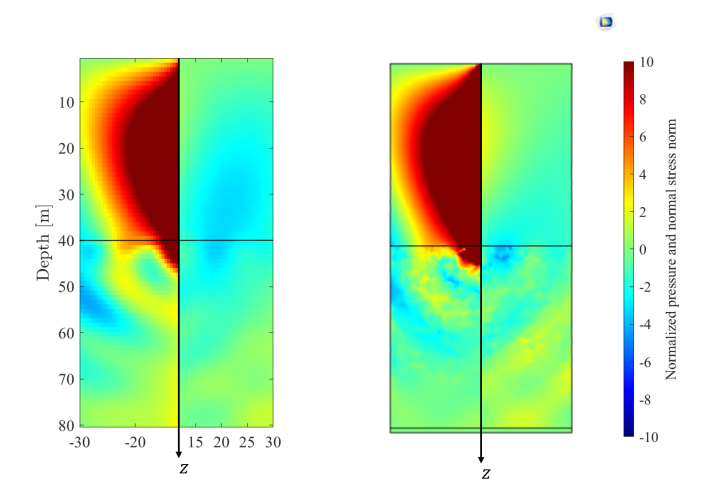


Figure 2.27: Comparison of Boundary Integral Formulation from the proposed model (left) and FEM (right) at excitation frequencies 30 Hz as indicated in Fig. 2.22. The pressure field in the fluid and the normal stress of the soil  $\sigma_{zz}$  for  $\theta = 15^{\circ}$  and  $195^{\circ}$  are shown.

# 2.5 Conclusions

To advance the mathematical and computational treatments of the boundary value problem involving a three-dimensional acousto-elastic multilayered half-space, the derivation of the fundamental Green's functions for the acousto-elastodynamic problem is presented. Using the method of displacement potentials, an elegant mathematical structure underlying this class of 3D elastodynamic problems is revealed, warranting further attention. To handle arbitrarily distributed loads, ring-load Green's functions for stresses and displacements are expressed through contour line integration. The complex wavenumber integration technique adopted in the latter advances the mathematical treatment of the Green's function for an acousto-elastic layered half-space. The choice of the branch cut ensures both stability and convergence of the obtained solution. The attenuation in multilayered soil half-space is included by identifying the exact poles and branch cuts in the complex wavenumber plane, which is especially important for wave propagation in large distances.

The Green's functions and boundary integral equation developed in this chapter will find application in sound propagation analysis for pile driving noise. Given the substantial energy radiated into the soil domain during pile driving, accurate description of the frequency-dependent characteristics of wave attenuation, along with the geometry and properties of the acousto-elastic halfspace, is crucial for an effective representation of the ocean environment. The boundary integral equation model can also be utilized to couple the frequency- and depth-dependent transmission coefficient of noise mitigation systems, such as air bubble curtain systems, to derive the mitigated sound field. This approach has broad applicability in various engineering disciplines, including underwater acoustics, fluid-soil-structure interaction, and seismology. The mathematical tools developed in this chapter will be used in the subsequent chapters when analysing sound emissions from impact piling including the implementation of various noise mitigation systems.

3

# NEAR- AND FAR-FIELD NOISE AND VIBRATION PREDICTION DUE TO OFFSHORE PILE DRIVING

A computationally efficient modelling approach is presented for predicting underwater noise radiation from offshore pile driving. The complete noise prediction model comprises two modules. First, a sound generation module is adopted to capture the interaction between the pile, the fluid, and the seabed, aiming at modelling the sound generation and propagation in the vicinity of the pile. Second, a sound propagation module is developed using the dynamic Green's functions and the boundary integral equations (BIEs) formulated in Chapter 2 to propagate the sound field at larger distances from the pile. The model advances the computational efficiency and flexibility of the noise prediction in both near- and far-fields from the pile. Finally, model predictions are benchmarked against a theoretical scenario and validated using measurement data from a recent offshore pile-installation campaign.

The structure of this chapter is as follows. In Section 3.1, the governing equations and model description are presented. In Sections 3.2 and 3.3, the solution method is presented as a two-step approach that utilizes the sound generation module and the sound propagation module. In Section 3.4, the numerical evaluation of the solutions is presented based on the normal mode solution with complex wavenumber integration addressing both numerical stability and convergence. The choice of the branch cuts and the physical interpretation of contributions from discrete poles are also discussed. Section 3.5 is dedicated to a numerical analysis of several benchmark cases, which proves the validity of the model for the prediction of underwater noise from offshore pile driving. In Section 3.6, the seabed vibration is discussed and the particle velocity is examined for an offshore pile installation case. Finally, the conclusions are given in Section 3.7.

# 3.1 Model description and governing equations

In this section, the description of the model and the governing equations of the fully coupled vibroacoustic system are introduced. The geometry and material properties of the system are given first, followed by the equations of motion of the vibrating shell, the fluid, and the soil together with the boundary and interface conditions. Finally, a schematic overview of the computational method is presented.

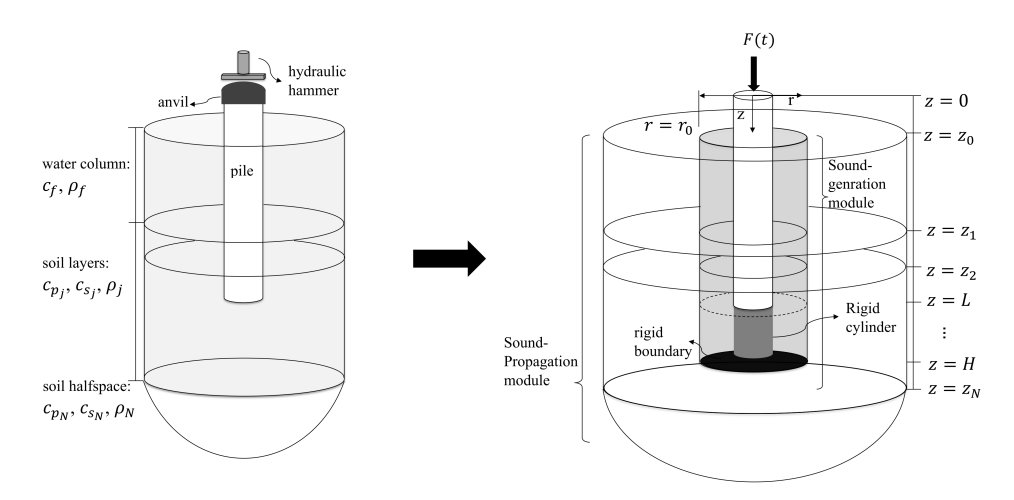


Figure 3.1: Schematic of the complete system (left) and the coupled model (right):  $r_0$  is the radial distance of the coupled cylindrical surface;  $z_0$  is the level of the sea surface;  $z_1$  is the level of the seabed,  $z_j$  is the bottom level of the  $j-1_{th}$  soil layer (j=2,3...N); L indicates the level of the bottom of pile tip; H indicates the level of the rigid boundary applied in the sound-generation module.

# 3.1.1 Description of the model

The total system consists of the pile structure, the hydraulic hammer, and the surrounding fluid and soil media as shown in Fig. 3.1 (left). A symmetric cylindrical coordinate system  $(r, \phi, z)$  is introduced for the fluid and soil domains with the depth z being positive downward and r being the radial distance from the z axis. The geometry of the model is assumed

to be horizontally stratified, with material properties in both the fluid and soil considered to be range-independent. The displacement field is described as  $\mathbf{u}_{\xi} = [\mathbf{u}_{\xi}, \mathbf{v}_{\xi}, \mathbf{w}_{\xi}]$  with  $\xi = f$  or j indicating the fluid layer or soil layer j. Because of axial symmetry, the displacement in the  $\phi$  direction  $v_{\xi}$  is trivially zero. Based on the assumption that the fluid and the soil inside the pile do not significantly influence the vibration of the pile and the radiated energy in the surrounding medium [15], the water column and the soil inside the pile are not included in this model. This assumption is verified through a comparison of the temporal evolution of the pressure field, sound exposure level, and peak levels at various distances from the monopile, for models both with and without the inclusion of the fluid and soil within the monopile [118–120].

The complete model consists of two modules, a sound generation module, and a sound propagation module. The sound generation module comprises the pile modelled as a linear elastic thin shell and the surrounding media modelled as a horizontally stratified acoustoelastic waveguide [16, 55]. A rigid cylinder of the same radius as the pile and of height H-L is placed below the pile tip which allows one to employ a closed-form semi-analytical solution for the pile-seawater-soil vibrations in the generation module. By doing so, the radiation of elastic waves from the tip of the pile into the deeper soil layers is omitted. However, this assumption is not expected to influence the noise predictions and the elastic wave propagation in the shallow soil layers close to the seafloor at distances close to the pile. The hydraulic hammer and anvil are not modeled explicitly but substituted by an external force exerted at the top of the pile (z = 0). The forcing function is obtained from available measurement data or numerical models [14, 26]. The dynamic response of the shell structure is described by a linear high-order shell theory [121]. The higher-order shell theory is chosen to accommodate all combinations of pile sizes and excitation frequencies as the high-order approximation are more accurate at higher frequency bands and do not involve any extra computational cost in the solution approach adopted [55, 121]. The pile occupies the domain  $0 \le z \le L$ , with the material and geometrical constants E, v, R,  $\rho$  and t being the complex modulus of elasticity in the frequency domain, the Poisson ratio, the radius of the mid-surface of the shell, the density and the thickness of the shell, respectively. In both modules, the fluid is modelled as a three-dimensional inviscid compressible medium with constants  $c_f$ ,  $\rho_f$  being the wave speed and the density of the fluid, which occupies the domain  $z_0 \le z \le z_1$  with  $R \le r \le r_0$  for the sound generation module and  $r \ge r_0$  for the sound propagation module. The soil is modeled as a threedimensional elastic continuum occupying the domain  $z \ge z_1$ . The constants  $\lambda_i$ ,  $\mu_i$  and  $\rho_i$ correspond to the Lamé coefficients and the density of the solid, with the index j = 1, 2, ..., Nspecifying the soil layers including the bottom soil half-space. The material dissipation (damping) in the soil is introduced in the form of complex Láme constants  $\widetilde{\lambda}_j$  and  $\widetilde{\mu}_j$ as  $\widetilde{\lambda}_j = \lambda_j (1 + i \cdot \alpha_{1_j})$  and  $\widetilde{\mu}_j = \mu_j (1 + i \cdot \alpha_{2_j})$ . The attenuation coefficients  $\alpha_{1_j}$  and  $\alpha_{2_j}$  are defined as  $(20\pi \log_{10} e)\alpha_{p_i}$  and  $(20\pi \log_{10} e)\alpha_{s_i}$  respectively, with  $\alpha_{p_i}$  and  $\alpha_{s_i}$  being the compressional and shear damping coefficients in units of dB per wavelength.

# 3.1.2 GOVERNING EQUATIONS

The following partial differential equations govern the dynamic response of coupled system consisting of the shell structure and the acousto-elastic media in time domain:

$$\mathbf{L}\mathbf{u} + \mathbf{I}\ddot{\mathbf{u}} = -(H(z - z_1) - H(z - L))\mathbf{t}_s + (H(z - z_0) - H(z - z_1))\mathbf{p}_f + \mathbf{f}_e,$$
(3.1)

$$\nabla^2 p_f(r, z, t) - \frac{1}{c_f^2} \ddot{p}_f(r, z, t) = 0 , \qquad (3.2)$$

$$(\lambda_j + 2\mu_j)\nabla(\nabla \cdot \mathbf{u}_j) - \mu_j \nabla \times (\nabla \times \mathbf{u}_j) = \rho_j \ddot{\mathbf{u}}_j. \tag{3.3}$$

In Eq. (3.1),  $\mathbf{u} = [u_z(z,t) \ u_r(z,t)]^T$  is the displacement vector of the mid-surface of the shell with 0 < z < L. The operators L and I are the stiffness and modified inertia matrices of the shell, respectively [16]. The stiffness operator is defined by the following matrix:

$$L = \begin{bmatrix} L_{zz} & L_{zr} \\ L_{rz} & L_{rr} \end{bmatrix} \tag{3.4}$$

The stiffness operator exhibits symmetry, meaning that  $L_{ij} = L_{ji}$  for i, j = z, r, and its components are described by the following expressions:

$$L_{zz} = \frac{2Eh}{(1-v^2)} \frac{\partial^2}{\partial z^2} + \frac{Eh}{R^2(1+v)} \frac{\partial^2}{\partial \theta^2}$$
(3.5)

$$L_{zr} = L_{rz} = \frac{2Eh\nu}{R(1-\nu^2)} \frac{\partial}{\partial z}$$
(3.6)

$$L_{rr} = \frac{2Eh}{3R^2(1-\nu^2)} \left( \frac{\partial^4}{\partial z^4} + \frac{h^2}{R^2} \frac{\partial^4}{\partial \theta^4} + 2h^2 \frac{\partial^4}{\partial z^2 \partial \theta^2} \right)$$
(3.7)

The modified inertia operator is described as [121]:

$$I = \begin{bmatrix} I_{zz} & I_{zr} \\ I_{rz} & I_{rr} \end{bmatrix}$$
 (3.8)

in which its terms are given by the following expressions:

$$I_{zz} = -2\rho h + a \frac{\partial^2}{\partial z^2} - b \frac{\partial^4}{\partial z^2 \partial t^2} - c \frac{\partial^6}{\partial z^2 \partial t^4}$$
(3.9)

$$I_{rr} = 2\rho h + d\frac{\partial^2}{\partial z^2} + \frac{d}{R^2}\frac{\partial^2}{\partial \theta^2} + e\frac{\partial^2}{\partial t^2} + f\frac{\partial^4}{\partial z^2 \partial t^2} + \frac{f}{R^2}\frac{\partial^4}{\partial \theta^2 \partial t^2}$$
(3.10)

$$I_{zr} = I_{rz} = 0 (3.11)$$

where  $a = 2\rho h^3 v^2 / 3(1 - v)^2$ .

The coefficients are defined as follows:

$$b = \frac{4\rho^2 h^5 v^2 (3 - 5\nu - \nu^2)(1 + \nu)}{45(1 - \nu)^3 E}$$
(3.12)

$$c = \frac{2\rho^3 h^7 v^2 (-17 + 56\nu - 33\nu^2 - 28\nu^3 + 5\nu^4)(1+\nu)^2}{315(1-\nu)^4 E^2}$$
(3.13)

$$d = \frac{2\rho h^3(7\nu - 17)}{(1-\nu)} \tag{3.14}$$

$$e = \frac{4\rho^2 h^3 (422 - 424\nu - 33\nu^2)(1+\nu)}{(1050 - 1050\nu)E}$$

$$f = \frac{2\rho^2 h^5 (32 - 96\nu + 261\nu^2 - 197\nu^3)(1+\nu)}{7875(1-\nu)^2 E}$$
(3.15)

$$f = \frac{2\rho^2 h^5 (32 - 96\nu + 261\nu^2 - 197\nu^3)(1 + \nu)}{7875(1 - \nu)^2 E}$$
(3.16)

The term  $t_s$  represents the boundary stress vector that takes into account the reaction of the soil surrounding the shell  $z_1 \le z \le L$ ,

$$\mathbf{t_s} = \begin{bmatrix} \sigma_{rz,s} \\ \sigma_{rr,s} \end{bmatrix} \tag{3.17}$$

The term  $\mathbf{p}_f$  represents the fluid pressure exerted at the outer surface of the shell at  $z_0 \le z \le z_1$ ,

$$\mathbf{p_f} = \begin{bmatrix} 0 \\ p_f \end{bmatrix} \tag{3.18}$$

The functions  $H(z-z_i)$  are the Heaviside step functions. The vector  $\mathbf{f}_e = [f_z(z,t) f_r(z,t)]^T$  represents the externally applied force on the surface of the shell. In Eq. (3.2),  $p_f(r,z,t)$  is the pressure field of the fluid. In Eq. (3.3),  $\mathbf{u}_j = [w_j(r,z,t) u_j(r,z,t)]^T$  is the vector including the vertical and radial displacements of soil layer j.

The Helmholtz decomposition is applied to the fluid-soil domain as:

$$\mathbf{u}_f = \nabla \phi_f, \quad \mathbf{u}_j = \nabla \phi_j + \nabla \times (0, -\frac{\partial \psi_j}{\partial r}, 0)$$
 (3.19)

Substitution of Eq. (3.19) into Eqs. (3.2) and (3.3) yields [101]:

$$\nabla^2 \phi_f(r, z, t) = \frac{1}{c_f^2} \frac{\partial^2 \phi_f}{\partial t^2} , \qquad (3.20)$$

$$\nabla^{2} \phi_{j}(r, z, t) = \frac{1}{c_{p_{j}}^{2}} \frac{\partial^{2} \phi_{j}}{\partial t^{2}}, \qquad (3.21)$$

$$\nabla^2 \psi_j(r, z, t) = \frac{1}{c_{s_j}^2} \frac{\partial^2 \psi_j}{\partial t^2} \ . \tag{3.22}$$

In the equations above,  $c_{p_j}$  and  $c_{s_j}$  denote the complex-valued speeds of the compressional and shear waves in soil layer j, respectively.

The pressure release boundary condition is applied at the sea surface. When incident waves interact with a rough sea surface, they scatter at various angles and experience different travel times, resulting in time shifts and amplitude variations. The validity of this assumption depends on the sea state, with low sea states showing minimal influence at lower frequencies [122]. At the fluid-soil interface  $z=z_1$ , the vertical stress equilibrium and the vertical displacement continuity are imposed, while the shear stress vanishes since no shear stresses are present in a perfect fluid. For the sound generation module, the interface at z=H is substituted by a rigid boundary at a great depth, whereas the bottom soil is extended to infinity to mimic realistic ocean environments in the sound propagation module. In the following examined cases,  $H=z_N$ . The choice of the  $z_N$  ( $z_N \ge H$ ) in practice is related to the depth of the soil layer, which is determined by the soil profiles provided by the offshore geotechnical survey. The rigid cylinder below the pile is not expected to have a significant influence on the energy distributions and the resulted pressure level in the fluid. This assumption is confirmed in the sequel by direct comparison with the measured data. To minimize the effect of the artificial reflection from the rigid boundary, the sound

generation module is coupled to the sound propagation module at a very close distance to the pile surface, so the influence of the rigid boundary becomes insignificant.

Given the full-contact at the soil-soil interface, both stress equilibrium and displacement continuity are applied. This set of boundary and interface conditions reads:

$$p_f(r, z_0, t) = 0, \quad r \ge R,$$
 (3.23)

$$\sigma_{zz_1}(r, z_1, t) + p_f(r, z_1, t) = 0, \quad u_{z,f}(r, z_1, t) = w_{s_1}(r, z_1, t), \quad \sigma_{zr_1}(r, z_1, t) = 0, \quad r \ge R,(3.24)$$

$$w_i(r, z_i, t) = w_{i-1}(r, z_i, t), \quad u_i(r, z_i, t) = u_{i-1}(r, z_i, t), \quad 2 \le j \le N, \quad r \ge R,$$
 (3.25)

$$\sigma_{zz_i}(r, z_j, t) = \sigma_{zz_{i-1}}(r, z_j, t), \quad \sigma_{zr_i}(r, z_j, t) = \sigma_{zr_{i-1}}(r, z_j, t), \quad 2 \le j \le N, \quad r \ge R.$$
 (3.26)

In Eq. (3.26),  $\sigma_{zz_j}$  and  $\sigma_{zr_j}$  designate the normal and tangential stresses in the soil layer j. For  $r < r_0$ , a rigid surface is placed at z = H (in the sound generation module) as depicted in Fig. 3.1 (right). At the pile-water interface, the pressure equilibrium and displacement continuity are imposed. Under the assumption of no pile slip, a perfect contact condition is applied at the pile-soil interface. For impact pile driving, the contact relaxation of pile-soil interface allowing the relative vertical motion of the pile relative to the soil is insignificant for the underwater noise and soil vibration. However, it gains importance when predicting underwater noise in vibro-piling scenarios, as the interaction between the pile and soil plays a significant role in capturing the quasi-steady state of the system [59, 62]. The set of kinematic conditions at the interface of the shell and the surrounding media (r = R) are given as:

$$u_r(z,t) = u_f(R,z,t), \quad z_0 \le z \le z_1$$
  
 $u_r(z,t) = u_j(R,z,t) \quad \text{and} \quad u_z(z,t) = w_j(R,z,t), \quad z_1 \le z \le L, \quad 1 \le j \le N$ 
(3.27)

Following the application of the forward Fourier transform, the governing equations in the frequency domain are obtained. The Fourier transform pair utilized in this thesis is expressed in Eq. (2.12). The transformed system of the equations of motion Eqs. (3.1)–(3.3) reads:

$$L\tilde{\mathbf{u}} + \tilde{\mathbf{I}}\tilde{\mathbf{u}} = -(H(z - z_1) - H(z - L))\tilde{\mathbf{t}}_s + (H(z - z_0) - H(z - z_1))\tilde{\mathbf{p}}_f + \tilde{\mathbf{f}}_e,$$
 (3.28)

$$\nabla^2 \tilde{p}_f(r, z, \omega) + \frac{\omega^2}{c_f^2} \tilde{p}_f(r, z, \omega) = 0, \qquad (3.29)$$

$$(\lambda_j + 2\mu_j)\nabla(\nabla \cdot \tilde{\mathbf{u}}_j) - \mu_j \nabla \times (\nabla \times \tilde{\mathbf{u}}_j) = -\rho_j \omega^2 \tilde{\mathbf{u}}_j. \tag{3.30}$$

The motion of the fluid and sediment are characterised by scalar potential as:

$$\nabla^2 \tilde{\phi}_f(r, z, \omega) + \frac{\omega^2}{c_f^2} \tilde{\phi}_f(r, z, \omega) = 0, \qquad (3.31)$$

$$\nabla^2 \tilde{\phi}_j(r, z, \omega) + \frac{\omega^2}{c_{p_j}^2} \tilde{\phi}_j(r, z, \omega) = 0, \qquad (3.32)$$

$$\nabla^2 \tilde{\psi}_j(r, z, \omega) + \frac{\omega^2}{c_{s_j}^2} \tilde{\psi}_j(r, z, \omega) = 0, \qquad (3.33)$$

(3.34)

The transformed boundary and interface conditions read:

$$\tilde{p}_f(r, z_0, \omega) = 0, \quad r \ge R,\tag{3.35}$$

$$\tilde{\sigma}_{zz_1}(r, z_1, \omega) + \tilde{p}_f(r, z_1, \omega) = 0, \quad \tilde{u}_{z,f}(r, z_1, \omega) = \tilde{w}_{s_1}(r, z_1, \omega), \quad \tilde{\sigma}_{zr_1}(r, z_1, \omega) = 0, \quad r \ge R,$$
(3.36)

$$\tilde{w}_j(r,z_j,\omega) = \tilde{w}_{j-1}(r,z_j,\omega), \quad \tilde{u}_j(r,z_j,\omega) = \tilde{u}_{j-1}(r,z_j,\omega), \quad 2 \leq j \leq N, \quad r \geq R, \quad (3.37)$$

$$\tilde{\sigma}_{zz_{j}}(r,z_{j},\omega) = \tilde{\sigma}_{zz_{j-1}}(r,z_{j},\omega), \quad \tilde{\sigma}_{zr_{j}}(r,z_{j},\omega) = \tilde{\sigma}_{zr_{j-1}}(r,z_{j},\omega), \quad 2 \leq j \leq N, \quad r \geq R.$$
(3.38)

$$\tilde{u}_r(z,\omega) = \tilde{u}_f(R,z,\omega), \quad z_0 \le z \le z_1 \tag{3.39}$$

$$\tilde{u}_r(z,\omega) = \tilde{u}_j(R,z,\omega)$$
 and  $\tilde{u}_z(z,\omega) = \tilde{w}_j(R,z,\omega)$ ,  $z_1 \le z \le L$ ,  $1 \le j \le N$  (3.40)

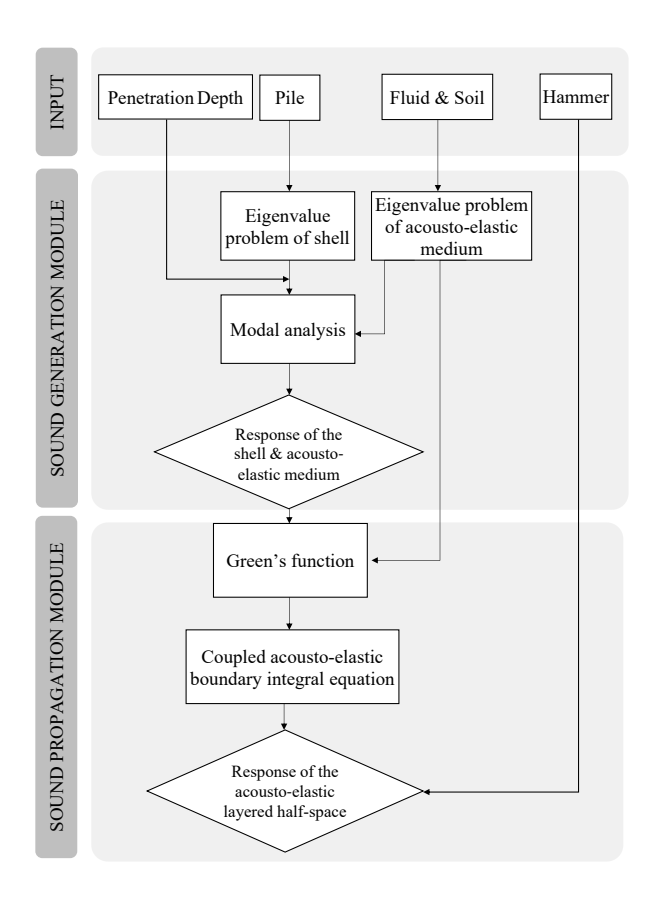


Figure 3.2: Diagram of the computational approach of the model and its components.

# 3.1.3 AN OVERVIEW OF THE COMPUTATIONAL METHOD

The diagram of the complete model is shown in Fig. 3.2, which presents the computational model and the process of the simulation. As indicated in the diagram, variation of certain input parameters, e.g., the penetration depth of the pile or the input forcing function, requires solely part of the simulation to be re-evaluated, which significantly improves the computation efficiency of the model for making it suitable for a large number of parametric studies.

# 3.2 Sound generation module

The sound generation module is based on a three-dimensional cylindrically symmetric vibroacoustic model developed by Tsouvalas and Metrikine [16]. The module captures the dynamic interactions between the pile and the surrounding media. A modal decomposition is applied both to the shell structure and the acousto-elastic waveguide. Based on the mode-matching technique, the response of a coupled pile-water-soil system is obtained in the frequency domain. The wavenumber spectrum associated with the evanescent waves of the waveguide is significant for the vibro-acoustic interaction problem as shown in [77]. A set of the response functions in terms of pressure, velocity, displacement and stress tensors are obtained as input for the sound propagation model discussed in section 3.3. The expressions for the fluid pressure, soil stresses and displacement are given as follows:

$$\tilde{p}_f(r, z, \omega) = \sum_{p=1}^{\infty} C_p H_0^{(2)}(k_p r) \tilde{p}_{f, p}(z)$$
(3.41)

$$\tilde{u}_{j}(r,z,\omega) = \sum_{p=1}^{\infty} \frac{1}{\sqrt{C_{p}}} H_{1}^{(2)}(k_{p}r) \tilde{u}_{j,p}(z)$$
(3.42)

$$\tilde{w}_{j}(r,z,\omega) = \sum_{p=1}^{\infty} \frac{1}{\sqrt{C_{p}}} H_{0}^{(2)}(k_{p}r) \tilde{w}_{j,p}(z)$$
(3.43)

$$\tilde{\sigma}_{zz_j}(r,z,\omega) = \sum_{p=1}^{\infty} \frac{1}{k_p r} \left( k_p \lambda_j \tilde{u}_{j,p}(z) + \rho_{s_j} c^2 L \frac{d \tilde{w}_{j,p}(z)}{dz} \right)$$
(3.44)

$$\tilde{\sigma}_{zr_j}(r,z,\omega) = \sum_{p=1}^{\infty} \mu_j \frac{C_p}{k_p r} \frac{d\tilde{u}_{j,p}(z)}{dz} - k_p \mu \tilde{w}_{j,p}(z)$$
(3.45)

$$\tilde{\sigma}_{rr_j}(r,z,\omega) = \sum_{p=1}^{\infty} \frac{1}{k_p r} \left( \frac{k_p \rho_s c^2 L}{u_{j,p}(z)} + \lambda_s \frac{d \tilde{w}_{j,p}(z)}{dz} \right)$$
(3.46)

with  $\tilde{\sigma}_{rr_j,p}^{H_0}(z) = k_{p,j}\rho_{s,j}c^2L\tilde{u}_{j,p}(z) + \lambda_j d\tilde{w}_{j,p}(z)/dz$  and  $\tilde{\sigma}_{rr_j,p}^{H_1}(z) = -2\mu_j \tilde{u}_{j,p}(z)$  in which the complex-valued coefficients  $C_p$  are determined by solving for the forced response of the complete coupled system,  $\tilde{p}_{f,p}(z)$  are the eigenfunctions of the pressure for the mode p.

Upon an appropriate linear combination of the set of the pile-water and pile-soil interface conditions at r = R and orthogonality properties of the acousto-elastic and the

shell structure modes, the solution to the complete system reads,

$$\sum_{q=1}^{\infty} C_q \left( L_{qp} + k_q H_1^{(2)}(k_q R) \Gamma_q \delta_{qp} - \sum_{m=1}^{\infty} \frac{R_{mq} Q_{mp}}{I_{0m}} \right) = \sum_{m=1}^{\infty} \frac{F_{0m} Q_{mp}}{I_{0m}}$$
(3.47)

in which  $R_{mp}$  indicates the dynamic stiffness of the soil–fluid domain,  $F_{0,m}$  is the modal force,  $Q_{mp}$  and  $L_{pq}$  are integrals over the pile-water and pile-soil interfaces as defined in [16]. The following orthogonality relation holds:

$$\Gamma_{p}\delta_{pq} = -\int_{z_{1}}^{z_{2}} \left(\frac{\tilde{v}_{f,r,q}(z)}{i\omega k_{q}}\tilde{p}_{f,p}(z)\right) dz 
+ \int_{z_{2}}^{L} \left(\zeta_{s}k_{p}^{2}\frac{\tilde{u}_{j,p}(z)\tilde{u}_{j,q}(z)}{k_{p}k_{q}} + \eta_{s}\tilde{u}_{j,q}(z)\frac{\tilde{\sigma}_{zz_{j},p}(z)}{k_{q}} - \tilde{u}_{j,q}(z)\frac{\tilde{\sigma}_{zr_{j},q}(z)}{k_{q}}\right) dz$$
(3.48)

in which  $\zeta_s = \rho_{s_j} [\rho_s c_{p_j}^4 - \left(c_{p_j}^2 - 2c_{s_j}^2\right)^2]/c_{p_j}^2$ ,  $\eta_s = c_{p_j}^2 - 2c_{s_j}^2/c_{p_j}^2$ . The acousto-elastic modes are normalized so that  $|\Gamma_p| = 1$ . Equation (3.47) can be solved for the unknown complex-valued coefficients of the layered medium,  $C_p$ . Once these are known, the inverse Fourier transform can provide the response of the complete system in the time domain.

Because the complete system is linear and the eigenvalue problems of the shell and the acousto-elastic waveguide are solved independently, only part of the simulations is required for a large number of predictions with various inputs. The sound generation module allows various scenarios (i.e., various forcing functions, soil conditions, penetration depths, etc.) to be investigated with significantly less computational effort compared to the finite element or finite difference models since only part of the simulation needs to be repeated when input parameters are varied.

# 3.3 Sound Propagation Module

The input to the sound propagation module is provided by the sound generation module through a boundary integral formulation [109, 115, 116]. This section comprises two parts. The first part describes the derivation of the Green's functions, whereas the second part discusses the formulation of the boundary integrals introduced in section 2.4.

The direct boundary element method (BEM) is adopted to couple the sound generation and sound propagation modules. The solution of the acousto-elastic wavefield employs Somigliana's identity in elastodynamics and Green's third identity in potential theory [115, 116]. The velocity, displacement and pressure/stresses on the cylindrical boundary surface  $r=r_s$  are obtained from the sound generation module. The Green's tensors obtained in section 2.2 are the fundamental solutions for the boundary integral equations. The fundamental solutions of Green's displacement tensors  $\widetilde{U}_{\alpha\beta}^{\Xi\xi}(\mathbf{r},\mathbf{r}_s,\omega)$  are derived from the potential functions [109] given the receiver point at  $\mathbf{r}=(r,z)$  (in medium  $\Xi$ ) in  $\alpha$ -direction due to a unit impulse at source  $\mathbf{r}_s=(r_s,z_s)$  (in medium  $\xi$ ) in  $\beta$ -direction:

$$\widetilde{U}_{\alpha\beta}^{s\xi}(\mathbf{r},\mathbf{r}_{s},\omega) = \nabla \widetilde{\phi}_{j,\xi}^{g}(\mathbf{r},\mathbf{r}_{s},\omega) + \nabla \times W, \qquad (3.49)$$

$$\widetilde{U}_{\alpha\beta}^{f\xi}(\mathbf{r},\mathbf{r}_{s},\omega) = \nabla \widetilde{\phi}_{f,\xi}^{g}(\mathbf{r},\mathbf{r}_{s},\omega). \tag{3.50}$$

in which  $W=-\partial \psi^g_{s_j,\xi}(\mathbf{r},\mathbf{r}_s,\omega)/\partial r$ . The displacement potential functions of acousto-elastic domain have been derived in section 2.2. The Green's stress tensors  $\widetilde{T}^{\Xi\xi}_{\alpha\beta}(\mathbf{r},\mathbf{r}_s,\omega)$  related to  $\widetilde{U}^{\Xi\xi}_{\alpha\beta}(\mathbf{r},\mathbf{r}_s,\omega)$  are obtained through substitution of potential functions given in section 2.2 into the constitutive equations [109]. By utilizing Betti's reciprocal theorem in elastodynamics [115] and Green's theorem for acoustic problem [116] as discussed in section 2.4.2, the complete solution for the acousto-elastic domain can be written as:

$$\widetilde{u}_{\alpha}^{\Xi}(\mathbf{r},\omega) = \widetilde{u}_{\alpha}^{\Xi,f}(\mathbf{r},\omega) + \widetilde{u}_{\alpha}^{\Xi,s}(\mathbf{r},\omega) = \sum_{\beta=r,z} \int_{S^{s}} \left( \widetilde{U}_{\alpha\beta}^{\Xi,s}(\mathbf{r},\mathbf{r}_{s},\omega) \cdot \widetilde{t}_{\beta}^{\mathbf{n}}(\mathbf{r}_{s},\omega) - \widetilde{T}_{\alpha\beta}^{\mathbf{n},\Xi,s}(\mathbf{r},\mathbf{r}_{s},\omega) \cdot \widetilde{u}_{\beta}(\mathbf{r}_{s},\omega) \right) dS^{s}(\mathbf{r}_{s}) + \int_{S^{f}} \left( \widetilde{U}_{\alpha r}^{\Xi,f}(\mathbf{r},\mathbf{r}_{s},\omega) \cdot \widetilde{p}(\mathbf{r}_{s},\omega) - \widetilde{T}_{\alpha r}^{\mathbf{n},\Xi,f}(\mathbf{r},\mathbf{r}_{s},\omega) \cdot \widetilde{u}_{r}(\mathbf{r}_{s},\omega) \right) dS^{f}(\mathbf{r}_{s}), \quad \mathbf{r} \in V$$
(3.51)

in which **n** is the outward normal to the cylindrical boundary. The cylindrical surface in both the fluid and the soil domains need to be discretized when employing the direct BEM associated with the acousto-elastic layered half-space Green's functions. The rule of thumb of using six elements per wavelength is adopted in the numerical integration of the line integral with the trapezoidal rule applied for the integration [117]. In the fluid domain, the integration is based on the shortest wavelength of the compressional waves, while in the soil domain, the size of the element is governed by the shortest shear wavelength at the maximum frequency of interest.

# 3.4 Numerical considerations

In this section, the numerical computation of the eigenvalues and the branch line integrations are presented, which determine stability and convergence of the complete solution. The case study examines an acousto-elastic layered half-space consisting of an upper sediment layer and a bottom half-space. The geometry and material properties of the model are summarized in Table 3.1.

Table 3.1: Basic input parameters for the case study.

Parameter	Fluid	Upper soil	Bottom sediment
Depth [m]	39.9	1.5	∞
$\rho  [\mathrm{kg/m^3}]$	1000	1670	1950
$c_p$ [m/s]	1500	1560	1979
$c_s$ [m/s]	-	94	349
$\alpha_p [dB/\lambda]$	-	0.55	0.27
$\alpha_s [dB/\lambda]$	-	1.36	1.09

# 3.4.1 ROOT-FINDING ALGORITHM AND POLES

There are two challenges associated with the root-finding algorithm: (i) root-search in the complex wavenumber plane; (ii) presence of the branch cuts due to the soil half-space.

Regarding the first item above, when dissipation is included in the form of complex Lam $\acute{e}$  constants, all roots become complex-valued.

This adds certain complexities in the root-searching in the complex  $k_r$ -plane compared to the search of the eigenvalues for the lossless seabed case, which solely takes place on the real axis for poles related to propagating waves [116, 123]. Poles related to evanescent waves migrate from their original position in the complex wavenumber plane, which leads to the asymmetric distribution of the roots in the third and fourth quadrant of the complex wavenumber plane. In contrast, for lossless seabed the symmetric feature requires the search of roots in only one of the quadrants.

Another challenge is associated with the branch cuts which are necessary when the bottom soil is modelled as a multilayered half-space. Compared to traditional root-searching for the acousto-elastic waveguide, this requires the root-finding to be performed on the correct Riemann surface across the branch cut to ensure the satisfaction of the radiation condition at  $z \to \infty$ . The configuration of the acousto-elastic half-space speeds up the root-searching since only a finite number of poles are required for the convergence of the solution.

In the computation presented in the sequel, the marine sediment layer is modelled by an almost fluidized thin soil layer at the upper part of the seabed, which is typically encountered in many offshore environments. This adds another challenge in the rootsearching, which leads to a larger real part of the pole associated with *Scholte* waves at the fluid-soil interface, which are the slowest propagating waves present in the media.

In Fig. 3.3, the complex-valued roots are obtained for two excitation frequencies f=50 and 500 Hz. As shown in the enlarged plots, by solving the characteristic equation for the configuration summarized in Table 3.1, all poles are located at the intersections of the blue and red lines, indicating  $\Re(det)=\Im(det)=0$ . The poles can be categorized into two types. One is related to the trapped modes, i.e., the first five modes shown in Fig. 3.4 (top) for f=50Hz, in which vibrations of the system are localized within one of the acousto-elastic layers along with the depth or on one interface while decaying outside this finite area. The other one is related to the leaky modes, as the sixth mode shown in Fig. 3.4, in which the energy radiates into the surrounding media (oscillatory patterns through the depth) as depicted in Fig. 3.4. As shown in Fig. 3.4, the trapped modes associated with Scholte and Stoneley waves are well captured. The grey-shaded area indicates the 1.5m-thick marine sediment layer, which plays a crucial role in channelling the energy radiated from the pile between the water column and the seabed.

# 3.4.2 THE BRANCH CUTS AND BRANCH LINE INTEGRALS

Due to the presence of the soil half-space, the branch cuts are introduced and branch line integrations are required to obtain the exact Green's functions [101]. The convergence of the solutions is influenced by choice of branch cuts. The criteria for assessing the convergence of the solution ensure that the ratio between the contribution of the branch line integration and the cumulative branch line integration is less than 1E-5 to allow high accuracy and convergence of the solution. The most commonly applied ones are the Pekeris and Ewing-Jardetsky-Press (EJP) branch cuts [97, 101, 124, 125]. For a fluid layer overlying an elastic half-space, the advantage of the EJP solution is that it only requires truncating the branch line integrations. In contrast, the Pekeris solution needs to truncate

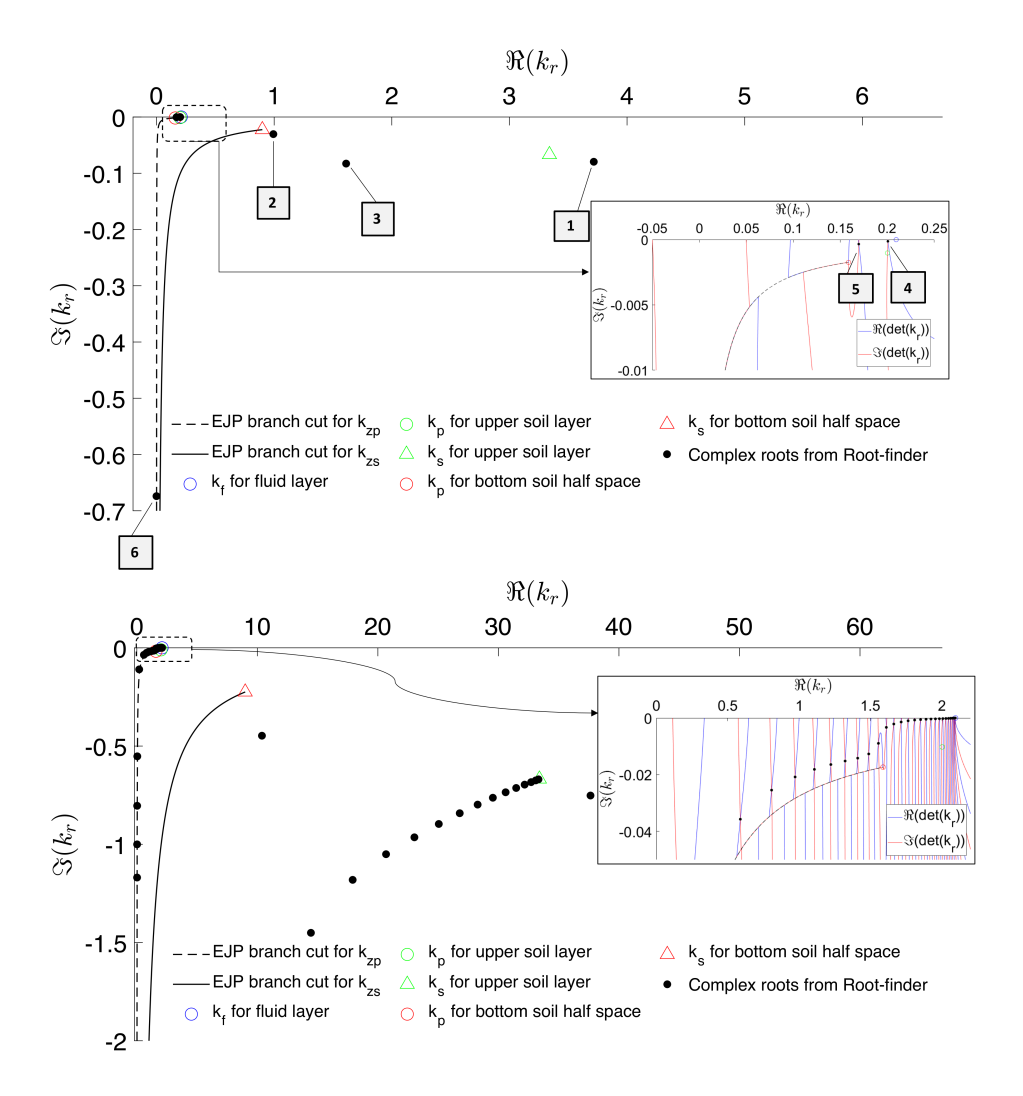


Figure 3.3: Complex roots for an acousto-elastic layered half-space with the parameters specified in Table 3.3 at 50 Hz (top) and 500 Hz (bottom). The enlarged plots (within the box of the dashed-line) verify the accuracy of the roots as the roots all locate at the intersections of the contour lines  $\Re(det) = 0$  (blue line) and  $\Im(det) = 0$  (red line).

both the vertical branch line integrations and normal modes [96]. The latter one is valid only when the observation point is located at a sufficiently shallow depth or a sufficiently large range, which is due to the numerical instability of the solutions that may easily violate the radiation condition along the z-direction. In contrast, the representation of the EJP solution is convergent at all ranges and depths, which ensures smooth convergence of the Green's tensors. In Fig. 3.3, most of the poles related to the propagating waves trapped in the water column and the poles associated with leaky waves that radiate energy into the

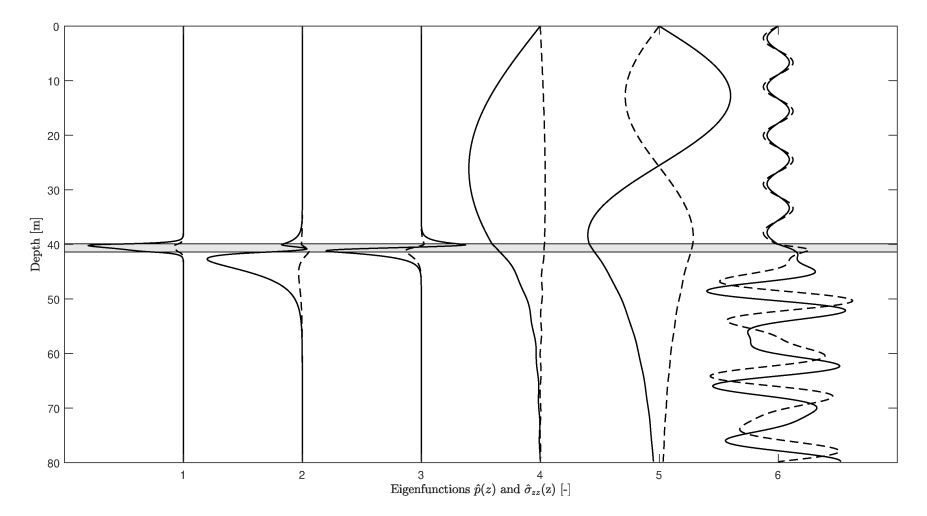


Figure 3.4: Eigenfunctions of pressure and stress  $\sigma_{zz}$  for an acousto-elastic layered half-space at 50 Hz for the wavenumbers as indicated in Fig. 3.3 (a): (1) the trapped mode associated with the Scholte wave; (2) the trapped mode associated with Stoneley wave; (3) the trapped mode in the marine sediment layer; (4) & (5) two trapped modes in the fluid domain; (6) the leaky mode. The solid line indicates the real part of the eigenfunctions and the dashed line represents the imaginary part.

surrounding media are located on the principal Riemann surface. The pole associated with the Scholte wave is found on the third Riemann surface.

# 3.5 Numerical results and model validation

In this section, the solution of the complete model is examined for several benchmark cases: (a) theoretical bench scenario from COMPILE workshop with numerical data from several different numerical models [118]; (b) validation case with measurement data from a recent offshore wind farm in the German North Sea. The material and geometrical parameters are obtained from the literature [118] for case (a) and available geotechnical reports at the pile installation site for case (b). The results were obtained on a quad-core 3.6 GHz processor running the 64-bit Windows operating system. The total computation time for the solution is the sum of  $T_{total} = t_f^{\text{CPU}} \cdot N_f = t_{f,g}^{\text{CPU}} \cdot N_f \cdot N_g$ , in which  $N_f$  is the number of frequencies considered,  $N_g$  is the number of grid points considered in which output is required,  $t_f^{\text{CPU}}$  represents the average computation time per frequency and  $t_{f,g}^{\text{CPU}}$  represents the average computation time per frequency.

# 3.5.1 THEORETICAL BENCHMARK CASE COMPILE I

In this section, the case examined is based on a generic theoretical benchmark case for underwater noise prediction for offshore pile driving. At the COMPILE workshop in 2014, seven different modeling approaches were presented [118]. As given in Table 3.2, the model consists of a pile with a Young's modulus of 210 GPa, a Poisson ratio of 0.3 and a fluid layer overlying a soil half-space. The forcing function is reported in [118] and the computation involves 3000 equally spaced frequencies ranging from ~0.8333Hz to 2500Hz.

The average computation time for the solution per output grid per frequency is  $t_{f,g}^{\rm CPU}=0.02$  s. In the models at the COMPILE workshop, the material damping in the pile is introduced in the embedded section of the pile through compressional and shear wave speed, which is different from the approach of introducing a frequency independent structural loss factor for the shell structure used in this model.

Table 3.2: Basic input parameters for the COMPILE benchmark case [118].

Parameter	Pile	Parameter	fluid	soil
Length [m]	25	Depth [m]	10	$\infty$
Density [kg/m³]	7850	Density [kg/m³]	1025	2000
Outer diameter [m]	2	$c_p$ [m/s]	1500	1800
Wall thickness [mm]	50	$c_s$ [m/s]	-	170
Final penetration depth [m]	15	$\alpha_p [dB/\lambda]$	-	0.469
Structural damping [-]	0.001	$\alpha_s [dB/\lambda]$	-	1.69

The zero-to-peak pressure level ( $L_{p,pk}$ ) in dB re 1  $\mu$ Pa and the sound exposure level SEL in units of dB re 1  $\mu$ P $a^2$ s are defined as [118]:

$$L_{p,pk} = 20 \log_{10} \left( \frac{\max |p(t)|}{p_0} \right), \quad \text{SEL} = 10 \log_{10} \left( \frac{1}{T_0} \int_{T_1}^{T_2} \frac{p^2(t)}{p_0^2} dt \right)$$
(3.52)

in which  $T_1$  and  $T_2$  are the starting and ending of the predicted time signature with the sound event in between and pulse duration  $T_0 = T_2 - T_1$  being 1 second and  $p_0 = 10^{-6} \text{Pa}$  is the reference underwater sound pressure.

The evolution of the pressure in time is shown in Fig. 3.5 for a point positioned 1 m above the seabed at 750 m and 1500 m radial distances from the pile. The  $L_{p,pk}$  and SEL of receiver points at radial distances up to 750 m are shown in Fig. 3.5. As can be seen, the predicted SEL and  $L_{p,pk}$  at 750 m from the pile are 164.9 dB and 189.6 dB, respectively, while the arithmetic mean values from COMPILE are 166.7 dB for the SEL and 191.2 dB for the  $L_{p,pk}$ . At 1500m, the predicted SEL and  $L_{p,pk}$  are 160.2 dB and 181 dB, respectively, while the arithmetic mean values from COMPILE are 161.3 dB for the SEL and 184 dB for the  $L_{p,pk}$ . Thus, the accuracy of the computation is less than  $\pm 2$  dB for SEL and around  $\pm 3$  dB for  $L_{p,pk}$  when compared to the arithmetic mean values determined by the various models at COMPILE workshop. As expected, the variation of SEL along the radial direction is smoother while the prediction of the  $L_{p,pk}$  is more oscillatory mainly because the latter reflects a single peak of the pressure which can be influenced by many factors and is more sensitive to the location of the observation point.

The comparison of the evolution of the pressure in time at a receiver position of r=11 m and z=5 m in the vicinity of the pile is shown in Fig. 3.6 for the comparison of different modelling techniques. The results show that all models can predict the arrivals of the primary Mach cones. The difference between this model and the models at the COMPILE workshop are mainly due to the different modelling approaches of the seabed, the latter modelled the seabed as equivalent fluid while this model describes the soil as an elastic medium. The modelled pressure field in the time domain is found to be in a relatively good agreement with the numerical results from the JASCO model compared to the other

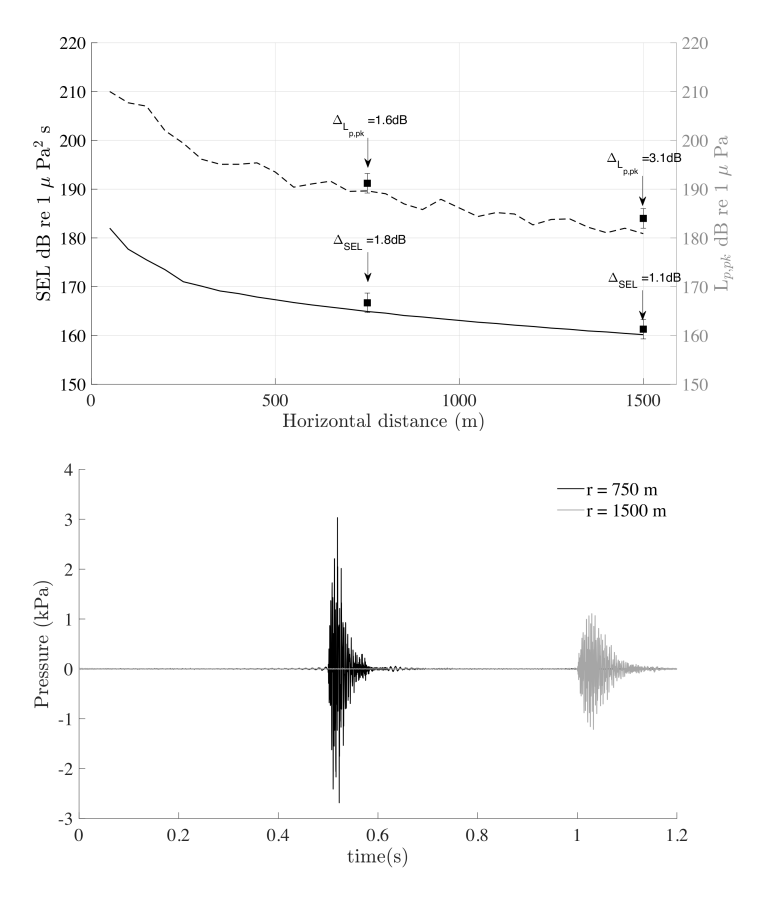


Figure 3.5: COMPILE: comparison of SEL and  $L_{p,pk}$  at several radial distances from the pile and 1 m above the seabed (top); computed time histories of the pressure in the water at various radial distances at 1 m above the seabed (bottom).

numerical models. Because the JASCO model uses a time-domain finite-difference model for pile vibrations with the pile modelled as a cylindrical thin shell in the similar approach as in this model.

Fig. 3.7 shows the pressure levels (dB re  $1\mu Pa^2/\text{Hz}$ ) in one-third octave bands at various radial distances from the pile. Assuming that the energy in all the defined bandwidths (one-third octave) results from an effective source, the bandwidth energies add directly to give the total energy in one frequency band. The derivation of the sound pressure level in the unit of dB re 1  $\mu Pa^2$  s<sup>-1</sup> reads:

$$SPL_{1/3 \text{ octave}} = 10 \log_{10} \sum_{i=m}^{n} \left( \frac{|\tilde{p}_i(\omega)|^2}{p_0^2} \right)$$
 (3.53)

As can be seen in Fig. 3.7, the spectrum shows that most of the energy is concentrated at the critical frequency range (being  $0.5f_r \sim 0.8f_r$ ) associated with the ring frequency of the

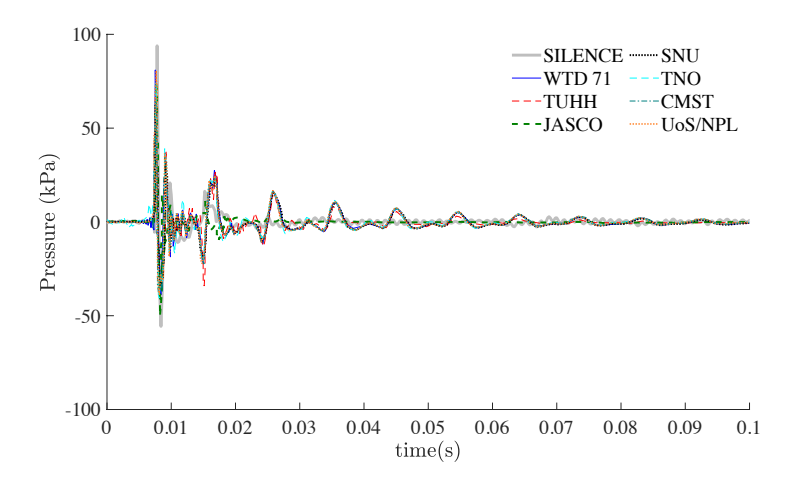


Figure 3.6: COMPILE scenario: comparison of the evolution of the pressure field at a receiver position of r = 11 m and z = 5 m.

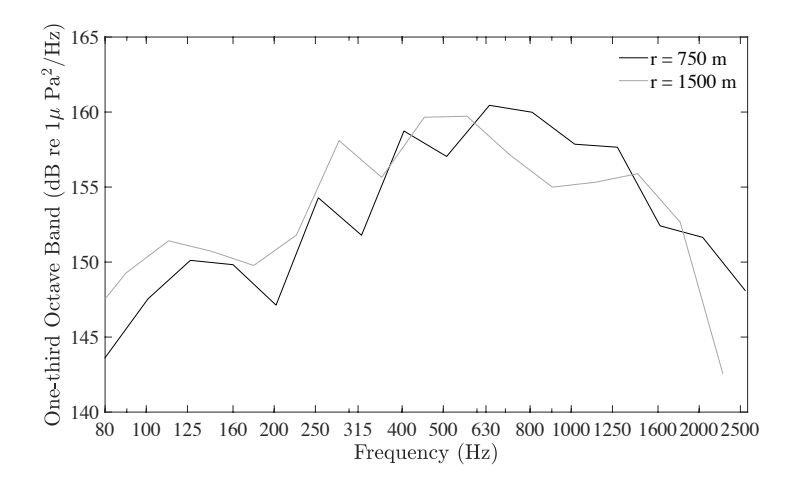
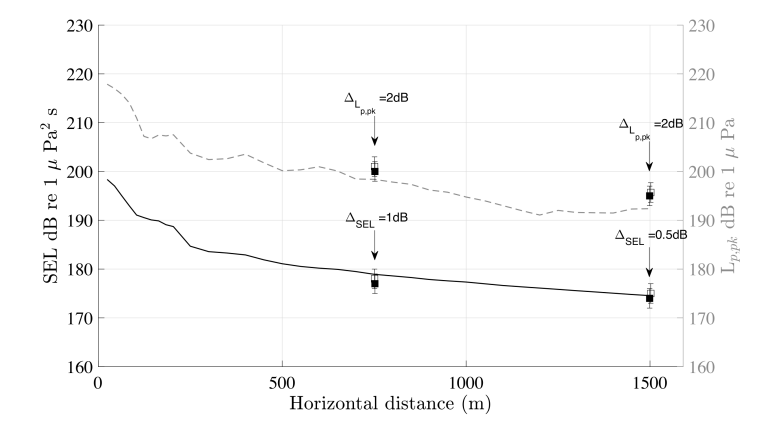


Figure 3.7: COMPILE scenario: one-third octave band spectrum for a point positioned 1m above the seabed in the fluid and at r = 750 m & 1500 m from the pile.

pile ( $f_r$  = 857 Hz), which is consistent with the characteristics of the pile dimension and the noise spectrum discussed in [58].

Table 3.3: Basic input parameters for the simulations at the offshore wind farm in the German North sea.

Parameter	Pile	Parameter	Fluid	Upper soil	Bottom sediment
Length [m]	76.9	Depth [m]	39.9	1.5	∞
Density [kg/m³]	7850	$\rho  [\text{kg/m}^3]$	1000	1670	1950
Outer diameter [m]	8	$c_p$ [m/s]	1500	1560	1979
Wall thickness [mm]	90	$c_s$ [m/s]	-	94	349
Final penetration depth [m]	32.7	$\alpha_p [dB/\lambda]$	-	0.55	0.27
Maximum Blow Energy [kJ]	1750	$\alpha_s [dB/\lambda]$	-	1.36	1.09



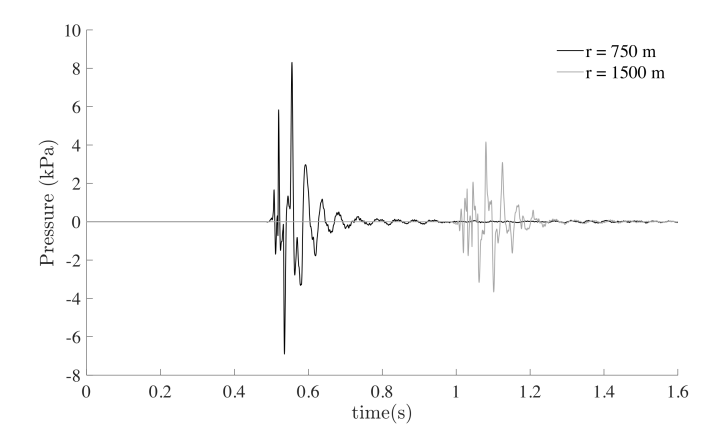


Figure 3.8: Offshore Wind Farm scenario: Pressure field at a point located at 2 m above the seabed at various radial distances from the pile: comparison of SEL and  $L_{p,pk}$ , in which the black error bar indicating the lower bound of sound levels from measurement and the hollow error bar represents the upper bound (top); computed time histories of the pressure in the water (bottom).

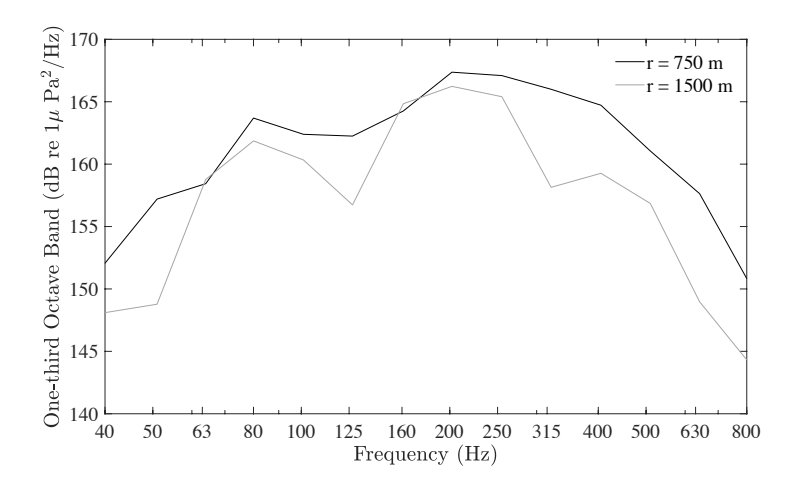


Figure 3.9: Offshore Wind Farm scenario: one-third octave band spectrum for a point positioned 2m above the seabed in the fluid and at r = 1500 m from the pile.

# 3.5.2 Offshore wind farm in German North Sea

In this section, noise predictions using the developed model are compared with measured noise data collected during installation of a foundation pile in the German North Sea in 2018. The measurement of the hydro-sound emissions was conducted at horizontal distances of 750 m and 1500 m from the pile and at a water depth of about 2 m above the seabed. The material properties and the geometry of the model are given in Table 3.3. The material of the pile is chosen to be standard steel with a Young's modulus of 210 GPa and a Poisson ratio of 0.3. The seabed consists of a thin marine sediment layer overlaying a stiffer soil half-space. The upper thin layer corresponds to a water-saturated marine sediment whereas the bottom layer corresponds to a very fine sand layer. The actual penetration depth of the pile was around 32.7 m. The forcing function (in MN) is defined as the smoothed exponential impulse:

$$F(t) = \begin{cases} F_A \sin(F_B(t - t_0)) e^{-F_C(t - t_0)}, & t_0 < t < t_1 \\ 0, & t < t_0 \text{ or } t > t_1 \end{cases}$$
(3.54)

in which  $t_0$  being 0.001s represents the start time and  $t_1$  being 0.05 s represents the end time of the pulse. The other parameters in the forcing function are given as follows:  $F_A = 503$ ,  $F_B = 149$ ,  $F_C = 150$ . This force correspondent generates approximately 1750 KJ blow energy into the system, which is in line with the measured value. The computation involves 2000 frequencies at 0.625-Hz steps ranging from  $\sim$ 0.625Hz to 1250Hz. The computation time for the solution per frequency per output grid in average is  $t_{f,g}^{\rm CPU} = 0.022$  s.

In Fig. 3.8 (bottom), the evolution of the pressure in time is shown for a point positioned 2 m above the seabed at 750 m and 1500 m radial distances from the pile. As can be seen, the arrival of the pressure cones is at around 0.5s and 1s respectively after the impact of the pile, which is in line with the expectations regarding the arrival time of the direct

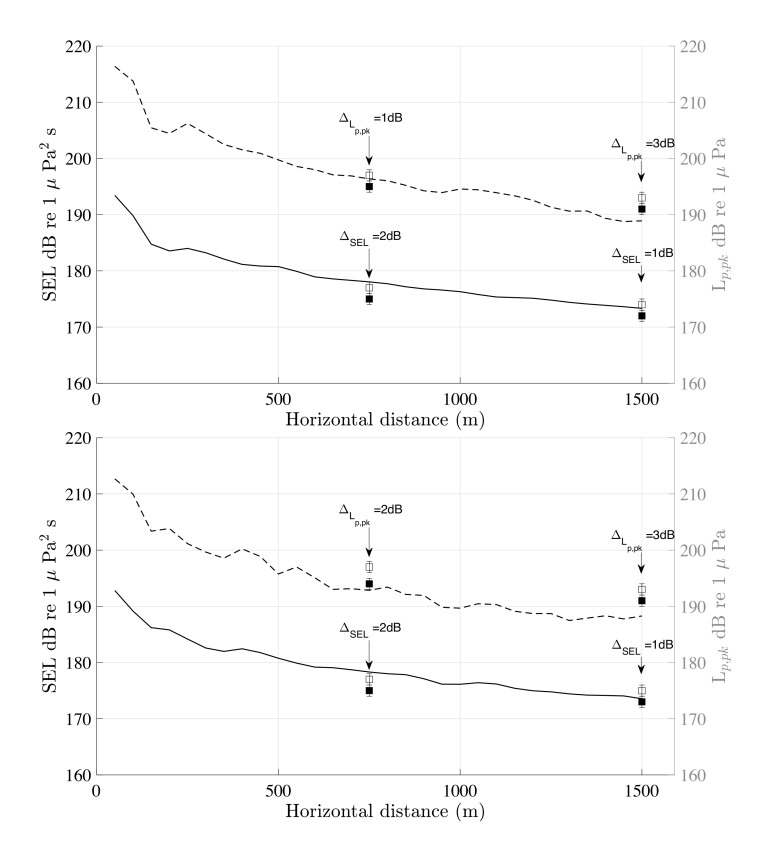


Figure 3.10: Offshore Wind Farm scenario: comparison of SEL and  $L_{p,pk}$  for the pressure field at a point located at 2 m above the seabed at various radial distances from the pile: 20-m pile penetration depth (top); 10-m pile penetration depth, in which the black error bar indicating the lower bound of sound levels from measurement and the hollow error bar represents the upper bound (bottom).

sound waves travelling with the speed of sound in the water at those distances. The  $L_{p,pk}$  and the sound exposure level (SEL) of receiver points at radial distances up to 1500 m are shown in Fig. 3.8 (top). As can be seen, the difference between the predicted SEL and the averaged measured values are 1 dB and 0.5 dB at 750 m and 1500 m radial distances from the pile respectively. The SEL indicates the averaged amount of energy radiated into the surrounding media and  $L_{p,pk}$  evaluates the impulsiveness of the pressure waves from the pile. In practice, the hydrophones were not deployed exactly at 750m and 1500m from the pile but with a deviation of up to 2 m, therefore both upper and lower bound of the SEL and  $L_{p,pk}$  from at 750m and 1500m horizontal distance from the pile and 2 m above the seabed are used as the comparison with a measurement error of  $\pm 2$  dB. The results verify the validity of the complete model, which can provide predictions that lies within the accuracy of the measurement equipment ( $\pm$  1 or 2 dB). As can be seen in Fig. 3.9, the spectrum shows that most of the energy is concentrated at low frequencies and up to around 400 Hz.

At around 10-m and 20-m pile penetration depth, the blow energy recorded was 550

kJ and 1350 kJ, respectively. Based on the measurement data, SEL and  $L_{p,pk}$  are obtained for these two cases at 750 m and 1500 m from the pile. As can be seen in Fig. 3.10, the predicted SEL and  $L_{p,pk}$  are consistent with the recorded sound levels. For the pile with 10-m penetration depth, the deviation to the central measured data point is both 2 dB for SEL and  $L_{p,pk}$  at 750 m and is 1 dB for SEL and 3 dB for  $L_{p,pk}$  at 1500 m. For the pile with 20-m penetration depth, the deviation to the central measured data point is 2 dB for SEL and 1 dB  $L_{p,pk}$  at 750 m and is 1 dB for SEL and 3 dB for  $L_{p,pk}$  at 1500 m.

As indicated in Fig. 3.2, the variation of the penetration depth of the pile does not influence the eigenvalues of the shell and acousto-elastic media. Therefore, the eigenvalue problems do not need to be recomputed for each frequency. Instead, the modal analysis and the final response of the coupled system solely needs to be solved, which largely reduces the computation time as presented in Fig. 3.11. This reduction in the computation time, as depicted by the two bars in Fig. 3.11, shows the advantage of the model when employed in parametric studies.

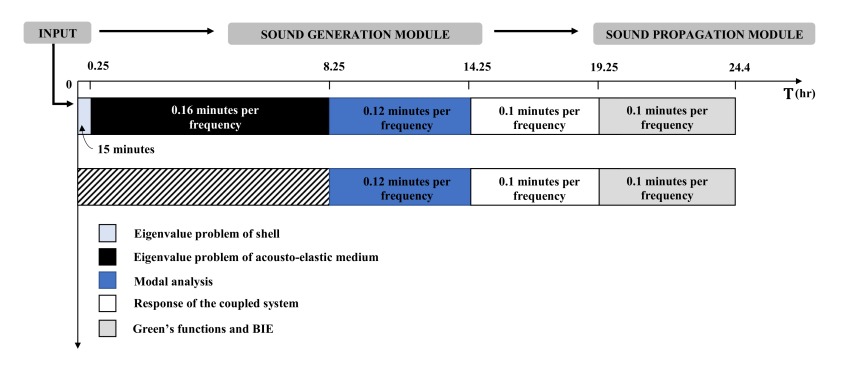


Figure 3.11: Offshore Wind Farm scenario: activity plot for the computational time of individual blocks in the model including CPU time per frequency and total execution time T, in which the first bar indicates the complete simulation and the second bar represents the computation time for 10m- or 20m-pile penetration depth.

# 3.6 PARTICLE MOTION IN SEAWATER AND SEABED VIBRATION

### 3.6.1 Prediction of seabed vibration

The evolution of the radiated wave field in pressure and volumetric stress is depicted in Fig. 3.12. Volumetric stress in the soil is defined by the equation:

$$\tau_s = -K\nabla^2 \phi = -\frac{\sigma_{zz} + \sigma_{rr} + \sigma_{\theta\theta}}{3} = -(\lambda + \frac{2}{3}\mu)\nabla \mathbf{u}$$
(3.55)

Here, the displacement  $\mathbf{u} = [u, v, w]$  and the normal stress tensors are denoted as  $\sigma_{zz}$ ,  $\sigma_{rr}$ , and  $\sigma_{\theta\theta}$ . The choice of volumetric stress aligns with the pressure waves in the fluid.

Following the impact, compressional waves within the monopile propagate downwards at supersonic speeds, inducing radial expansion and motion in the radial direction within the seawater. The wave velocity within the monopile exceeds that of the pressure waves

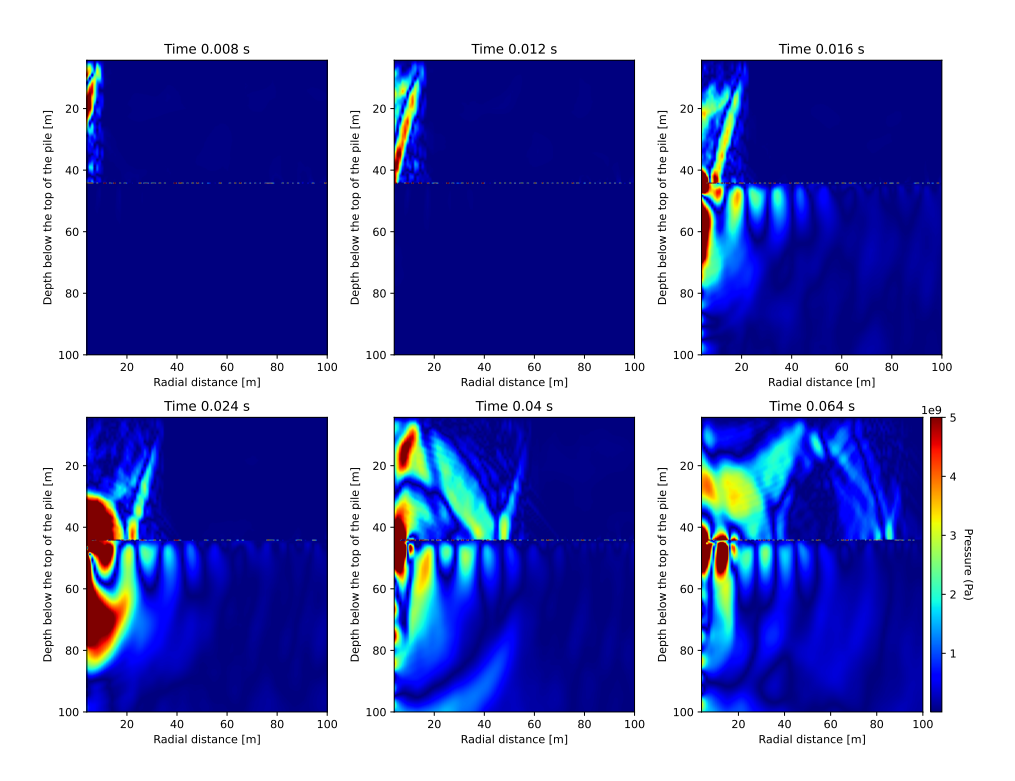


Figure 3.12: Offshore Wind Farm scenario: pressure in the fluid and Volumetric stress in the soil for various time moments after the impact of the monopile.

in the fluid, resulting in the formation of a Mach cone, clearly identifiable in Fig. 3.12. Reflected waves from the seabed give rise to secondary upward-travelling waves. Subsequently, pressure waves experience faster decay primarily due to cylindrical spreading and energy transmission into the seabed. Additional attenuation may occur due to chemical relaxation in the seawater, contingent upon factors such as pressure, temperature, and salinity. However, these are not considered herein, as the impact is minor compared to other damping mechanisms at the examined frequencies.

Soil behaviour is primarily influenced by shear and compressional waves. In this scenario, a 1.5m-layer of fluidized marine sediment overlays a stiffer medium sandy soil. In the volumetric stress plot, it is evident that shear waves exhibit higher amplitudes due to their slower propagation compared to compressional waves within the soil. The decay of these waves is attributed to both geometric spreading and material damping, with the latter being dependent on the frequency and geometric characteristics of the soil.

Scholte waves characterized by the lowest speed, can be observed along the seabed-water interface. These waves are identifiable by the poles illustrated in Fig. 3.3 and the mode shape indicated in Fig. 3.4. They play a significant role in carrying energy near the interface and are acknowledged by various models, including the elastic seabed model [16, 55, 74]. Ground roll motion, a key property induced by these waves, is identified in

the particle motion plot depicted in Fig. 3.13.

# 3.6.2 Prediction of particle motion

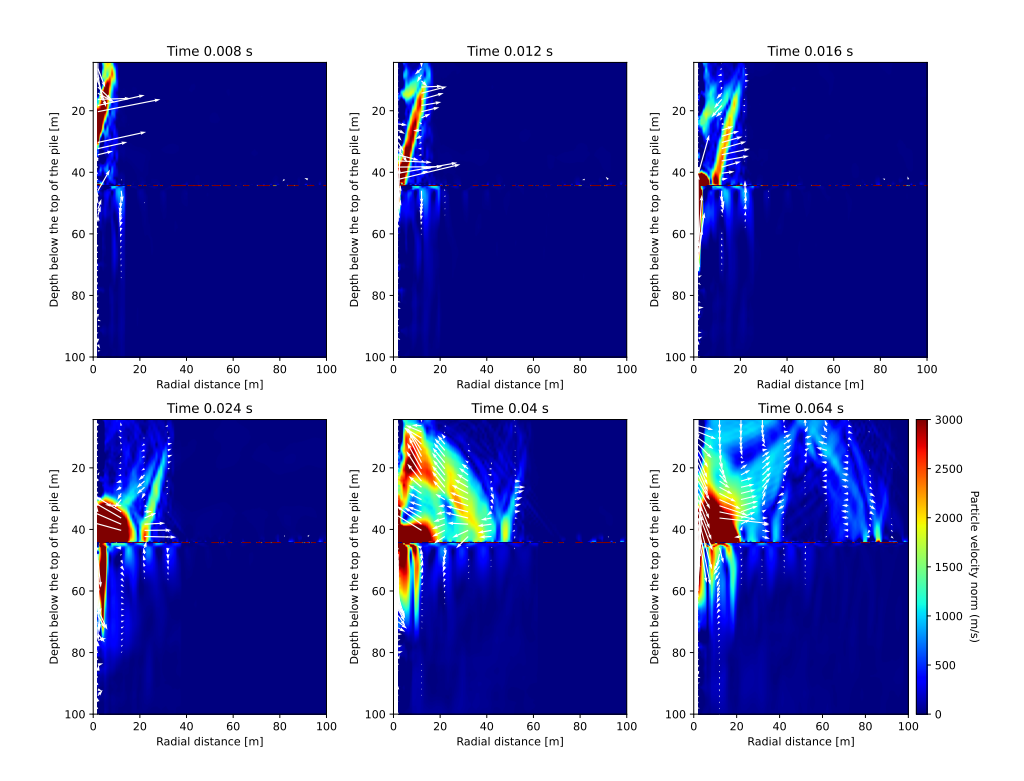


Figure 3.13: Offshore Wind Farm scenario: particle velocity norm in the unit of m/s in both fluid and soil for various time moments after the impact of the monopile.

In addition to the radiated wave field expressed by the pressure and stresses, the particle motion is also an important indicator to describe the wave field. This movement of fluid and soil particles holds particular relevance for underwater benthic communities, which inhabit the seabed closely [126]. While many species can detect and utilize particle accelerations and velocities, only a small group is capable of sensing acoustical pressure directly [44].

The evolution of the radiated wave field, as expressed by particle velocity norms in the offshore wind farm case discussed in section 3.5.2, is illustrated in Fig. 3.13, with the directionality of particle motion indicated by white arrows. It is evident that the primary transmission path for noise is through water particles, highlighted by the Mach cone, followed by vertically conical wave fronts dominated by shear waves. Regarding particle motion, notably higher velocity amplitudes are observed in the vicinity of the seabed within the water column, which constitutes vital habitats for most benthic species. We need to note here that the amplitude of the Scholte waves maybe slightly overestimated by the fact that a full bond is assumed between pile and soil in the linear model adopted in this work. In reality, pile slips relative to the soil at the front of the stress pulse propagating

3

downwards the pile which in fact may somewhat relax the amount of energy radiated in the form of interface (and shear waves) reducing their amplitude. The degree of reduction of this amplitude depends on the highly non-linear pile-soil interface dynamics and is not part of the work examined here. Furthermore, both the amplitude and directionality of particle motion undergo significant changes over short time intervals, potentially impacting marine life such as benthic crustaceans and fishes.

# 3.7 Conclusions

A computationally efficient method is developed for noise predictions over large horizontal distances in offshore pile driving. The complete model comprises a sound generation module and a sound propagation module. The former aims at describing accurately the pile-soil-water interaction and the wavefield generated at the surrounding acousto-elastic domain in the vicinity of the pile. The latter aims to propagate this wavefield at larger distances from the pile (up to a few kilometers) provided that bathymetry changes are insignificant. The mathematical statement of the complete problem is presented and the adopted method of solution is described in great detail. The direct boundary integral equation (BIE) formulation is used to couple the two modules and propagate the wavefield from the vicinity of the pile to larger distances. Numerical accuracy and solution stability are discussed in great detail together with the different physical interpretations of the various eigenmodes. One theoretical case study is examined to benchmark the model by comparison with seven different modelling techniques. Noise predictions are then performed for a pile-installation campaign in 2018 and the results are compared to the measurement data for the pile driven at various penetration depths. The results show that the model is able to capture the SEL within an accuracy of 2 dB and the  $L_{p,p,k}$  within an accuracy of around 3 dB for distances up to 1500 m from the pile at various penetration depths. The computational time is presented for each case study, which indicates the efficiency of the model. For various configurations of the system, e.g. different penetration depth, various forcing functions, various sizes of the pile, etc, it requires solely parts of the model to be recomputed, which largely reduce the computational effort and later can be used in probabilistic analysis of noise prediction.

4

# UNCERTAINTY QUANTIFICATION IN SOIL DYNAMIC CHARACTERIZATION AND ITS EFFECT ON SOUND LEVELS

Modelling the underwater sound emissions from pile driving is a challenging task due to the large uncertainty in the identification of the input parameters, mainly the dynamic properties of the marine sediment over a wide frequency range. To evaluate the significance of the uncertainties and quantify its influence over the range, a probabilistic quantification framework is established. A copula-based multivariate probabilistic model is then used to analyse the dependencies between multiple soil variables. The developed probabilistic framework is integrated to an existing computational model for the sound prediction. The sound levels and their probability distributions were evaluated without the use of a noise mitigation system. An investigation was conducted to highlight correlations between soil properties and sound levels. Copula models were utilized to compute the input samples based on the dependence between the input variables in the soil properties. After modelling the sound levels using these input data samples, the uncertainties in the input parameters were propagated to the simulation results. Consequently, the risk of the noise level exceeding a certain threshold could be estimated. This study focuses on the influence of the dynamic properties in the soil, however, this probabilistic modelling framework can be further developed to include other input parameters involving uncertainties.

In this chapter, a probabilistic framework is developed to address the uncertainties in the input parameters of the seabed in the prediction of underwater sound. The statistical distribution of the parameters are first defined by fitting the proposed distributions to the input data samples. After generating the input data samples, a series of simulations are performed, which provides the sound levels related to the input data sets. The results will allow defining the probability of exceeding a certain sound level. The correlations between specific soil features and the sound levels are identified. The structure of this chapter is as follows. In Section 4.1, the description of the near-source module is given together with the governing equations and the method of the solution. In Section 4.2, the geoacoustic modelling of the seabed is discussed with a focus on the uncertainties in determining the dynamic properties of the marine sediment. In Section 4.3, the mathematical basis of the complete model is established. In Section 4.4, a case study is analysed and discussion of the results is presented. Finally, Section 4.5 gives an overview of the main conclusions of the chapter.

# 4.1 Model description

Modelling underwater noise generated during the installation of offshore foundation piles remains a challenging task, despite the development of numerous models in recent decades [13, 14, 29, 30]. One reason for this challenge is the large amount of uncertainties involved in the simulations. To address this issue, more detailed analytical models have been proposed, including a three-dimensional description of the water-saturated seabed as a layered elastic medium [15, 16]. Models which include elastic description of the seabed are considered to be more accurate due to the fact that a significant part of the energy is released in the soil during pile driving. Without such detailed description the sources of sound cannot be adequately captured. Despite the advances in the modelling of the seabed, uncertainties stemming from data obtained from offshore geotechnical surveys cannot be eliminated. In addition, soil properties obtained on the basis of standard Cone Penetration Tests (CPTs) are incomplete and cannot fully characterise the seabed for acoustic simulations. A first attempt to consider uncertainties in seabed properties was investigated through a probabilistic approach, utilizing a finite element (FE) model for noise generation and a wavenumber integration (WNI) model for sound propagation [24]. The model employs an equivalent fluidized seabed and point sources in the sound propagation model to reduce computational efforts for Monte Carlo simulations, with up to 800 runs. However, this model requires a sufficiently large number of combinations of parameters of interest to account for random combinations between various parameters in the seafloor, despite sampling techniques [128] to avoid a fully random analysis. Gaussian distributions are used for all parameters, i.e. soil density, compressional wave speed, damping, and layer thickness. The main drawback of this model is the simplistic description of the seabed which does not account for shear rigidity, oversimplifying the dynamics of the process in which large amount of energy is transformed into shear waves.

For noise prediction modelling in offshore pile driving, uncertainty mainly arises from the data used for vibroacoustic simulations as well as assumptions in the models. To reduce uncertainty in model assumptions, more detailed underwater noise prediction models can be employed, such as the coupled pile-water-soil model including a three-dimensional description of the water-saturated seabed. Both FE models and semi-analytical models

4

can be adopted; however, computational efficiency is significant as statistical modelling usually requires simulation of a large number of cases. Assumptions in most acoustic models involve constant bathymetry and soil properties that remain invariant over the radial and azimuthal directions. Uncertainties due to assumptions can be evaluated together with dynamic soil properties of the seabed based on offshore geotechnical surveys, which often provide the basis for determining whether such assumptions are valid in acoustic simulations within the range of interest. Range- and azimuth-dependent models should be adopted when considering sound propagation modelling over large distances or when abrupt changes in water depth and soil stratification and material properties are observed in the foundation site to be evaluated. This discussion focuses on uncertainties stemming from the dynamic properties of the soil and the stratification of soil layers.

To address variability in input parameters and quantify uncertainties, probabilistic and statistical approaches have gained popularity in various engineering fields [129-134]. Uncertainty Quantification (UQ) is often used to determine how uncertain input parameters can influence simulation results [129]. In underwater noise prediction for offshore pile driving, the main uncertainties arise from soil properties and soil stratifications, assuming spatial variation in range and azimuthal directions is insignificant within the range of interest [127, 135, 136]. In this modelling framework, based on offshore geotechnical surveys obtained in OWFs, the distribution of each uncertain input parameter can be determined. To narrow down uncertain input parameters, soil stratifications can be statistically determined through analysis of variance (ANOVA). In most offshore geotechnical surveys, downhole cone penetration tests (CPT) are performed, providing cone resistance, friction ratio, and other parameters for estimating dynamic soil properties. Seismic cone penetration tests (SCPT) are also performed at some foundation sites, where shear wave velocities can be directly estimated, reducing uncertainty related to some of the parameters. Depending on the type of correlations between the remaining uncertain properties, input samples are generated using the Copula model. This approach efficiently defines input datasets based on dependence through ranking coefficients, eliminating the need for joint probabilistic distributions between the input variables, which are unknown for the acoustic simulations. The input samples are then fed into the numerical model to obtain the output sound metrics of interest. Based on the results from the model, the cumulative density function of the predicted sound levels can be derived, which indicates the probability of exceeding a certain noise threshold. The use of Copula can reveal the dependence between the input parameters, but also the one between the output sound level and each variables in the system, such as the compressional and shear wave speed, density, and damping of the sediment, etc. The model is further described in the next sections.

# 4.2 Geoacoustic modelling of the seabed

Offshore geotechnical surveys often consist of borehole drilling, geotechnical logging, in-situ testing, and sampling. The geotechnical log can provide a vertical profile of the sediment strata and bathymetry measurement. It includes the soil behaviour type index  $I_c$ , which is used to distinguish different soil types over the depth of examination. Moreover, data from multiple investigation locations can be presented for various selected tools. For example, the P and S Suspension Logger (PSSL) can provide recordings for shear wave velocities and compressional velocities by exciting flexural waves as well as compressional

waves through acoustic dipole sources. Assumptions regarding laterally homogeneous conditions in the marine sediment are required during data processing.

The typical in-situ tests include the cone penetration test (CPT), which produces parameters such as cone resistance, sleeve friction, friction ratio, and pore pressure [137–139]. Friction-cone, piezocone, and other penetrometers allow additional measurements for parameters such as shear wave velocity, compressional wave velocity, permeability, and other properties [138, 139]. Based on a large amount of data from in-situ tests, the correlation between shear wave speed, compressional wave speed, and density with the cone resistance and sleeve friction of the soil is obtained [140]. The seismic cone penetration test (SCPT) measures the travel time between a seismic wave source and an array of geophones or accelerometers at a certain depth below the seabed to obtain the shear and compressional wave velocities at certain depths in the sediment [138]. Ground conditions can induce uncertainties in the postprocessed data, such as wave attenuation or absorption and wave interferences through reflection and refraction [141]. Under practical constraints, the CPT or SCPT at certain locations often has to be terminated at a shallow depth to prevent further damage to the equipment.

In the following subsections, various geotechnical models for the derivation of compressional and shear wave speeds, density, and attenuation coefficients are discussed, presenting the correlation between these parameters and the CPT results. Based on the compressional and shear wave speeds and density, the Young's modulus, Poisson's ratio, or Lamé constants can be obtained, which are important for solving soil dynamic and acoustic problems. As the seafloor around the world exhibits considerable variability, no standard formula can be universally applied to all oceans. Therefore, the uncertainties in these equations or statistical correlations must be considered among the reasons for the uncertainties discussed in this chapter.

# 4.2.1 SHEAR WAVE SPEED

Shear waves are important in underwater sound propagation, especially for evaluating pile driving sound emissions. The large part of the sound sources are embedded in the seabed, and all marine sediments possess dynamic rigidity to transmit shear waves. Compressional waves can also convert to shear waves and Stoneley waves as they are reflected at interfaces between different sediment layers. Based on data obtained from the CPT, many different correlations can be found for the derivation of shear wave speed. Hegazy and Mayne proposed the following expressions between shear wave speed and CPT data for clays, sand, and other soil types [137].

Clays: 
$$V_s = 14.13 q_c^{0.359} e_0^{-0.473}$$
 (4.1)

$$V_s = 3.18q_c^{0.549}f_s^{0.025} (4.2)$$

Sands: 
$$V_s = 13.18 q_c^{0.192} \sigma_{vo'}^{0.179}$$
 (4.3)

$$V_s = 12.02q_c^{0.319} f_s^{-0.0466} (4.4)$$

All: 
$$V_s = (10.1\log_1 0q_c - 11.4)^{1.67} (f_s/q_c \cdot 100)^{0.3}$$
 (4.5)

They extended the formulation in 2006 with the development of a global statistical correlation for the shear wave velocity with the normalised cone resistance  $q_{c_N}$  and soil behaviour

index  $I_c$  as [142]:

$$V_s = 0.0831 q_{c_N} \frac{\sigma_{v0'}}{P_a}^{0.25} e^{1.786I_c}$$
(4.6)

The soil behaviour type index  $I_c$  expressed below:

$$I_c = ((3.47 - \log_{10} q_{c1N})^2 + (\log_{10} F + 1.22)^2)^{0.5}$$
(4.7)

$$F = \frac{f_s}{q_c - \sigma_{vo}} 100\% \tag{4.8}$$

$$q_{c1N} = \frac{q_c - \sigma_{vo}}{\sigma'_{vo}} \tag{4.9}$$

in which  $\sigma_{vo}$  is the in-situ vertical stress (primarily due to the weight of the soil above the point of interest), and  $\sigma'_{vo}$  is the effective vertical stress adjusted for pore water pressure u, i.e.  $\sigma'_{vo}(z) = \sigma_{vo}(z) - u(z)$ .

Robertson and Cabal [143] present a correlation incorporating net cone resistance applicable to a wide range of soil types:

$$V_s = \left(\alpha_{vs} \frac{q_t - \sigma_{vo}}{P_a}\right)^{0.5} \tag{4.10}$$

in which  $\alpha_{vs} = 10^{0.55I_c + 1.68}$ ,  $q_t$  is the corrected cone resistance,  $\sigma_{vo}$  is the total in situ vertical stress and  $P_a$  is atmospheric pressure [kPa].

# 4.2.2 DENSITY

The saturated density can be obtained from the density of the seawater  $\rho_w$ , density of the grain  $\rho_g$  and the sediment porosity n as,

$$\rho_s = n\rho_w + (1-n)\rho_g \tag{4.11}$$

However, the values and variation of parameters with depth are not always available. Consequently, the estimation of density is often achieved through statistical correlations of Cone Penetration Test (CPT) data or in relation to the shear wave velocity  $V_s$ . Numerous statistical equations offer potential correlations between Vs and density. Burns and Mayne [138] presented the following correlation based on collected data:

$$\rho_s = 6.87 \frac{(V_s)^{0.227}}{(\sigma'_{v0})^{0.057}} \frac{10^3}{g}$$
(4.12)

in which the shear wave speed  $V_s$  is given in m/s and  $\sigma'_{v0}$  is the effective overburden stress in the unit of kPa, g is the gravitational constant.

With additional data, Mayne [144] presented a correlation between the unit weight and the shear wave speed  $V_s$  and depth of the sediment z as,

$$\rho_s = (8.31 \log_{10}(V_s) - 1.61 \log_{10}(z)) \frac{10^3}{g}$$
(4.13)

However, as the shear wave speeds are estimated from the CPT data, the further estimation of the density from this parameters can result in more uncertainties and less reliability. Alternatively, Mayne et al. [145] derive the density of sand, silt and clay soils as:

$$\rho_s = 1.95 \rho_w \left(\frac{\sigma'_{v0}}{P_a}\right)^{0.06} \left(\frac{f_t}{P_a}\right)^{0.06} \tag{4.14}$$

with atmospheric pressure  $P_a$  given in kPa. For very soft clay, organic soils, and peat, Lengkeek and Brinkgreve proposed a new formulation for estimating the density of these soil types based on CPT data,

$$\rho_{s} = \rho_{sat,ref} - \beta \frac{\log(\frac{q_{t,ref}}{q_{t}})}{\log(\frac{R_{f,ref}}{R_{f}})}$$
(4.15)

in which  $\rho_{sat,ref}$  is the reference unit weight,  $q_{t,ref}$  is the reference cone resistance,  $R_{f,ref}$  is the reference friction ratio,  $\beta$  is a measure for the inclination of the equal unit weight contours. These fitting reference parameters are chosen for the considered soil data and is applicable for the range of firm sandy soil to clay, organic soil and peat.

# 4.2.3 Compressional wave speed

Quantifying the compressional wave speed is crucial for examining sound generation and propagation in the ocean environment, particularly when sources are embedded in the seafloor and low-frequency sound energy can be refracted through the sediment and channelled back into the seawater. Hamilton links shear and compressional wave speeds (both in km/s) for both silt-clay soils and sandy soils [146],

$$V_s = 21.05 - 24.617 V_p + 7.215 V_p^2$$
, for water-saturated sand (4.16)

$$V_s = \left\{ \begin{array}{cccc} 3.884V_p - 5.757 & \text{for} & 1.512 < V_p < 1.555 \\ 1.137V_p - 1.485 & \text{for} & 1.555 < V_p < 1.650 \\ 0.470V_p^2 - 1.136V_p + 0.991 & \text{for} & 1.650 < V_p < 2.150 \\ 0.780V_p - 0.962 & \text{for} & 2.150 < V_p \end{array} \right. \qquad \text{for silt-clay sediment}$$

(4.17)

Hamilton later extended the studies of the compressional wave speed as a function of depth D (in km) based on additional data [147, 148], with a primary focus on deep-sea applications.

$$V_p = \begin{cases} 1.806(1000D)^{0.015} & \text{for for water-saturated sand} \\ 1.511 + 1.304D - 0.741D^2 + 0.257D^3 & \text{for for silt-clay sediment} \end{cases}$$
 (4.18)

The results from this analysis reveal variations in the ratio of compression to shear wave speed and Poisson's ratio in marine sediments. For silt-clays, the ratio of compression to shear wave speed decreases from approximately 13 at the seafloor to about 2.6 at a depth of 1000 meters. For sand, this ratio decreases from 31 at the seafloor to 6.4 at a depth of 20 meters. Poisson's ratios vary from above 0.49 at the seafloor to about 0.41 at 1000 meters for silt-clay and 0.48 at a depth of 20 meters for sand [147].

# 4.2.4 ATTENUATION

In situ measurements of compressional and shear wave attenuation are challenging, leading to significant uncertainty and reduced reliability in modelling underwater sound propagation, particularly when substantial energy is radiated in the marine sediment. Hamilton [146, 149, 150] and Kibblewhite [151] compiled attenuation coefficients to address this issue. Hamilton's analysis assumed a linear relationship between attenuation and frequency, whereas extensive research has demonstrated a nonlinear dependence of attenuation on frequency [152–159].

Attenuation	$k_p  [\mathrm{dB/m/kHz}]$	$k_s$ [dB/m/kHz]	Reference
Sand	0.093	7.88	[149, 150]
	0.2	16.4	[150, 160]
Clay	0.087	1.4	[160]
	0.326	18.95	[150, 160]
Mud (clay-silt)	0.075	0.512	[150, 160]
	0.242	17.3	[149, 150]
Sandy clay	0.01	-	[160]
	0.203	-	[150]
Sandy silt	0.013	0.5	[160]
	0.35	5.29	[150, 160]

Table 4.1: Typical values of compressional- and shear-wave attenuation coefficients for marine sediment.

Published data on compressional wave attenuation [146, 149–151] show significant scatter at low frequencies. This variability indicates uncertainties and differences in regions, sediment types, layering, sediment depth, measurement frequencies, and other factors affecting attenuation. Shear-wave attenuation presents even more challenges due to the relatively limited data compared to compressional-wave attenuation, especially at lower frequencies, as extrapolation from high-frequency data lacks adequate validation. Shear-wave attenuation shows a rapid decrease within the upper sediment layer and a sharp increase at greater depths. Detailed compilations of compressional and shear-wave attenuation data are provided in [141, 146, 150, 160]. Typical values of attenuation coefficients are listed in Table 4.1.

It is suggested by Hamilton that attenuation, measured in dB/m, exhibits a linear dependence on frequency and can be expressed as [146, 149, 150],

$$\alpha_{m,\xi} = k_{\xi} \cdot f \tag{4.19}$$

in which  $\xi = p$ , s indicates the compressional or shear waves. For the attenuation coefficient expressed in the unit of dB/ $\lambda$ ,

$$\alpha_{\lambda,\xi} = k_{\xi} \cdot \frac{c_{\xi}}{1 \text{kHz}} \tag{4.20}$$

The complex wave speed can be used to account for the absorption losses in the layer as:

$$C_p = \frac{c_p}{1 - i\eta\alpha_p} = \frac{c_p \cdot (1 + i\eta\alpha_p)}{1 - \eta^2\alpha_p^2} \tag{4.21}$$

$$C_s = \frac{c_s}{1 - i\eta\alpha_s} = \frac{c_s \cdot (1 + i\eta\alpha_s)}{1 - \eta^2\alpha_s^2}$$
(4.22)

with  $\eta$  defined as  $(40\pi \log_{10} e)^{-1}$ . Thus, by substituting the wave speed, the solution for the Green's function as discussed in Section 2 can be obtained for describing the wave propagation in attenuating medium, which leads to complex eigenvalues of the propagating modes. This adds certain complexity for finding the complete set of the roots.

When  $\eta^2 \alpha_p^2 \ll 1$ , the complex wave speed  $c = c_r + c_i$  can be expressed as:

$$C_p \approx c_p (1 + i\eta \alpha_p) \tag{4.23}$$

$$C_s \approx c_s (1 + i\eta \alpha_s) \tag{4.24}$$

thus,  $c_i = \eta \alpha \cdot c_r$  Now, the amplitude of the compressional wave with attenuation can be expressed as:

$$A = \exp(-ikx) = \exp(-i\frac{\omega}{C_p}x) = \exp(-i\omega x \frac{c_r - ic_i}{c_r^2 - c_i^2})$$
(4.25)

Since  $c_r^2 >> c_i^2$  , the above expression can be expressed as:

$$A = \exp(-ikx) \approx \exp(-i\omega x \frac{c_r - ic_i}{c_r^2}) = \exp(-i\omega x \cdot (\frac{1}{c_r} - \frac{ic_i}{c_r^2})) = \exp(-i\frac{\omega}{c_r} x - \frac{c_i\omega x}{c_r^2}))$$
(4.26)

Therefore, the transmission loss can be expressed as:

$$\alpha' = \text{TL} = 20 \log_{10}(\frac{A}{A_0}) = 20 \log_{10}(\exp(\frac{c_i \omega x}{c_r^2}))$$
 (4.27)

with  $A_0 = exp(-ik_rx)$ . By substituting  $c_i = \eta \alpha \cdot c_r$ ,

$$\alpha' = 20\log_{10}(\exp(\frac{\eta\alpha \cdot \omega x}{c_r})) = 20\log_{10}(\exp(\frac{\eta\alpha \cdot \omega x}{c_r})) = 20\log_{10}(\exp(\frac{\eta\alpha \cdot 2\pi x}{\lambda}))$$

$$= 20\log_{10}(\exp(\frac{\eta\alpha \cdot 2\pi x}{\lambda})) = \eta\alpha \frac{x}{\lambda} \cdot 40\pi\log_{10}e = \alpha \frac{x}{\lambda}$$
(4.28)

With  $x = \lambda$ , the attenuation can be obtained as  $\alpha_{p,s}$  in the unit of  $dB/\lambda$ . Alternatively, the material dissipation in the sediment can be expressed in the form of complex *Lamé constant*  $\lambda, \mu$  as  $\hat{\lambda} = \lambda(1 + i \cdot \alpha_p)$  and  $\hat{\mu} = \mu(1 + i \cdot \alpha_s)$ .

# 4.2.5 Conclusions

As can be seen, there is a variety of empirical formulae to obtain the dynamic soil parameters required in acoustic simulations. More importantly, the collected data from standard CPT or SCPT tests do not allow for a full dynamic characterisation of the seabed. The water-saturated nature of the marine sediments add to the complexity making the behaviour strongly frequency dependent. Thus, it becomes clear that deterministic estimation of the

sound levels contains large uncertainties and should be largely avoided. Any reasonable prediction of the sound levels to be expected during pile installation can only be reliable when it is accompanied by its statistical distribution. This will be the matter of discussion in the upcoming sections.

# 4.3 STATISTICAL SOIL MODELLING

In this section, the probabilistic analysis of the soil samples is performed to determine the soil stratification based on the best-fit probability distribution and to generate the input data samples for the acoustic simulations based on the Copula model.

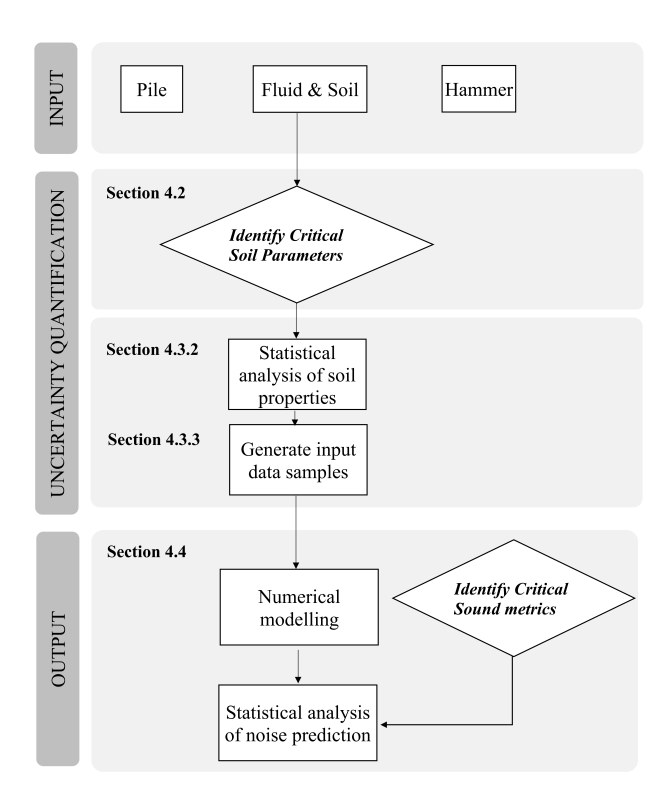


Figure 4.1: Diagram of the Uncertainty Quantification modelling process in soil dynamic properties and its components.

The steps are illustrated in the diagram shown in Fig. 4.1 and are as follows:

- Identifying sound metrics of interest,
- Identifying the uncertainties in the problem inputs, such as the material properties, pile configurations, soil parameters, bathymetry, soil stratifications,
- · Narrowing down of the uncertain variables,

- Generating the input data samples based on the distribution of the uncertain parameters.
- Running simulations using the numerical model to propagate uncertainties to the output variables,
- Determining how the uncertainties affect sound metrics obtained from the underwater noise predictions.

The consideration of input parameter uncertainty is crucial in numerical modelling techniques, especially in underwater acoustic modelling [161]. Depending on the nature and degree of uncertainty, as well as its impact on the physical quantities of interest, various methods can be employed, such as interval arithmetic or Monte Carlo methods [129]. Assigning input parameters to the materials involved is essential for solving vibro-acoustic problems. However, numerous uncertainties arise, particularly concerning dynamic properties, due to measurement challenges and the high spatial variation in marine environments [146, 162].

The lack of, or difficulties, in performing geotechnical investigations in these environments makes it challenging to accurately define characteristics such as shear or compressional velocity, attenuation, density, and other features, as discussed extensively in section 4.2. In this section, a method to identify uncertainties and generate input data samples based on the distribution of uncertainties in the parameters will be presented, relying on experimental results obtained from an offshore wind farm (OWF) in the German North Sea. The geometry of the model and the material properties for the case study examined in this section are provided in Table 4.2. Following underwater acoustic simulations, the uncertainties will be propagated, and sound metrics will be determined.

Table 4.2: Input parameters for the case study. Values that are not provided will be treated with appropriate distributions.

Parameter	Fluid	Upper soil	Bottom sediment
Depth [m]	39.9	1.5	∞
$ ho~[\mathrm{kg/m^3}]$	1000	-	-
$c_p$ [m/s]	1500	-	-
$c_s$ [m/s]	-	-	-
$\alpha_p [dB/\lambda]$	-	0.55	0.27
$\alpha_s [dB/\lambda]$	-	1.36	1.09

#### 4.3.1 STATISTICAL ANALYSIS OF THE SOIL STRATIFICATIONS

As the initial step in determining uncertainties in input parameters, soil stratification must be evaluated for underwater sound propagation models. Soil behaviour type index can be employed to differentiate between different soil layers. However, for underwater sound propagation modelling, it is convenient to group sediments into a few marine sediment layers based on their acoustic characteristics and geotechnical properties of the soil stratification.

The objective of the analysis is to determine whether at least one of the considered groups of soil properties within each layer obtained from the CPT exhibits a significant difference compared to the others. In statistics, the division of layers can be accomplished by grouping data exhibiting similar means and minimum standard deviations. Analysis of variance (ANOVA) is utilized in this process to evaluate two or more sets of data groups so to determine the soil stratification for the acoustic simulations. Depending on the number of independent variables involved in the measured data samples, ANOVA can be single, double, or triple factor.

Based on shear-wave velocities and density derived from the CPT, the p-values obtained from ANOVA analysis provide a statistical measure to determine whether significant differences exist between the means of each data group [163, 164]. Interpreting the p-value helps identify possible combinations of layers. By comparing the p-values to the significance level (commonly set at 0.05), it is determined whether there is strong evidence against the null hypothesis, which posits that all layers are equal. The criterion for choosing cases for soil stratification is based on the minimum p-value obtained.

The sum of squares (SS) is first evaluated to determine the F-ratio, which can be divided into two parts: one referring to model variability and the other to random error.

$$SS_{total} = SS_{model} + SS_{error} (4.29)$$

$$\sum_{i=1}^{a} \sum_{j=1}^{b} (X_{ij} - \bar{X})^2 = \sum_{j=1}^{b} a(\bar{X}_j - \bar{X})^2 + \sum_{i=1}^{a} \sum_{j=1}^{b} (X_{ij} - \bar{X})^2$$
(4.30)

in which  $X_{ij}$  is the  $i^{th}$  observation of the  $j^{th}$  layer,  $\bar{X}$  is the mean of all layers,  $\bar{X}_j$  is the mean of the  $j^{th}$  layer, a is number of elements and b is the number of groups. The F-ratio is defined as:

$$F = \frac{SS_{model}/(b-1)}{SS_{error}/(N-1)}$$

$$\tag{4.31}$$

Once the F-ratio is obtained, specific tables allow for the evaluation of the probability of the null hypothesis, which is then referred to as the p-value. The soil stratification for this analysis consists of two predefined layers: the upper layer, characterized by a softer sand-clay mixture, and the bottom layer, classified as medium to dense sandy soil. In practice, a trade-off must be made when choosing the number of layers, balancing the fit between the data and the soil layers, and the computational cost of the analysis. ANOVA analysis is conducted to determine the optimal thickness of each layer, with the best scenario based on CPT data. The selection of layer depth is made based on the minimum p-value, as shown in Table 4.3. It can be observed that even a 1-meter variation in soil thickness results in noticeable changes in p-values.

Alternatively, the soil behaviour type index  $I_c$  can be directly used to classify marine sediment into different layers. This index is calculated using cone tip resistance, sleeve friction, and pore water pressure. The  $I_c$  value assists in identifying various soil types, such as sands, silts, and clays. However, proper criteria must be defined to compare the choice of layering when multiple sediment types are recognized by  $I_c$ . The method presented in this section serves as a statistical approach for choosing soil stratification and can be applied in various applications involving the modelling of sound transmission through marine sediment.

Soil stratification	Depth of two layers [m]	μ	σ	F	$F_{crit}$	p-value
Layering 1	0-21	288.50	32.12	86.67	4.03	1.401e-12
	21-55	431.38	62.24			
Layering 2	0-22	292.60	36.29	84.19	4.03	2.23e-12
	22-55	433.20	62.24			

Table 4.3: Typical values of ANOVA analysis for the soil stratification of two layers.

#### 4.3.2 STATISTICAL ANALYSIS OF THE SOIL PROPERTIES

Once the layers have been defined, the identification of the critical parameters need to be performed and their distributions of the parameters need to be determined. In this section a practical framework for determining the optimal parameters for the distributions considered is presented. The coefficients of the distributions are obtained through maximum likelihood estimation (MLE) [129].

#### MAXIMUM LIKELIHOOD ESTIMATORS

The maximum likelihood estimator is used to estimate properties of a selected distribution. The uncertainty of whether this chosen distribution could fit the data of our analysis should be considered in order to generate the input data samples at the following steps in the statistical analysis. The maximum likelihood estimator is used to quantify how the choice of the distribution can affect the results or the conclusions of the analysis. In order to choose the most suitable distribution representing the available data, the Akaike information criterion (AIC) is employed [129, 163].

The likelihood is a function of the distribution coefficients, represents the joint probability of the n recordings, and is obtained by multiplying their probability density function:

$$L(\theta|x) = \prod_{i=1}^{N} f(x_i|\theta)$$
(4.32)

The distribution has a set of parameters denoted as  $\theta$  to describe it. The maximum likelihood estimate assumes that the prior distribution on  $\theta$  is uniform and then finds the values of  $\theta$  that maximize the likelihood function,  $\prod_{i=1}^{n} f(x_i|\theta)$ . Assuming the normal distribution, N samples are considered for the following analysis,

$$\Pi_{i=1}^{N} f(x_i | \theta) = \Pi_{i=1}^{N} \frac{1}{\sqrt{2\pi\sigma^2}} \exp\left(-\frac{(\mu - x_i)^2}{2\sigma^2}\right) 
= \left(\frac{1}{\sqrt{2\pi\sigma^2}}\right)^N \exp\left(-\Pi_{i=1}^{N} \frac{(\mu - x_i)^2}{2\sigma^2}\right)$$
(4.33)

To maximize this function, we set its derivative equal to zero. First we take the logarithm (we can do this because the likelihood is non-negative):

$$\log \Pi_{i=1}^{N} f(x_i | \theta) = -\frac{N}{2} \log \sigma^2 - \frac{N}{2} \log 2\pi - -\Pi_{i=1}^{N} \frac{(\mu - x_i)^2}{2\sigma^2}$$
(4.34)

The derivative with respect to  $\mu$  equals:

$$\frac{d}{d\mu}\Pi_{i=1}^{N}f(x_{i}|\theta) = -\Pi_{i=1}^{N}\frac{(\mu - x_{i})^{2}}{2\sigma^{2}}$$
(4.35)

4

Solving Eq. (4.35) for  $\mu$  yields,

$$\mu = \frac{1}{N} \Pi_{i=1}^{N} x_i \tag{4.36}$$

The derivative with respect to  $\sigma^2$  yields:

$$\frac{d}{d\sigma^2} \Pi_{i=1}^N f(x_i | \theta) = -\frac{N}{2\sigma^2} - \frac{1}{2\sigma^4} \Pi_{i=1}^N (\mu - x_i)^2$$
(4.37)

Setting the derivative to zero and solving for  $\sigma^2$  yields [129],

$$\sigma^2 = \frac{1}{N} \prod_{i=1}^{N} (\mu - x_i)^2$$
 (4.38)

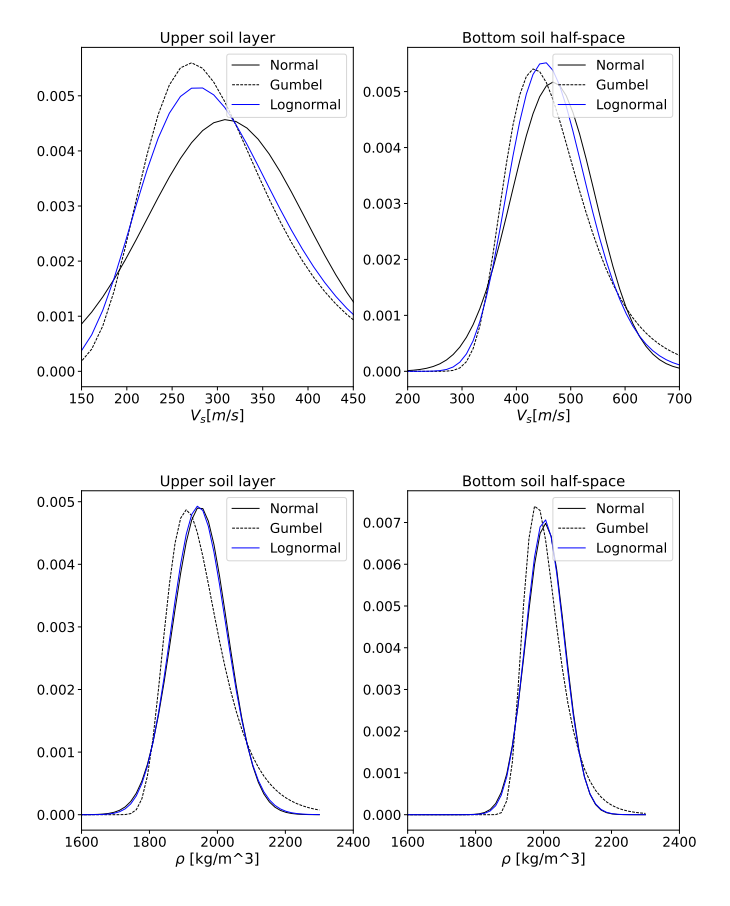


Figure 4.2: Probabilistic density function for the shear wave speed and density within the upper and bottom sediment layers for various theoretical distributions.

#### NORMAL DISTRIBUTION

As discussed above, the normal distribution is one of the most widely adopted distributions. Its probability and cumulative density functions are defined as,

$$\begin{cases} f(x|\mu,\sigma^2) &= \frac{1}{\sqrt{2\pi\sigma^2}} \exp\left(-\frac{(x-\mu)^2}{2\sigma^2}\right) \\ F(x|\mu,\sigma^2) &= \frac{1}{\sqrt{2\pi\sigma^2}} \int_{-\infty}^x \exp\left(-\frac{(s-\mu)^2}{2\sigma^2}ds\right) \end{cases}$$
(4.39)

The coefficients of the distribution that best describe N samples are obtained,

$$\begin{cases}
\mu = \frac{1}{N} \prod_{i=1}^{N} x_i \\
\sigma^2 = \frac{1}{N} \prod_{i=1}^{N} (\mu - x_i)^2
\end{cases}$$
(4.40)

#### GUMBEL DISTRIBUTION

The probability density function and the cumulative distribution function are shown below [165],

$$\begin{cases} f(x|\mu,\beta) &= \frac{1}{\beta} \exp(-z - e^{-z}), z = \frac{x - \mu}{\beta} \\ F(x|\mu,\beta) &= \exp(-e^{-z}) F^{-1}(p) = \mu - \beta \cdot \ln(-\ln(p)) \end{cases}$$
(4.41)

The derivation of the maximum Likelihood estimates of  $\mu$  and  $\beta$  are given in details in [165] with as the numerical solutions of the following equations:

$$\mu = -\beta \left( \ln n - \ln \sum_{i=1}^{n} \exp \left( -\frac{x_i}{\beta} \right) \right)$$
 (4.42)

and

$$\bar{x} = \beta + \frac{\sum_{i=1}^{n} x_i \exp{-\frac{x_i}{\beta}}}{\sum_{i=1}^{n} \exp{-\frac{x_i}{\beta}}}$$
(4.43)

#### LOGNORMAL DISTRIBUTION

The probability density function and cumulative of lognormal distribution are defined as

$$\begin{cases} f(x|\mu,\sigma^2) &= \frac{1}{\sqrt{2\pi\sigma^2}} \exp\left(-\frac{(x-\mu)^2}{2\sigma^2}\right) \\ F(x|\mu,\sigma^2) &= \frac{1}{\sqrt{2\pi\sigma^2}} \int_{-\infty}^x \exp\left(-\frac{(s-\mu)^2}{2\sigma^2}ds\right) \end{cases}$$
(4.44)

The the maximum Likelihood estimates of coefficients  $\mu_{LN}$  and  $\sigma_{LN}$  are obtained as ,

$$\begin{cases} \mu = \frac{1}{N} \prod_{i=1}^{N} \ln(x_i) \\ \sigma^2 = \frac{1}{N} \prod_{i=1}^{N} (\ln(x_i) - \mu)^2 \end{cases}$$
(4.45)

The probability density functions of the shear wave speed and density for various soil layers are presented in Fig. 4.2, illustrating the Normal, Gumbel, and lognormal distributions.

#### Akaike Information criterion

The Akaike Information criterion (AIC) estimates the goodness of fit for the probabilistic model for a given data set, and is given as [166]:

$$AIC = 2k - 2\ln(L(\theta|x)) \tag{4.46}$$

in which k is the standard deviation of the distribution, and L is the maximized value of the likelihood function for the model as defined in Eq. (4.32). When AIC becomes lower and the Likelihood is higher, a better fit to the actual data sets can be expected for the given distributions. Based on the chosen soil stratifications presented in section 4.3.1, the AIC evaluation was performed, and the results for the two soil layers are presented for the considered distribution types. As shown in Table 4.4, the normal distribution provides the lowest AIC. This suggests that the normal distribution is the most suitable model for characterizing the soil properties in the given stratification and offers a better representation of the data set for both upper and bottom soil layers.

The type of distributions	$V_s$	ρ	$V_p$
Upper soil layer			
Normal	1208	1302	1401
Gumbel	1313	1399	1408
LogN	1319	1323	1400
Bottom soil layer			
Normal	1201	1268	1335
Gumbel	1250	1340	1368
LogN	1256	1285	1348

Table 4.4: Typical values of AIC for the data set examined for the density, compressional and shear wave speeds.

#### QUANTILE PLOT

Another visual approach to verify the assumption of a distribution is quantile plots. Quantile plots are a powerful tool for visually assessing the goodness of fit of a data set to a theoretical distribution, also known as a quantile-quantile (Q-Q) plot [167]. It can be used to compare the distribution of a data set with a theoretical distribution (such as a normal distribution) as shown in Fig. 4.3. The purpose of a Q-Q plot is to assess whether the data follows a specified distribution or to check for similarities between the distributions of two different data sets. In a Q-Q plot, the quantiles of a given data set are compared to the quantiles of a chosen theoretical distribution. The closer the points are to the straight line representing the theoretical distribution, the better the fit.

#### 4.3.3 GENERATION OF INPUT DATA SAMPLES

The Copula model, based on the rank methods, is used to investigate the dependence between several random variables [129, 130, 132, 168]. Other common models such as the bivariate joint distribution modelling can also be used for representing the relationship between several variables, however, the main constraint of such an approach is that one

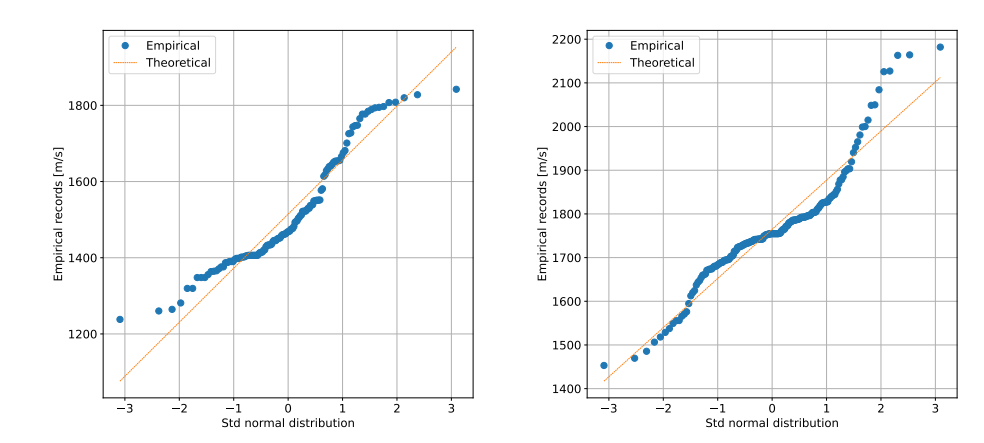


Figure 4.3: QQ plots for compressional speed data points within the upper and bottom sediment layers against theoretical normal distribution.

needs to specify the joint probability density function (pdf) or cumulative distribution function (cdf) directly. The main advantage provided by the Copula approach is that the selection of an appropriate model for the dependence between data sets, represented by the copula, can then proceed independently from the choice of the distributions. Copula models are often preferred when dealing with complex dependencies, thus it is chosen here for quantification of the uncertainties in the noise prediction for offshore pile driving, in which complex marine environment and uncertainties in the measurement data are required to be considered. The copula C(u,v), joins random variables X and Y if the joint CDF can be written as below [129, 130, 168]:

$$F_{XY}(x, y) = C\{F_X(x), F_Y(y)\}, \quad x, y \in \mathbb{R}$$
 (4.47)

in which  $F_X(x)$  and  $F_Y(y)$  are the marginal distribution of any pair of variables (X,Y). For a given copula, we can define the joint PDF as

$$f(x,y) = c\{F_X(x), F_Y(y)\}f_X(x), \quad x, y \in \mathbb{R}$$
(4.48)

where the copula density c(u,v) is defined as  $\frac{\partial^2}{\partial u\partial v}C(u,v)$ . The relationships between variables can be characterized by different measures, such as Pearson correlations, Spearman rank correlations, and Kendall's tau, which in turn determine the type of copula to use, such as the normal (Gaussian) copula or the t-copula. The following analysis will utilize the normal copula, which is appropriate for systems that do not exhibit strong tail dependence. In practice, the best estimate (BE) input parameters for predicting noise from pile driving are obtained from the given system parameters or measured geotechnical properties. This approach emphasizes the importance of the mean values, while extreme cases are less dominant in the uncertainty quantification (UQ) process. In contrast, the t-copula is more suitable for analysing systems where outliers or extreme values might be present, posing a

high risk. For example, when one variable approaches infinity, the probability of the other variable doing the same approaches zero [129].

To construct a copula model, the marginal distributions of each variable are considered separately, as discussed in section 4.3.2. A copula is then used to describe the dependence structure between these variables. Simple numerical techniques are presented for selecting an appropriate model, estimating its parameters, and checking its goodness-of-fit. The Spearman rank coefficients are chosen to address monotonic correlations, investigating whether high values of one variable are paired with high or low values of another. Given N samples of X and Y, the rank function ( $R_i$ ,  $S_i$ ) is defined by taking the rank of  $x_i$  or  $y_i$  and returning the rank of that sample among the N samples, as follows:

$$R_i = \text{rank of } x_i \text{ in sample X}, \quad S_i = \text{rank of } y_i \text{ in sample Y}$$
 (4.49)

in which  $R_i$  and  $S_i$  are the pair of rank of the original data samples, x and y indicate the index of the parameters in the sediment. The Spearman correlation coefficient can then be defined as,

$$\rho_N(X,Y) = \frac{\sum_{i=1}^N (R_i - \bar{R})(S_i - \bar{S})}{\sqrt{\sum_{i=1}^N (R_i - \bar{R})^2 \sum_{i=1}^N (S_i - \bar{S})^2}} \in [-1,1]$$
(4.50)

where

$$\bar{R} = \frac{1}{N} \sum_{i=1}^{N} R_i = \frac{N+1}{2} = \frac{1}{N} \sum_{i=1}^{N} S_i = \bar{S}$$
 (4.51)

which can also be expressed in the form [130],

$$\rho_N = \frac{12}{N(N+1)(N-1)} \sum_{i=1}^{N} R_i S_i - 3 \frac{N+1}{N-1}$$
(4.52)

With the definition of Spearman correlation, a correlation matrix  $\mathbf{R}_S$  for a collection of random variables  $\mathbf{X} = (X_1, ..., X_p)^T$  is given as [129],

$$\mathbf{R}_{S,ij} = \rho_N(X_i, Y_i) \tag{4.53}$$

Based on the soil stratification and its probabilistic distribution demonstrated in this analysis, the correlation matrix for the complete system for UQ can be derived as:

$$R_{c_{p},c_{s},\rho} = \begin{bmatrix} \rho_{1,1} & \rho_{1,2} & \rho_{1,3} & & & & & & & & \\ \rho_{2,1} & \rho_{2,2} & \rho_{2,3} & & & & & & & \\ \rho_{3,1} & \rho_{3,2} & \rho_{3,3} & \cdots & & & & & & & \\ & & & \ddots & & & \vdots & & & \\ & & & \rho_{4,4} & \rho_{4,5} & \rho_{4,6} & & & & & \\ & & & \rho_{5,4} & \rho_{5,5} & \rho_{5,6} & & & & \\ 0 & & & \rho_{6,4} & \rho_{6,5} & \rho_{6,6} & \cdots & & \\ & & & & R_{NN} \end{bmatrix}$$

$$(4.54)$$

in which  $c_{p,i}, c_{s,i}, \rho_i$  indicating the compressional- and shear wave speeds and density within the sediment layer i. When the correlation coefficient vanishes or have a very small

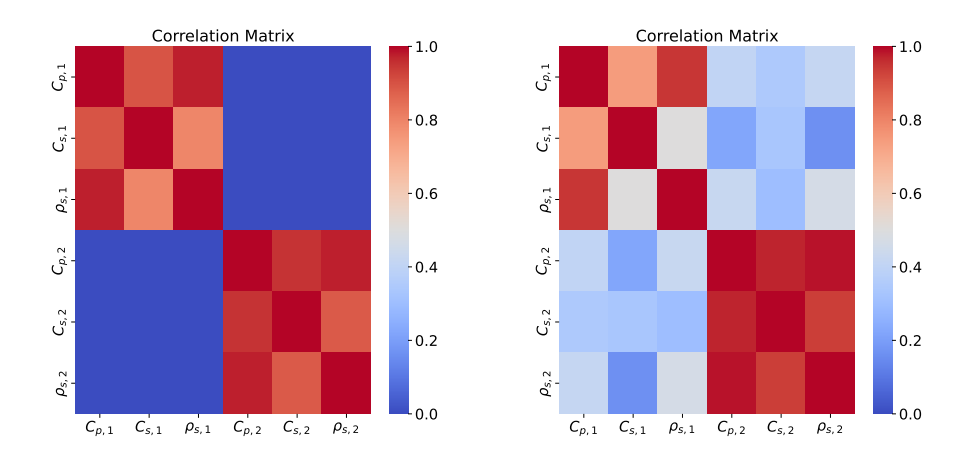


Figure 4.4: Correlation matrix: (left) based on the marginal distributions of parameters, (right) based on the raw samples, parameters obtained from the CPT data analysis.

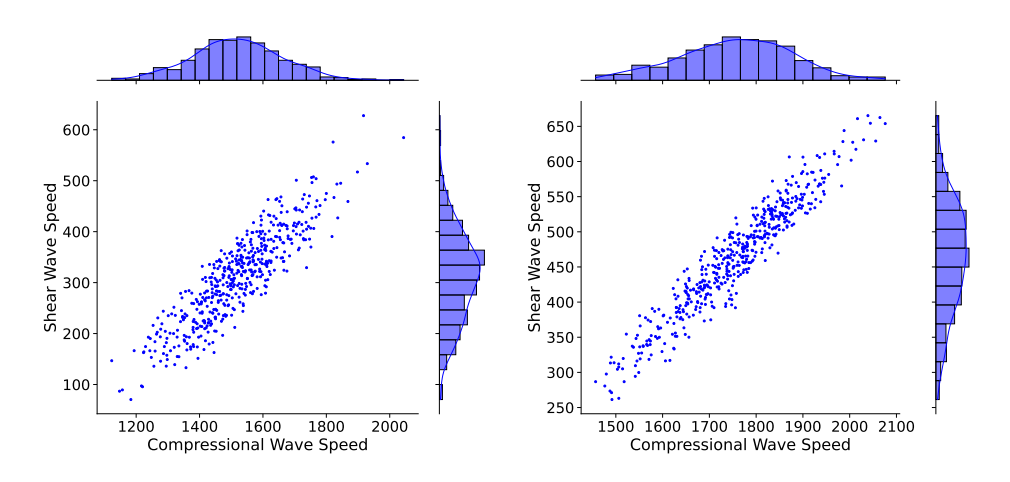


Figure 4.5: Example for the generation of soil samples for (left) the upper soil layer; (right) the bottom soil layer, and their bivariate distribution for the compressional and shear velocity.

value, it indicates that the variables are independent. In this analysis, the independence of parameters between the soil layers is assumed.

An example of this correlation matrix is presented in Fig. 4.4, showing the correlations between each variable considered in this analysis. The left matrix indicates the correlation within each layer based on the chosen marginal distribution. The assumption of independence between sediment layers results in zero values for the correlation coefficients. The right figure uses raw samples obtained directly from the CPT data analysis to verify the assumptions and local input parameter distributions used in this study. The compari-

4.4 Numerical results 101

son between the two matrices indicates a good representation of the chosen probabilistic distribution between the variables and validates the assumptions made.

Once the correlation matrix is obtained, sampling from the multivariate copula can be performed. The sampling results are shown in Fig. 4.5. The left figure shows results based on chosen probabilistic distributions, while the right figure presents the raw data sample obtained from the CPT analysis. The close comparison between the two scenarios indicates a good fit between the chosen marginal distributions and the distribution of the raw CPT data. This example focuses on compressional and shear wave speeds, with their marginal distributions depicted via histograms on both the x and y axes. As illustrated in Fig. 4.4, the bottom sediment layer exhibits a stronger correlation compared to the upper soil layer. This is because soil at greater depths tends to be stiffer, particularly in the sandy soil considered for this example, leading to less variability in the samples for the bottom sediment parameters.

The generated samples will serve as input parameters for the noise prediction modelling of impact pile driving, as described in section 4.4. Other parameters, such as pile diameter, length, penetration depth, hammer force, blow energy, material properties of the pile, water depth, and sound speed in the water column, are assumed constant. It should be noted that other parameters can also contribute to uncertainties in the prediction results. However, this analysis focuses on the uncertainties due to soil conditions, as the measurement data obtained from the geotechnical survey are the most critical factors. The other input parameters are relatively well-defined or can be varied with a limited number of samples, which can be assessed through a sensitivity analysis.

#### 4.4 Numerical results

In this section, the input parameters based on the samples generated in section 4.3 are used for noise prediction in impact pile driving. The case under examination is based on data collected from an offshore wind farm in the German North Sea in 2018, as discussed in section 3.5.2 [29]. The forcing function, presented in Eq. (3.54), is a smoothed exponential impulse that results in approximately 1750 kJ of input energy into the pile. The material properties and geometry of the model are detailed in Table 4.5. For the monopile's material properties, the Young's modulus of the steel is 210 GPa, and the Poisson's ratio is 0.3, used as default values. The seabed consists of an upper sediment layer overlaying a bottom soil half-space. The modelling of the seabed properties, which is indicated in Table 4.2, is performed via statistical modelling of the soil samples generated through the copula model in section 4.3.

The statistical seabed modelling is performed following the procedure described in section 4.3. Firstly, the main uncertainties in the system are identified as the compressional wave speed, shear wave speed, and sediment density. Next, the best fit for the soil stratification and the combination of local probabilistic distributions are determined. It should be noted that, in principle, using more layers can lead to a better fit for the soil stratification. However, a balance must be sought for considering the high computational efforts involved with more layers. The analysis is performed with two soil layers and depth of the soil layers chosen by the ANOVA, and the same statistical modelling framework can be extended to configurations with more than two layers.

Using the copula model, input samples for the identified random variables are generated

Table 4.5: Input parameters for the UQ simulations at the offshore wind farm in the German North sea.

Parameter	Pile
Length [m]	76.9
Density [kg/m³]	7850
Outer diameter [m]	8
Wall thickness [mm]	90
Final penetration depth [m]	32.7
Maximum Blow Energy [kJ]	1750

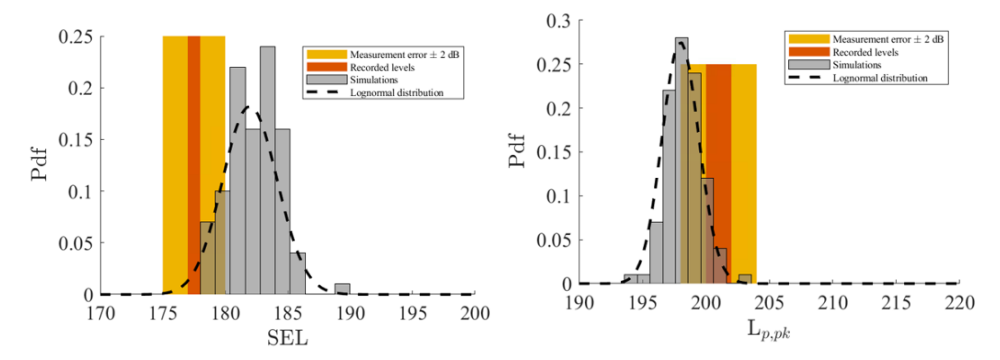
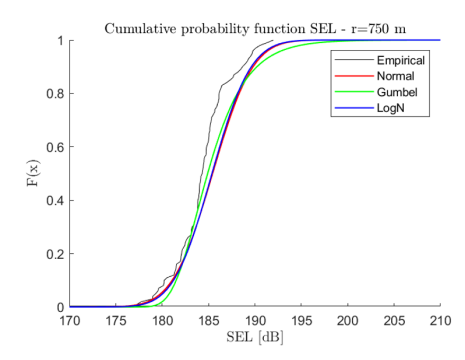


Figure 4.6: Comparison of probabilistic density function of SEL (left) and  $L_{p,pk}$  (right) at 750m from the pile and 2 m above the seabed.

and presented as scatter plots in Fig. 4.5. The distribution of shear wave speed and the density are presented by the normal distributions in Fig. 4.2. The compressional wave speeds are obtained through the correlation formula presented in section 4.2.3. The correlation matrices are shown in Fig. 4.4, assuming independence between soil layers. Simulations based on the generated samples are performed, propagating the uncertainties in the input parameters to the output sound metrics. The peak pressure level ( $L_{p,pk}$ ) and sound exposure level (SEL) at receiver points up to 750 meters radially and 2 meters above the seabed are obtained, as shown in Fig. 4.6. The cumulative probabilistic density functions are presented in Fig. 4.7. In the case presented, the number of samples performed is n = 200 is sufficient to capture the distribution of the raw data samples and correlation between various variables as indicated in Fig. 4.4. However, a larger number of simulations could improve the determination of a proper sound distribution and enhance insights into the correlation between soil parameters and the resulting sound levels.

The probabilistic density functions presented in Fig. 4.6 are compared to the measurement data, indicated by the dark orange area, with an accuracy of  $\pm 2$  dB to account for standard deviations due to measurement errors. The comparison between the distribution of the predicted sound metrics and the measured sound data highlights the importance of uncertainty quantification, as significant influences of input parameter uncertainties are evident in the simulation results. Such analysis allows one to evaluate the probability of the resulting noise level exceeding certain thresholds defined in regulations, as expressed

4.5 Conclusions 103



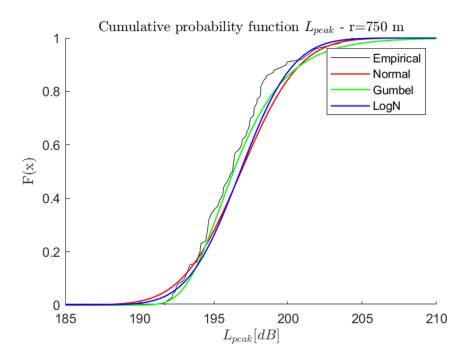


Figure 4.7: Comparison of (left) cumulative probabilistic density function of SEL and (right)  $L_{p,p,k}$  at 750m from the pile and 2 m above the seabed, with the three distributions.

in the cumulative probabilistic function shown in Fig. 4.7. The fit to other probabilistic distributions demonstrates how well the modelled results correspond to normal, Gumbel, or lognormal distributions. These results are crucial in indicating whether proper noise mitigation strategies are necessary and determining the required noise reduction levels to lower the risk of exceeding noise thresholds.

#### 4.5 Conclusions

This chapter focuses on investigating uncertainties in soil modelling and their impact on sound propagation. The framework presented includes several statistical and probabilistic intermediate steps. The primary focus of this chapter is to investigate uncertainties in soil modelling and probabilistically quantify their effects on sound metrics. The ultimate goal is to correlate soil parameters with resulting noise levels to provide more reliable noise predictions and prevent harmful impacts on marine mammals. This work is divided into two main parts: uncertainties in soil and their correlation with sound emissions. The methodology presented here aims to overcome limitations of previous works [29] on soil property uncertainty and its significant effects on sound propagation.

Dynamic soil properties, particularly when part of the sound source is embedded in the seabed during pile driving, are identified as the most challenging parameters to determine in acoustic modelling. Sediment conditions significantly influence both sound generation and propagation. Data from geotechnical surveys are typically used to derive sediment layer properties for offshore pile driving noise predictions. However, uncertainties in these derived input parameters arise from measurement inaccuracies and empirical formulas. Therefore, better estimations of sound levels and more accurate correlations between input parameter uncertainties and resulting outputs are required.

The framework also addresses uncertainties in the marine environment and the resulting variability in sound levels. It accounts for inevitable variations in soil properties by conducting multiple simulations representing different, yet realistic, environments, yielding the most likely outcomes. These results offer insights into the potential challenges of an environment based on the predicted sound levels. Despite approximations, comparisons with experimental measurements demonstrate good agreement and validate the method's

efficacy. With defined probability functions, it is possible to estimate the critical sound levels in the environment under consideration. While some assumptions need verification and simplifications may require correction, the framework presented in this thesis provides a simple, flexible, and accurate tool for evaluating the risks of excessive sound levels in the targeted environment.

5

# STUDY OF SOUND ESCAPE WITH THE USE OF AN AIR BUBBLE CURTAIN

Underwater noise pollution generated by offshore pile driving has raised serious concerns over the ecological impact on marine life. To comply with the strict governmental regulations on the threshold levels of underwater noise, bubble curtains are usually applied in practice. This chapter examines the effectiveness of an air bubble curtain system in noise reduction when foundation piles are driven offshore with the use of impact hammers. The focus is placed on the evaluation of the noise transmission paths, which are essential for the effective blockage of sound propagation. Green's functions developed in Chapter 2 are applied through the boundary integral formulation to account for the waterborne and soilborne wave transmission paths to large distances. The complete model consists of two modules: a noise prediction module for offshore pile driving aiming at the generation and propagation of the wave field up to the position of the air-bubble curtain, as presented in Chapter 3 and a noise reduction module for predicting the sound transmission loss when sound waves pass through the air bubble curtain. With the proposed model, underwater noise prognosis is examined in the following cases: (i) free-field noise without the air bubble curtain, (ii) waterborne path fully blocked at the position of the air bubble curtain while the rest of the wave field is propagated at the target distance, (iii) similarly to (ii) but with a non-fully blocked waterborne path close to the seabed, and (iv) air bubble curtain modelled explicitly using an effective medium theory. The results provide a clear indication of the amount of energy that is channelled through the seabed and through possible gaps in the water column adjacent to the seabed. The model allows for a large number of simulations and for a thorough parametric study of the sound emissions when a bubble curtain is applied offshore.

The structure of this chapter is as follows. In Section 5.1, the governing equations and model description are presented. In Section 5.2, the noise prediction model is introduced for the non-mitigated field which comprises the sound generation and propagation modules. In Section 5.3, the derivation of the transmission coefficients based on the effective medium theory is presented through an air-bubble curtain. In Section 5.4, the validation study of the effective wavenumber approach is discussed by comparing the results to those available in literature. In Section 5.5, the validation study of the complete model is presented using data from a recent offshore installation campaign. Finally, important conclusions are summarized in Section 5.6.

### 5.1 Model description and mathematical statement

In this section, the description of the model and the governing equations of the pile-watersoil and air bubble curtain system are introduced. The geometry and material properties of the system are given. The equations of motion of the vibrating shell, the fluid, the soil and the turbulent gas-liquid mixture are presented.

#### 5.1.1 Description of the model

As shown in Fig. 5.1 (left), the system is composed of the foundation pile, the vibratory shaker or the hydraulic hammer, the air-bubble curtain and the surrounding seawater and sediment. It is assumed that the geometry of the domain and the boundary and interface conditions are cylindrically symmetric. The complete model consists of two modules as shown in Fig. 5.1(right): the noise prediction module aiming at describing the vibro-acoustic behaviour of the pile-soil-water system without the presence of the air-bubble curtain [29], and the noise reduction module used to describe the air bubble curtain. The noise reduction module is integrated to the noise prediction module through depth- and frequency-dependent transfer functions, aiming to capture the insertion loss of the air-bubble curtain.

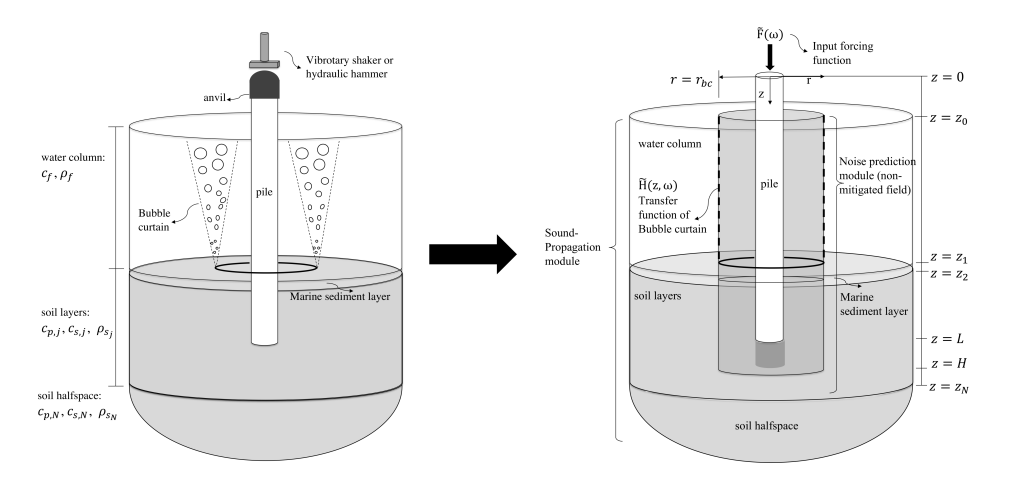


Figure 5.1: Schematic of the complete system (left) and the coupled model (right).

The pile is modelled as an elastic thin shell described by a linear high-order shell theory [121]. The shell is then coupled to a fluid layer overlying a layered elastic waveguide through the mode matching technique [16, 55]. At the top of the pile z = 0, the load induced by the hammer is described by a vertical force. The length of the pile is L and the material constants E,  $\nu$ , R,  $\rho$  and t are the complex modulus of elasticity in the frequency domain, the Poisson ratio, the radius of the mid-surface of the shell, the density and the thickness of the shell, respectively. The seawater is described as an ideal, linearly elastic fluid with  $c_f$  being the sound speed and  $\rho_f$  being its density. The soil is modelled as a linear elastic continuum with  $c_{p,j}$ ,  $c_{s,j}$  being the compressional and shear wave speeds,  $\rho_{s,j}$ being the density of the soil with the index j = 1, 2, ..., N specifying the soil layers including the bottom soil half-space. The frequency-dependent attenuation coefficients  $\alpha_{1_i}$  and  $\alpha_{2_i}$ are defined as  $(20\pi \log_{10} e)\alpha_{p_i}$  and  $(20\pi \log_{10} e)\alpha_{s_i}$  respectively, with  $\alpha_{p_i}$  and  $\alpha_{s_i}$  being the compressional and shear damping constants per layer in units of dB per wavelength. The sea surface is positioned at  $z = z_0$ , the seabed at  $z = z_1$  and the various interfaces between soil layers at  $z = z_k$  with k = 2, ..., N. At the location of the air bubble curtain, i.e. at  $r = r_{bc}$ , the transmission coefficients of the air bubble curtain are derived and introduced in the noise prediction model through a boundary integral formulation.

#### 5.1.2 GOVERNING EQUATIONS

The set of partial differential equations describing the linear vibrations of the complete pile-water-soil system and the complex turbulent two-phase flow are given as:

$$\mathbf{L}\mathbf{u} + \mathbf{I}\ddot{\mathbf{u}} = -(H(z-z_1) - H(z-L))\mathbf{t}_s + (H(z-z_0) - H(z-z_1))\mathbf{p}_f + \mathbf{f}_e\delta(z), \quad 0 < z < L \quad (5.1)$$

$$\nabla^2 p_f(r, z, t) - \frac{1}{c_f^2} \ddot{p}_f(r, z, t) = 0, \quad z_0 < z < z_1, \quad R < r < r_{bc} - b(z), \quad r > r_{bc} + b(z) \quad (5.2)$$

$$(\lambda_{s_j} + 2\mu_{s_j}) \nabla (\nabla \cdot \mathbf{u}_{s_j}) - \mu_{s_j} \nabla \times (\nabla \times \mathbf{u}_{s_j}) = \rho_{s_j} \ddot{\mathbf{u}}_{s_j}, \quad z_j < z_1 < z_{j+1}, \quad R < r < \infty$$
 (5.3)

$$\nabla \cdot (\epsilon_f \rho_f \bar{\mathbf{u}}_f \times \bar{\mathbf{u}}_f + \epsilon_f \rho_f \overline{\delta \mathbf{u}_f \times \delta \mathbf{u}_f}) = \epsilon_g \rho_g g, \quad z_0 < z < z_1, \quad r_{bc} - b(z) < r < r_{bc} + b(z) \quad (5.4)$$

$$\nabla \cdot (\epsilon_f \rho_f \bar{\mathbf{u}}_f) = 0, \quad z_0 < z < z_1, \quad r_{bc} - b(z) < r < r_{bc} + b(z)$$

$$\tag{5.5}$$

$$\frac{\partial n(v_p)}{\partial t} + \nabla \cdot (n(v_p)\mathbf{u}_g) = \int_{v_p}^{\infty} r_1(v_p, v_q) n(v_q) dv_q - \int_{0}^{v_p} v_q r_1(v_p, v_q) dv_q \frac{n(v_q)}{v_p}$$

$$+\frac{1}{2} \int_{v_p}^{\infty} r_2(v_p, v_p - v_q) n(v') n(v_p - v_q) dv_q - \int_{v_p}^{\infty} r_2(v_p, v_p - v_q') n(v_q) n(v_p) dv_q,$$

$$z_0 < z < z_1, \quad r_{bc} - b(z) < r < r_{bc} + b(z)$$
(5.6)

in which b(z) is the half-width of the bubbly layer,  $r_{bc}$  is the centre position of the air-bubble curtain. In Eq. (5.1), L and I are the stiffness and modified inertia matrices of the shell,  $\mathbf{u}$  is the displacement vector of the mid-surface of the shell,  $H(z-z_i)$  are the Heaviside step functions,  $\mathbf{p}_f$  represents the fluid pressure exerted at the outer surface of the shell within the water column and  $\mathbf{f}_e\delta(z)$  is the forcing vector representing the load applied at the top of the pile with  $\delta(z)$  being the Dirac delta function. In Eq. (5.2),  $p_f(r,z,t)$  represents the pressure of the fluid with  $r_{bc}$  being the radius of the air bubble curtain and b(z) being the half-width of the air-bubble curtain which is a function of water depth. In

Eq. (5.3),  $\mathbf{u}_{s_j}$  is the displacement vector of the soil layer j. The governing equations for bubble flow include the momentum balance for the gas-fluid mixture, as shown in Eq. (5.4) [169], the conservation of fluid mass in Eq. (5.5), and the population balance for turbulent bubbly flow in Eq. (5.6) [170]. In Eqs. (5.4)–(5.5),  $\epsilon_f$  and  $\epsilon_g$  are fluid and gas fractions, respectively,  $\mathbf{g}$  is the gravitational constant,  $\mathbf{u}_f$  is the mean liquid flow velocity while  $\delta \mathbf{u}_f$  is its fluctuation. In Eq. (5.6),  $n(v_p)$  is the bubble number density with  $v_p$  and  $v_q$  being the bubble volumes,  $r_1(v_p, v_q)$  represents the breakup kernel function, which quantifies the rate at which bubble fragments with volume  $v_q$  are generated per unit time and volume due to the breakup of bubbles with volume  $v_p$ . On the other hand,  $r_2(v_p, v_q)$  is a coalescence kernel function, predicting the likelihood of two bubbles with volumes  $v_p$  and  $v_q$  coalescing.

At the pile-water interface, the pressure/stress equilibrium and displacement continuity are satisfied at both pile-water and pile-soil interface; the latter under the assumption of a perfect contact condition of no pile slip:

$$u_r(z,t) = u_f(R,z,t), \quad z_0 \le z \le z_1$$
  
 $u_r(z,t) = u_s(R,z,t) \quad \text{and} \quad u_z(z,t) = w_s(R,z,t), \quad z_1 \le z \le L$  (5.7)

In Eq. (5.7),  $u_r$  and  $u_z$  are the radial and vertical displacements of the shell,  $u_f$  is the radial displacement of the fluid, and  $u_s$ ,  $w_s$  are the radial and vertical displacements of the soil.

At the sea surface  $z=z_0$ , the pressure release boundary condition is applied with no surface roughness. At the fluid-soil interface  $z=z_1$ , the continuity of both the vertical displacement and normal to the interface traction are applied. A rigid boundary condition is applied in the sound generation module at a great depth  $z=z_N$ . In the sound propagation module, the seabed is described as a horizontally stratified elastic half-space. At the soil-soil interfaces, both stress equilibrium and displacement continuity are applied. This set of boundary and interface conditions read:

$$p_f(r, z_0, t) = 0, \quad r \ge R$$
 (5.8)

$$\sigma_{zz_1}(r, z_1, t) + p_f(r, z_1, t) = 0, \quad u_{z,f}(r, z_1, t) = w_{s_1}(r, z_1, t), \quad \sigma_{zr_1}(r, z_1, t) = 0, \quad r \ge R$$
 (5.9)

$$w_{s_j}(r, z_j, t) = w_{s_{j-1}}(r, z_j, t), \quad u_{s_j}(r, z_j, t) = u_{s_{j-1}}(r, z_j, t), \quad 2 \le j \le N, \quad r \ge R$$
 (5.10)

$$\sigma_{zz_{j}}(r,z_{j},t) = \sigma_{zz_{j-1}}(r,z_{j},t), \quad \sigma_{zr_{j}}(r,z_{j},t) = \sigma_{zr_{j-1}}(r,z_{j},t), \quad 2 \leq j \leq N, \quad r \geq R \quad (5.11)$$

In Eqs. (5.8)–(5.11),  $u_{z,f}$  are the vertical displacement components of the fluid,  $w_{s_j}$  and  $u_{s_j}$  are the vertical and radial displacement components in the  $j_{\text{th}}$  soil layer and  $\sigma_{zz_j}$  and  $\sigma_{zr_j}$  are the normal and tangential stress components in the  $j_{\text{th}}$  soil layer, respectively. Equations (5.1)–(5.11) including the radiation conditions of  $r \to \infty$  describe fully the dynamics of the total system in the time domain.

### 5.2 Noise predictions of non-mitigated field

The noise prediction model for the non-mitigated field consists of two modules. The noise source for offshore pile driving is firstly characterized by the sound generation module, which is based on a three-dimensional vibroacoustic noise prediction model developed earlier by Tsouvalas and Metrikine [16]. The prediction from the sound generation module has been verified against the data available in the literature from various measurement

campaigns and one theoretical benchmark [31]. This module describes the dynamic response of the coupled pile-water-soil system. The eigenvalue problems of the shell and acousto-elastic waveguide are solved first. Next, the mode matching technique is applied to couple the pile to the surrounding fluid-sediment layers. A set of response functions at the location of the bubble curtain  $r = r_{bc}$  are generated in the frequency domain, which involves pressure, velocity, displacement and stress tensors. As the system is linear and divided into sub-systems, only part of the simulation needs to be evaluated for examining various scenarios including varying forcing functions, pile configurations, and soil conditions. This way the computational efforts are reduced significantly compared to finite element or finite difference models.

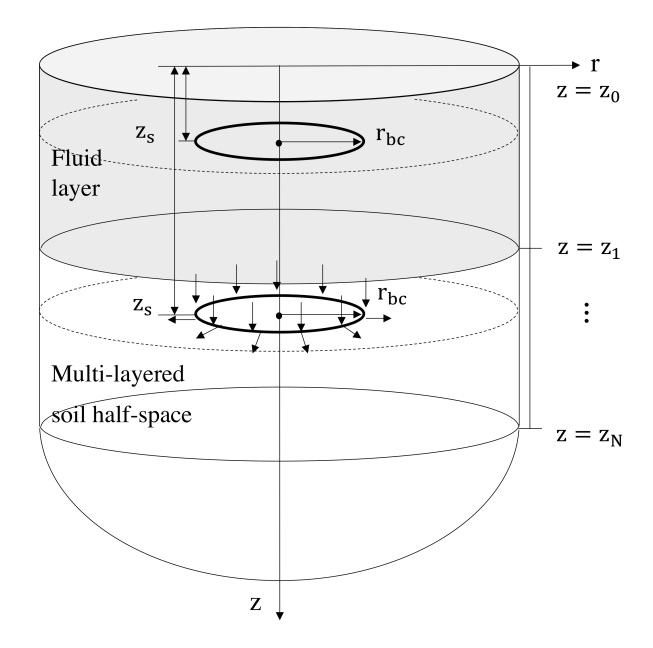


Figure 5.2: Schematic of the ring source at  $r = r_{bc}$  in the configuration of acousto-elastic layered half-space.

The sound propagation module is based on Green's functions for ring sources located on the cylindrical surface at  $r=r_{bc}$  as depicted in Fig. 5.2. By applying the contour integration technique (see details in Chapter 2), the expressions for displacement potential functions  $\widetilde{\Phi}^g_{\Xi,\xi}(r,z;r_{bc},z_s;\omega)$  in frequency domain are given as a summation over a number of poles supplemented by the Ewing-Jardetsky-Press (EJP) branch line integrations [101]:

$$\widetilde{\Phi}_{\Xi,\xi}^{g}(r,z;r_{bc},z_{s};\omega) = -\pi i \sum_{m=1}^{M} \left[ \operatorname{Res}(\widehat{\Phi}_{\Xi,\xi}^{g}(k_{r}^{(m)},z;r_{bc},z_{s})) H_{0}^{(2)}(k_{r}^{(m)}r) k_{r}^{(m)} \right] \\
+ \frac{1}{2} \int_{\alpha+\beta} \widehat{\Phi}_{\Xi,\xi}^{g}(k_{r},z;r_{bc},z_{s}) H_{0}^{(2)}(k_{r}r) k_{r} dk_{r} \tag{5.12}$$

in which Res $(f(k_r^{(m)}))$  indicates the residue of the function  $f(k_r)$  at the pole  $k_r^{(m)}$ ,  $H_0^{(2)}$  is

the zero order Hankel function of the second kind, M indicates the number of poles with m being the index,  $\alpha$  and  $\beta$  represent the branch cuts related to the branch point  $k_{p_N}$  and  $k_{s_N}$  with  $k_{p_N}$  and  $k_{s_N}$  being the compressional and shear wavenumbers, respectively.

The fundamental solutions of Green's displacement tensors  $\widetilde{U}_{\alpha\beta}^{\Xi\xi}(\mathbf{r},\mathbf{r}_s,\omega)$  are derived from the potential functions [109] given the receiver point at  $\mathbf{r}=(r,z)$  (in medium  $\Xi$ ) in  $\alpha$ -direction due to a unit impulse at source  $\mathbf{r}_s=(r_{bc},z_s)$  (in medium  $\xi$ ) in  $\beta$ -direction:

$$\widetilde{U}_{\alpha\beta}^{s\xi}(\mathbf{r},\mathbf{r}_{s},\omega) = \nabla \widetilde{\phi}_{s_{j},\xi}^{g}(\mathbf{r},\mathbf{r}_{s},\omega) - \nabla \times \left(\frac{\partial \psi_{s_{j},\xi}^{g}(\mathbf{r},\mathbf{r}_{s},\omega)}{\partial r}\right),\tag{5.13}$$

$$\widetilde{U}_{\alpha\beta}^{f\xi}(\mathbf{r},\mathbf{r}_{s},\omega) = \nabla \widetilde{\phi}_{f,\xi}^{g}(\mathbf{r},\mathbf{r}_{s},\omega). \tag{5.14}$$

The direct boundary element method (BEM) is adopted to couple the noise prediction model for non-mitigated field and noise reduction model for the air-bubble curtain as discussed further in section 5.3. The solution of the acousto-elastic wavefield employs Somigliana's identity in elastodynamics and Green's third identity in potential theory [109, 115, 116]. The response functions from the noise prediction model are coupled to the sound propagation module through a boundary integral formulation on the cylindrical boundary surface at  $r = r_{bc}$ . By utilizing Betti's reciprocal theorem in elastodynamics [115] and Green's theorem for acoustic problem [116], the complete solution for the acousto-elastic domain reads [29]:

$$\widetilde{u}_{\alpha}^{\Xi}(\mathbf{r},\omega) = \widetilde{u}_{\alpha}^{\Xi,f}(\mathbf{r},\omega) + \widetilde{u}_{\alpha}^{\Xi,s}(\mathbf{r},\omega) 
= \sum_{\beta=r,z} \int_{S^{s}} \left( \widetilde{U}_{\alpha\beta}^{\Xi s}(\mathbf{r},\mathbf{r}_{bc},\omega) \cdot \widetilde{t}_{\beta}^{\mathbf{n}}(\mathbf{r}_{bc},\omega) - \widetilde{T}_{\alpha\beta}^{\mathbf{n},\Xi s}(\mathbf{r},\mathbf{r}_{bc},\omega) \cdot \widetilde{u}_{\beta}(\mathbf{r}_{bc},\omega) \right) dS^{s}(\mathbf{r}_{bc}) 
+ \int_{S^{f}} \widetilde{H}(z,\omega) \left( \widetilde{U}_{\alpha r}^{\Xi f}(\mathbf{r},\mathbf{r}_{bc},\omega) \cdot \widetilde{p}(\mathbf{r}_{s},\omega) - \widetilde{T}_{\alpha r}^{\mathbf{n},\Xi f}(\mathbf{r},\mathbf{r}_{s},\omega) \cdot \widetilde{u}_{r}(\mathbf{r}_{bc},\omega) \right) dS^{f}(\mathbf{r}_{bc}), \quad \mathbf{r} \in V$$
(5.15)

in which **n** is the outward normal to the cylindrical boundary,  $\widetilde{H}(z,\omega)$  is the transmission coefficient function of the air bubble curtain with depth- and frequency dependence as discussed in section 5.3. The details of the derivation of Eq. (5.15) are given in chapter 2.

## 5.3 Modelling the air bubble curtain

In this section, the noise reduction module for capturing acoustic properties of the air bubble curtain is derived. The local wavenumber distribution is based on a fluid dynamic model developed by Bohne et al. [67], in which a turbulent two-phase bubble flow is well captured especially in the vicinity of the nozzle where a high gas fraction is present. Based on the distribution of the local effective wavenumbers over the entire water depth, the depth- and frequency-dependent transmission coefficients are obtained by a simplified one-dimensional acoustic wave propagation approach developed by Commander and Prosperetti [64]. The noise reduction module is coupled to the free-field noise prediction model through the boundary integral formulation given by Eq. (5.15).

#### 5.3.1 Local effective wavenumber in a bubble curtain

To obtain the local effective wavenumber of the air-bubble curtain, the model developed by Bohne et al. [67] is used. The governing equations based on momentum balance of the gas-liquid mixture, the conservation of mass of the liquid phase and population balance of a turbulent flow are already introduced in Eqs. (5.4)–(5.6). The bimodal bubble size distribution is introduced by Lethr et al. [170] with observations of small and large bubbles especially in the vicinity of the nozzle as depicted in Fig. 5.3. The detailed derivation is given in [67, 171] and is omitted here for the sake of brevity. The initial conditions for the bubble formation process are given as:

$$u_{lzm0} = \sqrt{\frac{-2M_0(2\lambda^2 + 1)}{\gamma b_0^2 \rho_f \pi (2\epsilon_{gm10}\lambda^2 + 2\epsilon_{gm20}\lambda^2 - 2\lambda^2 - 1)}}$$
(5.16)

$$b_{0} = \sqrt{\frac{\dot{m}_{0}(\lambda^{2} + 1)}{\lambda^{2}\pi\rho_{g0}(\lambda^{2} + 1)(\epsilon_{gm10}u_{rel1}(\bar{v}_{10}) + \epsilon_{gm20}u_{rel2}(\bar{v}_{20})) + \lambda^{2}u_{lzm0}\pi\rho_{g0}(\epsilon_{gm10} + \epsilon_{gm20})}}$$
(5.17)

$$\epsilon_{gm10} = 0.005 \tag{5.18}$$

$$\epsilon_{gm20} = 0.495 \tag{5.19}$$

$$\bar{v}_{20} = \frac{4}{3}\pi (1.1447 a_{\text{prim}})^3 \tag{5.20}$$

$$\bar{v}_{10} = \frac{\bar{v}_{20}}{30} \tag{5.21}$$

with the initial centerline velocity  $u_{lzm0}$ , the half width of the bubble curtain  $b_0$ , the initial gas fraction of the small bubble  $\epsilon_{gm10}$ , the initial gas fraction of the large bubble  $\epsilon_{gm20}$ , the initial arithmetic mean bubble volume of the small bubbles  $\bar{v}_{10}$ , the initial arithmetic mean bubble volume of the large bubbles  $\bar{v}_{20}$ .  $u_{rel1}(\bar{v}_1)$  and  $u_{rel2}(\bar{v}_2)$  are the relative velocities between the upward rising air bubbles and the mean flow of the fluid, which are functions of the local mean bubble size of each gas phase [172, 173].  $\dot{m}_0$  is the initial gas mass flow,  $M_0$  is the initial momentum of the mixture,  $d_{\text{prim}}$  and  $a_{\text{prim}}$  are the diameter and radius of the primary bubble, respectively, which are quantified at the nozzle as [171, 174],

$$M_0 = q_n \rho_{gn} u_{gn} + \frac{2q_n}{u_{gn}} (\rho_f - \rho_{gn}) g \cdot (6.2d_n)$$
 (5.22)

$$d_{\text{prim}} = \frac{1}{2} \left[ \frac{1.3\rho_f (q_n/d_{\text{prim}})^2 + \pi d_n \sigma + 15\eta q_n/d_{\text{prim}}}{(\rho_f - \rho_{gn})} \frac{6}{\pi} \right]^{1/3}$$
 (5.23)

in which  $u_{gn}$  is the gas velocity in the nozzle,  $q_n$  is gas volume rate in the nozzle,  $\rho_{gn}$  is the density of gas in the nozzle. In Eq. (5.23),  $d_{\text{prim}}$  is solved for by an iterative method. Derived from the Eqs. (5.4)–(5.6) and assuming Gaussian distributions of the mean fluid velocity and gas fractions, the resulting set of equations read:

$$\frac{d}{dz}(\mathbf{m}(\mathbf{u},z)) = \mathbf{q}(\mathbf{u},z) \tag{5.24}$$

In Eq. (5.24),  $\mathbf{u} = [u_{lzm}, b, \epsilon_{gm1}, \epsilon_{gm2}, \bar{v}_1, \bar{v}_2]^T$  represents the vector of six unknowns, in which  $u_{lzm}$  is the centerline velocity, b is the half width of the bubble curtain,  $\epsilon_{gm1}$  is the gas

fraction of the small bubble,  $\epsilon_{gm2}$  is the gas fraction of the large bubble,  $\bar{v}_1$  is the arithmetic mean bubble volume of the small bubbles and  $\bar{v}_2$  is the arithmetic mean bubble volume of the large bubbles. To solve the set of first order partial differential equations, the forward Euler method is used for integration along the z-coordinate with the initial condition given in Eqs. (5.16)–(5.20). Once the set of Eq. (5.24) are solved,  $\bf u$  are obtained as depth-dependent fluid dynamic properties, which will be used later in Eq. (5.44) to determine the local effective wavenumber and subsequently in Eq. (5.56) to determine the transmission coefficient functions of the air-bubble curtain.

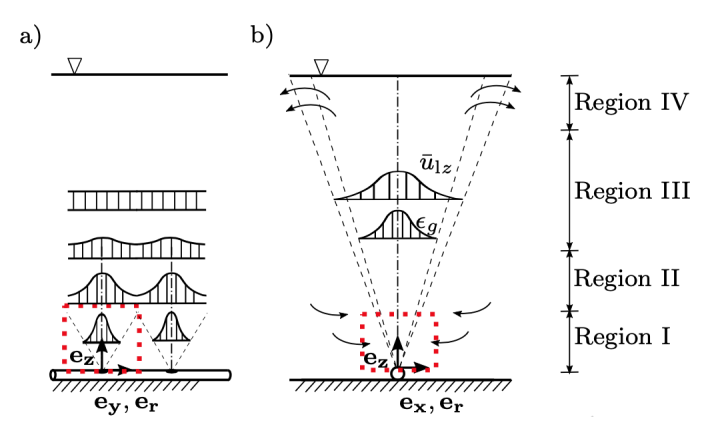


Figure 5.3: Schematic representation of the vertical mean liquid flow: a) velocity field; b) velocity field and the gas fraction in the x,z-plane of the bubble curtain. The dashed line denotes the estimated boundary of the flow field. The red box marks the region in which the formation process is examined [67].

The elements of the integral fluxes  $\mathbf{m}(\mathbf{u}, z) = [m_1, m_2, m_3, m_4, m_5, m_6]^T$  read:

$$m_1(\mathbf{u}, z) = 2\pi \gamma \rho_f u_{lzm}^2 \left( \frac{b^2}{4} - \epsilon_{gm1} \frac{\lambda^2 b^2}{2(2\lambda^2 + 1)} - \epsilon_{gm2} \frac{\lambda^2 b^2}{2(2\lambda^2 + 1)} \right)$$
 (5.25)

$$m_2(\mathbf{u}, z) = 2\pi \rho_f u_{lzm} \left( \frac{b^2}{4} - \epsilon_{gm1} \frac{\lambda^2 b^2}{2(2\lambda^2 + 1)} - \epsilon_{gm2} \frac{\lambda^2 b^2}{2(2\lambda^2 + 1)} \right)$$
 (5.26)

$$m_3(\mathbf{u}, z) = 2\pi \rho_g(z) \epsilon_{gm1} \left( u_{lzm} \frac{\lambda^2 b^2}{2(2\lambda^2 + 1)} + \frac{g\Delta \rho}{3\mu} (\frac{\bar{v}_1}{0.21}) (\frac{2}{3}) \frac{\lambda^2 b^2}{2} \right)$$
(5.27)

$$m_4(\mathbf{u}, z) = 2\pi \rho_g(z) \epsilon_{gm2} \left( u_{lzm} \frac{\lambda^2 b^2}{2(2\lambda^2 + 1)} + \frac{g\Delta \rho}{3\mu} \left( \frac{\bar{v}_1}{0.68} \right) \left( \frac{2}{3} \right) \frac{\lambda^2 b^2}{2} \right)$$
(5.28)

$$m_5(\mathbf{u}, z) = 2\pi \rho_g(z) \epsilon_{gm1} \bar{v}_1 \left( u_{lzm} \frac{\lambda^2 b^2}{2(2\lambda^2 + 1)} + \frac{g\Delta \rho}{3\mu} \left( \frac{\bar{v}_1}{0.21} \right) \left( \frac{2}{3} \right) \frac{\lambda^2 b^2}{2} \right)$$
(5.29)

$$m_6(\mathbf{u}, z) = 2\pi \rho_g(z) \epsilon_{gm2} \bar{v}_2 \left( u_{lzm} \frac{\lambda^2 b^2}{2(2\lambda^2 + 1)} + \frac{g\Delta \rho}{3\mu} \left( \frac{\bar{v}_1}{0.68} \right)^{\left(\frac{2}{3}\right)} \frac{\lambda^2 b^2}{2} \right)$$
(5.30)

with  $\Delta \rho$  being the difference between the density of fluid and air,  $\mu = 10^{-3} N \cdot s/m^2$  being the viscosity of the fluid,  $\gamma = 1$  being the amplification factor.

Similarly, the elements of the integral source terms  $\mathbf{q}(\mathbf{u}, z) = [q_1, q_2, q_3, q_4, q_5, q_6]^T$  are:

$$q_1(\mathbf{u}, z) = \pi g \rho_f \lambda^2 b^2 (\epsilon_{gm1} + \epsilon_{gm2})$$
(5.31)

$$q_2(\mathbf{u}, z) = 2\pi\alpha\rho_f u_{lzm} b \tag{5.32}$$

$$q_{3}(\mathbf{u},z) = Z_{2}\rho_{g}(z)\pi\lambda^{2}b^{2}\epsilon_{gm2} - \frac{0.9024 * r_{2}(\epsilon_{gm1},\epsilon_{gm2},\bar{v}_{2},5\bar{v}_{1})\rho_{g}(z)\epsilon_{gm1}\epsilon_{gm2}\pi\lambda^{2}b^{2}}{\bar{v}_{2}}$$

$$-\frac{3.1043\pi}{2}r_{2}(\epsilon_{gm1},\epsilon_{gm2},\bar{v}_{1},\bar{v}_{1})\rho_{g}(z)\epsilon_{gm1}^{2}\lambda^{2}b^{2}$$

$$q_{4}(\mathbf{u},z) = -Z_{2}\rho_{g}(z)\pi\lambda^{2}b^{2}\epsilon_{gm2} + \frac{0.9024 * r_{2}(\epsilon_{gm1},\epsilon_{gm2},\bar{v}_{2},5\bar{v}_{1})\rho_{g}(z)\epsilon_{gm1}\epsilon_{gm2}\pi\lambda^{2}b^{2}}{\bar{v}_{2}}$$

$$+\frac{3.1043\pi}{2}r_{2}(\epsilon_{gm1},\epsilon_{gm2},\bar{v}_{1},\bar{v}_{1})\rho_{g}(z)\epsilon_{gm1}^{2}\lambda^{2}b^{2}$$

$$(5.34)$$

$$q_{5}(\mathbf{u},z) = -Z_{1}\bar{v}_{1}\rho_{g}(z)\pi\lambda^{2}b^{2}\epsilon_{gm1} - \frac{0.9024 * r_{2}(\epsilon_{gm1},\epsilon_{gm2},\bar{v}_{2},5\bar{v}_{1})\rho_{g}(z)\epsilon_{gm1}\epsilon_{gm2}\pi\lambda^{2}b^{2}}{\bar{v}_{2}}\bar{v}_{1} + \frac{0.3463\pi}{2}r_{2}(\epsilon_{gm1},\epsilon_{gm2},\bar{v}_{1},\bar{v}_{1})\epsilon_{gm1}^{2}\lambda^{2}b^{2} + \frac{3.1043\pi}{2}r_{2}(\epsilon_{gm1},\epsilon_{gm2},\bar{v}_{1},\bar{v}_{1})\rho_{g}(z)\epsilon_{gm1}^{2}\lambda^{2}b^{2}\bar{v}_{1}$$

$$(5.35)$$

$$q_{6}(\mathbf{u},z) = -2Z_{2}\bar{v}_{2}\rho_{g}(z)\pi\lambda^{2}b^{2}\epsilon_{gm2} + 1.8048r_{2}(\epsilon_{gm1},\epsilon_{gm2},\bar{v}_{2},5\bar{v}_{1})\rho_{g}(z)\epsilon_{gm1}\epsilon_{gm2}\pi\lambda^{2}b^{2} + \frac{0.4250\pi}{2}r_{2}(\epsilon_{gm1},\epsilon_{gm2},\bar{v}_{2},\bar{v}_{2})\rho_{g}(z)\epsilon_{gm2}^{2}\lambda^{2}b^{2} + \frac{3.1043\pi}{2}r_{2}(\epsilon_{gm1},\epsilon_{gm2},\bar{v}_{1},\bar{v}_{1})\rho_{g}(z)\epsilon_{gm1}^{2}\lambda^{2}b^{2}$$

$$(5.36)$$

with  $r_2$  is the function of the air fraction and arithmetic mean bubble volume of the small and large bubbles as given in [67]. The density of the gas is a function of height from the nozzle based on an ideal gas law.

As the vertical distances from the nozzle increase, both the gas fraction ratio and the arithmetic mean bubble volume of large bubbles drop significantly and approach zero, and part of the components in the vector **q** are modified as follows:

$$q_3(\mathbf{u}, z) = q_4(\mathbf{u}, z) = 0 \tag{5.37}$$

$$q_5(\mathbf{u}, z) = -Z_1 \bar{v}_1 \rho_g(z) \pi \lambda^2 b^2 \epsilon_{gm1} + \frac{0.3463 \pi}{2} r_2(\epsilon_{gm1}, \epsilon_{gm2}, \bar{v}_1, \bar{v}_1) \epsilon_{gm1}^2 \lambda^2 b^2$$
 (5.38)

$$q_{6}(\mathbf{u},z) = -Z_{2}\bar{v}_{2}\rho_{g}(z)\pi\lambda^{2}b^{2}\epsilon_{gm2} + 0.9024r_{2}(\epsilon_{gm1},\epsilon_{gm2},\bar{v}_{2},5\bar{v}_{1})\rho_{g}(z)\epsilon_{gm1}\epsilon_{gm2}\pi\lambda^{2}b^{2} + \frac{0.4250\pi}{2}r_{2}(\epsilon_{gm1},\epsilon_{gm2},\bar{v}_{2},\bar{v}_{2})\rho_{g}(z)\epsilon_{gm2}^{2}\lambda^{2}b^{2}$$
(5.39)

while the other components remain the same.

Once the depth-dependent vector  $\mathbf{u}$  is known, the local bubble number density distribution are obtained by subdividing them into a fraction of large bubbles and a fraction of small bubbles

$$n(\mathbf{u}, r, z, a) = n_1(\mathbf{u}, r, z, a) + n_2(\mathbf{u}, r, z, a)$$
 (5.40)

with the equilibrium bubble radius a and the bubble number density  $n(\mathbf{u}, r, z, a)$ . The bubble number density distribution for the small bubble fraction  $n_1(\mathbf{u}, r, z, a)$  is approximated by a lognormal distribution and the large bubble fraction  $n_2(\mathbf{u}, r, z, a)$  by an exponential distribution [170],

$$n_1(\mathbf{u}, r, z, a) = \frac{\epsilon_{g1}(r, z)}{\bar{v}_1^2} \frac{2}{\pi} \frac{\bar{v}_1}{3v(a)} \exp(-\frac{2}{9} ln(e^{9/8} \frac{v(a)}{\bar{v}_1}))$$
 (5.41)

$$n_2(\mathbf{u}, r, z, a) = \frac{\epsilon_{g2}(r, z)}{\bar{v}_2^2} \exp(-\frac{v(a)}{\bar{v}_2})$$
 (5.42)

The gas fraction for both small and large bubbles is range- and depth-dependent as:

$$\epsilon_{gi}(r,z) = \epsilon_{gmi}(z) \exp(-\frac{r^2}{\lambda^2 b^2})$$
 (5.43)

The local effective wavenumber is written as:

$$k_m(\omega, r, z) = \frac{\omega^2}{c_f^2} + 4\pi\omega^2 \int_0^\infty \frac{an(\mathbf{u}, r, z, a)}{\omega_0^2(z, a) - \omega^2 + 2i\beta(z, a)\omega} da$$
 (5.44)

with the angular frequency  $\omega$ . The natural angular frequency  $\omega_0(z, a)$  and the damping constant  $\beta(z, a)$  are defined as [64]:

$$\omega_0(z,a) = \sqrt{\frac{p_g(z)}{\rho_f a^2} (3 - \frac{2\sigma}{p_g(z)a})}$$
 (5.45)

$$\beta(z,a) = \frac{\gamma_0 - 1}{10\gamma_0} \cdot \frac{p_g(z)}{\rho_f D} + \frac{2\mu}{\rho_f a^2}$$
 (5.46)

in which  $\sigma=0.073N/m$  is the surface tension of the water,  $\gamma_0=1.41$  is the ratio of specific heats and  $D=1.9\times 10^{-5}m^2/s$  is the gas thermal diffusivity.

#### 5.3.2 Local transmission coefficients of a bubble curtain

To obtain the sound transmission characteristics of a bubble curtain, a model for determining the depth- and frequency-dependent transmission coefficient of an air bubble curtain is developed, which is based on the approach of Commander and Prosperetti [64]. Consider an incident sinusoidal plane wave as shown in Fig. 5.4, the field is solely r-dependent and the bubbly mixture occupies the region  $r_{bc} - b < r < r_{bc} + b$  with  $r_{bc}$  being the location of the air bubble curtain and b being the half width varying with height from the nozzle as discussed in section 5.3.1. The water column and air bubble curtain are divided into M regions along the vertical coordinate. At each vertical domain, a one-dimensional problem is considered with an input incident wave and properties of the layers. The transmission coefficients are determined per z-coordinate and is constant within the vertical step size of the integration. The bubble layer is divided into  $N_{bc}$  layers as depicted by the grey area in Fig. 5.4. The assumption of plane wave propagation is justified because the thickness of each intermediate bubble-fluid mixture layer is extremely small compared to the wavelength of waves at the frequencies of interest. Consequently, the effect of

amplitude decay due to geometrical spreading is negligible. The bubble population is modelled using a lognormal distribution for small bubbles and an exponential distribution for large bubbles. The gas fraction for both small and large bubbles is approximated by an exponential distribution in the radial direction from the centreline of the air-bubble layer. This distribution is considered valid because the number of bubbles rapidly decreases near the interface between the bubbly layer and the seawater. The primary focus is on the energy transmission through the air-bubble curtain, and the back-scattering effect is not considered in this model. The reflection of waves between the monopile and the first bubble curtain, as well as between multiple bubble curtains, is not considered in the sound propagation. The actual transmission loss calculated by the full 2D model using coupled mode theory, including the backscattering effect, may yield different results, particularly at lower frequencies. This is due to the increased complexity in wave interactions at these frequencies, where the backscattering from the water column and the sediment layers can have a significant impact on sound propagation. The coupled mode approach, which accounts for mode coupling between different layers, is crucial for capturing these effects accurately [85]. However, these assumptions allow for the derivation of local transmission coefficients and the application of the Boundary Element Method (BEM) approach, thereby simplifying the solutions for the transfer coefficients of the bubbly layer.

The solutions of the pressure fields in three regions are expressed as [116]:

$$P_L(r,\omega) = P_i + P_r = A_1 \exp(-ikr) + A_2 \exp(ikr), \quad r < r_{bc} - b$$
 (5.47)

$$P_{BC,j}(r,\omega) = P'_{tj} + P'_{rj} = B_{1j} \exp(-ik_{mj}r) + B_{2j} \exp(ik_{mj}r), \quad r_{bc} - b < r < r_{bc} + b \quad (5.48)$$

$$P_R(r,\omega) = P_t = C_1 \exp(-ikr), \quad r > r_{bc} + b$$
 (5.49)

In Eqs. (5.47)—(5.49), the local effective wavenumber  $k_{mj}$  is obtained by Eq. (5.44) at layer j,  $P_L$ ,  $P_{BC,j}$  and  $P_R$  are the left-, air-bubble curtain and the right-pressure field, respectively.  $P_i$  is the incident plane wave propagating in the positive r-direction in the fluid,  $P_r$  is the reflected wave travelling in the negative r-direction in the fluid, similarly,  $P'_{tj}$  and  $P'_{rj}$  are the forward- and backward propagating waves in the bubbly mixture of layer j,  $P_t$  is the transmitted wave in the fluid on the right side of the bubbly mixture. The solutions assume a time dependence  $\exp(i\omega t)$ .

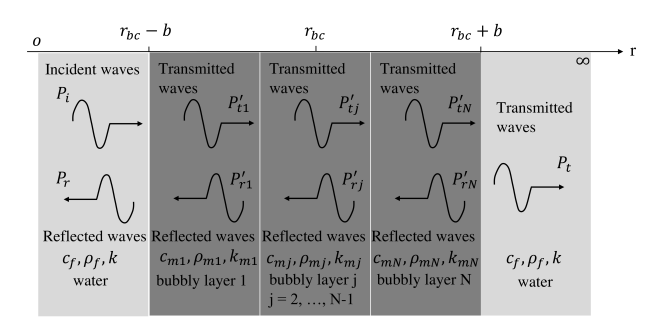


Figure 5.4: Schematic representation of the simulated regions: water column on the left side, layers of bubbly mixture and water column on the right side. The figure shows one of the M domains along the vertical coordinate.

At the interface between the bubbly mixture and seawater, and between bubbly layers, the continuity of the pressure and normal velocity is required as [64]:

$$p_f = p_{m1}, \quad p_f = p_{mN_{bc}}, \quad p_{mj} = p_{m(j+1)}, \quad j = 1, ..., N_{bc} - 1$$
 (5.50)

$$v_{r,f} = v_{r,m1}, \quad v_{r,f} = v_{r,mN_{bc}}, \quad v_{r,mj} = v_{r,m(j+1)}, \quad j = 1,..,N_{bc} - 1$$
 (5.51)

In Eq. (5.50),  $p_f$  and  $v_{r,f}$  is the pressure and the radial velocity in the fluid and  $p_m$  and  $v_{r,m}$  is the pressure and the radial velocity in the bubbly mixture. The radial velocity is defined as:

$$v_{r,i} = \frac{1}{\mathrm{i}\omega\rho_i} \frac{\partial p_i}{\partial r} \tag{5.52}$$

with the subscript i being f or m represents the fluid layer or bubbly layer. In the work of Commander and Prosperetti [64], the density of the bubbly mixture was approximated by the density of water. However, in Eq. (5.52), the density of the bubbly mixture is characterized by the depth-dependent gas and fluid fraction coefficients as derived by solving Eq. (5.24) as discussed in section 5.3.1.

The set of 2N+2 interface conditions reads:

$$P_L(r_{bc} - b, \omega) = P_{BC,1}(r_{bc} - b, \omega), \quad v_{r,f}(r_{bc} - b, \omega) = v_{r,m1}(r_{bc} - b, \omega)$$
 (5.53)

$$P_{BC,j}(r_{bc,j},\omega) = P_{BC,j+1}(r_{bc,j},\omega), \quad v_{r,mj}(r_{bc,j},\omega) = v_{r,m(j+1)}(r_{bc,j},\omega)$$
 (5.54)

$$P_{BC,N_{bc}}(r_{bc} + b, \omega) = P_R(r_{bc} + b, \omega), \quad v_{r,f}(r_{bc} + b, \omega) = v_{r,mN_{bc}}(r_{bc} + b, \omega)$$
 (5.55)

in which  $r_{bc,j} = r_{bc} - b + 2b(j-1/2)/N_{bc}$ , j = 1,...,N. By substituting the expressions in Eqs. (5.47)–(5.49) into the interface conditions at  $r = r_{bc} \pm b$  and  $r = r_{bc,j}$ , and assuming an incident wave of unit amplitude  $A_1 = 1$ , the amplitude coefficients  $A_2$ ,  $B_{1j}$ ,  $B_{2j}$  and  $C_1$  are obtained.

Next, the solutions are generalized by the depth-dependent acoustic properties of the air-bubble curtain including the half-width b(z) and effective medium wavenumber  $k_m(\omega, z)$ . The local transfer coefficient of the bubbly layer is defined by:

$$\widetilde{H}(z,\omega) = C_1 \tag{5.56}$$

The transfer coefficient function in Eq. (5.56) is coupled to the noise prediction model through boundary integral equation in Eq. (5.15). The local transmission loss (dB/m) is obtained as:

$$TL(z,\omega) = 10\log|C_1|^2$$
 (5.57)

# 5.4 Validation study of the effective wavenumber model

For the validation of the integral model for the effective wavenumber, the modelling results are compared to the numerical solutions by Bohne et al. [67] and measurement data from the experiment by Milgram [171]. The input parameters of the air bubble curtain system are given in the Table 5.1.

Parameter	Air bubble curtain
Water depth [m]	50
Density of the fluid [kg/m³]	1000
Nozzle diameter [mm]	50
Air flow rate $[m^3/s]$	0.024, 0.283 and 0.590
Spreading coefficient [m]	0.6
Amplification factor [-]	1
Entrainment coefficient [-]	0.18

Table 5.1: Basic input parameters of the air bubble curtain system.

The experiment took place at a lake with a water depth T of 50m at a local sinkhole spring in Florida, which fits the typical bathymetry of offshore pile-driving environments (shallow water up to  $40{\sim}50$  m water depth) with the application of an air bubble curtain system. Three air flow rates involving 0.024, 0.283 and 0.59 m $^3/s$  at atmospheric pressure are examined. In Fig. 5.5, the comparison of centerline velocities and half width of the bubbly layer are shown for the numerical results from literature and measured data set from the experiments [67, 171]. The numerical evaluation of both centerline velocity and half width of the bubble curtain show a relatively good agreement with the experiment, the small deviation from Bohne's model can be due to different numerical integration scheme and entrainment coefficient to achieve better fitting to the measured data set. As can be seen in Fig. 5.5 (left), the velocities decrease slowly as the distance from the nozzle increases. The maximum velocities are observed in the vicinity of the nozzle. In Fig. 5.5 (right), the width of the bubble plume is found to increase linearly with height above the nozzle, which is also in line with the observation of *cone shaped bubbly mixture* in offshore pile installation campaign with the application of the bubble curtain system.

In Fig. 5.6, the mean bubble volume and gas fraction ratio of both small and large bubbles are presented. Different fluid dynamic behaviors are observed for the large and small bubbles with the varying height from the nozzle. As the height from the nozzle increases, large bubbles break up into smaller ones as the gas fraction ratio of the small bubble increases while the volume of the large bubbles approaches the one of the small bubbles. The module captures the bubble formation process especially in the vicinity of the nozzle and forms the basis for calculation of more accurate acoustic properties of the air bubble curtain.

To validate the derivation of the transmission coefficients of the air bubble curtain, the modeled results are compared to the measured transmission loss obtained in the freshwater lake experiment [175]. The water depth T is 9.7m. The case with air flow rate being 0.0019 m<sup>2</sup>/s, nozzle interval  $\Delta y_n = 25$  cm and nozzle size being  $d_n = 1.4$  mm is evaluated. For the comparison of the different models and experiment data set, the overall transmission loss is defined as:

$$TL_{bc}(\omega) = -10\log\left[\sum_{1}^{N_z} |C_1|^2 \frac{\Delta z}{T}\right]$$
(5.58)

In Eq. (5.58), the rule of thumb for using six elements per wavelength is applied for the vertical step size  $\Delta z$ .

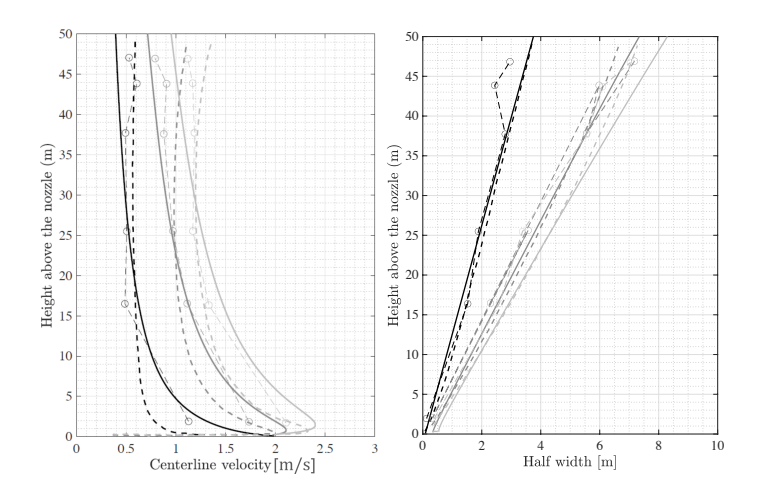


Figure 5.5: Comparison between centreline velocities and half width of the bubbly layer from the model, numerical results from Bohne et al. [67] and measured values from experiments [171]: (**left**) centreline velocities; (**right**) half width of the bubbly layer. The solid lines represent the computed results from the model, the dashed lines indicate the numerical results from the literature and the circles show the values measured experimentally. Three air flow rates involving 0.024 (black lines), 0.283 (dark grey lines) and 0.59 (light grey lines) m<sup>3</sup>/s.

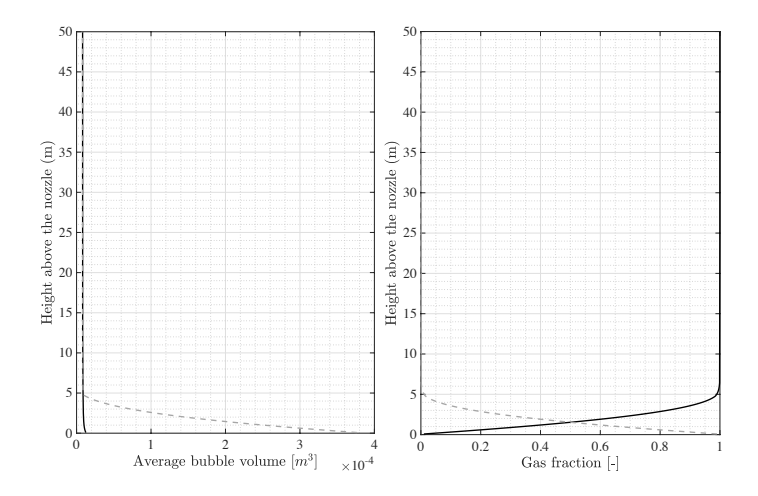


Figure 5.6: Computed depth-dependent variables for the case of the air flow rate being 0.024 m<sup>3</sup>/s: (**left**) the arithmetic mean bubble volumes; (**right**) gas fraction ratio ( $\frac{e_{gml}}{\epsilon_{gm1} + e_{gm2}}$ ) varying over the depth, in which the black solid line indicates the results for small bubbles and grey dashed line represents the results for large bubbles.

As shown in Fig. 5.7, the air bubble curtain model improves its performance as for the higher frequencies the transmission loss is close to the measured data and it does not require any assumption of the bubble size distribution coefficients [67]. As indicated by the black solid line, the model is more in line with the measurement data compared to

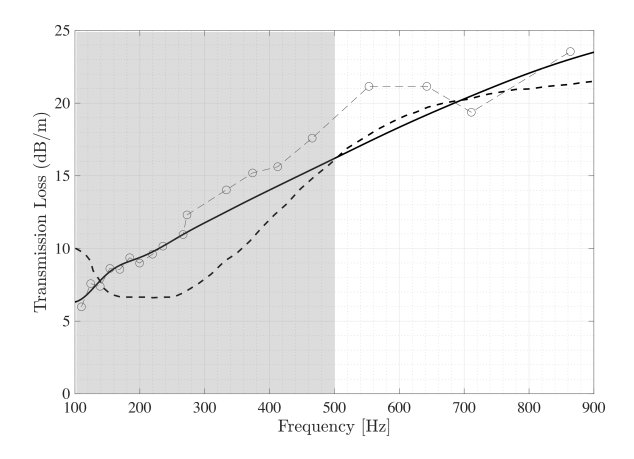


Figure 5.7: Comparison of the transmission loss between the modelling results (the black solid line) and the data from the measurement [175] (the line with circles) and the numerical air bubble curtain model [67] without the assumption of the bubble size distribution coefficients (the black dashed line). The light grey area indicates the frequencies of interest in offshore pile driving(< 500 Hz).

other numerical model for frequencies below 500 Hz, which is mainly due to the choice of the initial condition and control parameters including the spreading coefficients and the entrainment factor. Frequencies below 500 Hz are also important in offshore pile driving.

## 5.5 Validation study of the complete model including the air-bubble curtain

In this section, the model predictions are validated against measurement data collected from an offshore wind farm constructed in 2018 (hereafter referred to as project A). In Table 5.2, the material and geometrical parameters are estimated from the available geotechnical reports at the pile installation site.

Table 5.2: Basic i	input parameters	for the val	idation case	for project A

Parameter	Pile	Parameter	Fluid	Marine sediment	Bottom soil
Length [m]	75	Depth [m]	40.1	1.5	∞
Density [kg/m³]	7850	Density [kg/m³]	1000	1621.5	1937.74
Outer diameter [m]	8	$c_L$ [m/s]	1500	1603	1852
Wall thickness [mm]	90	$c_T$ [m/s]	-	82	362
The penetration depth [m]	30.5	$\alpha_p [dB/\lambda]$	-	0.91	0.88
Maximum Blow Energy [kJ]	2150	$\alpha_s [dB/\lambda]$	-	1.86	2.77

#### 5.5.1 MAXIMUM NOISE REDUCTION LEVEL

To predict the maximum noise reduction levels that can be achieved by the air-bubble curtain at the pile installation site, three scenarios are considered to distinguish the water-

and soil-borne noise transmission paths:

- scenario 1 noise prediction without the presence of air-bubble curtain (base case);
- *scenario 2* elimination of the water-borne path at the position of the air-bubble curtain leaving the propagation of the waves through the soil unaffected;
- *scenario 3* same as *scenario 2* but with an additional 1m gap at the lowest part of the seawater column in which the noise presumably leaks.

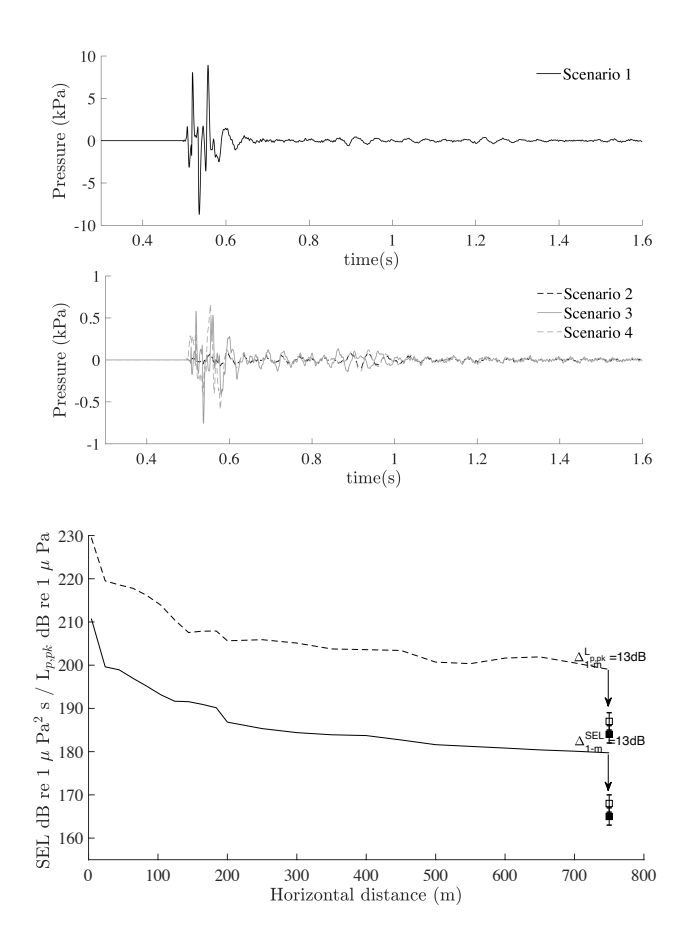


Figure 5.8: Prediction of the noise from the pile driving: (**top**) computed time histories of the pressure in the water at various radial distances at 2 m above the seabed, in which *scenario 1* is indicated by the black solid line; *scenario 2* indicated by the black dashed line; *scenario 3* indicated by the grey solid line; *scenario 4* indicated by the grey dashed line (to be discussed in section 5.5.2); (**bottom**) comparison of SEL and  $L_{p,pk}$  at 750m radial distance from the pile and 2 m above the seabed with the comparison between the *scenario 1* and arithmetic mean measured data.

In *scenario 2*, the noise sources in the water column are effectively cancelled (100% cancellation of the water-borne path) while the field in the soil is propagated undisturbed

in the exterior (to the air-bubble curtain) domain. This allows one to estimate the maximum noise reduction potential that a noise mitigation system can achieve with a theoretical efficiency of 100% in blocking the water-borne path. The difference between the results of the non-mitigated noise field (*scenario 1*) and the ones at which the water-borne path is fully or partially blocked (*scenarios 2* and *3*) give an estimate of the maximum noise reduction that can be achieved by eliminating the entire noise transmission path in the fluid and provide a clear indication of the influence of the zone of flow establishment in the vicinity of the nozzles (Region I depicted in the Fig. 5.3). Considering the possibility to eliminate the water-borne noise sources at any distance of interest, i.e. 10m, 50m, etc., the distance has been chosen here equal to the one of which the outer air-bubble curtain was placed (145m from the pile surface).

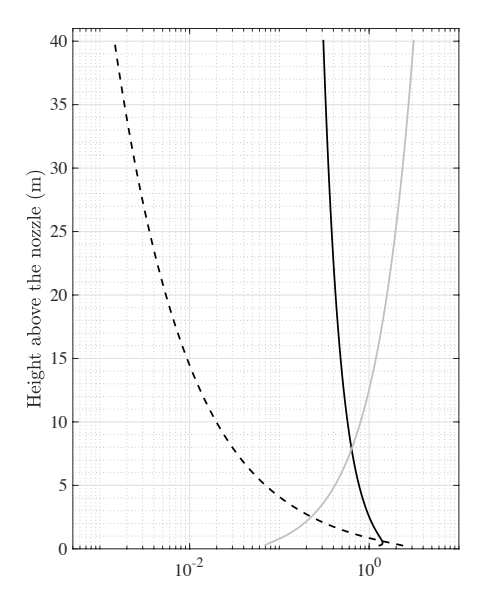


Figure 5.9: Variation of the fluid dynamic properties over the depth: (a) centerline velocity [m/s] (the black solid line); (b) the half width [m] (the grey solid line); (c) the overall gas fraction [-](the dark grey dashed line).

The Peak Level ( $L_{p,pk}$ ) in the unit of dB re 1  $\mu$ *Pa* is determined by the absolute maximum of the sound pressure following a single hammer blow:

$$L_{p,pk} = 20\log\left(\frac{p_{pk}}{p_0}\right) \tag{5.59}$$

In Eq. (5.59),  $p_{pk}$  is the zero-to-peak sound pressure and  $p_0=10^{-6}$  Pa is the reference underwater sound pressure level. The SEL in units of dB re 1  $\mu Pa^2s$  is defined as:

SEL = 
$$10\log\left(\frac{1}{T_0}\int_{T_1}^{T_2}\frac{p^2(t)}{p_0^2}dt\right)$$
 (5.60)

with  $T_1$  and  $T_2$  being the starting and ending of the predicted time signature with the sound event in between and  $T_0 = 1$  sec.

The peak pressure level ( $L_{p,pk}$ ) and sound exposure level (SEL) of receiver points at radial distances up to 750m are obtained here for the non-mitigated field (*scenario 1*) as shown in Fig. 5.8 (a). Through an indirect method, the noise reduction level achieved by the Noise Mitigation Systems can be examined by comparing the sound levels of the non-mitigated and mitigated fields. In Fig. 5.8 (b), the evolution of the pressure field in time is shown for a point positioned 2m above the seabed at various radial distances from the pile for *scenarios 1-3*. The numerical results for the three scenarios and the comparison to the measurement are summarized in Table 5.3. The measured SEL and  $L_{p,pk}$  are derived from the data collected from four hydrophones located at four difference angles as shown in Fig. 5.11. The range of the sound levels is given in Table 5.3 with their arithmetic mean values indicated in the parenthesis. The deviation of the sound levels in the measured data can be due to the existence of the currents and angular-dependent bathymetry changes in the offshore environment.

The maximum noise reduction level of  $\sim$  30.0 dB in terms of SEL and  $\sim$  35.0 dB in terms of L<sub>p,pk</sub> can be achieved respectively when the air-bubble curtain blocks the entire waterborne path (*scenario 2*). With the consideration of 1-m gap due to the bubble formation process in the vicinity of the nozzle (*scenario 3*), the predicted ideal noise reduction level by an air bubble curtain reduce to  $\sim$  20.9 dB for SEL and  $\sim$  21.4 dB for L<sub>p,pk</sub>.

The energy flux is given at the location of the outer bubble curtain  $r = r_{bc,2} = 145m$  in Fig. 5.10. Close to the seabed the amount of the energy is relatively high compared with the entire water depth and soil depth, which indicates that a great amount of energy could channel from the vicinity of the seabed back into the water column due to the thin air bubble layer close to the seabed. This also explains the difference in the noise reduction level of SEL and  $L_{p,pk}$  between  $\Delta_{1-2}$  and  $\Delta_{1-3}$ .

Table 5.3: The summary of predicted noise reduction levels and experiment data from the pile installation campaign.

Levels [dB]	Measured with DBBC	$\Delta_{1-m}$	Modeled scenario 1	Modeled scenario 2	Modeled scenario 3	$\Delta_{1-2}$	$\Delta_{1-3}$
$\begin{array}{c} \text{SEL} \\ \mathbf{L}_{p,pk} \end{array}$	165~168 (167) 184~187 (186)	` /	180 199	150 165	158.8 177.6	30.0 35.0	20.9 21.4

# 5.5.2 VALIDATION OF THE NOISE REDUCTION WITH THE MODEL OF THE AIR BUBBLE CURTAIN

In this section, the validation of the complete model including the double air bubble curtains is performed. The model is based on the configuration of an offshore pile installation campaign in 2018. The installation was executed for the pile using double big bubble curtain (DBBC), which are especially often used for large water depths (> 30m). Within the same offshore wind farm, another installation was executed for the pile without using any noise mitigation system, which has been used for the validation of the noise prediction model in [29]. The input parameters of the air bubble curtain system are given in Table 5.4,

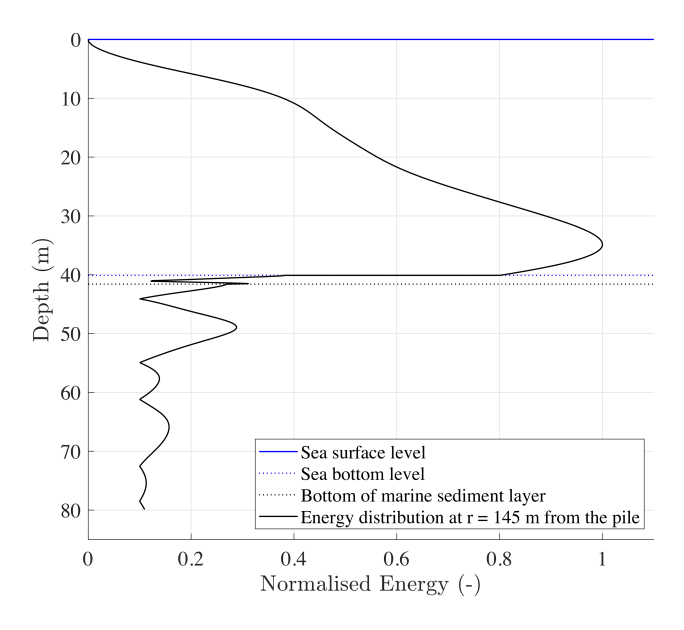


Figure 5.10: The energy flux at the location of the outer bubble curtain  $\mathbf{r} = r_{bc,2} = 145m$  over the fluid and soil domain.

while the material and geometrical parameters are those summarized already in Table 5.2. The locations of both the inner and outer bubble curtains, as well as the nozzle diameter and spacing, are determined from measured data. The air flow rate is derived from the compressible flow model. The spreading and entrainment coefficients are based on modeling assumptions. The layout of the DBBC system is shown in Fig. 5.11,  $r_{bc,1}$  and  $r_{bc,2}$  are the radius of the bubble curtain with the width being  $b_{bc,1}(z)$  and  $b_{bc,2}(z)$ , respectively.

Table 5.4: Basic input parameters of the air bubble curtain system.

Parameter	Air bubble curtain
location of the inner bubble curtain $r_{bc}$ [m]	105
location of the outer bubble curtain $r_{bc}$ [m]	145
Nozzle diameter $d_n$ [mm]	1.5
Nozzle spacing $y_n$ [m]	0.30
Air flow rate $q_{atm}$ [m <sup>3</sup> /s/m]	0.0087
Spreading coefficient $\lambda$ [-]	0.1
Entrainment coefficient $\alpha$ [-]	0.18

Based on the configuration of the bubble curtain system, the fluid dynamic and acoustic properties of the system are obtained first by the noise reduction module. Figure 5.9 shows the variation of the centreline velocity, width and total gas fraction of the bubble curtain over the depth. The transmission loss of the bubble curtain is derived as discussed in

section 5.3.2. As shown in Fig. 5.12 (left), the mitigation is less effective at low frequencies (<100 Hz). The variation of the damping coefficients along the entire water depth in Fig. 5.12 (right) shows that the attenuation is depth-dependent and reduces in the vicinity of the nozzle especially for the higher frequencies due to the zone of the flow establishment in the bubble formation process.

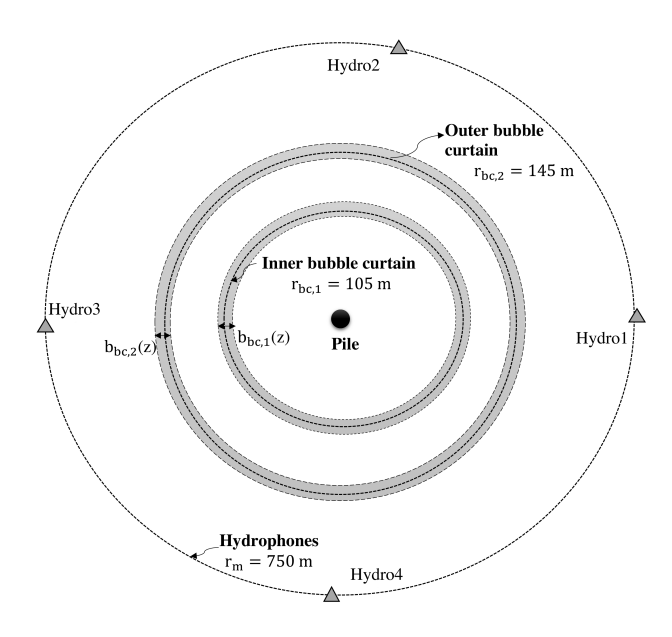


Figure 5.11: Layout of DBBC system.

Next, the noise source for the impact pile driving is generated by the noise prediction model for non-mitigated field and is propagated first to the location of the inner air-bubble curtain at  $r = r_{bc,1}$ . The direct BEM is used to couple the noise prediction model for non-mitigated field and noise reduction model for the air-bubble curtain as discussed in section 5.3. The wavefield is then propagated to the location of the outer air-bubble curtain at  $r = r_{bc,2}$  and is coupled to the noise reduction model for the outer air-bubble curtain through the BEM. The direct BEM gives us great flexibility to couple the non-mitigated field to a single or double air-bubble curtains.

The calculated SEL and  $L_{p,pk}$  are summarized in Table 5.5 compared to the measurement data collected during the pile installation campaign. The sound reduction predicted including the modeling of double air bubble curtains are  $\sim$  20 dB for SEL and  $\sim$  21 dB for  $L_{p,pk}$  at a distances of 750m.

The summary of the noise prognosis for the offshore campaign is given in Table 5.5 in terms of the SEL and the  $L_{peak}$ . The difference between the noise reductions for *scenario 2* and 3 is due to the 1-m gap in the fluid, which can lead to the channelling of great energy in the vicinity of the seabed back into the water column as indicated in Fig. 5.10. The noise reduction for SEL achieved by DBBC is slightly lower than the reduction by *scenario 3*, since *scenario 3* leads to a more conservative estimation by assuming the full blockage of

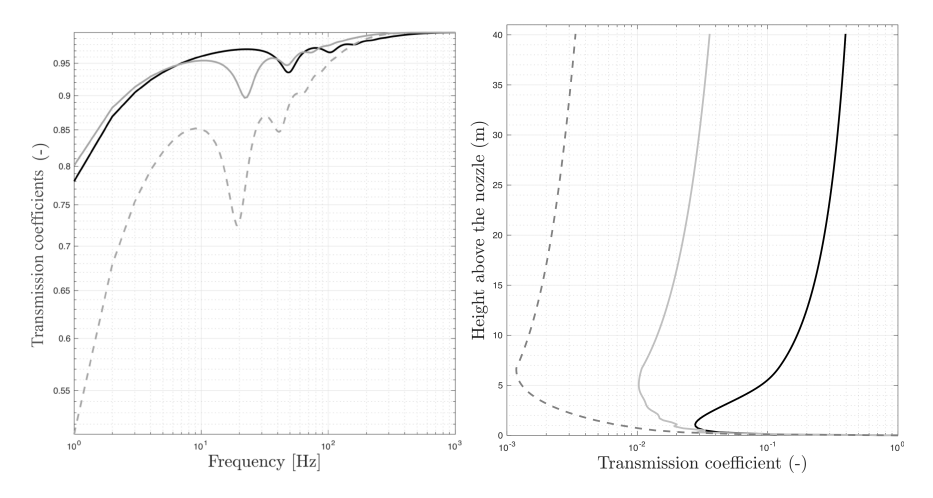


Figure 5.12: Prediction of the acoustic properties of the air bubble curtain: (**left**) the spectrum of transmission loss at three depths, in which the black solid line represents the results at 1-m above the nozzle, the grey solid line indicates the results at 5-m from the nozzle and the grey dashed line indicates the results at 20-m from the nozzle; (**right**) transmission loss for three different frequencies over the depth, in which the black solid line, the grey solid line, the grey dashed line represent f = 20,150,300 Hz, respectively.

the transmission in the fluid domain except the 1-m gap close to the seabed. Because the air-bubble curtain system has a much higher transmission loss at higher frequencies, the system works more efficiently in reducing the impulsiveness of the incoming waves as evaluated by  $L_{p,pk}$ . The currents and other environmental factors can play an important role in the noise mitigation as indicated by the deviation (3±2 dB) in the measured SEL and  $L_{p,pk}$  from different hydrophones. The deviation of 2 dB is considered as measurement error from the set-up of the test equipments, including the hydrophones and calibrators. The prediction of SEL by *scenario 4* including the DBBC ( $\Delta_{1-DBBC}$  =20 dB) and the *scenario 3* ( $\Delta_{1-3}$  =21 dB) are around 4 and 3 dB above the upper bound of the measured data ( $\Delta_{1-m}$  =15+2=17 dB), respectively. The noise reduction  $L_{p,pk}$  from the measurement data is much lower compared to both *scenario 3* and the *scenario 4* (DBBC), which indicates that both scenarios lead to conservative predictions. Further investigations regarding the sensitivity of the parameters of air-bubble curtain system and the influence of currents and other environmental factors are needed to provide a better estimation of the sound pressure levels and to optimize the use of the air-bubble curtain system.

Table 5.5: The summary of the noise prognosis for the offshore pile installation.

Noise Reduction Levels [dB]	$\Delta_{\mathbf{SEL}}$	$\Delta_{\mathbf{L}_{p,pk}}$	
Measurement $\Delta_{1-m}$	12 ±2~15±2 (13±2)	12 ±2~15 ±2 (13±2)	
Maximum noise reduction $\Delta_{1-2}$	30	35	
Estimation of noise reduction $\Delta_{1-3}$	21	21	
Computed noise reduction $\Delta_{1-DBBC}$	20	21	

#### 5.6 Conclusions

This chapter establishes a computationally efficient approach for noise reduction prediction in offshore pile driving with the application of a single or double air-bubble curtain system. The complete model consists of two modules: the noise prediction module that describes the vibroacoustic behaviour of the pile-soil-water interaction and propagates the wave field at larger distance from the pile, and the noise reduction module that describes the acoustic properties of an air bubble curtain. The solution approach is presented with the complete mathematical statement of the coupled vibroacoustic pile-water-soil system including the dynamics of the air-bubble cloud. The direct boundary integral equation (BIE) formulation is used to couple the three modules and propagate the wavefield from the vicinity of the pile to the location of the inner and outer bubble curtains and to the larger distances. The validation of the local effective wavenumber model is performed by comparison to available numerical solutions and reported experimental data sets. Noise predictions are then performed for a pile-installation campaign with the use of DBBC in 2018 and the results are compared to measurement data. The maximum noise reduction level of an ideal noise mitigation system is studied by eliminating the water-borne transmission path. The results indicate the maximum potential of the noise mitigation systems applied in the water column. The model can later be used for optimization of the air-bubble curtain system in order to improve the deployment strategy of the system. The modelling approach can be applied for modelling different noise mitigation techniques, which provides possibilities to examine the optimal combination of various noise mitigation techniques and position of the deployment of the system.

6

# A THREE DIMENSIONAL MULTI-PHYSICS MODEL OF AN AIR-BUBBLE CURTAIN

Assessment and mitigation of underwater noise are usually required to ensure that sound levels stay below the noise thresholds. The air-bubble curtain system is one of the most widely applied noise mitigation techniques. To advance the modelling approach for predicting underwater noise radiation in offshore pile driving, a three-dimensional multi-physics approach is introduced for modelling an air-bubble curtain system.

 ${f T}$  o examine the performance of an air-bubble curtain system, a multi-physics model is further developed in this chapter as extension of the model introduced in Chapter 5. In Chapter 5, a semi-analytical model [68] is presented where the hydrodynamic module for describing the bubble formation process is coupled to the vibroacoustic model for noise prediction from pile driving through a boundary integral formulation. The results indicate that an accurate description of the acoustic characteristics of the bubbly layer is critical for modelling noise mitigation using the air-bubble curtain system. However, the performance of the air-bubble curtains can vary significantly in azimuth direction due to the inherent variations in the airflow circulation through the perforated pipes positioned on the seabed surface. As the air flow rate through the nozzles can have a significant impact on bubble generation and development through the water column, there is a need to determine the flow velocity of the air in the perforated pipes which are positioned on the seabed surface [67].

In this chapter, a multi-physics model is developed for modelling noise mitigation using the air-bubble curtain system. The complete model consists of four modules: (i) a compressible flow model to account for the transport of compressed air in the perforated hose; (ii) a hydrodynamic model for capturing the characteristics of bubble clouds in varying development phases through depth and range; (iii) an acoustic model for predicting the sound insertion loss of the air-bubble curtain; and (iv) a vibroacoustic model for the prediction of underwater noise from pile driving which is coupled to the acoustic model in (iii) through a three-dimensional boundary integral formulation. The flow of the modelling activity is shown in Fig. 6.1. The structure of the Chapter is as follows. In Section 6.1, the description of the compressible flow model is given together with the governing equations. The description of the hydrodynamic and acoustic models is given in Section 6.2. Section 6.3 introduces the mathematical formulation for capturing the three-dimensional behavior of the air-bubble curtain system. In Section 6.4, a sensitivity study is performed to examine the acoustic characteristics of the bubble curtain. In Section 6.5, the validation study based on an offshore installation campaign is presented. Finally, Section 6.6 gives an overview of the main conclusions.

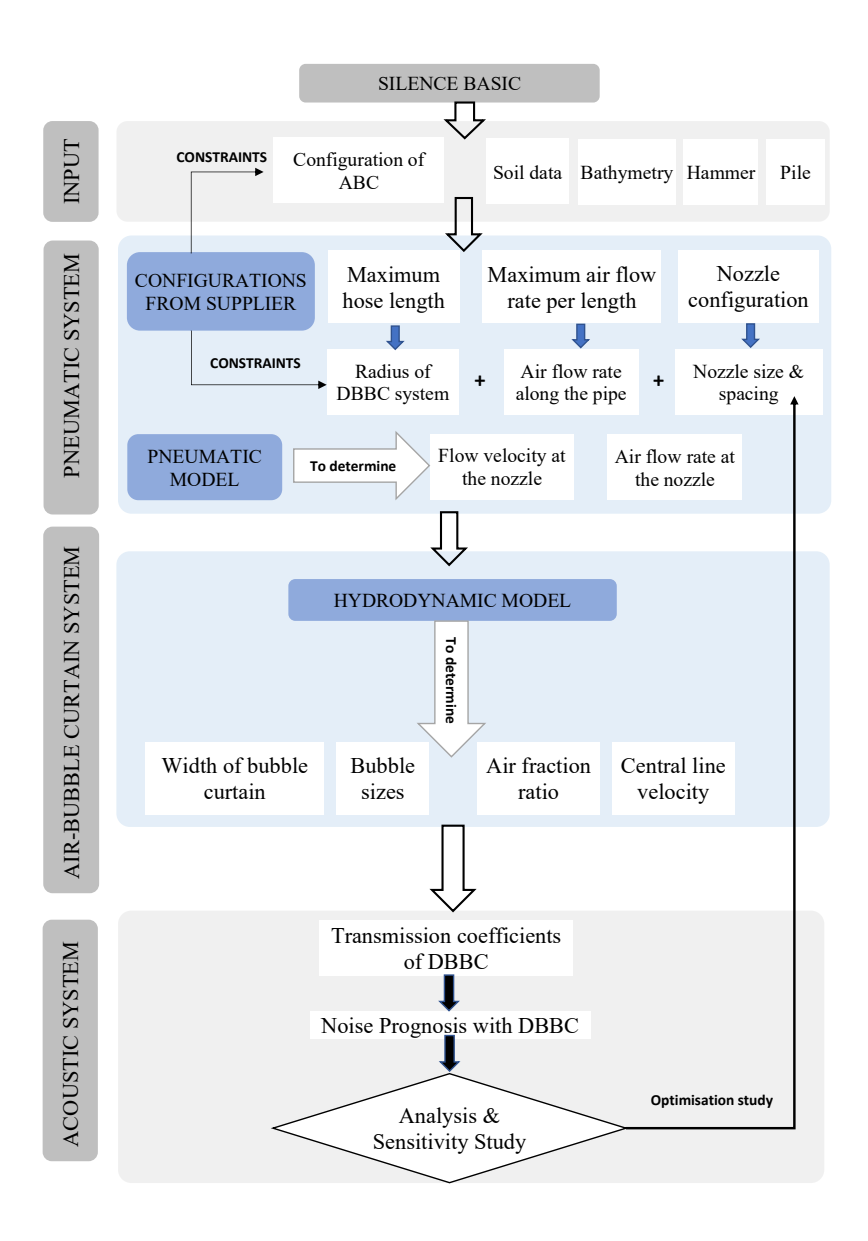


Figure 6.1: Activity flow of the complete model: 1) definition of the input of the model; 2) modelling of the pneumatic system; 3) modelling of the air-bubble curtain system; 4) modelling of the mitigated sound field with the use of DBBC.

# 6.1 COMPRESSIBLE FLOW MODEL

In this section, the pneumatic model is presented for modelling the transport of compressed air from the air-injection vessel to the perforated hose positioned on the seabed surface. The governing equations are given and the field test is presented for examining the pressure variation along the hoses for various airflow rates.

#### 6.1.1 Description of the model

An engineering model is developed using compressible flow theory to predict the operational parameters of a given hose-nozzle configuration used for bubble curtain generation. The total amount of air that is being delivered by the series of compressors is used as the main input and given as a volumetric flow rate at free air delivery conditions (FAD¹). The other input parameters consist of the density of seawater and air, water depth, and the geometrical characteristics of the feeding and perforated hose configuration. The results of the numerical model give the pressure distribution along the hose together with the average axial flow velocities and mass flow rates at each nozzle location. The total required upstream pressure considering the feeding hose can also be assessed.

The model considers a straight, horizontal hose with a constant diameter and uniform spacing of identical nozzles. In reality, the perforated pipes have a certain curvature, i.e.  $\kappa=1/R$ , which in our case is small enough so that the straight configuration is justified. The air is injected from two sides of the hose. Hence, the model assumes symmetry and only half of the total length is required to characterize the flow and pressure distribution; this is represented through a zero flow boundary condition to make sure that all the air is depleted at 180deg from the injected position. This assumption is based on the ideal operation and deployment of the air bubble curtain, which enables the simplification of the modeling approach using a one-dimensional compressible flow model. The hose is discretized into a fixed number of segments according to the total length L and the nozzle spacing S as shown in the schematic of Fig. 6.2. A regular polygonal approximation will closely resemble a circle and is visually indistinguishable for most practical purposes.

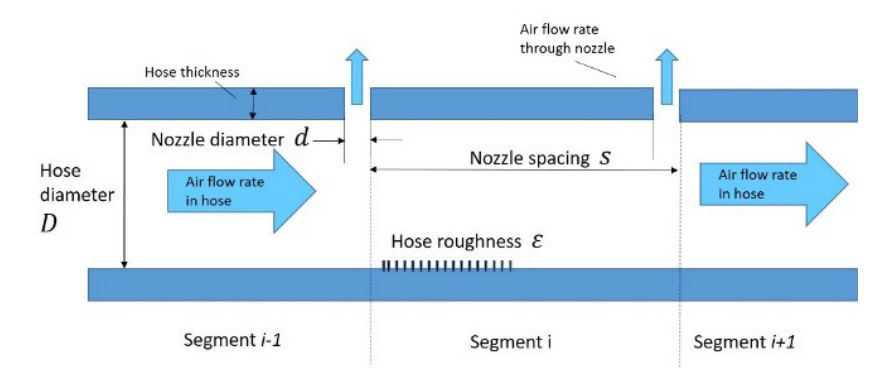


Figure 6.2: Schematic of the discretized model of the hose with nozzles for air transportation.

<sup>&</sup>lt;sup>1</sup>FAD conditions are defined at p = 101325Pa, T = 293.15K

### 6.1.2 GOVERNING EQUATIONS

For each segment i, isentropic compressible flow theory in combination with the state equation of the ideal gas is used to obtain the mass flow rate  $\dot{m}_{nz,i}$ , across the nozzle with diameter d and density  $\rho_i$  according to the following equations [177]:

$$\dot{m}_{nz,i} = C_d \frac{\pi d^2}{4} \left( \frac{2\gamma}{\gamma - 1} P_i \rho_i \left[ 1 - \left( \frac{P_{hst}}{P_i} \right)^{\frac{\gamma - 1}{\gamma}} \right] \left( \frac{P_{hst}}{P_i} \right)^{\frac{2}{\gamma}} \right)^{0.5}$$

$$(6.1)$$

$$\frac{P_i}{P_{hst}} = \left(1 + \frac{\gamma - 1}{2}M_i^2\right)^{\frac{\gamma}{\gamma - 1}} \tag{6.2}$$

$$M_i = \frac{U_i}{\sqrt{\gamma RT}} \tag{6.3}$$

where the discharge coefficient  $C_d = 0.55 \text{m}$  is used for each nozzle [178],  $\gamma = 1.402$  is the air adiabatic constant, R = 287 J/kg/K is the specific air gas constant, T = 291 K (18°C) is the air temperature,  $P_{hst}$  is the hydrostatic pressure outside the hose,  $P_i$  is the pressure inside the hose at each nozzle location,  $M_i$  and  $U_i$  are the Mach numbers and air velocities across the nozzles respectively. Conservation of mass is applied to the control volume of each segment to obtain the upstream mass flow rates  $\dot{m}_i$  as a function of the flow rates through the nozzle and from the downstream segment.

$$\dot{m}_i = \dot{m}_{nz,i} + \dot{m}_{i+1} \tag{6.4}$$

Assuming that the velocity and fluid properties are constant across sections normal to the flow (i.e. no radial gradients), one-dimensional, isothermal compressible flow in pipes with a constant area is used to calculate the upstream pressure of each hose segment including friction. The pressure losses in each segment of length  $l_i$  and hose diameter D include the friction factor f which is obtained by the Colebrook–White equation [179] according to the Reynolds number Re and hose roughness  $\epsilon$  as described in the following equations:

$$(P_i^2 - P_{i+1}^2) = \frac{\dot{m}_i^2 RT}{(\frac{\pi D^2}{4})^2} \left( 2\ln \frac{P_i}{P_{i+1}} + f_i \frac{l_i}{D} \right)$$
(6.5)

$$\frac{1}{\sqrt{f_i}} = -2\log\left(\frac{\epsilon}{3.7D} + \frac{2.51}{\text{Re}_i\sqrt{f_i}}\right) \tag{6.6}$$

#### 6.1.3 FIELD TESTS CAMPAIGN

A series of medium-scale tests were performed in Sliedrecht, the Netherlands in July 2022. The main objective of the tests is to provide measurements from the pneumatic system used to generate the bubble curtain in order to gain insights into the pressure distribution along the length of the hoses for different volumetric flow rates of injected air. The tests comprise several configurations with different hose sizes, hose lengths, spacing between nozzles, and nozzle diameters. In this section, the test results for one configuration with varying air flow rates are presented to show the effect on the pressure distribution.

The measurements of the flow rate, pressure, and temperature sensors are continuously recorded during the entire measurement campaign. For each time trace of both flow and

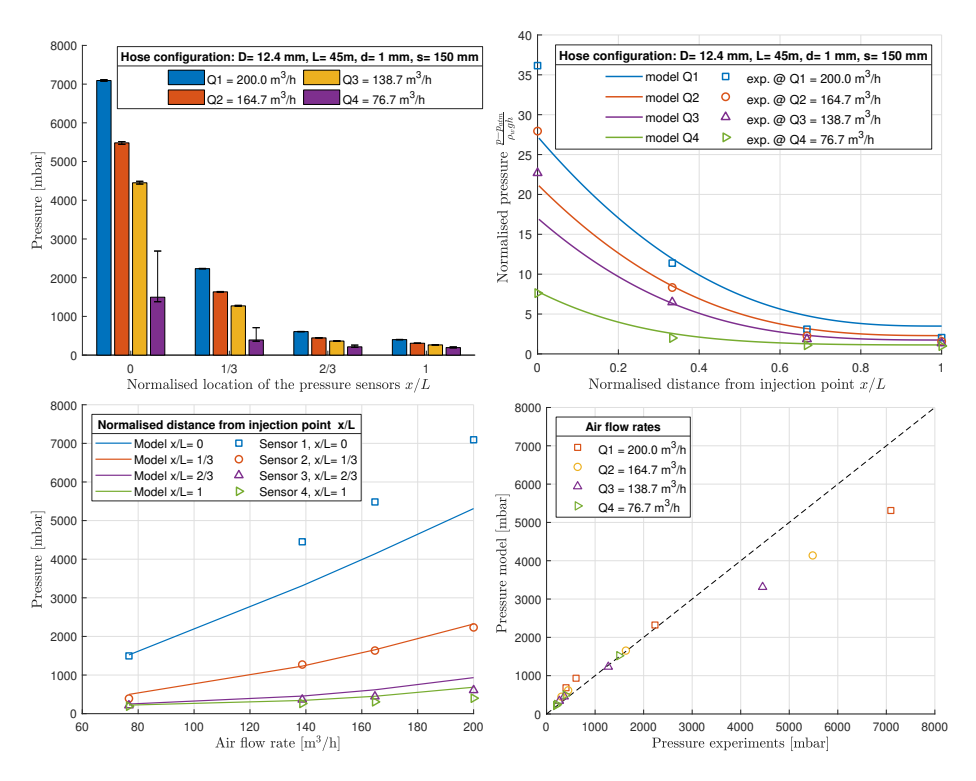


Figure 6.3: Comparison between simulation and experimental results for configuration tested at a water depth of 2.0m. L=45m, D=12.4mm, d=1.0mm, s=15cm. **Top**: Experimental results (left). Pressure distribution along hose length (right). **Bottom**: Pressure vs airflow rate (left). Comparison Model vs experiments (right).

Table 6.1: Test configuration for the wet experiments.

Configuration	Value	Unit
Hose diameter	0.0124	m
Nozzle spacing	0.15	m
Nozzle diameter	0.001	m
Air Flow rate	76.7 to 200	$m^3/hr$
Hose length	45	m

pressure measurements, several intervals under steady conditions were identified. The statistical values for each interval were calculated and reported for each pressure sensor located at certain distance from the feeding air as seen in Fig. 6.3.

The test configuration for one of the field tests is presented in Table 6.1 with varying flow rates from 76.7m<sup>3</sup>/hr to 200m<sup>3</sup>/hr. This particular configuration has the closest similarity to the current practice setup from the scaled parameters. As shown in Fig. 6.3 (A) and (B), for each flow rate, the pressure decreases nonlinearly with the distance between the pressure sensor and the air injection point. The pressure amplitude against the volume of air per unit time is also presented in Fig. 6.3 (C) for sensors at different horizontal distance

from the air injection point. The experimental results are compared to the model as shown in Fig. 6.3 (B-D), which indicates the numerical and field test results agree reasonably well for pressure measurements below 3 bar. However, when it comes to higher pressures above 4 bar, the simulation shows lower pressure at the feeding point for all flow rate cases as the pressure is underestimated. The discrepancy can be due to the impact of the non-linear decrease of pressure closer to the air feeding point. The error bar on the top of each bar indicates the deviation from the mean value in the pressure during the recording at a constant flow rate. The nonlinear pressure drop indicates that the airflow circulation leads to the variation of the pressure and air flow through the nozzles in the azimuth, which has a significant impact on the performance of the air bubble curtain system along the circumference. By comparing the various airflow rates in the given hose-nozzle configuration, pressure at each location of the sensor increases nonlinearly with the airflow rate. The field test verifies the influence of the volumetric flow rate of the injected air on pressure distribution along the hose, which indicates that the performance of the air-bubble curtain varies strongly along the circumference.

# 6.2 Hydrodynamic and acoustic model for air-bubble curtain

The hydrodynamic model aims to capture the characteristics of bubble generation and development. The model is introduced already in Chapter 5 and describes a turbulent two-phase bubble flow, in which the bubble plume is developed from a nozzle and followed by the breakup and coalescence of bubbles. The modelling of the bubble formation is based on an existing model developed in [66, 67]. Based on the airflow velocity through each nozzle derived from the hydraulic model, the input for the hydrodynamic model can be determined for a single bubble curtain configuration. The resulting set of equations reads,

$$\frac{d}{dz}\mathbf{m}(\mathbf{u}, z) = \mathbf{q}(\mathbf{u}, z) \tag{6.7}$$

In Eq. (6.7),  $\mathbf{u} = [u_{lzm}, b, \epsilon_{gm1}, \epsilon_{gm2}, v1, v2]$ . The model output after solving the set of equations include the half-width of bubble curtain b, gas fraction  $\epsilon_{gm1}$  and  $\epsilon_{gm2}$ , flow velocity  $u_{lzm}$ , and mean bubble volume v1 and v2, which vary with the depth z. The expressions for the vector of the integral fluxes  $m(\mathbf{u}, z)$  and the integral source term  $q(\mathbf{u}, z)$  are presented in detail in [67, 68] and are omitted here for the sake of simplicity.

The acoustic model as discussed in Chapter 5 includes the depth- and frequency-dependent transmission coefficients of each bubble curtain configuration. The model is based on a simplified one-dimensional acoustic wave propagation approach developed in [64]. Given the bubble characteristics obtained from the hydrodynamic model, the distribution of the local effective wavenumbers  $k_m(\omega,z,r)$  is determined over the entire water depth as described in [68]. The transmission coefficients  $\widetilde{H}(z,\omega)$  are then determined per z-coordinate and are constant within the vertical step size  $\Delta z$  of the integration. The transfer coefficient function is coupled to the noise prediction model through boundary integral equation. The average transmission loss over the water column (dB/m) is obtained

as [66, 68]:

$$TL(\omega) = 10\log(\sum_{i=1}^{M} |\widetilde{H}(z_i, \omega)|^2 \frac{\Delta z}{T})$$
(6.8)

in which T is the height of the bubble curtain,  $\Delta z$  is the integration step in the water column and M is the total number of vertical steps.

### 6.3 A THREE-DIMENSIONAL NOISE PREDICTION MODEL

The performance of the air-bubble curtains can vary significantly in azimuth due to the inherent variations in the airflow circulation through the perforated pipes positioned on the seabed surface. This section presents a new model which is based on a multiphysics approach and considers the three-dimensional behaviour of the air-bubble curtain system. The complete model employs three modules including the hydrodynamic model for capturing the characteristics of bubble clouds in varying development phases through depth; the acoustic model for predicting the sound insertion loss of the air-bubble curtain; and a vibroacoustic model for the prediction of underwater noise from pile driving which is coupled to the acoustic model through a three-dimensional boundary integral formulation. The three dimensional Green's function and the boundary integral model are described in detail in Chapter 2. The model allows for a comparison of various mitigation scenarios including the perfectly deployed air bubble curtain system, i.e. no azimuth-dependent field, and an imperfect system due to possible leakage in the bubbly sound barrier along the circumference of the hose.

In this section, the proposed method provides a foundation for evaluating the three-dimensional behaviour of the air bubble curtain system. The formulation of the problem for incorporating the azimuthal dependent behaviour of the air-bubble curtain is presented. Underwater noise prognosis is performed using realistic data from an offshore installation campaign in 2018, a non-fully blocked waterborne path with gaps in pre-defined angles is examined as a sample problem. The prediction results are compared to the free-field noise prediction and the scenario with full-blocked water borne path at the position of the air bubble curtain. The proposed modelling approach can be easily extended by incorporating a realistic transmission coefficient of the bubbly layer through the azimuthal coordinate.

A numerical approach is proposed for evaluating the noise emission from the impact pile driving with the use of the air-bubble curtain system. The hydrodynamic and the acoustic models have been described in Chapter 5. In this section, we focus on the coupled dynamic problem in an axisymmetric acousto-elastic medium with non-axisymmetric boundary conditions at the position of the bubble curtain.

Based on potential theory and Green's third theorem, the boundary integral equation for three-dimensional case reads:

$$\tilde{\boldsymbol{u}}_{\alpha}^{\Xi} = \int_{S^{f}} \left( \widetilde{U}_{\alpha r}^{\Xi f}(\boldsymbol{r}, \boldsymbol{r}_{s}) \cdot \widetilde{p}(\boldsymbol{r}_{s}) \widetilde{H}(\boldsymbol{r}_{s}) - \widetilde{T}_{\alpha r}^{\Xi f}(\boldsymbol{r}, \boldsymbol{r}_{s}) \cdot \widetilde{u}_{r}^{f}(\boldsymbol{r}_{s}) \widetilde{H}(\boldsymbol{r}_{s}) \right) dS^{f}(\boldsymbol{r}_{s}) 
+ \sum_{\beta = r} \int_{S^{s}} \left( \widetilde{U}_{\alpha\beta}^{\Xi s}(\boldsymbol{r}, \boldsymbol{r}_{s}, \omega) \cdot \widetilde{t}_{\beta}^{n}(\boldsymbol{r}_{s}) - \widetilde{T}_{\alpha\beta}^{n,\Xi s}(\boldsymbol{r}, \boldsymbol{r}_{s}, \omega) \cdot \widetilde{u}_{\beta}(\boldsymbol{r}_{s}) \right) dS_{s}^{s}(\boldsymbol{r}_{s})$$
(6.9)

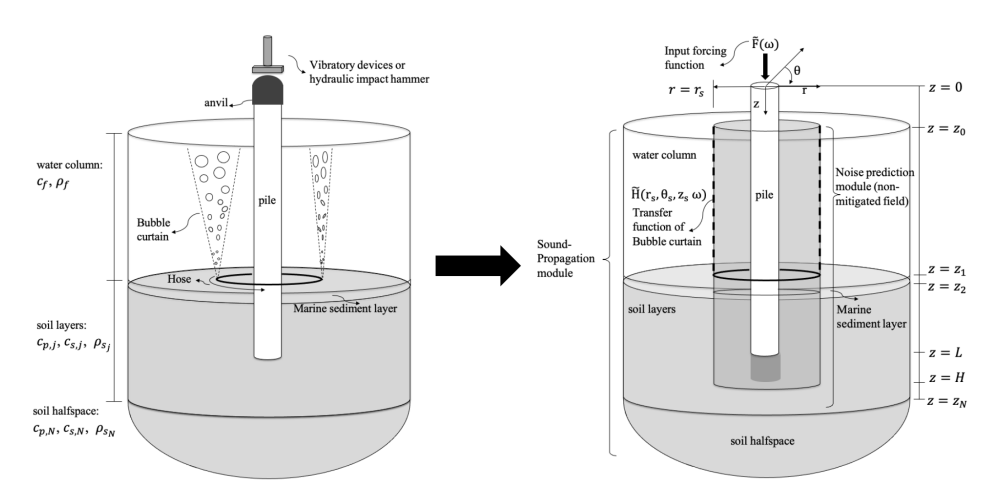


Figure 6.4: Schematic of the complete system (left) and the coupled model (right).

in which  $\Xi=f$  or s indicates the location of the source in fluid or soil, respectively,  $\tilde{H}(\boldsymbol{r}_s)$  is the angular and frequency dependent transmission coefficient of the bubble curtain,  $\tilde{u}_r^f(\boldsymbol{r}_s)$ ,  $\tilde{p}(\boldsymbol{r}_s)$ ,  $\tilde{t}_{\beta}^n(\boldsymbol{r}_s)$ ,  $\tilde{u}_{\beta}(\boldsymbol{r}_s)$  are the source terms obtained from the noise prediction module while generating the non-mitigated field from pile driving [29]. In the case of the axisymmetric non-mitigated field, the boundary integral equation is reduced to

$$\tilde{\boldsymbol{u}}_{\alpha}^{\Xi} = \int_{S^{f}} \left( \tilde{U}_{\alpha r}^{\Xi f}(\boldsymbol{r}, \boldsymbol{r}_{s}) \cdot \tilde{p}(r_{s}, z_{s}) \tilde{H}(\boldsymbol{r}_{s}) - \tilde{T}_{\alpha r}^{\Xi f}(\boldsymbol{r}, \boldsymbol{r}_{s}) \cdot \tilde{u}_{r}^{f}(r_{s}, z_{s}) \tilde{H}(\boldsymbol{r}_{s}) \right) dS^{f}(\boldsymbol{r}_{s}) 
+ \sum_{\beta = r, \theta, z} \int_{S^{s}} \left( \tilde{U}_{\alpha \beta}^{\Xi s}(\boldsymbol{r}, \boldsymbol{r}_{s}, \omega) \cdot \tilde{t}_{\beta}^{\boldsymbol{n}}(r_{s}, z_{s}) - \tilde{T}_{\alpha \beta}^{\boldsymbol{n}, \Xi s}(\boldsymbol{r}, \boldsymbol{r}_{s}, \omega) \cdot \tilde{u}_{\beta}(r_{s}, z_{s}) \right) dS_{s}^{s}(\boldsymbol{r}_{s})$$
(6.10)

For a general formulation, we expand the boundary displacement and the tractions in Eq. (6.9) using the Fourier series, i.e.:

$$\sum_{m=-\infty}^{\infty} \hat{\boldsymbol{u}}_{\alpha m}^{\Xi}(\boldsymbol{r}, z) e^{ik\theta} =$$

$$\sum_{m=-\infty}^{\infty} \int_{L^{f}} R_{bc} \left( \widehat{U}_{\alpha r, m}^{\Xi f}(\boldsymbol{r}', \boldsymbol{r}'_{s}) \cdot \widehat{p}_{m}^{*}(z_{s}) - \widehat{T}_{\alpha r, m}^{\Xi f}(\boldsymbol{r}', \boldsymbol{r}'_{s}) \cdot \widehat{u}_{rm}^{f*}(z_{s}) \right) dL^{f}(z_{s})$$

$$+ \sum_{m=-\infty}^{\infty} \sum_{\beta=r,\theta,z} \int_{L^{s}} R_{bc} \left( \widehat{U}_{\alpha\beta,m}^{\Xi s}(\boldsymbol{r}, \boldsymbol{r}'_{s}, \omega) \cdot \widehat{t}_{\beta}^{n}(z_{s}) - \widehat{T}_{\alpha\beta,m}^{n,\Xi s}(\boldsymbol{r}', \boldsymbol{r}'_{s}, \omega) \cdot \widehat{u}_{\beta m}(z_{s}) \right) dL_{s}^{s}(z_{s})$$
(6.11)

in which *L* is the line of the boundary in (r,z) plane,  $R_{bc}$  is the radius of the bubble curtain system, the coordinate  $\mathbf{r'} = (r', z')$  and  $\mathbf{r'}_s = (r'_s, z'_s)$  is in the (r-z) plane. The Green's tensor

is defined as,

$$\widehat{U}_{\alpha\beta,m}^{\Xi\Phi}(\mathbf{r}',\mathbf{r}'_s) = \frac{1}{2\pi} \int_0^{2\pi} \widetilde{U}_{\alpha\beta}^{\Xi\Phi}(\mathbf{r},\mathbf{r}_s) e^{\mathrm{i}m\theta} d\theta$$
 (6.12)

$$\widehat{T}_{\alpha\beta,m}^{\Xi\Phi}(\mathbf{r}',\mathbf{r}_s') = \frac{1}{2\pi} \int_0^{2\pi} \widetilde{T}_{\alpha\beta}^{\Xi\Phi}(\mathbf{r},\mathbf{r}_s) e^{\mathrm{i}m\theta} d\theta. \tag{6.13}$$

In view of periodicity of  $\widetilde{U}_{\alpha\beta}^{\Xi\Phi}$  and  $\widetilde{T}_{\alpha\beta}^{\Xi\Phi}$  and  $e^{\mathrm{i}k\theta}$  with the period of  $2\pi$ 

$$\widehat{U}_{\alpha\beta,m}^{\Xi\Phi}(\mathbf{r}',\mathbf{r}_s') = \bar{U}_{\alpha\beta}^{\Xi\Phi}(\mathbf{r}',\mathbf{r}_s')e^{\mathrm{i}m\theta_s}$$
(6.14)

$$\widehat{T}_{\alpha\beta,m}^{\Xi\Phi}(\mathbf{r}',\mathbf{r}'_s) = \bar{T}_{\alpha\beta}^{\Xi\Phi}(\mathbf{r}',\mathbf{r}'_s)e^{\mathrm{i}m\theta_s}$$
(6.15)

where  $\bar{U}_{\alpha\beta}^{\Xi\Phi}$  and  $\bar{T}_{\alpha\beta}^{\Xi\Phi}$  are defined as,

$$\bar{U}_{\alpha\beta}^{\Xi\Phi}(\mathbf{r}',\mathbf{r}_s') = \frac{1}{2\pi} \int_0^{2\pi} \widetilde{U}_{\alpha\beta}^{\Xi\Phi}(\mathbf{r},\mathbf{r}_s) e^{\mathrm{i}m\theta} d\theta$$
 (6.16)

$$\bar{T}_{\alpha\beta}^{\Xi\Phi}(\mathbf{r}',\mathbf{r}_s') = \frac{1}{2\pi} \int_0^{2\pi} \widetilde{T}_{\alpha\beta}^{\Xi\Phi}(\mathbf{r},\mathbf{r}_s) e^{\mathrm{i}m\theta} d\theta$$
 (6.17)

The reduced boundary integral equation (BIE) for the three-dimensional boundary conditions is obtained as [180, 181]:

$$\hat{\boldsymbol{u}}_{\alpha m}^{\Xi}(\boldsymbol{r}, z) = 
\int_{L^{f}} R_{bc} \left( \bar{U}_{\alpha r, m}^{\Xi f}(\boldsymbol{r}', \boldsymbol{r}'_{s}) \cdot \hat{p}_{m}^{*}(z_{s}) - \bar{T}_{\alpha r, m}^{\Xi f}(\boldsymbol{r}', \boldsymbol{r}'_{s}) \cdot \hat{u}_{rm}^{f*}(z_{s}) \right) dL^{f}(z_{s}) 
+ \sum_{\beta = r, \theta, z} \int_{L^{s}} R_{bc} \left( \bar{U}_{\alpha \beta, m}^{\Xi s}(\boldsymbol{r}, \boldsymbol{r}'_{s}, \omega) \cdot \hat{t}_{\beta}^{n}(z_{s}) - \bar{T}_{\alpha \beta, m}^{n, \Xi s}(\boldsymbol{r}', \boldsymbol{r}'_{s}, \omega) \cdot \hat{u}_{\beta m}(z_{s}) \right) dL_{s}^{s}(z_{s})$$
(6.18)

The angular Fourier decomposition is employed in the boundary integral equation formulation, which enables more efficient computation. The source terms are obtained by solving the vibro-acoustic model for the prediction of underwater noise from pile driving as described in [29].

#### 6.4 Sensitivity analysis

In this section, a parametric study based on the axisymmetric model is presented to examine the sensitivity of the acoustic characteristics of the air-bubble curtain system to the air volume injection rate, size of the bubble curtain, nozzle size of the hose, and DBBC configurations (see Fig. 6.5). As shown in Table 6.2, 13 scenarios are built-up by varying the nozzle spacing and size and various flow velocities due to different air injection ratio and size of the bubble curtain. The base case nozzle configuration consists of a nozzle spacing of 0.3m, a nozzle diameter of 2mm, and a flow velocity of 100m/s. To examine configurations for DBBC, three sets of analyses are performed for the varying radii of the outer BBC keeping the inner one at a fixed position, i.e., at 50m, 75m and 100m. For each configuration, three predictions are performed for the lower, upper and median values of the air flow rate.

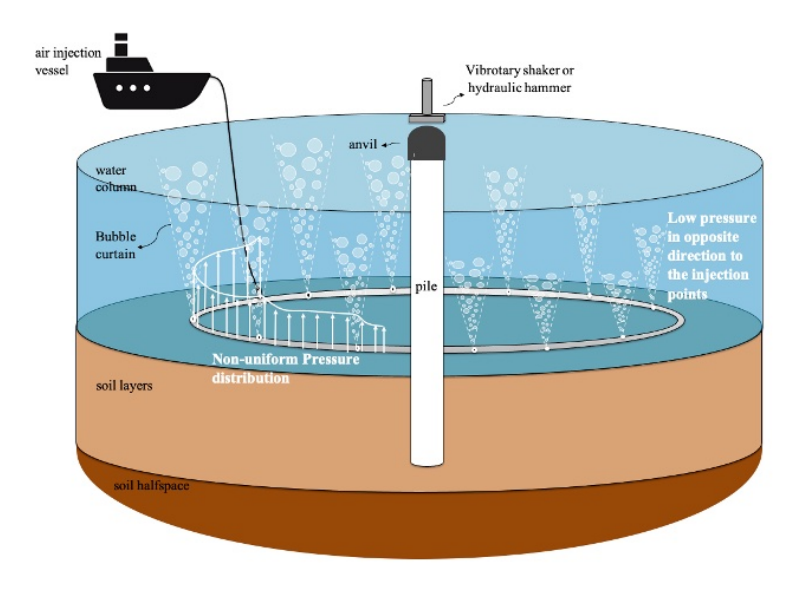


Figure 6.5: Schematic depiction of the non-uniform pressure distribution in the hose.

Table 6.2: Varying input parameters of the bubble curtain system.

Case Nr.	Varying	Value	Unit
	parameters		
1	Nozzle spacing	0.2	m
2	Nozzle spacing	0.3	m
3	Nozzle size	1	mm
4	Nozzle size	2	mm
5	Nozzle size	3	mm
6	Flow velocity	30	m/s
7	Flow velocity	50	m/s
8	Flow velocity	80	m/s
9	Flow velocity	100	m/s
10	Flow velocity	150	m/s
11	Flow velocity	200	m/s
12	Flow velocity	250	m/s
13	Flow velocity	300	m/s

# 6.4.1 Air volume injection rate

The air is injected into the perforated hose through two risers connecting to the air compressors and is distributed equally into two semi-circles. Based on this deployment approach, the model adopts equal volumetric flow rates as the input for two semi-circles of the hoses. As shown in Fig. 6.6, the increase in the air volume injection rate can lead to an increase in the flow velocity at each nozzle along half of the hose length, while the other

half has the same performance.

The air volume injection can significantly impact the bubble curtain formation characteristics along the main hose. For the bubble curtain with a radius of 75m, the variation in the flow velocity along the hose length, for a given volume injection rate, is relatively small. However, when the air volume injection is varied, differences up to  $\sim 20 \text{m/s}$  ( $\Delta u$ ) in the computed flow velocities at the nozzles are obtained. Subsequently, this can significantly change the initial kinetic energy at the nozzle and, thus, influence the air-bubble cloud formation process. The same naturally holds for bubble curtains of larger radii but those suffer additionally from a significant drop in the flow velocity at positions away from the air feeder lines.

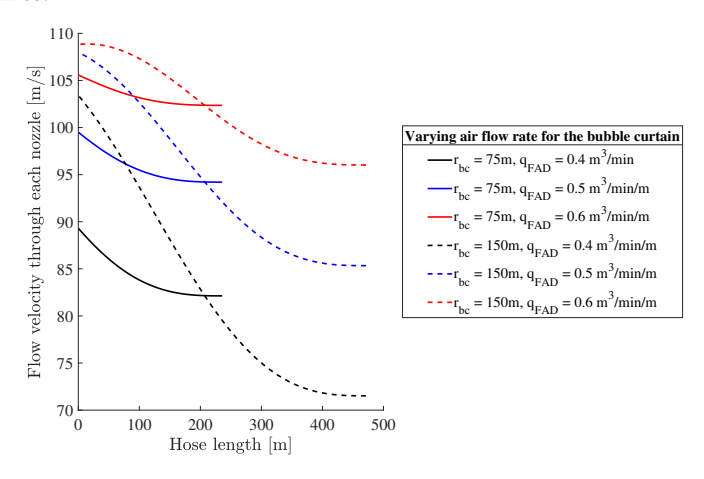


Figure 6.6: Computed flow velocities at the nozzles along the hose length for varying air volume injection rate for two different cases of bubble curtain radii, i.e. 75m and 150m.

#### 6.4.2 Size of the bubble curtain

As shown in Fig. 6.7, with the increase of the size of the BBC, the mean and lower bound of the flow velocity decreases, while the maximum of the velocity which appears in the vicinity of the air injection inlet remains within a small range. As the air is released from a nozzle, the pressure within the hose drops instantly, which leads to a decrease in the kinetic energy in the airflow. Considering the variation of the flow velocity due to both various air injection rates and the radius of the bubble curtain, the various flow velocities from 30m/s to 300m/s at the nozzle are considered in the analysis as shown in Table 6.2.

With the hydrodynamic model, the bubble formation process at the nozzle is predicted. To investigate the transmission of the bubble curtain over depth, the local distribution of the sound speed at 300Hz is depicted in Fig. 6.8. The effective wave speed reduces up to 200m/s in the vicinity of the centreline. The darker zones indicate a large impedance mismatch between the seawater and air-seawater bubbly mixture, which widens as the flow velocity increases from left to right. Accordingly, this results in an increase in the transmission loss of the bubble curtain system as shown in Fig. 6.9 from cases 6 to 13. Based on the deployed set of hoses, higher air injection rates can increase the acoustic performance of the bubble curtain. With an increase in the size of the bubble curtain, the

6.4 Sensitivity analysis 139

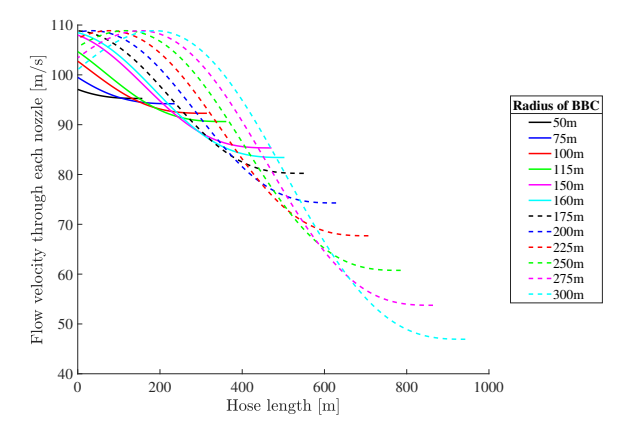


Figure 6.7: Computed flow velocities at the nozzles along the hose length for the varying radius of the bubble curtain.

efficiency of the bubble curtain can drop at positions away from the air-feeding lines due to the significant expected drop in the flow velocity.

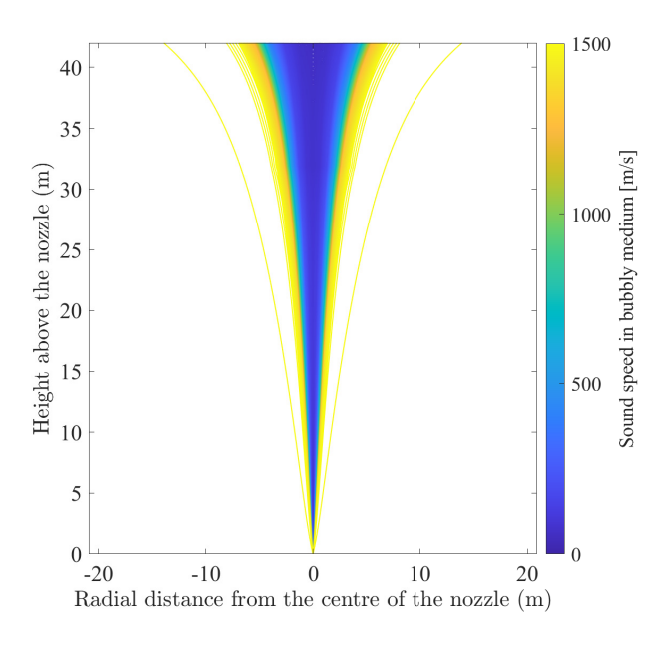
#### 6.4.3 Nozzle configuration

Typical nozzle sizes and spacing usually stay within a limited range in practice. In this analysis, a series of theoretical cases are built up. In cases 1 to 5, the nozzle configuration is investigated with the nozzle spacing being 0.2m and 0.3m and the nozzle size being 1mm to 3mm. Together with the variation in the flow velocities, the input for the varying parameters is shown in Table 6.2. To examine the impact of the aforementioned parameters on the acoustic insertion loss of the air-bubble curtain, the acoustic model is used to determine the transmission loss for each scenario. Figure 6.9 (A) indicates that, within the typical nozzle configuration range, the acoustic insertion loss of the bubble curtain is more sensitive to nozzle size when flow velocity is constant, especially in the critical frequency range of  $\sim 60Hz$  to 200Hz.

#### 6.4.4 Configuration of the DBBC

The sensitivity analysis is performed to examine the configuration of the DBBC, in which the scope of the operational constraints are considered. Three sets of the radii of the outer BBC are used, i.e., at 50m, 75m and 100m, while the inner one is at a fixed position. For each configuration, three predictions are performed for the median values of the air flow rates at the nozzle. The base case is set as the radius of the inner and outer BBC being 75m and 150m, respectively. The volumetric airflow rate in the hose is set as  $0.5 \, \mathrm{m}^3/\mathrm{min/m}$ .

As can be seen in Fig. 6.10, the noise reduction levels in both SEL and  $L_{p,pk}$  increase with the radius of the inner bubble curtain shown by the blue, red and black lines. It is also clear that given a fixed position of the inner bubble curtain, there is an optimum distance in which the outer one could be placed. This may seem as counterintuitive in the first place as one would expect that a larger distance is always favourable. However, a longer pipe can result in larger pressure and air flow velocity drops away from the air-feeding lines



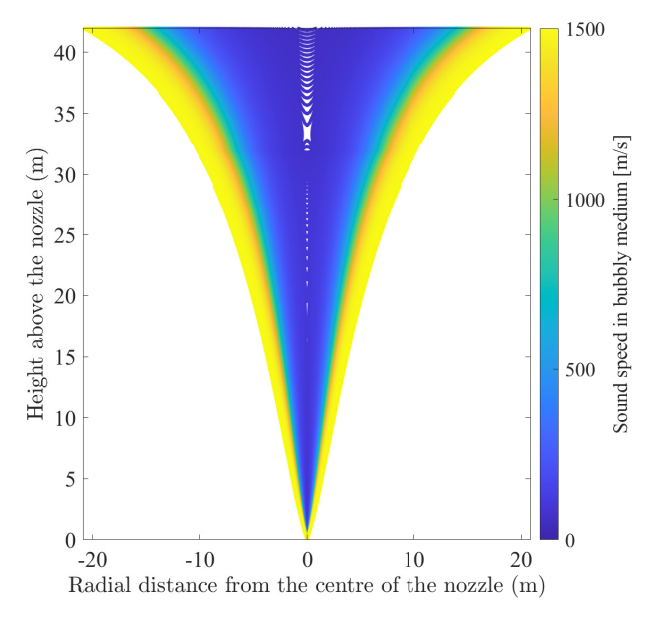


Figure 6.8: Comparison of the effective wave speed for various flow velocities of (top) 30m/s, (bottom) 300m/s for the frequency 300Hz.

which result in a suboptimal performance of the system on average.

The red and blue markers indicate the configuration of the base case with the volumetric

6.4 Sensitivity analysis 141

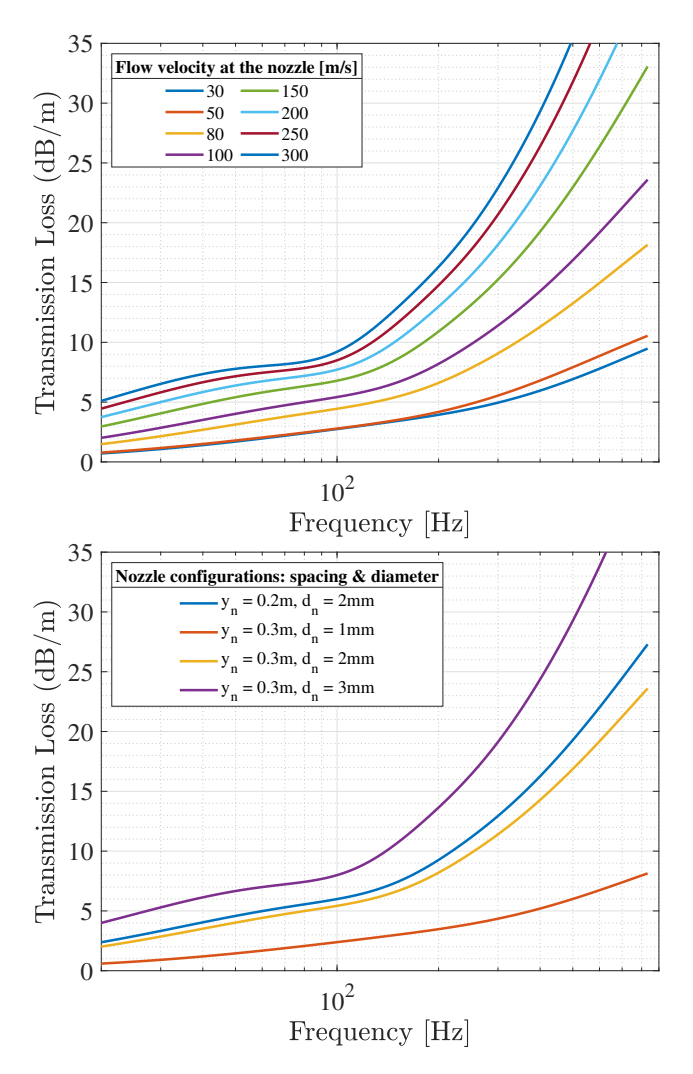


Figure 6.9: Transmission loss (TL) computed as a function of frequency for the cases examined in Table 6.2. Various nozzle configurations: spacing and diameter (top). Flow velocity at the nozzle (bottom).

airflow rate being 0.4 and 0.6m³/min/m, respectively. The bars and the marker indicate the predictions are performed for the same configuration and at the lower, higher and median values of the air flow rates at the nozzle using axisymmetric model. The comparison indicates that the increase in the mass flow rate by  $0.1\text{m}^3/\text{min/m}$  in the hose can lead to up to ~1dB for both SEL and  $L_{p,pk}$ . However, the increase in the noise level cannot be obtained linearly from the volumetric airflow rate being  $0.4\text{m}^3/\text{min/m}$  to  $0.5\text{m}^3/\text{min/m}$  or  $0.5\text{m}^3/\text{min/m}$ . As discussed in section 6.1.3, the pressure increases with the mass airflow rate, which leads to the nonlinear acoustic characteristics of the bubble curtain with increasing air flow rates. By comparing the noise levels for the lower, median

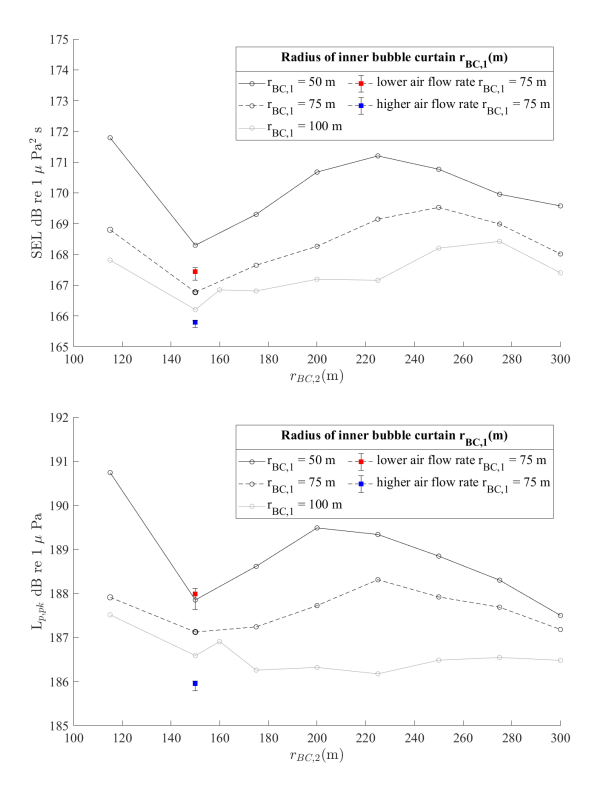


Figure 6.10: OWF foundation: comparison of the sound pressure levels for varying diameter of the outer bubble curtain with the radius of the inner bubble curtain being 50m (black line), 75m (red line) and 100m (blue line). SEL (top).  $L_{p,pk}$  (bottom). Sound levels are given at 750m from the centre axis of the pile and at 2m above the seabed surface.

and higher values of the air flow rates at the nozzle, a deviation of 1 dB can be expected as can be read from Fig. 6.10. As observed from the field test, the pressure decreases nonlinearly with the distance between the sensor and the air feeding point, which leads to the variation in the airflow at the nozzle. The performance of the air-bubble curtain system relies strongly on both the volumetric airflow rates and the geometrical configuration of the DBBC.

#### 6.4.5 Summary of the analysis

Due to the uneven distribution of the air flow velocity along the main hose, the acoustic insertion loss of the air-bubble curtain depends strongly on the air injection rate and the size of the bubble curtain. Within the critical frequency spectrum of interest in this project, the nozzle size and spacing seem to have less impact on the acoustic performance of the bubble curtain. However, the flow velocity through each nozzle can drop significantly away from the air-feeding points especially for longer pipes. This, in turn, can result in a strong azimuth-dependent acoustic field, i.e., the noise reduction achieved at different azimuthal positions may vary significantly due to the inhomogeneous air-bubble cloud

#### 6.5 VALIDATION

In this section, the case examined is based on an offshore wind farm (OWF) foundation installation campaign in 2018 [29, 68]. The material properties and the geometry of the model are summarised in Table 6.3. The forcing function is defined as the smoothed exponential impulse as shown in Fig. 6.11 (A), which results in approximately 2000kJ input energy into the pile. The seabed at this foundation consists of a thin marine sediment layer overlaying a stiff bottom soil half-space. The configuration of the DBBC system is presented in Table 6.4. The inner bubble curtain is positioned at 105m from the pile and the outer bubble curtain is positioned at 145m from the pile.

#### 6.5.1 Axisymmetric model

The validation study for the cylindrically symmetric noise prediction model is examined first to ensure the model's accuracy in predicting sound propagation. This validation case involves comparing the model's predictions with field data from OWF foundation installation.

The variation in the flow velocity through the nozzles is shown in Fig. 6.11 (top), which is due to the drop of the pressure during the transportation of the air. In Fig. 6.12 (bottom), the evolution of the pressure field in time is shown for the point positioned 2m above the seabed at 750m radial distances from the pile. The arrival of the pressure cones at around 0.5s after the impact of the pile is in line with the expectations regarding the arrival time of the direct sound waves travelling with the speed of sound in the water at the distance of 750m from the pile. As can be seen in the one-third octave band for both the unmitigated (the black line) and mitigated (the grey line) fields in Fig. 6.12 (top), the performance of the bubble curtain is more efficient at higher frequency bands approximately above 500Hz.

The overall SEL and  $L_{p,pk}$  for both unmitigated and mitigated fields are summarised in Table 6.5. The zero-to-peak pressure level ( $L_{p,pk}$ ) in dB re 1  $\mu$ Pa and the sound exposure level SEL in units of dB re 1  $\mu$ Pa²s are defined as:

$$L_{p,pk} = 20 \log \left( \frac{\max |p(t)|}{p_0} \right), \quad \text{SEL} = 10 \log \left( \frac{1}{T_0} \int_{T_1}^{T_2} \frac{p^2(t)}{p_0^2} dt \right)$$
(6.19)

in which  $T_1$  and  $T_2$  are the starting and ending of the predicted time signature with the

Table 6.3: Basic input parameters for the validation case.

Parameter	Pile	Parameter	Fluid	Marine sediment	Bottom soil
Length [m]	75	Depth [m]	40.1	1.5	∞
Density [kg/m³]	7850	Density [kg/m <sup>3</sup> ]	1000	1621.5	1937.74
Outer diameter [m]	8	$c_L$ [m/s]	1500	1603	1852
Wall thickness [mm]	90	$c_T$ [m/s]	-	82	362
The penetration depth [m]	30.5	$\alpha_p [dB/\lambda]$	-	0.91	0.88
Maximum Blow Energy [kJ]	2150	$\alpha_s [dB/\lambda]$	-	1.86	2.77

6

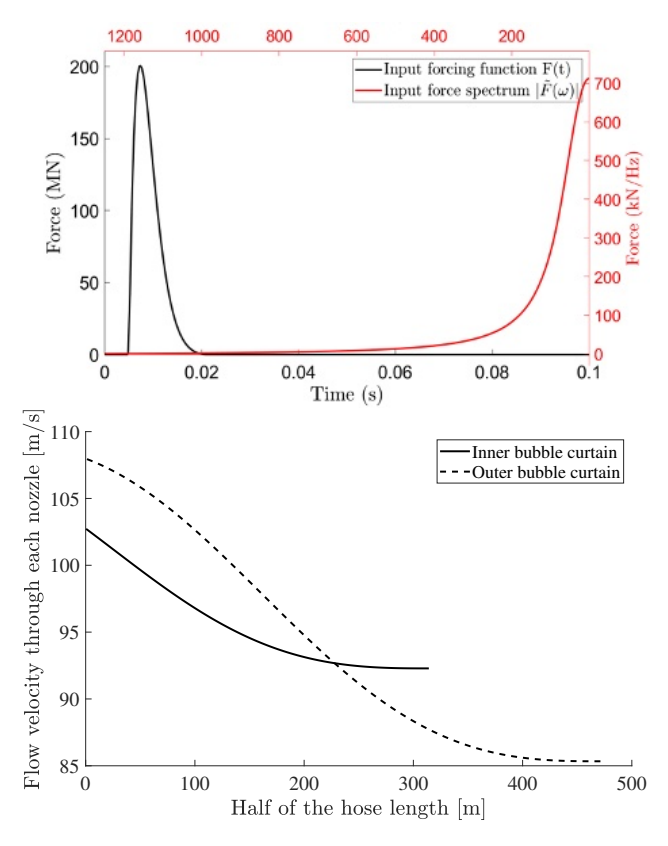


Figure 6.11: OWF foundation: (top) input forcing function in time and frequency domain; (bottom) flow velocity through each nozzle along the hose with the solid line indicating the air flow at the inner BBC and the dash line being the outer one.

Table 6.4: Basic input parameters of the air-bubble curtain system.

Parameter	Value
location of the inner bubble curtain $r_{bc}$ [m]	105
location of the outer bubble curtain $r_{bc}$ [m]	145
Nozzle diameter $d_n$ [mm]	1.5
Nozzle spacing $y_n$ [m]	0.30
Air flow rate $q_{FAD}$ [m <sup>3</sup> /min/m]	0.5
Spreading coefficient $\lambda$ [-]	0.1

sound event in between and pulse duration  $T_0 = T_2 - T_1$  being 1 second and  $p_0 = 10^{-6} Pa$  is the reference underwater sound pressure.

The sound field without noise mitigation systems is predicted by the model developed in [29]. The prediction lies within the accuracy of the measurement equipment of the deviation within 1 or 2dB from the measured sound levels. The measured sound levels

6.5 Validation 145

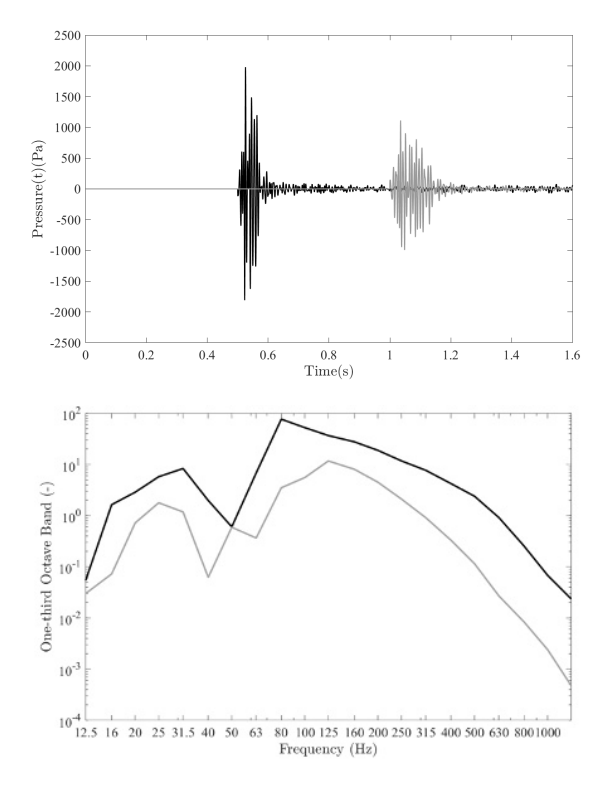


Figure 6.12: OWF foundation: (top) evolution of the pressure field for the mitigated field with the use of DBBC system at 750m (black line) and 1500m (grey line) from the pile; (bottom) one-third octave band of the pressure field at 750m for both unmitigated field (black line) and mitigated field (grey line).

Table 6.5: Noise mitigation assessment at the foundation. All values are given at a distance of 750m and 1500m from the pile. SEL are given in the unit of dB re  $1\mu$   $Pa^2$ s and  $L_{p,pk}$  in the unit of dB re  $1\mu$  Pa.

Scenarios @750m	SEL	$\mathbf{L}_{p,pk}$
Noise prediction for the unmitigated field	182	201
Noise prediction for the mitigated field with DBBC system	$166 \pm 1$	$185 \pm 1$
Measurement sound levels	165 168	184 187
Modelled noise reduction $\Delta_s$	$15 \pm 1$	$15\pm1$
Measured noise reduction $\Delta_m$	14 ~17	14 ~17
Scenarios @1500m	SEL	$\mathbf{L}_{p,pk}$
Scenarios @1500m  Noise prediction for the unmitigated field	<b>SEL</b> 178	$\frac{\mathbf{L}_{p,pk}}{196}$
Noise prediction for the unmitigated field	178	196
Noise prediction for the unmitigated field Noise prediction for the mitigated field with DBBC system	178 164±1	196 181±1

indicate a range of 14 to 17dB noise reduction at 750m achieved by the DBBC system for both SEL and  $L_{p,pk}$ . At a further distance, the 1500m away from the pile, the noise reduction of 14 to 15dB can be achieved for SEL and 11 dB for  $L_{p,pk}$ . The modelling of the DBBC system showed an average noise reduction of 15dB for both SEL and  $L_{p,pk}$  at 750m, and 14dB for SEL and 15dB for  $L_{p,pk}$  at 1500m. Due to variations in flow velocity through the nozzle at different azimuthal directions, a deviation of  $\pm 1$ dB in the noise reduction levels can be expected. The upper and lower bounds of the sound levels show that the range of prediction is within the measured data range, which indicates a great agreement between the noise prediction and the measured data at various horizontal distances from the pile, and verifies the validity of the complete model.

#### 6.5.2 THREE-DIMENSIONAL MODEL

To examine the maximum noise reduction potential and the influence of a gap in the azimuthal direction of the air-bubble curtain, the following two scenarios are considered by using the three-dimensional model:

- *scenario 1* elimination of the water-borne path at the position of the air-bubble curtain leaving the propagation of the waves through the soil unaffected;
- scenario 2 same as scenario 1, but with an additional gap throughout the seawater column, in which noise presumably leaks due to the malfunctioning of the air-bubble curtain.

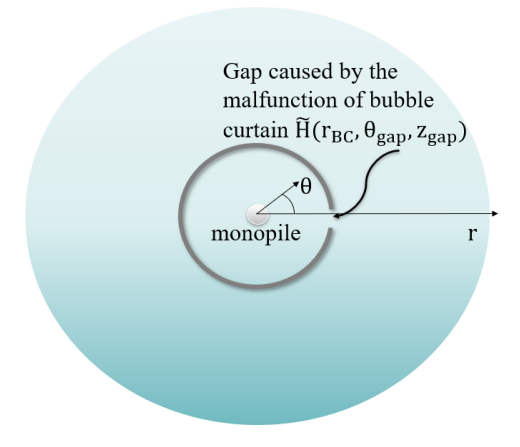


Figure 6.13: Schematic depiction for the gap in the ideal noise barrier caused by the malfunction of the noise mitigation system.

Similarly to the discussion in the section 5.5.1, in *scenario 1*,the noise sources in the water column are completely eliminated while the waves emitted from the soil source propagate in the exterior domain, representing an ideal noise blockage in the water column. The *scenario 2* includes an additional gap, as illustrated in Fig. 6.13. This gap is incorporated into the model to simulate the impact of a malfunctioning air-bubble curtain. The transfer function accounting for this gap is detailed in Fig. 2.23 in the section 2.4.4 in the azimuthal

6.6 Conclusions 147

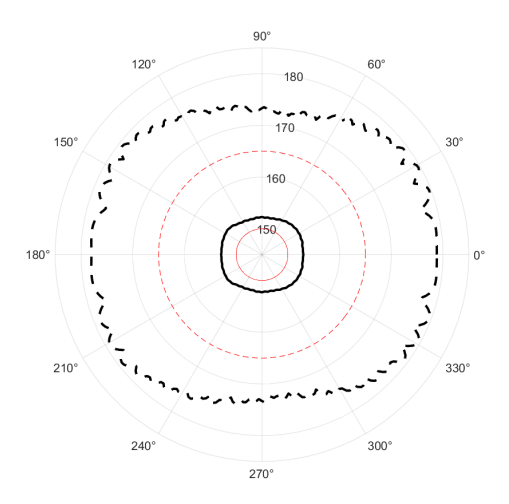


Figure 6.14: Azimuthal dependent SEL and  $L_{p,pk}$  for partially blockage of the water borne path with a thin gap over the entire water depth: the red solid line indicates the SEL and the red dashed line reads the  $L_{p,pk}$  for the fully blockage of the water borne transmission path; the black solid and dashed lines are SEL and  $L_{p,pk}$  for partially blockage case.

direction. The *scenario 2* simulates real-world imperfections that might lead to noise leakage. The comparison between the two scenarios provides insight into the curtain's noise reduction potential and how sensitive it is to any malfunctions of the bubble curtain. The problem is solved using a three-dimensional acousto-elastic boundary integral formulation, as discussed in section 6.6. The maximum noise reduction potential is determined by comparing the difference between the results from the unmitigated sound field and the one from *scenario 1*. The difference between the *scenario 1* and *scenario 2* allows for an examination of the influence of the gap in the air-bubble curtain.

As shown in Fig. 6.14, modelling perfect noise mitigation at the position of the outer bubble curtain results in maximum noise reduction levels of 32 dB for SEL and 36 dB for  $L_{p,pk}$ . When a gap in the bubble curtain exists, the SEL deviates by up to 1 dB at a receiver positioned at  $\theta=0^\circ$  and by up to 6 dB for  $L_{p,pk}$ . The variation of  $L_{p,pk}$  in the azimuthal direction is much larger, while the variation in SEL is less significant. Since most of the energy is channelled through the seabed, the influence of a small gap over the water depth is less critical, leading to an increase of 2 to 3 dB in SEL.

#### 6.6 Conclusions

This chapter presents a multi-physics model for modelling the noise emission for offshore pile driving with the use of a DBBC system. The mathematical statement of the complete problem is given and the adopted method of solution is described for each module. The compressible flow model is developed to predict the operational parameters for bubble curtain generation from the hose and the nozzle. Nonlinear characteristics of the pressure distribution are observed both in the model results and in the field test. The pressure

amplitude increases with volumetric airflow rates and decreases with the distance from the air injection point. The field test reveals the inherent variation in the airflow circulation, which leads to the varying performance of air-bubble curtain in azimuth direction. The hydrodynamic model aims to capture the fluid and bubble dynamic properties during the development of bubble curtains. The transmission coefficients derived from the acoustic module are coupled to the existing noise prediction model for the unmitigated field from pile driving. The sensitivity study has been performed to examine the critical parameters for the performance of the air-bubble curtain system. Both volumetric airflow rates and the configuration of the DBBC play significant roles in the efficiency of the air bubble curtain system. Results are presented for an offshore pile installation campaign in the German North Sea. The comparison between the measured data and model predictions provides the validation case of the model. The modelling approach couples four sub-modules and facilitates more accurate representation of the noise mitigation system. The multi-physics model allows for the examination of the optimal hose-nozzle and DBBC configurations under the operational constraints.

With the use of a multi-physics model for each subsystem, a three-dimensional boundary integral formulation is developed for the solution of the three-dimensional coupled vibro-acoustic problem in offshore pile driving. The developed model allows to examine the performance of the air-bubble curtains that can vary significantly in azimuth due to the inherent variations in the airflow circulation through the perforated pipes positioned on the seabed surface or other environmental conditions. The ideal perfect noise blockage is examined for an offshore pile driving, which provides the maximum noise reduction potential. When a small gap is included through the BIE, it leads to a deviation of up to 1 dB for SEL and 6 dB for  $L_{p,pk}$  as compared to the fully-blockage case. The measured levels indicate there is up to 3 dB variation in azimuth during the installation with the use of DBBC system. To further investigate this phenomenon, the insertion loss of the bubble curtain system should be calculated based on the configuration of the system. The proposed formulation can be further implemented for arbitrary boundary conditions including three-dimensional wave field from pile driving or transmission losses varying in the circumference.

# SOUND MAPS FOR IMPACT PILE DRIVING

The installation of foundation piles in offshore wind using traditional hydraulic impact hammers raises concerns about the impact of underwater noise on marine life. To address this issue, the offshore wind industry investigates noise mitigation techniques, such as air bubble curtain system, hydro-sound damper system and other resonator-based noise mitigation systems, to reduce sound levels and expedite installation. Modelling underwater noise requires various approaches for sound propagation in the vicinity of the pile and sound propagation at large distance with varying bathymetry. A modelling framework for propagating the underwater sound in a range-dependent environment is introduced in this Chapter. Sound maps can be used for regulators and other experts to assess the noise impact on the environment.

 $\mathbf{W}$  ith more offshore wind farms being constructed at greater water depths, the impact of anthropogenic noise is escalating due to the increased number of offshore foundations for wind turbines. To ensure the sustainability of offshore wind energy, underwater noise generated during pile installation is monitored and regulated. Various noise mitigation systems are implemented to lessen the impact of impulsive noise. Regulatory bodies impose standards, particularly in Germany, focusing on dual sound metrics such as SEL<sub>05</sub> and L<sub>p,pk</sub> at a given distance from the pile [36]. Environmental impact assessments are mandatory before offshore foundation construction to minimize threats to marine and other species [6]. These assessments require evaluation not only of dual sound metrics within 750m of the pile but also of sound impact across broader areas, necessitating the generation of sound maps indicating noise impact on habitats of resident species. Assessment typically involves evaluating various sound sources, including shipping noise, seismic airgun noise, and other anthropogenic noise [183]. Quantitative assessment of sound exposure thresholds informs impact studies, which often focus on evaluation of species quantities within effect zones and cumulative exposure to successive pile driving events. While acoustic modelling for shipping noise and seismic airguns is well-developed, focus on pile driving noise and its spatial propagation in the ocean environment is limited.

Noise modelling for environmental impact assessments often employs simplified models because most noise sources are situated in the water column or below the sea surface [184, 185]. For modelling offshore pile driving noise, simplified models like cylindrical spreading models are common for evaluating marine species' effect zones [81]. Other models based on parabolic equation and wavenumber integration approach often approximate the seabed as an equivalent fluid medium [161, 186, 187]. However, these models lack accuracy when specific soil conditions need to be considered or when the majority of the energy is radiated in the soil in the form of elastic wave as is the case in pile driving operations. Detailed modelling of the seabed, which involves considering both shear and compressional waves, is often disregarded in shipping and airgun noise models because the acoustic sources are located in the seawater column. These models typically treat the seabed as an equivalent fluid. However, this modelling assumption is usually inadequate for impact pile driving, where a significant amount of energy is radiated from the pile embedded into the seabed to a considerable depth.

This chapter introduces a methodology to create sound maps in the case of impact piling including mitigation and considering the complex nature of the sound generation mechanism introduced in earlier chapters. The model consists of sub-models, including source field generation and sound propagation in range-dependent shallow water environments. The sound source model utilizes a three-dimensional axisymmetric pile-soil-water model for impact pile installation in layered media, as described in Chapter 3. Modelling approaches for mitigating the field using air bubble curtain systems are described in Chapter 6. The sound propagation model used for generating sound maps is a normal mode model designed to simulate propagation loss in range-dependent acousto-elastic half spaces with varying bathymetry. This chapter concludes with a theoretical case study of underwater noise emission from an impact pile installation in the North Sea with and without the use of an air-bubble curtain system. Numerical simulations employing the adopted modelling framework can be utilized by marine biologists to assess the environmental impact of underwater sound on marine species.

7.1 Model description 151

# 7.1 Model description

The ocean environment including the pile driving noise sources with and without the use of noise mitigation systems is depicted in Fig. 7.1. Complex environmental conditions, i.e. currents, surface waves, geographical configurations, and varying bathymetry, often impact sound propagation and the efficacy of various noise mitigation systems employed in offshore pile driving. By subdividing the modelling approach into subsystems, a more detailed noise generation model can be employed in the vicinity of the noise source, where range-dependence is less dominant, and the domain can be modelled as a horizontally stratified acousto-elastic half space. For large-range sound propagation modelling, due to the spatial scale of the model, the normal mode model adopts the adiabatic approximation for range dependency. Other approaches such as the mode-flux theory and wavenumber integration approaches, though not discussed here, can be adopted as alternative approaches for modelling the propagation loss when layered elastic properties can be disregarded, especially when considering higher frequencies.

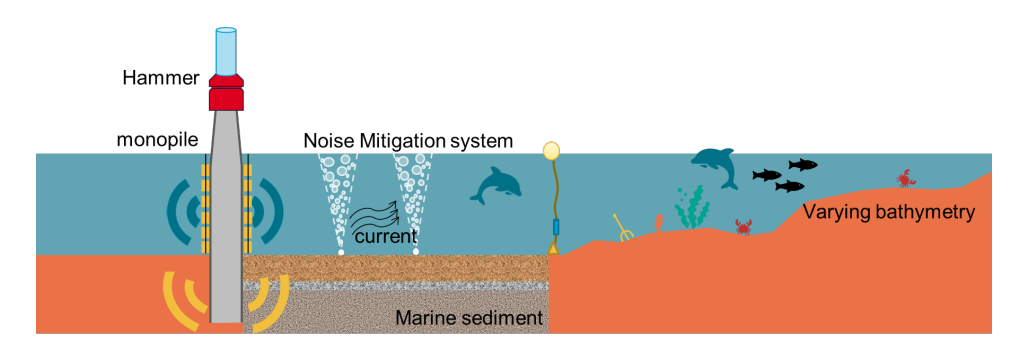


Figure 7.1: Schematic plot for range-dependent ocean environment, where it consists of multiple sound sources, marine life, seawater, marine sediment and sound recording system. © Delft Cymatics.

The primary objective of environmental impact assessment is to determine the received noise level (RL) based on the sound source level (SL) and propagation loss level (PL). The relationship between the two is expressed as follows [183, 188, 189]:

$$RL = SL - PL \tag{7.1}$$

Thus, a multi-model approach is typically necessary to separately model the noise source and sound propagation, as indicated in the adopted approach in Fig. 7.2. In Section 7.2, the modelling approach for the sound source level (SL) is outlined, including the transformation of the sound source level for both fluid and soil sources. In Section 7.3, the normal-mode propagation modelling approach is utilized to determine propagation losses (PL), providing a description for the range-dependent environment in the far field. In Section 7.4, a case study is conducted to generate sound maps based on an offshore wind farm in the North Sea. The main conclusions of this chapter are presented in Section 7.5.

#### 7.2 Sound source modelling

A semi-analytical model is used for evaluating the noise emission from the impact pile driving with or without the use of the air-bubble curtain system. The dynamic response of coupled system, consisting of the shell structure and the acousto-elastic media, is solved first through the noise generation module in the vicinity of the pile as described in Chapter 3. A set of the response functions in terms of pressure, velocity, displacement and stress tensors are obtained as input for the sound propagation model to propagate the wave field at larger distances as discussed in section 3.3.

The input to the sound propagation module is provided by the sound generation module through a boundary integral formulation [109, 115]. The solution of the acousto-elastic wavefield employs Somigliana's identity in elastodynamics and Green's third identity in potential theory [115, 116]. The velocity, displacement and pressure/stresses on the cylindrical boundary surface  $r = r_s$  are obtained from the sound generation module. The cylindrical surface in both the fluid and the soil domains need to be discretized when employing the direct BEM associated with the acousto-elastic layered half-space Green's functions. The boundary integral equation formulated in the three-dimensional case is given as:

$$\tilde{\boldsymbol{u}}_{\alpha}^{\Xi} = \int_{S^{f}} \left( \widetilde{U}_{\alpha r}^{\Xi f}(\boldsymbol{r}, \boldsymbol{r}_{s}) \cdot \widetilde{p}(\boldsymbol{r}_{s}) \widetilde{H}(\boldsymbol{r}_{s}) - \widetilde{T}_{\alpha r}^{\Xi f}(\boldsymbol{r}, \boldsymbol{r}_{s}) \cdot \widetilde{u}_{r}^{f}(\boldsymbol{r}_{s}) \widetilde{H}(\boldsymbol{r}_{s}) \right) dS^{f}(\boldsymbol{r}_{BC})$$

$$+ \sum_{\beta = r, \theta, z} \int_{S^{s}} \left( \widetilde{U}_{\alpha \beta}^{\Xi s}(\boldsymbol{r}, \boldsymbol{r}_{s}, \omega) \cdot \widetilde{t}_{\beta}^{n}(\boldsymbol{r}_{s}) - \widetilde{T}_{\alpha \beta}^{n, \Xi s}(\boldsymbol{r}, \boldsymbol{r}_{s}, \omega) \cdot \widetilde{u}_{\beta}(\boldsymbol{r}_{s}) \right) dS_{s}^{s}(\boldsymbol{r}_{BC})$$

$$(7.2)$$

in which  $\tilde{H}(\boldsymbol{r}_s)$  is the angular dependent transmission coefficient of the bubble curtain. In the case of unmitigated sound field,  $\tilde{H}(\boldsymbol{r}_s)=1$ . The displacements and stresses/pressure on the cylindrical surface at  $\boldsymbol{r}=\boldsymbol{r}_s$ ,  $\tilde{u}_r^f(\boldsymbol{r}_s)$ ,  $\tilde{p}(\boldsymbol{r}_s)$ ,  $\tilde{t}_{\beta}^n(\boldsymbol{r}_s)$ ,  $\tilde{u}_{\beta}(\boldsymbol{r}_s)$ , are the source terms obtained from the noise prediction module generating the non-mitigated field from pile driving [29]. The solution allows for solving the dynamic problem in an axisymmetric acousto-elastic medium with non-axiymmetric sources at the position of the bubble curtain. The angular Fourier decomposition is employed in the boundary integral equation formulation, which enable the acceleration of computation. The complete modelling chain for the derivation of the transfer function  $\tilde{H}(\boldsymbol{r}_s)$  of the bubble curtain has been described in Chapter 6.

# 7.3 SOUND PROPAGATION IN RANGE-DEPENDENT ENVIRON-MENTS

A crucial aspect involves appropriately assessing the soundscape by modelling the spatial and spectral distribution of sound radiated during pile driving. Predicting the Sound Exposure Level (SEL) from pile-driving activities necessitates intensive computations for multiple sources and receiver points across a broad frequency band, accounting for the hearing range and swimming depths of marine animals. To propagate the wave field at larger distances, up to hundreds of kilometres away from the noise sources, a detailed modelling approach is often required to capture variations in bathymetry, sediment properties, and wave speeds in range-dependent environments. Various modelling approaches, such as normal mode methods (NM) [190], parabolic equation approaches [186, 187], wavenumber

integration methods (WNI) [116], ray tracing [191], and energy flux approaches [122, 192], have been applied in long-range sound propagation studies [193]. Depending on prevailing environmental conditions and the frequency range of interest, different approaches are preferred. In recent decades, propagation models have been commonly applied to analyse shipping noise, seismic airgun noise, and predict sound from sonars. With the growing demand for renewable energies, pile driving noise has begun to contribute to the soundscape, necessitating specific tailored approaches for modelling long-range sound propagation, particularly for low-frequency waves and sources embedded in the seabed. These factors trigger more energy exchange and interaction with the sediment.

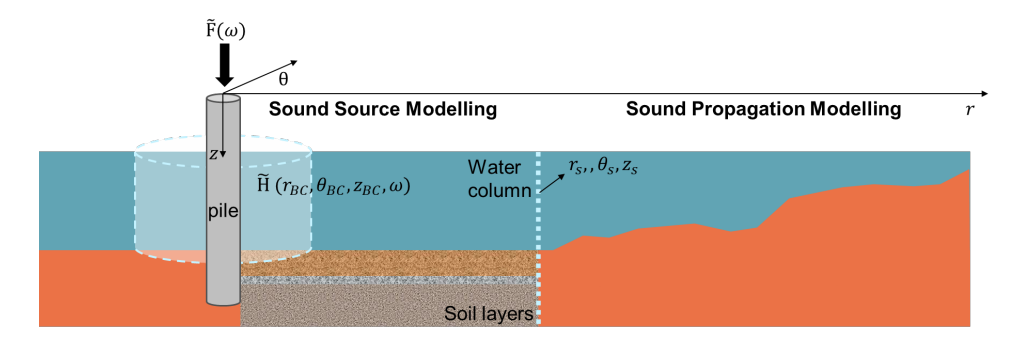


Figure 7.2: Geometry of the model for the simulation of the pile-driving noise: 1) noise generation model aiming at the sound source; 2) sound propagation model focuses on the coupling of the sound source model to the range-dependent propagating model.

In this section, a sound propagation model based on a normal mode approach in the range-dependent offshore environment is utilized to propagate the wave field generated from the detailed noise source model up to 750m away from the pile. This model describes the elastic properties of the seabed, allowing for the capture of energy emitted in the sediment layers. With the application of noise mitigation systems, such as air bubble curtain systems, this effect becomes significant, as a large amount of energy can tunnel under the air-bubble curtain and leak back into the water column.

As illustrated in Fig. 7.2, the sound source model generates fluid and soil sources at the cylindrical surface  $\mathbf{r} = \mathbf{r}_s$  up to a closer radial distance from the pile, where the sound propagation model is coupled to the noise generation model. The sound sources in both the fluid and sediment are computed by the sound source model, which determines the amplitude of the pressure sources and the soil volumetric source at the coupling distance from the pile. This coupling depth encompasses the entire water column and extends to a certain depth below the penetration depth of the pile to ensure convergence of the result.

As discussed in Chapter 3, the direct Boundary Element Method (BEM) is often used to accurately propagate fluid and soil sources to the exterior field. However, the Green's function used in this approach is applicable to stratified fluid and elastic media. To propagate the wave field in a range-dependent environment, different solutions are required, as the analytical solution discussed in Chapter 2, which involves wavenumber integration, cannot be directly employed. Models such as coupled normal mode (NM), adiabatic mode approximation, and Parabolic Equation (PE) models are most practical for solving sound

propagation in range-dependent bathymetry [161]. However, the range-dependent NM and PE solutions are computationally intensive. The solutions have been widely applied for underwater sound propagation when the source is solely located within the water column.

To overcome computational problems in shallow waters, mode-flux model and adiabatic NM model (KRAKEN) are both essential tools to model sound propagation. The energy flux model brings together the accuracy of the adiabatic range-dependent normal mode and the speed of Weston's flux theories for the shallow water propagation problems [194]. As a hybrid method based on the normal mode and flux theories[122], the model considers the bathymetric variations, range-dependent sediment properties, the sea surface and seabed influences. The accuracy of the model is verified against a detailed multi-model comparison based on the propagation loss calculations of various methods (adiabatic mode theory, coupled modes, ray tracing, parabolic equation, and flux theory) [122] and compared with the measurements for the shipping [192] and explosions [195].

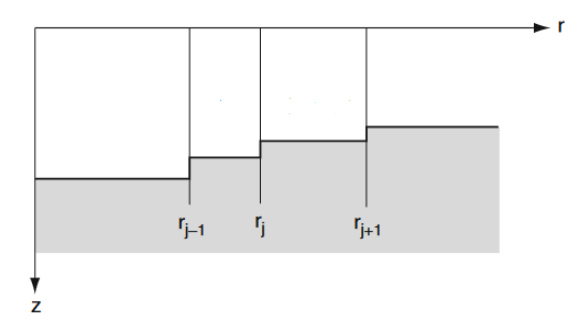


Figure 7.3: Example of range segmentation for the coupled-mode formulation in KRAKEN [161].

The normal mode model used in this chapter is based on KRAKENC [190], including the elastic properties of the sediments and adiabatic approximation for the range dependency. KRAKEN as depicted in Fig. 7.3 is a normal mode program designed for range-varying underwater acoustic environments. KRAKENC is an extended version of KRAKEN that calculates complex eigenvalues, enabling the computation of leaky modes and accounting for material attenuation in elastic media. The results generated by the KRAKEN model provide a field represented as an array, considering a specified range and a series of source depths. The adiabatic approximation was initially introduced by Pierce in [196], with the derivation of the solution further detailed in [190, 197, 198]. This approximation, used in the KRAKENC model, assumes that there is no transfer of energy between different modes, allowing the contributions of partially coupled matrices to be neglected. This simplification significantly reduces computational costs.

To characterize the noise sources generated from pile driving, particularly when a pile is embedded to a significant depth in marine sediment, it is essential to accurately model the sources in both fluid and elastic media due to the substantial energy exchange between the water column and seabed. With the source modelling discussed in section 7.2, the pressure and velocity fields in the water column and the stress and displacement fields in the sediment can be obtained. In the fluid domain, the amplitude of the noise sources is characterized by the pressure as shown in Eq. (7.3). In the sediment, where both

compressional and shear waves exist, the source amplitude must be properly quantified. The stress tensor in the elastic medium can be expressed as the sum of a volumetric stress tensor and a deviatoric component. The volumetric stress tensor can be considered as the equivalent pressure in the elastic medium and is used in this analysis to quantify the amplitudes of the soil source as shown in Eq. (7.4).

The volumetric source level at  $r = r_s$  in both the water column and the soil domain is defined as follows:

$$\tilde{P}_f(z_i, \theta_n, \omega) = \tilde{p}_f(r_s, \theta_s, z_s, \omega), \quad i = 1, ..., N_f; n = 1, ..., N_{\theta}$$
 (7.3)

$$\tilde{P}_s(z_j,\theta_n,\omega) = -K\nabla^2 \tilde{\phi}(r_s,\theta_s,z_s,\omega) = -(\lambda + \frac{2}{3}\mu)\nabla \tilde{u}_s(r_s,\theta_s,z_s,\omega), \quad j=1,...,N_s; n=1,...,N_\theta$$
(7.4)

In which  $N_f$  and  $N_s$  indicate the total number of sources in fluid and soil, respectively. The pressure  $\tilde{p}_f$  in the water column and the displacement tensors in the soil are obtained from the noise generation model through a boundary element integration as presented in Eq. (7.2). The source level for each fluid and soil source is defined as follows:

$$SL_{f,\theta_{n},j} = 10\log_{10}\left(\frac{|\tilde{P}_{f}(z_{i},\theta_{n},\omega)|^{2}}{\tilde{p}_{ref}^{2}}\right), \quad i = 1,...,N_{f}; \quad n = 1,...,N_{\theta}$$
 (7.5)

$$SL_{s,\theta_{n},j} = 10\log_{10}\left(\frac{|\tilde{P}_{f}(z_{j},\theta_{n},\omega)|^{2}}{\tilde{p}_{ref}^{2}}\right), \quad j = 1,...,N_{s}; \quad n = 1,...,N_{\theta}$$
 (7.6)

For each source, the sound propagation model is conducted within an angular slice, assuming no energy channelling between different slices. This assumption is valid when there is no substantial energy exchange in the azimuthal direction, such as when the transitions between slices are relatively smooth. The source level definition also eliminates phase information, as only energy is propagated. Since acoustic modelling is performed over large distances, the influence of phase differences between the sources is insignificant compared to the amplitude due to the energy carried by the waves.

The received sound level is then given by  $(\xi = f, s)$ ,

$$RL_{\xi,r,z,\theta_n} = SL_{\xi,\theta_n,j} - PL_{\xi,r,z,\theta_n,j}, \quad n = 1,...,N_{\theta}$$
(7.7)

The final received sound level is the sum of all sources as,

$$RL_{r,z,\theta_n} = 10\log_{10} \sum_{\xi}^{N_f + N_s} 10^{\frac{RL_{\xi,r,z,\theta_n}}{10}}, \quad n = 1, ..., N_{\theta}$$
 (7.8)

The broad-band SEL can be expressed by the summation of received sound levels from all frequency of interest,

$$SEL(r, z, \theta_n) = 10 \log_{10} \sum_{\omega_c}^{N_f} 10^{\frac{RL_{r, z, \theta_n}(\omega)}{10}}, \quad n = 1, ..., N_{\theta}$$
 (7.9)

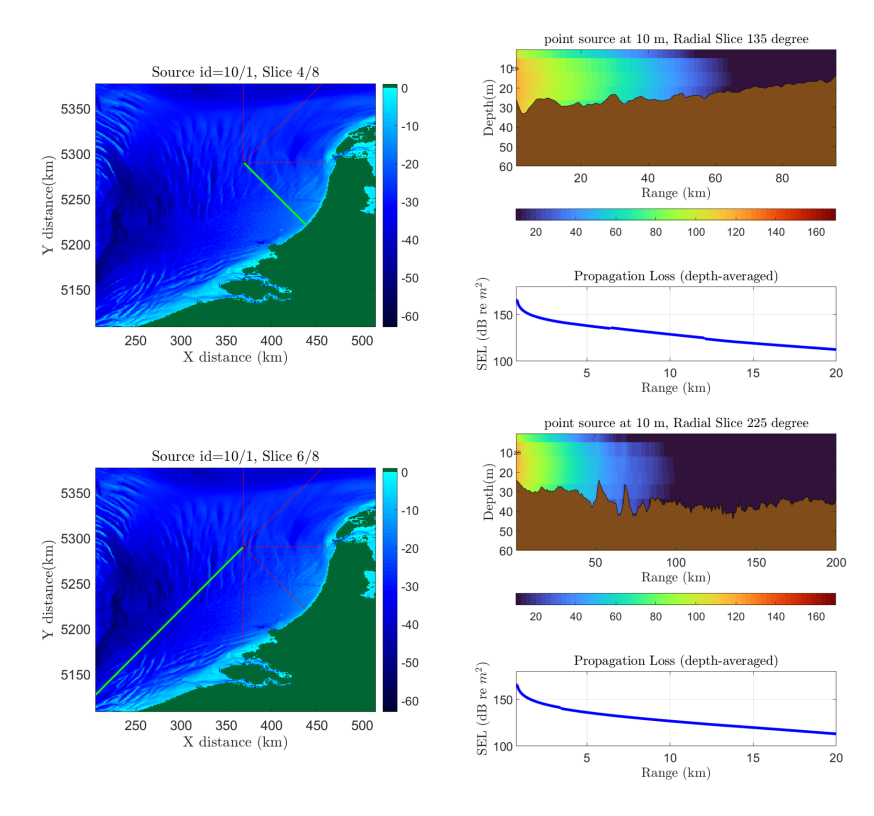


Figure 7.4: The radial slicing of bathymetry as input of sound mapping (on the left panel). Selected water depth profiles from the same area (on the right panel). Propagation losses obtained for the configuration with the fluid source positioned at 10m water depth.

Range-dependent propagation modelling using KRAKEN can be employed to generate sound maps, offering insights into the Sound Exposure Level (SEL) during offshore wind farm constructions. Sound maps can be computed based on a series of radial slices between the source location and receiver point, as depicted in Fig. 7.4. Notably, the bathymetry slices reveal that range-dependent differences are typically minor in the close distance from the sources, where a range-independent modelling approach is applied.

# 7.4 Numerical implementation

In this section, the case study is considered of an offshore wind farm in the North Sea, employing a double bubble curtain system (DBBC). The procedure for generating the sound map is illustrated in Fig. 7.5. The selection of the offshore wind farm location is based on potential sites outlined in the EMODNET Human Activities data portal [199], as depicted in the bathymetry map in Fig. 7.6. The pile parameters reflect monopile properties detailed in Chapter 3 [29]. Specifically, the pile dimensions are: pile length of 76.9 m, diameter of 8 m, and wall thickness of 90 mm. The water depth at the piling location is 39.9 m. The seabed composition comprises a thin marine sediment layer atop a stiff bottom soil half-space.

All soil and fluid layers are assumed horizontally stratified. The maximum blow energy applied is 1750 kJ and the force signature is similar to that considered in section 3.5.2.

Initially, the pressure field is modelled using the noise generation model for sound sources up to a radial distance of 750 m from the pile. The Source Level (SL) is determined based on the wave field at 750 m and calculated for multiple receiver depth locations with a resolution of 0.1 m. It is worth noting that this resolution may need refinement following convergence tests for improved accuracy. Beyond the 750 m range, assuming a vertical line source, sound propagation is computed using the normal mode method with adiabatic approximation. The sound pressure level is then averaged over the depth.

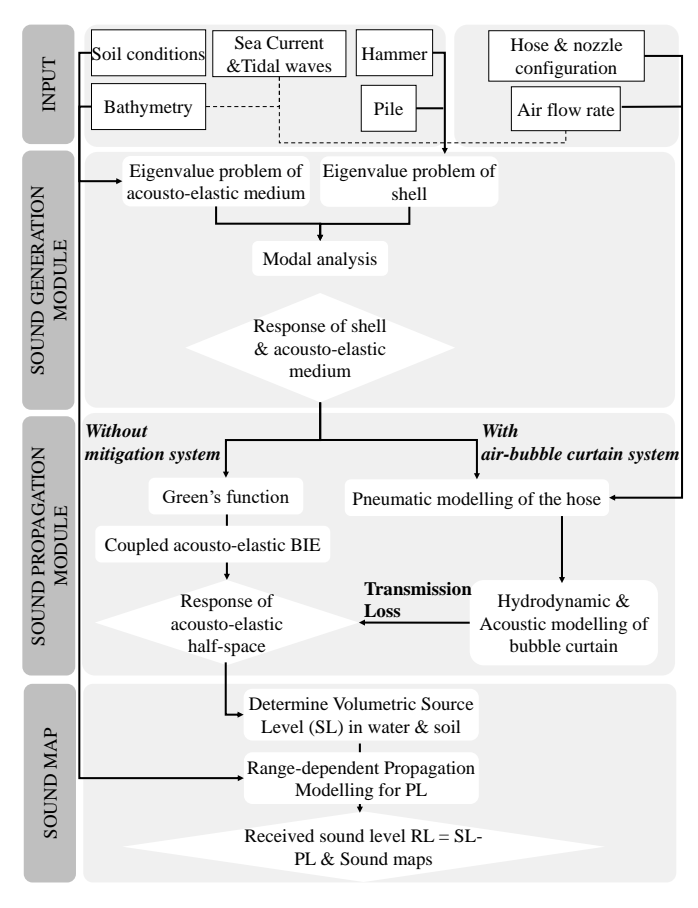


Figure 7.5: Activity flow for generating a sound map of impact pile installation with and without noise mitigation systems. The process includes: (1) defining input parameters such as soil conditions, bathymetry, environmental conditions, pile and hammer type, configuration, and air flow rate for the air-bubble curtain; (2) modeling underwater sound generated by impact pile driving; (3) modeling sound propagation up to a distance with constant bathymetry and soil layering; (4) modeling the air-bubble curtain system when noise mitigation is applied; and (5) propagating sound in a range-dependent environment and generating sound maps by integrating the results.

The approach taken in this analysis to handle range dependency involves discretizing

the range-dependent domain into multiple segments, as illustrated in figure 7.3. When transitioning between these segments, the acoustic modes couple adiabatically, indicating no significant energy transfer to higher or lower modes. Additionally, the analysis computes the sound field on an azimuthal slice basis, assuming negligible energy transition between different azimuthal slices. While these modelling assumptions may impact the results, they align with standard practices in underwater acoustics and have been demonstrated to offer a reasonable approximation of the Sound Exposure Level (SEL) at considerable distances from the acoustic source.

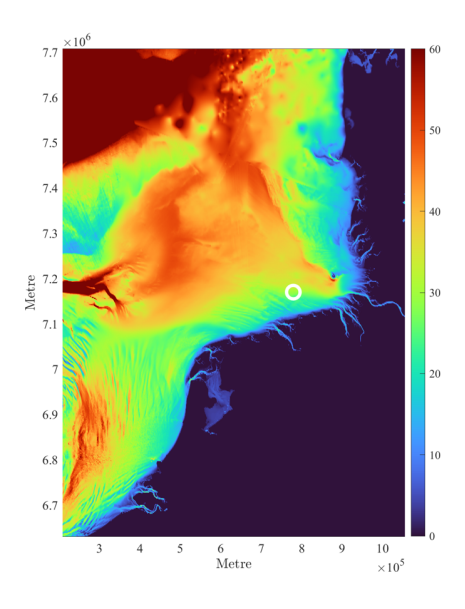


Figure 7.6: Bathymetry map and the location of the foundation in this analysis.

In the process of creating sound maps, the sound propagation model calculates underwater acoustic propagation for selected radial slices obtained from the bathymetry, as depicted in Fig. 7.4. The SEL is then computed for each radial slice with a 3-degree angular resolution, with each slice corresponding to distinct bathymetry and range-dependent sediment properties.

Figure 7.7 illustrates a sound map generated using the approach described above, depicting both the mitigated and unmitigated sound fields. Both scenarios show greater energy propagation toward deeper water areas. The mitigated wave field is assessed under the assumption of employing a Double Bubble Curtain (DBBC) system with standard configuration. Specifically, the inner bubble curtain is positioned 75m from the pile, the outer bubble curtain is situated 150m from the pile, and the flow rate is set at 0.5  $m^3/s/m$ . In this analysis, the DBBC system is modelled using the complete modelling chain outlined in Chapter 6. The sound map is calculated across a broadband Sound Exposure Level (SEL) spectrum, covering the frequency bandwidth of interest.

Figure 7.8 illustrates a sound map generated for a single-frequency excitation at 125

7.5 Conclusions 159

Hz based on the force amplitude of a single impact piling strike, applied to the same pile at a different location where more abrupt bathymetry changes are present. The deep trench, represented by the dark orange shades in the bathymetry map, clearly allows more propagating modes to carry energy, extending the sound field further. In contrast, sound propagation is significantly less efficient in the thinner shallow areas compared to the deeper water regions.

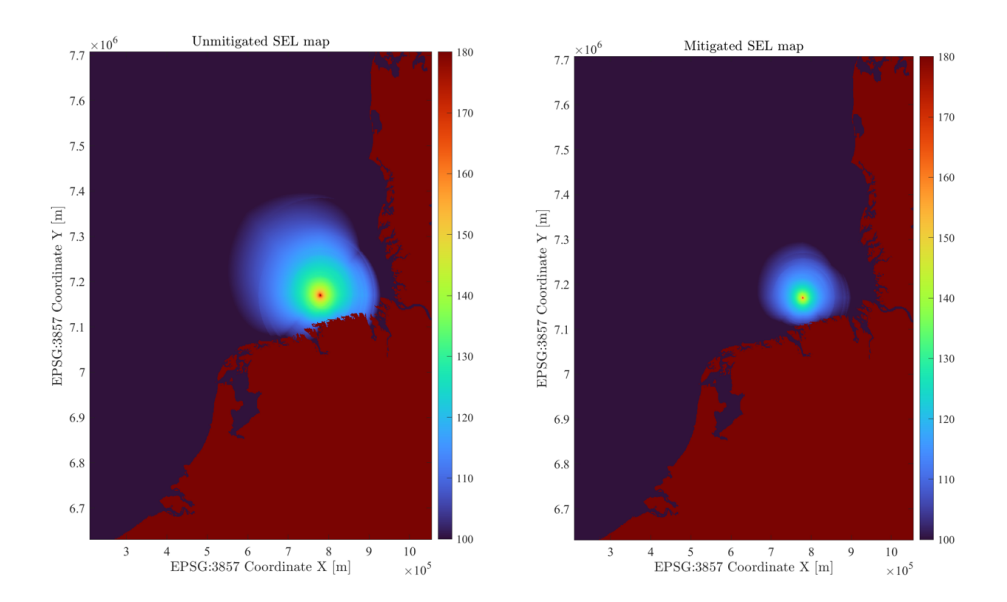


Figure 7.7: Sound map based on a single impact piling strike with (right) and without noise mitigation system (left).

# 7.5 Conclusions

This chapter introduces a comprehensive framework for modelling underwater noise generated by impact pile driving, with and without the implementation of an air bubble curtain system. The framework accounts for various environmental factors, such as elastic multilayered sediments and range-dependent water depth, crucial for accurately predicting sound propagation during offshore wind farm constructions [35, 37]. The utilization of sound mapping facilitates the estimation of maximum impact distances based on different sensitivity thresholds of marine animals. Additionally, these sound maps can be weighted according to marine animals' hearing sensitivities and swimming depths across a broad frequency spectrum, providing valuable input for biologists.

In summary, the following procedure outlines the steps involved in generating sound fields during offshore wind farm constructions:

Modelling underwater sound for impact pile driving in the near-field.

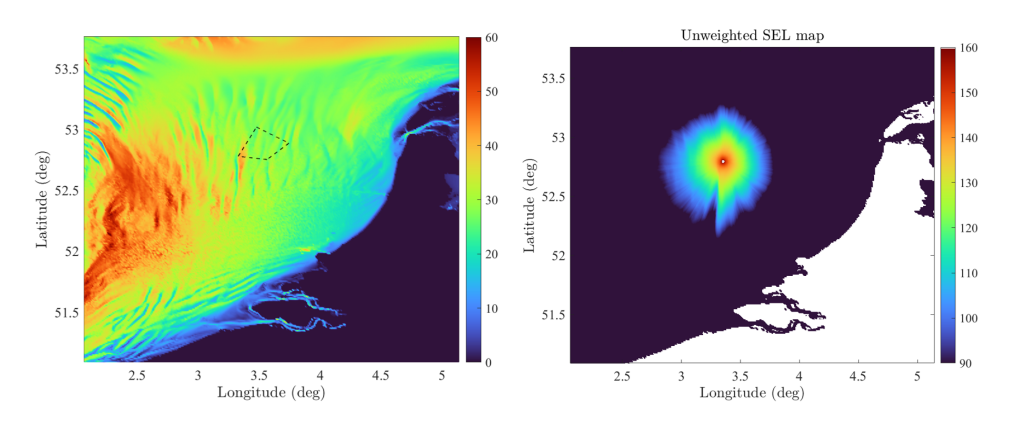


Figure 7.8: Effect of trench effect: sound mapping based on the bathymetry (left) for the simulation pile-driving noise. The sound pressure is averaged over the depth. SEL is calculated for a single-frequency excitation at 125 Hz (right).

- Modelling the air bubble curtain system when such a noise mitigation system is applied.
- Modelling sound propagation up to a distance of constant bathymetry and soil layering using a high-fidelity sound propagation model that considers range-independent elastic properties, including particle motion and pressure.
- Transformation of the wave field into Source Level (SL) for both fluid and soil sources.
- Propagation of SL and prediction of the propagation loss (PL) in the range-dependent elastic half-space beyond 750 m.
- Generation of sound maps by combining modelling results for individual radial slices and sources over the water column and the seabed.

The proposed approach advocates the utilization of a diverse suite of mathematical models at distances that are both accurate and feasible to implement. Uncertainty in environmental and pile parameters can be examined individually for each region. The pile-driving source model can generate outputs for sound pressure, particle velocity, and acceleration in the water column, as well as stresses and displacements in the sediment layers, essential for assessing the impact of sound on fish and invertebrates. More detailed propagation modelling tools for longer distances could be employed in future research. Additionally, the sound propagation modelling approach for the air bubble curtain could be enhanced by considering detailed backscattering effects and adhering to continuity conditions for acousto-elastic waveguides.

# CONCLUSIONS AND RECOMMENDATIONS

#### 8.1 Conclusions

Environmental noise resulting from offshore impact pile driving has raised concerns regarding its potential threat to marine mammals and fishes. Although alternative wind turbine foundations, such as floating turbines, are under development, the industry still faces many technical challenges. Given that monopiles are the primary foundation type, the installation of larger foundation piles leads to the radiation of more energy at lower frequencies. Predicting the noise levels prior to installation becomes crucial for environmental impact assessments. Understanding the risk of noise levels before construction enables the preparation of noise mitigation plans that can be adjusted based on potential risks.

The main strategies to mitigate underwater noise from offshore impact pile driving fall into two categories: controlling the noise at the source and blocking noise transmission paths. The former is achieved through alternative piling technologies such as vibratory pile driving or by elongating the pulse of the impact hammer. Predicting the noise when the piles are installed by means of vibratory tools requires modelling the pile-soil interface with a non-linear model to capture friction interaction and pile-soil slip. This thesis focuses on modelling impact pile driving with the assumption of a non-slip condition between the pile and the soil. Elongating the pulse could shift the frequency spectrum of the radiated waves by directing more energy towards lower frequencies, potentially reducing the amplitude of the radiated acoustic waves. However, this alternative piling technology usually requires combination with other noise mitigation systems either in the near-field or the far-field. In many cases, various combinations of near-field and far-field noise mitigation systems are necessary to meet noise thresholds set by regulators.

Chapter 2 delved into the mathematical formulation necessary for addressing acoustoelastic problems in offshore environments. By deriving fundamental Green's functions and boundary integral equations, this chapter provided a robust framework for analysing noise propagation, particularly in scenarios involving complex soil layers and large distances. The Green's function in the chapter tailored to the ocean environment with the description of the soil as a layered elastic half-space, allowing for soil decompositions and outgoing waves satisfying the radiation condition of the problem. A robust root-finding algorithm based on the argument principle was used, considering the searching domain crossing various branch lines on different Riemann planes. The methodology is universally applicable in different engineering problems given a smoothed characteristic function. The formulation of the Green's function laid the basis for the derivation of the fundamental solution for Green's tensor to be employed in the boundary integral equation (BIE). The BIE formulation allows coupling between the near-source model and the sound propagation model. The Green's function and BIE formulation are extended into three dimensions, allowing for angular dependence in the sound source model. The same approach is later adopted to include the transmission coefficient of the air-bubble curtain and can also be applied for other noise mitigation systems at various radial distances from the pile.

Building upon this theoretical foundation, Chapter 3 introduces a computationally efficient method for predicting the wave field radiated from impact pile driving over extensive horizontal distances. By combining accurate descriptions of pile-soil-water interactions with far-field sound propagation modelling, this chapter presented a framework that can achieve high precision and stability in underwater noise predictions. The methodology involves a two-step approach: firstly, solving the coupled interaction problem of the pile vibration in the acousto-elastic waveguide, then propagating the wave field to the far-field using the BIE. Furthermore, the validation of these predictions against real-world data underscored the reliability and effectiveness of the developed methodology.

The prediction of the sound level due to offshore pile driving involves considerable uncertainties, especially in the input of such a model. The influence of the soil condition, blow energy, hammer force, and environmental conditions such as surface waves and currents can affect the predicted noise level to varying extents. Among all uncertainties discussed here, the soil is considered the most uncertain component in noise prediction as the dynamic properties of the sediment are often missing, and certain assumptions are required. Thus, Chapter 4 shifted focus towards understanding the uncertainties inherent in soil modelling and their impact on noise propagation. Through an exploration of statistical and probabilistic methods, this chapter aimed to establish correlations between soil parameters and resulting sound levels. By identifying these uncertainties, the uncertainties in the soil parameters are quantified through a statistical framework. The methodology provides more robust and reliable noise predictions, crucial for mitigating potential harm to marine ecosystems.

Efforts to address noise pollution were further advanced in Chapter 5, where a computational approach for predicting noise reduction using air-bubble curtain systems was introduced. By coupling detailed noise prediction models with the air bubble curtain system, this chapter demonstrated the noise mitigation potential using such a system in offshore pile driving activities. The model includes the consideration of the development of the air-bubble curtain over depth through an initial phase hydrodynamic model. Based on the output of the hydrodynamic model, the acoustic properties of such a bubble mixture layer can be obtained through an effective medium approach. The optimization of mitigation strategies and deployment configurations promises to further enhance the effectiveness of noise reduction efforts in marine environments.

In practice, the air bubble curtain system comprises multiple components, including

8.1 Conclusions 163

the injection of air volume from the air compressor vessel (ACV), the transportation of air along the riser and hoses positioned on the seabed, and the release and development of the bubble-water mixture over the entire water depth. Without a comprehensive understanding of the multiphysics process involved in generating the air bubble curtain system, accurately estimating its acoustic properties becomes challenging. In an effort to address this knowledge gap, Chapter 6 introduces a multi-physics model for noise emission during offshore pile driving, integrating various subsystems to depict the complex interactions accurately. This complete modelling chain encompasses the compressible flow model for air transportation from the ACV to the hoses, the hydrodynamic model considering two-phase turbulent flow and the various phases of bubble formation, and the depth- and frequency-dependent acoustic model based on properties derived from earlier steps. Through sensitivity analysis, this chapter highlights critical parameters influencing air bubble curtain system performance, offering insights into optimal configurations and operational constraints crucial for noise mitigation strategies.

Lastly, Chapter 7 presents a comprehensive method for modelling underwater sound generation and propagation in range-dependent ocean environments. This final chapter outlines a framework for modelling sound maps generated by impact pile driving, with and without the implementation of an air bubble curtain system. Considering various environmental conditions, such as elastic multilayered sediments and range-dependent water depth, this framework is essential for accurately predicting sound propagation during offshore wind farm constructions. Sound mapping is valuable in estimating maximum impact distances based on different marine animals' sensitivity thresholds, providing important input for biologists. This chapter advocates using diverse mathematical models at distances that are both accurate and feasible to implement, allowing examination of uncertainty in environmental and pile parameters for each region. The pile-driving source model outputs sound pressure, particle velocity, and acceleration in the water column, as well as stresses and displacements in sediment layers, essential for assessing the impact of sound on marine life. Future research could employ more detailed propagation modelling tools at longer distances and enhance the sound propagation modelling approach for air bubble curtains by considering detailed backscattering effects and continuity conditions for acousto-elastic waveguides.

In conclusion, this thesis represents a significant contribution to advancing the understanding of noise pollution in offshore environments due to impact pile driving and offers practical solutions for mitigating its adverse effects. By bridging theoretical developments with practical applications, these findings hold implications for environmental management, sustainable offshore development, and the preservation of marine ecosystems. Moving forward, continued research and innovation in this field promise to further enhance the ability to safeguard marine life while harnessing the potential of offshore renewable energy.

## 8

### 8.2 RECOMMENDATIONS

Based on the key findings of this thesis, several recommendations for future research, noise regulators, and industry practices are outlined below.

The development and application of the Green's function in Boundary Integral Equation, as presented in Chapter 2, offer significant potential for modelling wave fields in various engineering domains, extending beyond offshore environments. This methodology can be adapted for acoustic problems in the atmosphere and interior spaces, as well as vibration issues in onshore settings.

Expanding the modelling framework to incorporate additional noise mitigation strategies, such as resonator-based systems in the near field and combinations of various mitigation methods, would enhance its versatility. Further investigation into alternative hammers, like Pulse units for prolonging impulsive durations, could also be explored using the current modelling framework.

In terms of environmental impact assessment, there is a need to focus on a broader range of noise metrics beyond the conventional dual sound metrics, including SEL and  $L_{p,pk}$ . Parameters such as particle motions and the kurtosis index, which are more sensitive indicators for many underwater species, should be considered, as they respond more directly to motion rather than pressure variations. In many countries, noise thresholds vary significantly, often overlooking the influence of the frequency content of the emitted sound on various species. As pile sizes increase and offshore wind farms are built in deeper waters, standard dual sound metrics may no longer adequately reflect the impact on marine mammals and fish populations. Tailored noise thresholds, such as particle motions and kurtosis, could be adopted to better quantify environmental impacts. The developed modelling framework in this thesis allows for prediction of a wide range of sound metrics which can be chosen upon collaboration with marine biologists.

The industry should explore innovative mitigation techniques by combining different noise reduction systems, including alternative piling methods to decrease sound levels at the source and noise mitigation systems employed in the seawater at various distances from the pile. New vibratory installation technologies, such as Gentle Pile Driving (GDP) [60], are under development, aiming to achieve better installation efficiency and reduce emitted sound levels. The industry should also optimize existing noise mitigation systems for various environmental conditions, including soil variations and the presence of waves and currents. Conducting uncertainty quantification on expected noise levels is crucial to mitigate the risks of exceeding noise thresholds and ensure effective noise management practices. This thesis explores a method to incorporate uncertainties into sound prediction, however, further investigation is required.



# APPENDIX

By substituting the expressions into the boundary and interface conditions shown in Eqs. (2.8)-(2.11), the final set of linear algebraic equations with unknowns  $A_i^g$  for i = 1, 2, ..., 4N + 2 reads:

$$\frac{1}{-\rho\omega^2} \frac{e^{-\mathrm{i}k_{z,f}(z_s-z_0)}}{4\pi\mathrm{i}k_{z,f}} + A_1^g e^{\mathrm{i}k_{z,f}z} + A_2^g e^{-\mathrm{i}k_{z,f}z_0} = 0 \tag{A.1}$$

$$\frac{e^{-ik_{z,f}(z_1-z_s)}}{4\rho\omega^2\pi} - A_1^g ik_{z,f}e^{-ik_{z,f}z_1} + A_2^g ik_{z,f}e^{k_{z,f}D1i} = -A_3^g ik_{z,p_1}e^{-ik_{z,p_1}z_1} + A_4^g ik_{z,p_1} \cdot e^{k_{z,p_1}z_1} - A_5^g k_{z,s_1}^2 e^{-ik_{z,s_1}z_1} - A_6^g k_{z,s_1}^2 e^{k_{z,s_1}z_1} + k_{s_1}^2 (A_5^g e^{-ik_{z,s_1}z_1} + A_6^g e^{k_{z,s_1}z_1})$$
(A.2)

$$\begin{split} &\frac{e^{-\mathrm{i}k_{z,f}(z_1-z_8)}\mathrm{i}}{4\rho\omega^2\pi k_{z,f}} + A_1^g e^{-\mathrm{i}k_{z,f}z_1} + A_2^g e^{k_{z,f}z_1\mathrm{i}} = -\frac{1}{\rho\omega^2} \bigg( -\lambda_1 k_{p_1}^2 \bigg[ A_3^g e^{-\mathrm{i}k_{z,p_1}z_1} \\ &+ A_4^g e^{k_{z,p_1}z_1\mathrm{i}} \bigg] + 2\mu_1 \bigg[ -A_3^g k_{z,p_1}^2 e^{-\mathrm{i}k_{z,p_1}z_1} - A_4^g k_{z,p_1}^2 e^{k_{z,p_1}z_1\mathrm{i}} + A_5^g k_{z,s_1}^3 e^{-\mathrm{i}k_{z,s_1}z_1\mathrm{i}} \\ &- A_6^g k_{z,s_1}^3 e^{k_{z,s_1}z_1\mathrm{i}} \mathrm{i} + k_{s_1}^2 (-A_5^g k_{z,s_1} e^{-\mathrm{i}k_{z,s_1}z_1} \mathrm{i} + A_6^g k_{z,s_1} e^{k_{z,s_1}z_1\mathrm{i}} \mathrm{i} \bigg) \bigg] \bigg) \end{split} \tag{A.3}$$

$$\begin{split} &-2\mathrm{i} A_3^g k_{z,p_1} e^{-\mathrm{i} k_{z,p_1} z_1} + 2\mathrm{i} A_4^g k_{z,p_1} e^{\mathrm{i} k_{z,p_1} z_1} - 2A_5^g k_{z,s_1}^2 e^{-\mathrm{i} k_{z,s_1} z_1} - 2A_6^g k_{z,s_1}^2 e^{\mathrm{i} k_{z,s_1} z_1} \\ &+ k_{s_1}^2 (A_5^g e^{-\mathrm{i} k_{z,s_1} z_1} + A_6^g e^{\mathrm{i} k_{z,s_1} z_1}) = 0 \end{split} \tag{A.4}$$

$$\begin{split} &-A_{4j+3}^g \mathrm{i} k_{z,p_{j+1}} e^{-\mathrm{i} k_{z,p_{j+1}} z_{j+1}} + A_{4j+4}^g \mathrm{i} k_{z,p_{j+1}} e^{\mathrm{i} k_{z,p_{j+1}} z_{j+1}} - A_{4j+5}^g k_{z,s_{j+1}}^2 e^{-\mathrm{i} k_{z,s_{j+1}} z_{j+1}} \\ &-A_{4j+5}^g k_{z,s_{j+1}}^2 e^{\mathrm{i} k_{z,s_{j+1}} z_{j+1}} + k_{s_{j+1}}^2 \left( A_{4j+5}^g e^{-\mathrm{i} k_{z,s_{j+1}} z_{j+1}} + A_{4j+6}^g e^{\mathrm{i} k_{z,s_{j+1}} z_{j+1}} \right) \\ &= -A_{4j-1}^g \mathrm{i} k_{z,p_j} e^{-\mathrm{i} k_{z,p_j} z_{j+1}} + A_{4j}^g \mathrm{i} k_{z,p_j} e^{\mathrm{i} k_{z,p_j} z_{j+1}} - A_{4j+1}^g k_{z,s_j}^2 e^{-\mathrm{i} k_{z,s_j} z_{j+1}} \\ &-A_{4j+1}^g k_{z,s_j}^2 e^{\mathrm{i} k_{z,s_j} z_{j+1}} + k_{s_j}^2 \left( A_{4j+1}^g e^{-\mathrm{i} k_{z,s_j} z_{j+1}} + A_{4j+2}^g e^{\mathrm{i} k_{z,s_j} z_{j+1}} \right), \quad j=1,..,N \end{split} \tag{A.5}$$

166 A Appendix

A

$$\begin{split} &A_{4j+3}^{g}e^{-\mathrm{i}k_{z,p_{j+1}}z_{j+1}}+A_{4j+4}^{g}e^{\mathrm{i}k_{z,p_{j+1}}z_{j+1}}-A_{4j+5}^{g}\mathrm{i}k_{z,s_{j+1}}e^{-\mathrm{i}k_{z,s_{j+1}}z_{j+1}}+A_{4j+6}^{g}\mathrm{i}k_{z,s_{j}}e^{\mathrm{i}k_{z,s_{j}}z_{j+1}}\\ &=A_{4j-1}^{g}e^{-\mathrm{i}k_{z,p_{j}}z_{j}}+A_{4j}^{g}e^{\mathrm{i}k_{z,p_{j}}z_{j}}-A_{4j+1}^{g}\mathrm{i}k_{z,s_{j}}e^{-\mathrm{i}k_{z,s_{j}}z_{j}}+A_{4j+2}^{g}\mathrm{i}k_{z,s_{j}}e^{\mathrm{i}k_{z,s_{j}}z_{j}},\quad j=1,..,N \end{split} \tag{A.6}$$

$$\begin{split} &-\lambda_{j+1}k_{p_{j+1}}^2(A_{4j+3}e^{-\mathrm{i}k_{z,p_{j+1}}z_{j+1}}+A_{4j+4}e^{\mathrm{i}k_{z,p_{j+1}}z_{j+1}})+2\mu_{j+1}(-A_{4j+3}k_{z,p_{j+1}}^2\cdot\\ &e^{-\mathrm{i}k_{z,p_{j+1}}z_{j+1}}-A_{4j+4}k_{z,p_{j+1}}^2e^{\mathrm{i}k_{z,p_{j+1}}z_{j+1}}+A_{4j+5}\mathrm{i}k_{z,s_{j+1}}^3e^{-\mathrm{i}k_{z,s_{j+1}}z_{j+1}}-A_{4j+6}\mathrm{i}k_{z,s_{j+1}}^3\cdot\\ &e^{\mathrm{i}k_{z,s_{j+1}}z_{j+1}}+k_{s_{j+1}}^2(-A_{4j+5}\mathrm{i}k_{z,s_{j+1}}e^{-\mathrm{i}k_{z,s_{j}}z_{j+1}}+A_{4j+6}\mathrm{i}k_{z,s_{j+1}}e^{\mathrm{i}k_{z,s_{j+1}}z_{j+1}}))\\ &=-\lambda_{j}k_{p_{j}}^2(A_{4j-1}e^{-\mathrm{i}k_{z,p_{j}}z_{j+1}}+A_{4j}e^{\mathrm{i}k_{z,p_{j}}z_{j+1}})+2\mu_{j}(-A_{4j-1}k_{z,p_{j}}^2e^{-\mathrm{i}k_{z,p_{j}}z_{j+1}}\\ &-A_{4j}k_{z,p_{j}}^2e^{\mathrm{i}k_{z,p_{j}}z_{j+1}}+A_{4j+1}\mathrm{i}k_{z,s_{j}}^3e^{-\mathrm{i}k_{z,s_{j}}z_{j+1}}-A_{4j+2}\mathrm{i}k_{z,s_{j}}^2e^{\mathrm{i}k_{z,s_{j}}z_{j+1}}+k_{2j}(-A_{4j+1}\mathrm{i}k_{z,s_{j}}e^{-\mathrm{i}k_{z,s_{j}}z_{j+1}})),\quad j=1,..,N \end{split} \tag{A.7}$$

$$\begin{split} &\mu_{j+1}(-2\mathrm{i}A^g_{4j+3}k_{z,p_{j+1}}e^{-\mathrm{i}k_{z,p_{j+1}}z_{j+1}}+2\mathrm{i}A^g_{4j+4}k_{z,p_{j+1}}e^{\mathrm{i}k_{z,p_{j+1}}z_{j+1}}-2A^g_{4j+5}k^2_{z,s_{j+1}}e^{-\mathrm{i}k_{z,s_{j+1}}z_{j+1}}\\ &-2A^g_{4j+6}k^2_{z,s_{j+1}}e^{\mathrm{i}k_{z,s_{j+1}}z_{j+1}}+k^2_{s_{j-1}}(A^g_{4j+5}e^{-\mathrm{i}k_{z,s_{j+1}}z_{j+1}}+A^g_{4j+6}e^{\mathrm{i}k_{z,s_{j+1}}z_{j+1}}))=\\ &\mu_{j}(-2\mathrm{i}A^g_{4j-1}k_{z,p_{j}}e^{-\mathrm{i}k_{z,p_{j}}z_{j+1}}+2\mathrm{i}A^g_{4j}k_{z,p_{j}}e^{\mathrm{i}k_{z,p_{j}}z_{j+1}}-2A^g_{4j+1}k^2_{z,s_{j}}e^{-\mathrm{i}k_{z,s_{j}}z_{j+1}}\\ &-2A^g_{4j+2}k^2_{z,s_{j}}e^{\mathrm{i}k_{z,s_{j}}z_{j+1}}+k^2_{s_{j}}(A^g_{4j+1}e^{-\mathrm{i}k_{z,s_{j}}z_{j+1}}+A^g_{4j+2}e^{\mathrm{i}k_{z,s_{j}}z_{j+1}})), \quad j=1,..,N \end{split} \tag{A.8}$$

# **BIBLIOGRAPHY**

### REFERENCES

- [1] International Energy Agency. Offshore wind outlook 2019. Technical report, IEA, Paris, 2019. Licence: CC BY 4.0.
- [2] European Commission: Directorate-General for Environment. *Guidance Document on Wind Energy Developments and EU Nature Legislation*. Publications Office of the European Union, Luxembourg, 2020. Accessed on 2025-03-03.
- [3] Global Wind Energy Council. Global wind report 2024. Technical report, GWEC, Brussels, Belgium, 2024.
- [4] WindEurope Market Intelligence and Ramírez, Lizet. Offshore wind energy 2022 statistics. Technical report, WindEurope asbl/vzw, Brussels, Belgium, 2023. Accessed on 2025-03-03.
- [5] C. Vazquez Hernandez and T. Telsnig. Wind energy: Technology market report. Technical report, European Commission, Joint Research Centre, 2019.
- [6] H. Bailey, B. Senior, D. Simmons, J. Rusin, G. Picken, and P. M. Thompson. Assessing underwater noise levels during pile-driving at an offshore windfarm and its potential effects on marine mammals. *Marine Pollution Bulletin*, 60(6):888–897, 2010.
- [7] National Research Council (NRC). *Ocean Noise and Marine Mammals*. National Academies Press, Washington, DC, 2003. Accessed on 2025-03-03.
- [8] James E. Herbert-Read, Louise Kremer, Rick Bruintjes, Andrew N. Radford, and Christos C. Ioannou. Anthropogenic noise pollution from pile-driving disrupts the structure and dynamics of fish shoals. *Proceedings of the Royal Society B*, 284(1864):20171627, 2017.
- [9] I. van der Knaap, H. Slabbekoorn, T. Moens, D. Van den Eynde, and J. Reubens. Effects of pile driving sound on local movement of free-ranging atlantic cod in the belgian north sea. *Environmental Pollution*, 300:118913, 2022.
- [10] Ian T. Jones, Jenni A. Stanley, and T. Aran Mooney. Impulsive pile driving noise elicits alarm responses in squid (doryteuthis pealeii). *Marine Pollution Bulletin*, 150:110792, 2020.
- [11] H. Slabbekoorn, N. Bouton, I. van Opzeeland, A. Coers, C. ten Cate, and A.N. Popper. A noisy spring: the impact of globally rising underwater sound levels on fish. *Trends in ecology & evolution*, 25(7):419–27, 2010.

[12] Subhamoy Bhattacharya. Design of foundations for offshore wind turbines, 2019.

- [13] P. G. Reinhall and P. H. Dahl. Underwater mach wave radiation from impact pile driving: theory and observation. *The Journal of the Acoustical Society of America*, 130(3):1209–16, 2011.
- [14] M. Zampolli, M. J. Nijhof, C. A. de Jong, M. A. Ainslie, E. H. Jansen, and B. A. Quesson. Validation of finite element computations for the quantitative prediction of underwater noise from impact pile driving. *The Journal of the Acoustical Society of America*, 133(1):72–81, 2013.
- [15] A. Tsouvalas and A. V. Metrikine. A semi-analytical model for the prediction of underwater noise from offshore pile driving. *The Journal of Sound and Vibration*, 332(13):3232–3257, 2013.
- [16] A. Tsouvalas and A. V. Metrikine. A three-dimensional vibroacoustic model for the prediction of underwater noise from offshore pile driving. *The Journal of Sound and Vibration*, 333(8):2283–2311, 2014.
- [17] Marshall V. Hall. A semi-analytical model for non-mach peak pressure of underwater acoustic pulses from offshore pile driving. *Acoustics Australia*, 41(1):42–51, 2013.
- [18] M. V. Hall. An analytical model for the underwater sound pressure waveforms radiated when an offshore pile is driven. *The Journal of the Acoustical Society of America*, 138(2):795–806, 2015.
- [19] Q. Deng, W. Jiang, M. Tan, and J. Xing. Modeling of offshore pile driving noise using a semi-analytical variational formulation. *Applied Acoustics*, 104:85–100, 2016.
- [20] Q. Deng, W. Jiang, and W. Zhang. Theoretical investigation of the effects of the cushion on reducing underwater noise from offshore pile driving. *The Journal of the Acoustical Society of America*, 140(4):2780, 2016.
- [21] A. O. MacGillivray. Finite difference computational modeling of marine impact pile driving. *The Journal of the Acoustical Society of America*, 136(4):2206, 2014.
- [22] D. R. Wilkes, T. P. Gourlay, and A. N. Gavrilov. Numerical modeling of radiated sound for impact pile driving in offshore environments. *IEEE Journal of Oceanic Engineering*, 41(4):1072–1078, 2016.
- [23] D. R. Wilkes and A. N. Gavrilov. Sound radiation from impact-driven raked piles. *The Journal of the Acoustical Society of America*, 142(1):1, 2017.
- [24] T. Lippert and O. von Estorff. The significance of parameter uncertainties for the prediction of offshore pile driving noise. *The Journal of the Acoustical Society of America*, 136(5):2463–71, 2014.
- [25] H. Kim, G. R. Potty, J. H. Miller, K. B. Smith, and G. Dossot. Long range propagation modeling of offshore wind turbine noise using finite element and parabolic equation models. *The Journal of the Acoustical Society of America*, 131(4):3392, 2012.

[26] Moritz B. Fricke and Raimund Rolfes. Towards a complete physically based forecast model for underwater noise related to impact pile driving. *The Journal of the Acoustical Society of America*, 137(3):1564–1575, 2015.

- [27] P. H. Dahl and D. R. Dall'Osto. On the underwater sound field from impact pile driving: Arrival structure, precursor arrivals, and energy streamlines. *The Journal of the Acoustical Society of America*, 142(2):1141, 2017.
- [28] J. von Pein, E. Klages, S. Lippert, and O. von Estorff. A hybrid model for the 3d computation of pile driving noise. In *OCEANS* 2019 Marseille, pages 1–6, 2019.
- [29] Y. Peng, A. Tsouvalas, T. Stampoultzoglou, and A. Metrikine. A fast computational model for near-and far-field noise prediction due to offshore pile driving. *The Journal of the Acoustical Society of America*, 149(3):1772–1790, 2021.
- [30] P. H. Dahl, D. R. Dall'Osto, and D. M. Farrell. The underwater sound field from vibratory pile driving. *The Journal of the Acoustical Society of America*, 137(6):3544–54, 2015.
- [31] A. Tsouvalas and A. V. Metrikine. Structure-Borne Wave Radiation by Impact and Vibratory Piling in Offshore Installations: From Sound Prediction to Auditory Damage. *Journal of Marine Science and Engineering*, 4(3):44, aug 2016.
- [32] Michael A. Ainslie, Michele B. Halvorsen, Roel A. J. Müller, and Tristan Lippert. Application of damped cylindrical spreading to assess range to injury threshold for fishes from impact pile driving. *The Journal of the Acoustical Society of America*, 148(1):108–121, 2020.
- [33] M. A. Ainslie, Mi. B. Halvorsen, and S. P. Robinson. A terminology standard for underwater acoustics and the benefits of international standardization. *IEEE Journal of Oceanic Engineering*, 47(1):179–200, 2022.
- [34] International Organization for Standardization. Underwater acoustics—terminology. Standard ISO 8405:2017, International Organization for Standardization, Geneva, Switzerland, 2017.
- [35] B. L. Southall, A. E. Bowles, William T. Ellison, J. J. Finneran, Roger L. Gentry, C. R. Greene, D. Kastak, D. R. Ketten, J. H. Miller, P. E. Nachtigall, W. J. Richardson, J. A. Thomas, and P. L. Tyack. Marine mammal noise exposure criteria: Initial scientific recommendations. *The Journal of the Acoustical Society of America*, 125(4):2517, 2009.
- [36] U. Stöber and F. Thomsen. Effect of impact pile driving noise on marine mammals: A comparison of different noise exposure criteria. *The Journal of the Acoustical Society of America*, 145(5):3252, 2019.
- [37] B. Southall, D. Nowacek, A. Bowles, V. Senigaglia, L. Bejder, and P. Tyack. Marine mammal noise exposure criteria: Assessing the severity of marine mammal behavioral responses to human noise. *Aquatic Mammals*, 45(5):421–464, 2021.

[38] Svenja Tidau and Mark Briffa. Review on behavioral impacts of aquatic noise on crustaceans. In *Proceedings of Meetings on Acoustics*, volume 27, page 010028, December 2016.

- [39] K. F. Whyte, D. J. F. Russell, C. E. Sparling, B. Binnerts, and G. D. Hastie. Estimating the effects of pile driving sounds on seals: Pitfalls and possibilities. *The Journal of the Acoustical Society of America*, 147(6):3948–3958, 06 2020.
- [40] A. Chahouri, N. Elouahmani, and H. Ouchene. Recent progress in marine noise pollution: A thorough review. *Chemosphere*, 291:132983, 2022.
- [41] A.N. Popper, L. Hice-Dunton, E. Jenkins, D. M. Higgs, J. Krebs, A. Mooney, A. Rice, L. Roberts, F. Thomsen, K. Vigness-Raposa, D. Zeddies, and K. A. Williams. Offshore wind energy development: Research priorities for sound and vibration effects on fishes and aquatic invertebrates. *The Journal of the Acoustical Society of America*, 151(1):205–215, 01 2022.
- [42] A.N. Popper. Hearing diversity in 34000 fish species: A personal perspectives. *The Journal of the Acoustical Society of America*, 154(3):1351–1361, 09 2023.
- [43] J. J. Finneran, C. E. Schlundt, and J. Mulsow. Temporary threshold shift in bottlenose dolphins exposed to steady-state, 1/6-octave noise centered at 0.5 to 80 khz. *The Journal of the Acoustical Society of America*, 154(2):1324–1338, 08 2023.
- [44] A.N. Popper and A.D. Hawkins. The importance of particle motion to fishes and invertebrates. *The Journal of the Acoustical Society of America*, 143(1):470–488, 01 2018.
- [45] A. D. Hawkins, Ri. A. Hazelwood, A. N. Popper, and P. C. Macey. Substrate vibrations and their potential effects upon fishes and invertebrates. *The Journal of the Acoustical Society of America*, 149(4):2782–2790, 04 2021.
- [46] International Maritime Organization. Guidelines for the reduction of underwater noise from commercial shipping to address adverse impacts on marine life. Technical report, IMO, 2014.
- [47] National Oceanic and Atmospheric Administration. Technical guidance for assessing the effects of anthropogenic sound on marine mammal hearing: Underwater acoustic thresholds for onset of permanent and temporary threshold shifts. Technical report, NOAA Technical Memorandum NMFS-OPR-55, 2016.
- [48] R. Williams, E. Ashe, L. Blight, M. Jasny, and L. Nowlan. Marine mammals and ocean noise: Future directions and information needs with respect to science, policy and law in canada. *Marine Pollution Bulletin*, 86(1):29–38, 2014.
- [49] Nathan D. Merchant, Rosalyn L. Putland, Michel André, Eric Baudin, Mario Felli, Hans Slabbekoorn, and René Dekeling. A decade of underwater noise research in support of the european marine strategy framework directive. *Ocean & Coastal Management*, 228:106299, 2022.

[50] Emily Chou, Brandon L. Southall, Martin Robards, and Howard C. Rosenbaum. International policy, recommendations, actions and mitigation efforts of anthropogenic underwater noise. *Ocean & Coastal Management*, 202:105427, 2021.

- [51] T. Verfuß. *Noise mitigation systems and low-noise installation technologies.* Wiesbaden : Springer Fachmedien Wiesbaden : Springer Spektrum, 2014.
- [52] K.M. Lee, A.R. McNeese, P.S. Wilson, and M.S. Wochner. Using arrays of air-filled resonators to attenuate low frequency underwater sound. *Proceedings of Meetings on Acoustics*, 22(1):045004, 2014.
- [53] G. Nehls, A. Rose, A. Diederichs, M. Bellmann, and H. Pehlke. Noise Mitigation During Pile Driving Efficiently Reduces Disturbance of Marine Mammals. Advances in Experimental Medicine and Biology 2214-8019. New York, NY: Springer New York: Springer, 2016.
- [54] K. M. Lee, P. S. Wilson, and M. S. Wochner. Attenuation of low-frequency underwater sound using an array of air-filled balloons and comparison to effective medium theory. *The Journal of the Acoustical Society of America*, 142(6):3443–3449, 12 2017.
- [55] A. Tsouvalas. *Underwater noise generated by offshore pile driving*. PhD thesis, Delft University of Technology, 2015.
- [56] S. Koschinski and K. Lüdemann. Noise mitigation for the construction of increasingly large offshore wind turbines. Technical report, Federal Agency for Nature Conservation (Bundesamt für Naturschutz, BfN), 2020.
- [57] E. Klages, S. Lippert, and O. von Estorff. A noise-reduced impact hammer for offshore pile driving. *Proceedings of Meetings on Acoustics*, 44(1):070016, 06 2021.
- [58] A. Tsouvalas. Underwater noise emission due to offshore pile installation: A review. *Energies*, 13(12):3037, 2020.
- [59] A. Tsetas, A. Tsouvalas, and A. V. Metrikine. A non-linear three-dimensional pile-soil model for vibratory pile installation in layered media. *International Journal of Solids* and Structures, 269:112202, 2023.
- [60] A. Tsetas, A. Tsouvalas, and A. V. Metrikine. The mechanics of the gentle driving of piles. *International Journal of Solids and Structures*, 282:112466, 2023.
- [61] A. Tsetas, A. Tsouvalas, S. S. Gómez, F. Pisanò, E. Kementzetzidis, T. Molenkamp, A.S.K. Elkadi, and A.V. Metrikine. Gentle driving of piles (gdp) at a sandy site combining axial and torsional vibrations: Part i - installation tests. *Ocean Engineering*, 270:113453, 2023.
- [62] T. Molenkamp, A. Tsouvalas, and A. Metrikine. The influence of contact relaxation on underwater noise emission and seabed vibrations due to offshore vibratory pile installation. *Frontiers in Marine Science*, 10, 2023.

[63] A. Tsouvalas and A. V. Metrikine. Noise reduction by the application of an air-bubble curtain in offshore pile driving. *Journal of Sound and Vibration*, 371:150–170, 2016.

- [64] K.W. Commander and A. Prosperetti. Linear pressure waves in bubbly liquids: Comparison between theory and experiments. *The Journal of the Acoustical Society of America*, 85(2):732–746, 1989.
- [65] K. Göttsche. Numerical prediction of underwater noise reduction during offshore pile driving by a small bubble curtain. In Proceedings of the International Congress and Exposition on Noise Control Engineering (INTER-NOISE), Innsbruck, Austria, 09 2013.
- [66] T. Bohne, T. Grießmann, and R. Rolfes. Modeling the noise mitigation of a bubble curtain. *The Journal of the Acoustical Society of America*, 146(4):2212, 2019.
- [67] T. Bohne, T. Grießmann, and R. Rolfes. Development of an efficient buoyant jet integral model of a bubble plume coupled with a population dynamics model for bubble breakup and coalescence to predict the transmission loss of a bubble curtain. *International Journal of Multiphase Flow*, 132, 2020.
- [68] Y. Peng, A. Tsouvalas, T. Stampoultzoglou, and A. Metrikine. Study of the sound escape with the use of an air bubble curtain in offshore pile driving. *Journal of Marine Science and Engineering*, 9(2):232, 2021.
- [69] M.A. Bellmann. Overview of existing noise mitigation systems for reducing piledriving noise. In INTERNOISE 2014 - 43rd International Congress on Noise Control Engineering: Improving the World Through Noise Control, 16-19, November 2014.
- [70] K. Elmer, J. Gattermann, C. Kuhn, and B. Bruns. Mitigation of underwater piling noise by air filled balloons and PE-foam elements as hydro sound dampers. *The Journal of the Acoustical Society of America*, 132(3):2056–2056, 09 2012.
- [71] B. Bruns, P. Stein, C. Kuhn, H. Sychla, and J. Gattermann. Hydro sound measurements during the installation of large diameter offshore piles using combinations of independent noise mitigation systems. In *Proceedings of the Inter-Noise 2014 Conference*, 2014.
- [72] T. Lippert and S. Lippert. Modeling of pile driving noise by means of wavenumber integration. *Acoustic Australia*, 40(3):178–182, 2012.
- [73] J. L. Nealy, J. M. Collis, and S. D. Frank. Normal mode solutions for seismo-acoustic propagation resulting from shear and combined wave point sources. *The Journal of the Acoustical Society of America*, 139(4):EL95, 2016.
- [74] R.A. Hazelwood and P.C. Macey. Modeling water motion near seismic waves propagating across a graded seabed, as generated by man-made impacts. *Journal of Marine Science and Engineering*, 4(3), 2016.

[75] R. A. Hazelwood, P. C. Macey, S. P. Robinson, and L. S. Wang. Optimal transmission of interface vibration wavelets—a simulation of seabed seismic responses. *Journal of Marine Science and Engineering*, 4:61, 2018.

- [76] A. Tsouvalas, T. Molenkamp, K. Canny, D. Kroon, M. Versluis, Y. Peng, and A. Metrikine. A mode matching technique for the seismic response of liquid storage tanks including soil-structure interaction. In *EASD Procedia EURODYN, International Conference on Structural Dynamics*, pages 1–14, Athens, Greece, November 2020.
- [77] A. Tsouvalas, K. N. van Dalen, and A. V. Metrikine. The significance of the evanescent spectrum in structure-waveguide interaction problems. *The Journal of the Acoustical Society of America*, 138(4):2574–88, 2015.
- [78] A. Tsouvalas, Y. Peng, and A. Metrikine. Underwater noise generated by offshore pile driving: A pile-soil-water vibroacoustic model based on a mode matching method. In *Proceedings of the 5th International Conference and Exhibition on Underwater Acoustics (UACE2019)*, Crete, Greece, August 2019.
- [79] Y. Peng, A. Tsouvalas, and A. Metrikine. A coupled modelling approach for the fast computation of underwater noise radiation from offshore pile driving. In EASD Procedia EURODYN, International Conference on Structural Dynamics, pages 2427– 2436, Athens, Greece, November 2020.
- [80] T. Lippert, M. A. Ainslie, and O. von Estorff. Pile driving acoustics made simple: Damped cylindrical spreading model. *The Journal of the Acoustical Society of America*, 143(1):310, 2018.
- [81] S. B. Martin and D. R. Barclay. Determining the dependence of marine pile driving sound levels on strike energy, pile penetration, and propagation effects using a linear mixed model based on damped cylindrical spreading. *The Journal of the Acoustical Society of America*, 146(1):109, 2019.
- [82] Y. Peng, A. Tsouvalas, and A. Metrikine. Modelling and development of a resonator-based noise mitigation system for offshore pile driving. In *Proceedings of the 25th International Congress on Sound and Vibration (ICSV2018)*, Hiroshima, Japan, July 2018.
- [83] Y. Peng, A. L. Laguna, J. Tang, Y. E. Hasadi, and A. Tsouvalas. A multi-physics model for modelling noise mitigation using an air-bubble curtain in impact pile driving. In Proceedings of the 28th International Congress on Sound and Vibration (ICSV 2022), Singapore, July 2022.
- [84] S. Lippert, M. Huisman, M. Ruhnau, O. Estorff, and Kees van Zandwijk. Prognosis of underwater pile driving noise for submerged skirt piles of jacket structures. In Proceedings of the UACE 2017 4th Underwater Acoustics Conference and Exhibition, 2017.
- [85] H.O. Sertlek and A. Tsouvalas. Underwater sound propagation through an air-bubble medium in an acousto-elastic waveguide. In *Proceedings of the 28th International Congress on Sound and Vibration*, 2022.

[86] S. Beelen, M. van Rijsbergen, M. Birvalski, F. Bloemhof, and D. Krug. In situ measurements of void fractions and bubble size distributions in bubble curtains. *Experiments* in Fluids, 64(2):31, 2023.

- [87] M. S. Wochner. Adbm noise mitigation system 2018 demonstration results. Technical report, AdBm Technologies, 2018.
- [88] A. Tsouvalas, Y. Peng, and A.V. Metrikine. A pile-soil-water vibroacoustic model based on a mode matching method. In *Proceedings of the 5th Underwater Acoustics Conference and Exhibition 2019 (UACE2019), Hersonissos, Greece, 30 June–5 July 2019; pp. 667–674.*, 2018.
- [89] A. Tsouvalas and A. V. Metrikine. A three-dimensional vibroacoustic model for the prediction of underwater noise from offshore pile driving. *Journal of Sound and Vibration*, 333(8):2283–2311, 2014.
- [90] C. L. Pekeris. *Theory of propagation of explosive sound in shallow water*, volume 27, pages 1–117. Geological Society of America, 1948.
- [91] W. M. Ewing, W. S. Jardetzky, and F. Press. *Elastic Waves in Layered Media*. Lamont Geological Observatory Contribution; No. 189. McGraw-Hill, New York, 1957.
- [92] C. L. Bartberger. Comparison of two normal-mode solutions based on different branch cuts. *The Journal of the Acoustical Society of America*, 61(6):1643–1643, 1977.
- [93] D. C. Stickler. Normal-mode program with both the discrete and branch line contributions. *The Journal of the Acoustical Society of America*, 57(4):856–861, 1975.
- [94] M. J. Buckingham and E. M. Giddens. On the acoustic field in a pekeris waveguide with attenuation in the bottom half-space. *The Journal of the Acoustical Society of America*, 119(1):123–42, 2006.
- [95] H.P. Bucker. Propagation in a liquid layer lying over a liquid half-space (pekeris cut). *The Journal of the Acoustical Society of America*, 65(4):906–908, 1979.
- [96] C. L. Bartberger. Comparison of two normal-mode solutions based on different branch cuts. *The Journal of the Acoustical Society of America*, 61(6):1643–1643, 1977.
- [97] D. C. Stickler. Normal-mode program with both the discrete and branch line contributions. *The Journal of the Acoustical Society of America*, 57(4):856–861, 1975.
- [98] E. K. Westwood, C. T. Tindle, and N. R. Chapman. A normal mode model for acousto-elastic ocean environments. *The Journal of the Acoustical Society of America*, 100(6):3631–3645, 1996.
- [99] J. Zhu and Y. Lu. Asymptotic solutions of the leaky modes and pml modes in a pekeris waveguide. *Wave Motion*, 45(3):207–216, 2008.
- [100] F. Press and M. Ewing. Propagation of explosive sound in a liquid layer overlying a semi-infinite elastic solid. *Geophysics*, 15(3):426–446, 1950.

[101] W. M. Ewing, W. S. Jardetzky, and F. Press. *Elastic waves in layered media*. Lamont Geological Observatory contribution; no. 189. McGraw-Hill, New York, 1957.

- [102] K. Aki and P. G. Richards. *Quantitative seismology*. University Science Books, Sausalito, Calif., 2nd ed. edition, 2002.
- [103] H. Schmidt and F. B. Jensen. A full-wave solution for propagation in multilayered viscoelastic media with application to gaussian-beam reflection at fluid-solid interfaces. Journal of the Acoustical Society of America, 77(3):813–825, 1985.
- [104] A. A. Bakr. *Axisymmetric Potential Problems*. Springer Berlin Heidelberg, Berlin, Heidelberg, 1986.
- [105] F.M. Labianca. Normal modes, virtual modes, and alternative representations in the theory of surface-duct sound propagation. *The Journal of the Acoustical Society of America*, 53(4):1137–1147, 1973.
- [106] C. T. Tindle, A. P. Stamp, and K. M. Guthrie. Virtual modes and the surface boundary condition in underwater acoustics. *Journal of Sound and Vibration*, 49(2):231–240, 1976.
- [107] E. K. Westwood, C. T. Tindle, and N. R. Chapman. A normal mode model for acousto-elastic ocean environments. *The Journal of the Acoustical Society of America*, 100(6):3631–3645, 1996.
- [108] M. Abramowitz and I. A. Stegun. *Handbook of mathematical functions with formulas, graphs, and mathematical tables.* United States. National Bureau of Standards. Applied mathematics series, 55. U.S. Govt. Print. Off., Washington, 1964.
- [109] J. D. Achenbach. Wave propagation in elastic solids. North-Holland series in applied mathematics and mechanics, v. 16. North-Holland Pub. Co.; American Elsevier Pub. Co., Amsterdam New York, 1973.
- [110] J. Berenger. A perfectly matched layer for the absorption of electromagnetic waves. *Journal of Computational Physics*, 114(2):185–200, 1994.
- [111] Q. H. Liu. Perfectly matched layers for elastic waves in cylindrical and spherical coordinates. *The Journal of the Acoustical Society of America*, 105(4):2075–2084, 04 1999.
- [112] COMSOL AB. COMSOL Multiphysics® v. 5.4. COMSOL AB, Stockholm, Sweden, 2020.
- [113] R. Y. S. Pak and B. B. Guzina. Three-dimensional green's functions for a multilayered half-space in displacement potentials. *Journal of Engineering Mechanics*, 128(4):449–461, 2002.
- [114] A. Khojasteh, M. Rahimian, M. Eskandari, and R.Y.S. Pak. Three-dimensional dynamic green's functions for a multilayered transversely isotropic half-space. *International Journal of Solids and Structures*, 48(9):1349–1361, 2011.

[115] D. E. Beskos. Boundary element methods in dynamic analysis. *Applied Mechanics Reviews*, 40(1):1–23, 1987.

- [116] F. B. Jensen, W. A. Kuperman, M. B. Porter, and H. Schmidt. *Computational Ocean Acoustics*. Springer New York, 2011.
- [117] S. Marburg. Six boundary elements per wavelength: is that enough? *Journal of Computational Acoustics*, 10(01):25–51, 2002.
- [118] S. Lippert, M. Nijhof, T. Lippert, D. Wilkes, A. Gavrilov, K. Heitmann, M. Ruhnau, O. von Estorff, A. Schäfke, I. Schäfer, J. Ehrlich, A. MacGillivray, J. Park, W. Seong, M. A. Ainslie, C. de Jong, M. Wood, L. Wang, and P. Theobald. COMPILE—A Generic Benchmark Case for Predictions of Marine Pile-Driving Noise. *IEEE Journal of Oceanic Engineering*, 41(4):1061–1071, oct 2016.
- [119] Stephan Lippert, Tristan Lippert, Kristof Heitmann, and Otto Von Estorff. Prediction of underwater noise and far field propagation due to pile driving for offshore wind farms. *Proceedings of Meetings on Acoustics*, 19(1):070036, 06 2013.
- [120] Marten J. J. Nijhof, Bas Binnerts, Christ A. F. De Jong, and Michael A. Ainslie. An efficient model for prediction of underwater noise due to pile driving at large ranges. In *INTER-NOISE and NOISE-CON Congress and Conference Proceedings*, volume 249, pages 5505–5514. Institute of Noise Control Engineering, 2014.
- [121] J.D. Kaplunov, L. Yu Kossovich, and E.V. Nolde. *Dynamics of Thin Walled Elastic Bodies*. Academic Press, 1998.
- [122] H.Ö Sertlek, M.A. Ainslie, and K.D. Heaney. Analytical and numerical propagation loss predictions for gradually range-dependent isospeed waveguides. *IEEE Journal of Oceanic Engineering*, 44(4):1240–1252, 2019.
- [123] B. A. McCollom and J. M. Collis. Root finding in the complex plane for seismo-acoustic propagation scenarios with green's function solutions. *The Journal of the Acoustical Society of America*, 136(3):1036, 2014.
- [124] Homer P. Bucker. Propagation in a liquid layer lying over a liquid half-space (pekeris cut). *The Journal of the Acoustical Society of America*, 65(4):906–908, 1979.
- [125] M. J. Buckingham and E. M. Giddens. On the acoustic field in a pekeris waveguide with attenuation in the bottom half-space. *The Journal of the Acoustical Society of America*, 119(1):123–42, 2006.
- [126] M.K. Prior, A.J. Duncan, H.Ö. Sertlek, and M.A. Ainslie. Modeling acoustical pressure and particle acceleration close to marine seismic airguns and airgun arrays. *IEEE Journal of Oceanic Engineering*, 44(3):611–620, 2019.
- [127] Y. Peng and A. Tsouvalas. Uncertainty quantification of soil properties in offshore pile-driving noise predictions with the air-bubble curtain system. In *Proceedings of the 7th International Conference and Exhibition on Underwater Acoustics (UACE2023)*, Kalamata, Greece, June 2023.

[128] MD McKay, RJ Beckman, and WJ Conover. Selecting values of input variables in the analysis of output from a computer code. *Technometrics*, 21:239–245, 1979.

- [129] R.G. McClarren. Uncertainty quantification and predictive computational science: a foundation for physical scientists and engineers. Springer, 2018.
- [130] C. Genest and A. Favre. Everything you always wanted to know about copula modeling but were afraid to ask. *Journal of Hydrologic Engineering*, 12(4):347–368, 2007.
- [131] B. Abdous and K. Ghoudi. Non-parametric estimators of multivariate extreme dependence functions. *Journal of Nonparametric Statistics*, 17(8):915–935, 2005.
- [132] C. Genest, J. Quessy, and B. Rémillard. Goodness-of-fit procedures for copula models based on the probability integral transformation. *Scandinavian Journal of Statistics*, 33(2):337–366, 2006.
- [133] G. Biau and M. Wegkamp. A note on minimum distance estimation of copula densities. *Statistics & Probability Letters*, 73(2):105–114, 2005.
- [134] H. Joe. Parametric families of multivariate distributions with given margins. *Journal of Multivariate Analysis*, 46(2):262–282, 1993.
- [135] A. Tsouvalas, Y. Peng, G. Caumo, and O. M. Napoles. Uncertainty quantification in underwater noise prediction for offshore pile driving. In *Proceedings of the 28th International Congress on Sound and Vibration (ICSV2022)*, Singapore, July 2022.
- [136] Y. Peng and A. Tsouvalas. A three-dimensional model of an air bubble curtain in offshore pile driving. *Journal of Physics: Conference Series*, 2647(23):232006, 2024.
- [137] Y.A. Hegazy and P. Mayne. Statistical correlations between vs and cpt data for different soil types. *Proc. Cone Penetration Testing (CPT'95)*, 2:173–178, 01 1995.
- [138] S. Burns and P. Mayne. Small and high-strain measurements of in situ soil properties using the seismic cone penetrometer. *Transportation Research Record*, 1548:81–88, 11 1996.
- [139] H. J. Lengkeek and R. B. J. Brinkgreve. *CPT-Based Unit Weight Estimation Extended to Soft Organic Clays and Peat: An Update*, pages 503–508. June 2022.
- [140] Y.A. Hegazy and P. Mayne. Statistical correlations between vs and cone penetration data for different soil types. In *Proceedings of the international symposium on cone penetration testing, CPT*, volume 95, pages 173–178, 1995.
- [141] M.J. Buckingham. Wave speed and attenuation profiles in a stratified marine sediment: Geo-acoustic modeling of seabed layering using the viscous grain shearing theory. *The Journal of the Acoustical Society of America*, 148(2):962–974, 08 2020.
- [142] Y. Hegazy and P. Mayne. A global statistical correlation between shear wave velocity and cone penetration data. In *Geotechnical Special Publication*, pages 243–248, May 2006.

[143] P. Robertson and K Cabal. Guide to Cone Penetration Testing, 7th ed. Gregg Drilling LLC., Martinez, CA, USA, 2022.

- [144] P. Mayne. Stress-strain-strength-flow parameters from enhanced in situ tests. international conference on in situ measurement of soil properties and case histories. *Situ 2001*, pages 27–48, 01 2001.
- [145] P. Mayne, J. Peuchen, and D. Bouwmeester. Soil unit weight estimation from cpts. In *Proceedings of the 2nd International Symposium on Cone Penetration Testing (CPT'10)*, Huntington Beach, California, USA, May 2010.
- [146] E.L. Hamilton. Geoacoustic modeling of the sea floor. *The Journal of the Acoustical Society of America*, 68(5):1313–1340, 11 1980.
- [147] E.L. Hamilton. Vp/Vs and Poisson's ratios in marine sediments and rocks. *The Journal of the Acoustical Society of America*, 66(4):1093–1101, 10 1979.
- [148] E.L. Hamilton. Sound velocity as a function of depth in marine sediments. *The Journal of the Acoustical Society of America*, 78(4):1348–1355, 10 1985.
- [149] E.L. Hamilton. Attenuation of shear waves in marine sediments. *The Journal of the Acoustical Society of America*, 60(2):334–338, 08 1976.
- [150] E.L. Hamilton. Sound attenuation as a function of depth in the sea floor. *The Journal of the Acoustical Society of America*, 59(3):528–535, 03 1976.
- [151] Alick C. Kibblewhite. Attenuation of sound in marine sediments: A review with emphasis on new low-frequency data. *The Journal of the Acoustical Society of America*, 86(2):716–738, 08 1989.
- [152] M. A. Biot. Theory of Propagation of Elastic Waves in a Fluid-Saturated Porous Solid. I. Low-Frequency Range. *The Journal of the Acoustical Society of America*, 28(2):168–178, 03 1956.
- [153] M. A. Biot. Theory of Propagation of Elastic Waves in a Fluid-Saturated Porous Solid. II. Higher Frequency Range. *The Journal of the Acoustical Society of America*, 28(2):179–191, 03 1956.
- [154] M. A. Biot. Mechanics of Deformation and Acoustic Propagation in Porous Media. *Journal of Applied Physics*, 33(4):1482–1498, 04 1962.
- [155] M. A. Biot. Generalized Theory of Acoustic Propagation in Porous Dissipative Media. *The Journal of the Acoustical Society of America*, 34(9A):1254–1264, 09 1962.
- [156] Robert D. Stoll. Experimental studies of attenuation in sediments. *The Journal of the Acoustical Society of America*, 66(4):1152–1160, 10 1979.
- [157] Robert D. Stoll. Theoretical aspects of sound transmission in sediments. *The Journal of the Acoustical Society of America*, 68(5):1341–1350, 11 1980.

[158] Robert D. Stoll. Marine sediment acoustics. *The Journal of the Acoustical Society of America*, 77(5):1789–1799, 05 1985.

- [159] Allan D. Pierce and William M. Carey. Low-frequency attenuation of acoustic waves in sandy/silty marine sediments. *The Journal of the Acoustical Society of America*, 124(5):EL308–EL312, 10 2008.
- [160] Frederick A. Bowles. Observations on attenuation and shear-wave velocity in fine-grained, marine sediments. *The Journal of the Acoustical Society of America*, 101(6):3385–3397, 06 1997.
- [161] F.B. Jensen, W.A. Kuperman, M.B. Porter, and H. Schmidt. *Computational Ocean Acoustics*. Springer New York, 2011.
- [162] M.J. Buckingham. Compressional and shear wave properties of marine sediments: Comparisons between theory and data. *The Journal of the Acoustical Society of America*, 117(1):137–152, 01 2005.
- [163] R. Christensen. *Plane Answers to Complex Questions: The Theory of Linear Models.* Springer, 5th edition, 2020.
- [164] Erich L. Lehmann and Joseph P. Romano. *Testing Statistical Hypotheses*. Springer, fourth edition, 2022.
- [165] S. Mahdi and M. Cenac. Estimating parameters of Gumbel distribution using the methods of moments, probability weighted moments and Maximum Likelihood. *Revista de Matematica: Teoria y Aplicaciones*, 12(1 & 2):151–156, 2005.
- [166] H. Akaike. A new look at the statistical model identification. *IEEE Transactions on Automatic Control*, 19(6):716–723, 1974.
- [167] H. C. Thode. Testing for normality. Statistics, textbooks and monographs. CRC Press, 2002.
- [168] J. Harry. Dependence modeling with copulas. CRC Press, 2015.
- [169] A. Sokolichin, G. Eigenberger, and A. Lapin. Simulation of buoyancy driven bubbly flow: Established simplifications and open questions. *AIChE Journal*, 50(1):24–45, 2004.
- [170] F. Lehr, M. Millies, and D. Mewes. Bubble-size distributions and flow fields in bubble columns. *AIChE Journal*, 48(11):2426–2443, 2002.
- [171] J. H. Milgram. Mean flow in round bubble plumes. *Journal of Fluid Mechanics*, 133:345–376, 1983.
- [172] J. K. Walters and J. F. Davidson. The initial motion of a gas bubble formed in an inviscid liquid. *Journal of Fluid Mechanics*, 17(03):321, 1963.
- [173] R. Clift, J.R. Grace, and M.E. Weber. *Bubbles, drops, and particles*. Academic Press, New York, 1978.

[174] H. Voit, R. Zeppenfeld, and A. Mersmann. Calculation of primary bubble volume in gravitational and centrifugal fields. *Chemical Engineering & Technology*, 10(1):99–103, 1987.

- [175] J. Rustemeier. Optimierung von Blasenschleiern zur Minderung von Unterwasser-Rammschall (Optimization of bubble curtains to reduce underwater pile-driving noise). PhD thesis, Institut für Statik und Dynamik, Hannover, Germany, 2016.
- [176] Y. Peng, A. Jarquin Laguna, and A. Tsouvalas. A multi-physics approach for modelling noise mitigation using an air-bubble curtain in impact pile driving. *Frontiers in Marine Science*, 10, 2023.
- [177] Ascher H. Shapiro. *The dynamics and thermodynamics of compressible fluid flow.* Ronald Press, New York, 1953.
- [178] G. Nehls and M. Bellmann. Weiterentwicklung und erprobung des "großenblasenschleiers" zur minderung der hydroschallemissionen bei offshore-rammarbeiten: Schlussbericht. Technical report, Bio-Consult SH GmbH & Company KG; itap GmbH Oldenburg; Hydrotechnik Lubeck, 2016.
- [179] E.S. Menon. *Transmission Pipeline Calculations and Simulations Manual.* Gulf Professional: Waltham, MA, 2015.
- [180] S.V. Tsinopoulos, J.P. Agnantiaris, and D. Polyzos. An advanced boundary element/fast fourier transform axisymmetric formulation for acoustic radiation and wave scattering problems. *The Journal of the Acoustical Society of America*, 105(3):1517–1526, 1999.
- [181] G. Ozkan and Y. Mengi. On the use of fft algorithm for the circumferential co-ordinate in boundary element formulation of axisymmetric problems. *International Journal for Numerical Methods in Engineering*, 40(13):2385–2412, 1997.
- [182] O. Sertlek, Y. Peng, and A. Tsouvalas. *Modelling Pile-Driving Sound and Mitigation in Realistic Environments*, pages 1–12. Springer International Publishing, Cham, 2023.
- [183] A. Farcas, P.M. Thompson, and N.D. Merchant. Underwater noise modelling for environmental impact assessment. *Environmental Impact Assessment Review*, 57:114–122, 2016.
- [184] LM Brekhovskikh. The average field in an underwater sound channel. *Sov. Phys. Acoust*, 11(2):126–134, 1965.
- [185] D.E. Weston. Intensity-range relations in oceanographic acoustics. *Journal of Sound and Vibration*, 18(2):271–287, 1971.
- [186] M.D. Collins. A split-step Padé solution for the parabolic equation method. *The Journal of the Acoustical Society of America*, 93(4):1736–1742, 04 1993.
- [187] M.D. Collins. The stabilized self-starter. *The Journal of the Acoustical Society of America*, 106(4):1724–1726, 10 1999.

GLOSSARY 181

- [188] Robert J Urick. Principles of underwater sound. New York: McGraw-Hill., 1975.
- [189] Mardi C. Hastings. Whitlow W.L. Au. *Principles of marine bioacoustics*. New York : Springer., 2008.
- [190] Michael B Porter. The kraken normal mode program. *Naval Research Laboratory, Washington DC*, 1992.
- [191] Michael B Porter and Yong-Chun Liu. Finite-element ray tracing. *Theoretical and computational acoustics*, 2:947–956, 1994.
- [192] H.O. Sertlek. Aria of the Dutch North Sea. PhD thesis, University of Leiden, 2016.
- [193] P.C. Etter. Underwater acoustic modeling and simulation. CRC press, 2018.
- [194] H.Ö Sertlek and M.A. Ainslie. A depth-dependent formula for shallow water propagation. *The Journal of the Acoustical Society of America*, 136(2):573–582, 08 2014.
- [195] E.M. Salomons, B. Binnerts, K. Betke, and A.M. von Benda-Beckmann. Noise of underwater explosions in the north sea. a comparison of experimental data and model predictions. *The Journal of the Acoustical Society of America*, 149(3):1878–1888, 03 2021.
- [196] Allan D. Pierce. Extension of the Method of Normal Modes to Sound Propagation in an Almost-Stratified Medium. *The Journal of the Acoustical Society of America*, 37(1):19–27, 01 1965.
- [197] H. Weinberg and R. Burridge. Horizontal ray theory for ocean acoustics. *The Journal of the Acoustical Society of America*, 55(1):63–79, 01 1974.
- [198] Juan I. Arvelo and H. Überall. Adiabatic normal-mode theory of sound propagation including shear waves in a range-dependent ocean floor. *The Journal of the Acoustical Society of America*, 88(5):2316–2325, 11 1990.
- [199] Emodnet human activities data portal. www.emodnet-humanactivities. eu. Accessed: 2024-03-15.

# ACKNOWLEDGEMENTS

I feel fortunate to have worked with so many great researchers during my PhD. Their guidance, insights, and encouragement have shaped my journey.

I am deeply grateful for the support and mentorship I received from Apostolos throughout my PhD. My research was built upon the strong foundations he laid during his own PhD, and his thesis—alongside several other classical books on wave propagation and ocean acoustics—became an essential part of my learning. Apostolos' work spans an impressive range, from the dynamics of various structures to fundamental wave propagation and nonlinear dynamics.

Thank you for being a kind and thoughtful leader, a supportive mentor, and an inspiring colleague. Your openness to discussion, no matter the complexity of the problem, has been invaluable. You not only guided me through research challenges but also encouraged me to grow as a teacher and researcher. By giving me opportunities to lead projects, organize courses and modules, and take on responsibilities beyond research, you helped me build confidence in both academia and education. For that, I am truly grateful.

Andrei's work bridges everything from practical engineering problems to the most fundamental aspects of wave propagation and structural dynamics. One of the things I admire most about him is his ability to see the world through the lens of waves—and to explain even the most complex physical concepts in the simplest and most relatable way. That clarity and depth of understanding is something I aspire to.

Before I fully realized Andrei's remarkable achievements in academia, I knew him simply as one of the best teachers I've ever had, dating back to my master's studies. If I were to borrow the words of Tao, who always refer to you as 老师 (lǎoshī) in Chinese, it is because you truly embody the essence of a teacher, mentor, and so much more. The impact you have had on me—and on so many other researchers and scientists—will continue to resonate far beyond this PhD.

Many people from the Offshore and DSS groups support me during my PhD. Ozkan, thank you for the research collaboration and the countless discussions we had. I deeply appreciate how you introduced me to everyone you knew at the UACE conference in Greece and encouraged me to grow as an independent researcher. Your enthusiasm for underwater acoustics made a real impact on my journey. Thanasis, I've really valued our discussions on research, career paths, and daily life—I look forward to more collaborations in the future. Timo, thank you for the discussions on our research and for sharing your experience of parenthood. I also appreciate the teamwork and shared vision in co-founding Delft Cymatics. Rens, your enthusiasm, hard work, and willingness to help have been truly inspiring. Thank you for all the interesting discussions and your constant support. Ina, it was a privilege to be your daily supervisor for your PhD and I have no doubt that your dedication and hard work will take you far. Peter, I don't know if you remember, but in my very first week as a PhD student, you helped me install my first Fortran program—one of those small but pivotal moments. Thank you for all the great conversations over the

184 Acknowledgements

years. Tao, Yang, and Mingjuan, you introduced me to the group when I first arrived, and I've truly enjoyed our discussions whenever I had questions, our hotpot and dumpling dinners, and your support throughout my PhD. Thank you, Antonio, for collaborating with me on modelling the air-bubble curtain system. It has been a pleasure working with you throughout the process. Matías, thank you for being my office mate, my paranymph, and a great friend. Your energy is contagious, and I've always appreciated our chats. It's been a special experience to go through parenthood at the same time. A special thank you to the lab staff—Kees van Beek, for your invaluable guidance in choosing and setting up the hydrophones, and Peter de Vries, for making the acrylic tank functional. I can't name everyone in the office, but I cherish every coffee chat, office conversation, seminar, drink, party at Andrei's house, and Christmas dinner with you all. To my co-founders at Delft Cymatics, thank you for making the journey of entrepreneurship so rewarding. To my days at YES!Delft, Edward, I am grateful to you for selecting me to work on the underwater acoustic project, as a master's thesis student. That opportunity was the spark that start my passion for acoustics and everything that followed. Marco, Willem, and Jeroen, thank you for those early days working in the company on the Helmholtz resonators.

I never imagined Frisbee would become such a big part of my life, but without Valentina and Francesca, I probably wouldn't have played nearly as much. It turned out to be one of the best decisions I made—not just for fun but for maintaining a healthy work-life balance, especially during the PhD years. Francesca, thank you for introducing me to the Frisbee world and for simply being such a warm and positive person, bringing great energy into our life. Valentina, sometimes you question the meaning of winning all the games and being one of the best female players in the Netherlands—but let's be honest, doesn't it feel great sometimes? Life throws us challenges, so one can truly live it to the fullest. Thank you for being more than a colleague, teammate, and friend. To my other friends in the Netherlands—thank you for your support, for making the Dutch weather more bearable on those windy and rainy days: Juan, Yolik, Reinier, Xiaoye, Fang, Nuoyi, Xiaoyu, Li Tan, Xiaozhi, Ding, Mengdi, Annika, Iris, Christophe and Giulia. I cannot imagine life without my cats. Thank you, Bo and Sisi, for always keeping me company during days and nights at my desk. Bo even made his own contribution to this thesis by typing random code into my programs.

My gratitude also goes to my family and friends in China. 谢谢老爸老妈对于我博士研究的支持,对于宝贝的悉心照顾,感谢一路成长给予我的信任,自由与爱护。谢谢我远在合肥的家人们,你们圆满了我对于家乡和亲情的定义。感谢刘畅畅,拥有和你一起成长的童年很幸福。还要感谢一路成长给予我支持的老师们和朋友们——小学,初中,高中,大学,你们让我的每一个学生时代充满美好的记忆。感谢张珏,徐园明,夏玲玲,江璐璐,陈昊天,刘星雨,白雪冰,陆亚萍。特别感谢"My Brilliant Friend",张琪,周雪君,我的童年伙伴和挚友,感谢你们从未让距离和时差阻碍我们的友谊。

Becoming a mother was never part of the plan during my PhD, and I couldn't have done it without Rui. You supported me through every step of this journey, and together we have grown—not just as individuals, but as parents. Sharing this journey with you, knowing that we are building a life together, raising Han and growing old, is one of the greatest experiences I could ever imagine.

# **CURRICULUM VITÆ**

## Yaxi Peng

1992/10/28 Date of birth in Hefei, Anhui, China

## **Academic Experience**

2011-2015	Bachelor in Civil Engineering				
	Hohai University, Nanjing, China				
2014-2015	Bachelor in Civil Engineering				
	University of Dundee, Scotland, UK				
2015-2017	Master in Offshore & Dredging Engineering				
	Delft University of Technology, the Netherlands				
2018-2024	PhD research, Delft University of Technology				
	Thesis: Underwater sound propagation and mitigation in				
	offshore pile driving Promotor: Prof.dr. A. V. Metrikine				
	Promotor: Dr.ir. A. Tsouvalas				
2022-2024	Lecturer				
	Delft University of Technology				
2024-Now	Postdoctoral researcher				
	Delft University of Technology				

## **Work Experience**

2017-2018	SeaState5, YesDelft, Delft
2024-Now	Delft Cymatics, Delft

# LIST OF PUBLICATIONS

#### Journal publications

- 1. Peng, Y., Tsouvalas, A., Stampoultzoglou, T., Metrikine, A. (2021). A fast computational model for near- and far-field noise prediction due to offshore pile driving. The Journal of the Acoustical Society of America, 149(3), 1772–1772. https://doi.org/10.1121/10.0003752
- 2. **Peng, Y.**, Tsouvalas, A., Stampoultzoglou, T., Metrikine, A. (2021). Study of the sound escape with the use of an air bubble curtain in offshore pile driving. Journal of Marine Science and Engineering, 9(2), 232–232. https://doi.org/10.3390/jmse9020232
- 3. Peng, Y., Jarquin Laguna, A., Tsouvalas, A. (2023). A multi-physics approach for modelling noise mitigation using an air-bubble curtain in impact pile driving. Frontiers in Marine Science, 10. https://doi.org/10.3389/fmars.2023.1134776
- 🖹 4. Sertlek, O., **Peng, Y.**, Tsouvalas, A. (2024). Modelling Pile-Driving Sound and Mitigation in Realistic Environments. In: Popper, A.N., Sisneros, J., Hawkins, A.D., Thomsen, F. (eds) The Effects of Noise on Aquatic Life. Springer, Cham. https://doi.org/10.1007/978-3-031-10417-6-149-1
- 5. Sertlek, O., Peng, Y., Michael A. Ainslie, Matthew W. Koessler, Alexander O. MacGillivray, Elizabeth T. Küsel, Alexander M. von Benda-Beckmann, Tsouvalas, A. (2024). Effects of sediment properties, distance from source, and frequency weighting on sound pressure and sound pressure kurtosis for marine airgun signatures. The Journal of the Acoustical Society of America, 156 (6): 4242–4255. https://doi.org/10.1121/10.0034709

#### Conference publications

- 1. Peng, Y., Tsouvalas, A., Metrikine, A. (2018). Modelling and Development of a Resonator-Based Noise Mitigation System for Offshore Pile Driving. Proceedings of the 25th International Congress on Sound and Vibration (ICSV2018), Hiroshima, Japan.
- 2. Peng, Y., Tsouvalas, A., Metrikine, A. (2019). Underwater Noise Generated by Offshore Pile Driving: A Pile-Soil-Water Vibroacoustic Model Based on a Mode Matching Method. Proceedings of the 5th International Conference and Exhibition on Underwater Acoustics (UACE2019), Crete, Greece.
- 3. Tsouvalas, A., Molenkamp, T., Canny, K., Kroon, D., Versluis, M., Peng, Y., Metrikine, A. (2020).

  A Mode Matching Technique for the Seismic Response of Liquid Storage Tanks Including Soil-Structure Interaction, EASD Procedia EURODYN, International Conference on Structural Dynamics, Athens, Greece.

188 List of Publications

4. Peng, Y., Tsouvalas, A., Metrikine, A. (2020). A Coupled Modelling Approach for the Fast Computation of Underwater Noise Radiation from Offshore Pile Driving, EASD Procedia EURODYN, International Conference on Structural Dynamics, Athens, Greece.

- 5. Tsouvalas, A., Peng, Y., Caumo, G., Napoles, O. M. (2022). Uncertainty Quantification in Underwater Noise Prediction for Offshore Pile Driving, Proceedings of the 28th International Congress on Sound and Vibration (ICSV2022), Singapore.
- 7. Peng, Y., Tsouvalas, A. (2023). Uncertainty Quantification of Soil Properties in Offshore Pile-Driving Noise Predictions with the Air-Bubble Curtain System, Proceedings of the 7th International Conference and Exhibition on Underwater Acoustics (UACE2023), Kalamata, Greece.
- 🖹 8. **Peng, Y.**, Tsouvalas, A. (2024). A Three-Dimensional Model of an Air Bubble Curtain in Offshore Pile Driving, Journal of Physics: Conference Series: 2647(23):232006.
- Peng, Y., Tsetas, A., Molenkamp, T., Sertlek, O., Tsouvalas, A.(2024). Underwater sound modelling and sound mapping in vibratory pile driving, 28th International Congress on Sound and Vibration (ICSV2024), Amsterdam, Netherlands.